

Dissolution-precipitation reactions in the system $\text{Al}_2\text{O}_3\text{-SiO}_2\text{-H}_2\text{O}$
and the formation of Al_2SiO_5

vorgelegt von
Dipl.-Min.
Dina Schultze
geb. in Zürich

von der Fakultät VI - Planen Bauen Umwelt
der Technischen Universität Berlin
zur Erlangung des akademischen Grades

Doktor der Naturwissenschaften
- Dr.-rer.nat. -

genehmigte Dissertation

Promotionsausschuss:

Vorsitzender: Prof. Dr. Wilhelm Dominik
Gutachter: Prof. Dr. Gerhard Franz
Gutachter: Prof. Dr. Max Wilke
Gutachter: Prof. Dr. Wilhelm Heinrich

Tag der wissenschaftlichen Aussprache: 10. November 2017

Berlin 2018

“Progress is made by trial and failure; the failures are generally a hundred times more numerous than the successes; yet they are usually left unchronicled.” (William Ramsay)

“...eine räthselhafte Erscheinung lässt sich nicht durch noch viel räthselhaftere vermuthete und nie beobachtete Vorgänge erklären.”
(Albert Heim)

Abstract

The study of mineral replacement reactions can provide detailed insight into chemical processes, if experimental simulation and natural observation are combined. Among all chemical systems, the Al_2O_3 - SiO_2 - H_2O is one of the most intensely studied but some of our knowledge about it is still inconsistent. Especially problematic is the inhibited reaction of corundum and quartz to Al_2SiO_5 polymorphs (kyanite, sillimanite, andalusite) in experiments, which appears to proceed without obstruction in nature. This reaction was the scope of this thesis and object to natural investigations and experiments likewise, in that the dissolution precipitation mechanisms during Al_2SiO_5 corona formation on corundum was studied.

Two natural samples of kyanite corona growth on corundum, from different geological contexts were studied in order to comprehend the crucial parameters of the reaction. Kyanite did not form as a result of silica influx via fluid into the silica undersaturated rocks, but formed between corundum porphyroblasts and adjacent muscovite or feldspar. The latter two underwent alteration and ultimately decomposition due to the interaction with alkali deficient fluids. Potassium and minor Na were leached of the aluminosilicates and removed along with the fluid, thereby providing silica to the kyanite growth along the corundum interface. Crystallographic characteristics of the corundum porphyroblast influence the growth pattern of kyanite in the corona, indicating prominent dissolution parallel to (0001) and limited dissolution perpendicular to (0001) of corundum.

Experiments on Al_2SiO_5 corona growth during the interaction of corundum single crystals with quartz saturated aqueous fluid or hydrous silicate melt (from dehydrating phyllosilicates) were performed in a P-T range of 500-1200 °C and 2-20 kbar, as approximation to the natural findings. As a result of fluid mediated Si diffusion the corundum developed a reaction rim, in which excess silica formed nanometer wide layers along the (0001) plane in the corundum host comparable to Si tetrahedral layers in phyllosilicates. The nano-phase allowed for accelerated Si influx parallel to (0001) and subsequent precipitation of quartz inside corundum instead of Al_2SiO_5 . Dissolution in [0001] of corundum in these runs was passivated. Moreover, thin plates of corundum precipitated in several experimental runs from fluid and silicate melt along with quartz. The shape of corundum with large basal plane and vanishingly small faces in {01 $\bar{1}$ 2} reflects inhibited growth in [0001] caused by the same silicate nano-layers as found in diffusion rims. This silicate nano-layer appears to have a profound impact on the chemical reactions of the ASH system, as it prevents the reaction of corundum and quartz to Al_2SiO_5 by shielding both bulk phases from another. The nucleation of Al_2SiO_5 in experiments may be suppressed compared to corundum and quartz due to the occurrence of this nano-phase.

Comparison of natural and experimental findings indicates that the interaction of corundum with silica saturated water or hydrous silicate melt does not lead to Al_2SiO_5 formation at the expense of corundum but instead supports the metastability of quartz and corundum, despite or even due to the presence of fluid. The formation of Al_2SiO_5 in natural samples points to more complex nucleation processes than can be recreated in closed system simulations (e.g. including fluid flux). Similarities emphasize the influence of crystallographic parameters of corundum on the studied dissolution precipitation processes. A passivated dissolution perpendicular and enhanced corundum dissolution parallel to the basal plane is observed in both experiments and natural samples. Whether silicate nano-layers also influence mineral reactions in nature will require further investigation.

Zusammenfassung

Die Kombination von natürlichen und experimentellen Beobachtungen kann beim Studium von Mineralumwandlungsprozessen detaillierte Einsicht in mineralchemische Reaktionen bieten. Unter allen chemischen Systemen ist das $\text{Al}_2\text{O}_3\text{-SiO}_2\text{-H}_2\text{O}$ eines der am intensivsten untersuchten, und dennoch ist unser Wissen über es lückenhaft. So ist die Reaktion von Korund und Quarz zu den Polymorphen von Al_2SiO_5 (Disthen, Sillimanit, Andalusit) in Experimenten gehemmt, obwohl sie in der Natur ungehindert abzulaufen scheint. Diese Reaktion steht im Fokus der vorgelegten Arbeit insofern, als dass die Lösungs-Fällungs-Mechanismen bei der Al_2SiO_5 -Koronabildung um Korund sowohl aus natürlicher als auch aus experimenteller Sicht untersucht worden sind.

Zwei natürliche Proben von Disthen-Korona um Korund, von unterschiedlicher geologischer Herkunft wurden untersucht, um die entscheidenden Reaktionsparameter zu bestimmen. Disthen bildet sich nicht aufgrund von Silikat-Eintrag in das silikatuntersättigte Gestein, sondern entsteht aus der Reaktion zwischen Korund und angrenzendem Muskovit oder Feldspat. Die letzteren beiden werden während der Interaktion mit alkaliuntersättigten Fluiden alteriert und zersetzt. Kalium und untergeordnet Na werden dabei aus den Alumosilikaten gelöst und im Fluid abtransportiert, was Silikat für das Disthen Wachstum im Kontakt mit dem Korund freisetzt. Kristallographische Charakteristika des Korunds beeinflussen das Wachstumsmuster des Disthens in der Korona und deuten auf eine gesteigerte Korund Löslichkeit parallel, und eine stark geminderte Löslichkeit senkrecht zu (0001).

Experimente zum Al_2SiO_5 -Koronawachstum als Resultat der Interaktion von Korund mit quarz-gesättigter wässriger Phase oder mit hydratisierter Silikatschmelze (aus Phyllosilikatzusammenbruch) in Annäherung an die natürlichen Proben, wurden bei 500-1200 °C und 2-20 kbar durchgeführt. In fluid-induzierten Si-Diffusionssäumen bildet überschüssiges Silikat Nanometer breite Lagen entlang (0001) im Korund, vergleichbar mit Si-Tetrahederlagen in Phyllosilikaten. Diese Nanophase erhöht den Si-Eintrag parallel zu (0001) und führt zur Fällung von Quarz, anstelle von Al_2SiO_5 in Korund. In diesen Experimenten ist die Löslichkeit von Korund in [0001] durch Passivierung verlangsamt. Ausserdem bildeten sich in mehreren Experimenten dünne Korundplättchen zusammen mit Quarz. Der Habitus des Korunds, mit einer sehr ausgeprägten Basisfläche und verschwindend kleinen Flächen in $\{01\bar{1}2\}$, deutet auf gehindertes Wachstum in [0001] aufgrund der Anwesenheit derselben silikatischen Nanolagen, wie sie in Lösungssäumen auftreten, hin. Diese silikatische Nanolage scheint einen substanziellen Einfluss auf die chemischen Reaktionen des ASH-Systems zu haben, da sie durch Abschirmung beider Hauptphasen die Umwandlung von Korund und Quarz zu Al_2SiO_5 verhindert. Die Keimbildung von Al_2SiO_5 im Experiment könnte zudem durch das Auftreten der Nanophase gegenüber Korund und Quarz unterdrückt sein.

Der Vergleich von natürlichen und experimentellen Ergebnissen zeigt, dass die Interaktion von Korund mit quarzgesättigtem Fluid oder mit hydratisierter Silikatschmelze nicht zur Bildung von Al_2SiO_5 auf Kosten von Korund führt, sondern die Metastabilität von Quarz und Korund fördert, trotz, oder sogar durch die Anwesenheit von Fluid. Die Bildung von Al_2SiO_5 in natürlichen Proben deutet auf einen komplexeren Keimbildungsvorgang, der nicht im geschlossenen System simuliert werden kann. Der untersuchte Lösungs-Fällungs Prozess scheint hingegen in der Natur und im Experiment von kristallographischen Parametern des Korunds abhängig zu sein. Die passivierte Lösung des Korunds senkrecht, und erhöhte Löslichkeit parallel zu (0001) scheint allgemein gültig. Ob auch in der Natur silikatische Nanolagen Einfluss auf Mineralreaktionen nehmen, muss in weiteren Untersuchungen geklärt werden.

Danksagung

Ich danke Prof. Dr. Gerhard Franz für die Formulierung und Vergabe dieses sehr vielseitigen und spannenden Themas, und für seine Unterstützung während dessen Bearbeitung. Die Jahre die ich mit dieser Arbeit zugebracht habe waren in verschiedenster Weise lehrreich und werden mich immer begleiten.

Prof. Dr. Max Wilke danke ich für seine gewohnt und geschätzt Fokus orientierte Kritik und seine konstruktiven Korrekturen der experimentellen Resultate, sowie für die Begutachtung dieser Arbeit. Prof. Dr. Wilhelm Heinrich danke ich für die Begutachtung der vorliegenden Arbeit und für seine Begeisterung für von mir vorgetragene Zwischenresultate während der Treffen der Forschungsgruppe.

Dr. Friedrich Lucassens Arbeit an Titanit-Koronnen um Rutil in der ersten Phase dieses Projekts und seine Hilfestellung bei verschiedenen experimentellen und thematischen Fragen waren mir wegweisend.

Ein spezieller Dank geht an Dr. Richard Wirth und Anja Schreiber für eine sehr erfolgreiche Zusammenarbeit am Transmissionselektronenmikroskop. Dr. Wirths Begeisterung und hartnäckigen Neugier für Nano-Prozesse hat die häufige Zusammenarbeit am TEM am GeoForschungsZentrum Potsdam zu einer aussergewöhnlichen Erfahrung gemacht.

Für die umfangreiche Unterstützung der Untersuchungen an Rasterelektronenmikroskop und Elektronenmikrosonde geht mein Dank an Iryna Driehorst und Jörg Nissen von der Zentral Einrichtung für Elektronen Mikroskopie and der Technischen Universität Berlin. Und für die Unterstützung der CL-Analysen am Rasterelektronenmikroskop am GFZ geht ein herzlicher Dank an Ilona Schäpan.

Ein ganz spezieller Dank geht an Dr. Bernd Wunder für die Betreuung der Piston Cylinder Experimente und die kreative Beratung von unterschiedlichen experimentellen Ansätzen am GeoForschungsZentrum Potsdam, und an Hans-Peter Nabein für die Nutzung der Hydrothermal Anlage, wann immer unsere hauseigene Anlage in Reparatur war.

Ich bin unendlich dankbar für fünf Jahre hitzige und fruchtbare Diskussion über verschiedenste Aspekte dieser Arbeit mit Dr. Anselm Loges. Ich hoffe all die hartnäckige Unterstützung und Kraft irgendwie zurückgeben zu können. Forschen hat nicht nur Sinn sondern macht auch immensen Spass mit Dir.

Für Ihre nachsichtige und liebevolle seelisch-moralische Unterstützung im gesamten Verlauf und für die graphische Betreuung zum Abschluss dieser Arbeit danke ich meiner Schwester Mara Schultze. Felix Kaufmann danke ich für punktgenaue Kritik an meiner stellenweise unfokussierten Arbeitsweise und für die Erfahrung wirklich guter Teamarbeit während meiner Zeit in Berlin.

Finanziert wurde diese Arbeit von der Deutschen Forschungs Gemeinschaft und fand im Rahmen der Forschergruppe FOR 741 "Nanoscale processes and geomaterial properties" statt.

Table of Contents

| | |
|---|-----|
| Abstract..... | I |
| Zusammenfassung..... | III |
| Danksagung..... | V |
| 1. Introduction..... | 1 |
| 1.1 Contextual overview..... | 1 |
| 1.2 Phase relations in the system $\text{Al}_2\text{O}_3\text{-SiO}_2\text{-H}_2\text{O}$ | 3 |
| 1.3 Fluid assisted mineral replacement reactions..... | 7 |
| 1.4 Mobility of Al and Si and precipitation of Al_2SiO_5 polymorphs..... | 9 |
| 2. Samples, experiments, and methods..... | 13 |
| 2.1 Natural samples..... | 13 |
| 2.1.1 Sample MI..... | 13 |
| 2.1.2 Sample KT..... | 14 |
| 2.2 Experiments..... | 15 |
| 2.2.1 Experimental approach..... | 15 |
| 2.2.2 Starting Materials..... | 18 |
| 2.2.3 Apparatus, conditions, preparation..... | 19 |
| 2.3 Analytical methods..... | 23 |
| 3. Kyanite corona formation on corundum (natural samples)..... | 27 |
| 3.1 Summary..... | 27 |
| 3.2 Results..... | 28 |
| 3.2.1 Sample MI (Mysore, India)..... | 28 |
| 3.2.2 Sample KT (Kilombero, Tanzania)..... | 36 |
| 3.3 Discussion..... | 42 |
| 3.3.1 Corundum and kyanite formation..... | 44 |
| 3.3.2 Comparison of samples MI and KT..... | 48 |
| 3.4 Conclusion..... | 54 |

| | |
|--|-----|
| 4. How Si diffusion into corundum promotes the metastable coexistence of corundum and quartz over the formation of Al_2SiO_5 - an experimental study (<i>experiments part 1</i>) | 57 |
| 4.1 Summary..... | 57 |
| 4.2 Results..... | 58 |
| 4.3 Discussion..... | 75 |
| 4.3.1 Corona formation..... | 75 |
| 4.3.2 Silica diffusion in corundum..... | 77 |
| 4.3.3 Corundum plus quartz and H_2O | 84 |
| 4.4 Conclusion..... | 85 |
| 5. The influence of a nanometric phase on mineral equilibration in the system Al_2O_3 - SiO_2 - H_2O (<i>experiments part 2</i>)..... | 87 |
| 5.1 Summary..... | 87 |
| 5.2 Results..... | 88 |
| 5.3 Discussion..... | 92 |
| 5.4 Conclusion..... | 96 |
| 6. Concluding remarks..... | 99 |
| 7. Outlook and future directions..... | 103 |
| 8. References..... | 113 |

Electronic Appendix:

- Appendix chapter 2
- Appendix chapter 3
- Appendix chapter 4
- Appendix chapter 5
- Appendix chapter 7

1. Introduction

1.1 Contextual overview

The studies presented in this thesis were part of the Deutsche Forschungsgesellschaft Research group 741 “Nanoscale processes and geo-material properties” specifically; project 10 “Fluid assisted mineral replacement processes”. The study was designed to complement an earlier study that focused on the fluid-mediated replacement of rutile (TiO_2) by titanite (CaTiSiO_5) (Lucassen et al. 2010, 2011, 2012a, 2012b). Commonly observed in nature, mono-mineralic titanite reaction coronas also formed spontaneously in experiments on rutile single crystals and thus provided an excellent opportunity for a comparative study on how this specific mineral replacement reaction proceeds. Experience with the rutile-titanite system strongly suggested similar investigation of other fluid-driven oxide-silicate replacement. Coronas of the aluminiumsilicate polymorphs kyanite, sillimanite, and andalusite (Al_2SiO_5) around corundum ($\alpha\text{-Al}_2\text{O}_3$) are known from nature, although far less common than rutile with titanite coronas. The replacement reaction of $\text{Al}_2\text{O}_3 + \text{SiO}_2 \rightarrow \text{Al}_2\text{SiO}_5$ in a hydrous fluid was chosen for the project presented here due to the chemical simplicity and importance of silica and alumina as components in natural rocks. Only very limited record of aluminium silicate coronas on corundum are available. The ones

that are conclude that the corona is caused by the infiltration of Si-bearing fluids into the rock and subsequent dissolution precipitation reactions at the corundum surface (Raith and Schumacher 2012).

Although chemically simple, the experimental handling of the system $\text{Al}_2\text{O}_3\text{-SiO}_2\text{-H}_2\text{O}$ (hereinafter “ASH”) is infamously intricate. Experiments often yield thermodynamically unpredictable outcome such as metastable instead of stable products that complicate the characterization of the stable phases and relationships among them (Kerrick 1990; Essene et al. 1994; Harlov et al. 2008). In the 1960s to 1980s, several authors investigated these unforeseeable irregularities with great effort and tried to characterize numerous metastable phases and reaction processes (e.g. Roy 1954; Giardini et al. 1961; Aramaki and Roy 1963; DeVries 1964). Since then, however, only a few studies attended to the subject (Hemingway 1992; Harlov and Milke 2002). One obstacle to answering some old but unanswered questions regarding experiments in the ASH system is a general notion that “successful” experiments are those that proceeded according to prediction or plan (usually related to thermodynamic calculations). It is fruitful to report on successful experiments,

simply because they are straightforward and do not evoke much controversy. By contrast, “unsuccessful” experiments with unpredicted results are often not reported at all, preserving inconsistencies and misconceptions in our understanding of this very fundamentally important system. Due to those inconsistencies natural samples and experiments are often incomparable and the interpretation of features or processes in natural samples based on experiments can be inaccurate. The ASH is one of the most relevant chemical systems in the Earth’s crust and thus it is crucial to comprehensively understand the corresponding processes better than we currently do.

In this thesis corona formation was specifically chosen, not only due to similar successful

experiments in the initial part of the project, but because it is beneficial to precisely locate the reactions in question. Corona growth preserves both products and reactants, and in some cases the reaction interface. For both natural and especially experimental studies this is of great value. Not to know what reaction features are to be expected makes their recognition difficult unless the reaction is pinned to the surface of a known reaction participant that is not entirely consumed by the reaction. The scope of this study was to understand the replacement reaction $\text{Al}_2\text{O}_3 + \text{SiO}_2 \rightarrow \text{Al}_2\text{SiO}_5$ by comparing natural examples with experiments and if possible eliminate some of the inconsistencies inherent to the nature-versus-experiment conundrum of the ASH-system.

1.2 Phase relations in the system $\text{Al}_2\text{O}_3\text{-SiO}_2\text{-H}_2\text{O}$

The petrogenetic grid of the ASH system shown in figure 1.1, calculated with the program *Perplex_X* (Connolly 2009), according to the internally consistent thermodynamic dataset of Holland and Powell (2011), displays the stability fields of the aluminium silicate polymorphs to high pressure and temperature. Towards ultrahigh pressures (>120 kbar), the stability of kyanite is limited by the transition $\text{kyanite} \rightarrow \text{corundum} + \text{stishovite}$, which was confirmed experimentally by Schmidt et al. (1997). Between 1200°C ; 1 bar and 2800°C ; 180 kbar the sillimanite and kyanite stability fields are restricted by the formation of aluminium silicate-melts (Fig. 1.1, $L(\text{AlSi})$). The calculated triplepoint of the polymorphs is located at 536°C ; 4.31 kbar (Fig. 1.1). However, the history of the experimental determination of this point is a prime example of the controversial behavior of the ASH system. All three polymorphs are notoriously difficult to nucleate experimentally, which lead to the use of natural aluminium silicate seeds in most experiments concerned with growth or dissolution of the phases (Newton 1969; Althaus 1966; Kerrick 1972; Harlov and Newton 1993; Harlov et al. 2008). Nevertheless, even seeded experiments showed highly variable results with regard to the determination of the univariant curves and the triplepoint (Fig. 1.2a). Sluggish kinetics and high activation energies of the reactions between the polymorphs are held

accountable for the discrepancies (Vrána 1973; Harlov and Milke 2002).

It remains unclear what triggers experimental aluminium silicate nucleation, although in nature nucleation and growth of the polymorphs does not normally appear to be inhibited. Some success was reported from experiments including hydrous aluminium and silica bearing gels (Bell 1963; Huang and Wyllie 1974; Hariya and Arima 1975), or decomposing natural kaolinite or muscovite (Coes 1960; Brearly and Rubie 1990). In other cases the addition of “various added fluorides and salts” (Coes 1960), or borax (Balconi 1941a, 1941b; Michel-Levy 1950) achieved unseeded aluminium silicate formation. However, a systematic procedure has not evolved, since many reports of successful synthesis were followed by reports of failure when using a similar experimental recipe as the predecessor (Balconi 1941a, 1941b; Aramaki and Roy 1963; Huang and Wyllie 1974; Brearly and Rubie 1990). Hemingway (1992) addressed the problem that two polymorphs often appear to nucleate and grow coevally, even if one polymorph is clearly metastable. He explained this phenomenon by applying Ostwald’s Step Rule, which states that instead of the thermodynamically stable phase a metastable phase often forms first in precipitation experiments, if the free energy of the metastable phase is closer to that of the reactants/parent phase(s) (Van Santen 1984).

The unseeded synthesis of Al_2SiO_5 frequently results in the formation of corundum and quartz, an association which is rare in nature (see Fig. 1.2b, Clark et al. 1957; Carr and Fyfe 1960; Giardini et al. 1961; Wahl et al. 1961; Aramaki and Roy 1962; Bratton and Brindley 1962; Aramaki and Roy 1963; DeVries 1964; Day 1973; Huang and Wyllie 1974; Saalfeld and Junge 1983; Brearley and Rubie 1990; Grapes 2011). This irregularity caused a controversy about a possible stability of corundum plus quartz with respect to kyanite and sillimanite at high P-T, which was later disproved (Anovitz et al. 1993; Guiraud et al. 1996; Shaw and Arima 1998; and Mouri et al. 2003, 2004; Harlov et al. 2008). High pressure experiments ≥ 20 kbar are most successful in producing kyanite (Coes 1955; Abs-Wurmbach and Langer 1975). However, even experiments conducted deep inside the stability fields of kyanite, at high pressure and promoted by catalyzing agents occasionally yielded the metastable corundum plus quartz paragenesis (Fig. 1.2b), indicating that unknown reaction-inhibiting factors influence the system.

Aluminium-rich mullite (Al-Mul), also called “2:1 mullite” ($2\text{Al}_2\text{O}_3\text{:1SiO}_2$) is thermodynamically stable at $> 2000^\circ\text{C}$. Its silica rich counterpart silica-mullite, “3:2 mullite” (Si-Mul) is only stable if the formation of sillimanite is repressed completely at $> 2000^\circ\text{C}$ (Fig. 1.1). The corresponding silica-mullite stability field and the modification of the sillimanite stability field are indicated in red in

figures 1.1 and 1.2b. The experimental production of both mullite types does not require such high temperatures as indicated by the calculation (Tkalcic et al. 2003; Schneider and Komarneni 2005), in fact, especially silica-mullite forms metastable at low temperatures not only in the sillimanite, but also in the andalusite stability field (Fig. 1.2b, Giardini et al. 1961; Scott and Carruthers 1969; Brearley and Rubie 1990; Grapes 2011).

Towards lower temperatures and almost independent of pressure the aluminium silicates are theoretically replaced by diaspore and quartz (or coesite/stishovite respectively) (Fig. 1.1, 1.2). In experiments and nature, however, the formation of the Al-hydroxide boehmite instead of the stable diaspore is not uncommon and was subject to spirited debates (Anovitz et al. 1991; Chesworth 1994; Essene et al. 1994).

Theories explaining the widespread experimental metastabilities are often poorly constrained and contradict the interpretation of natural examples. Natural occurrences of corundum and quartz, for example, in the absence of aluminium silicates are commonly explained with the lack of reaction enhancing fluids (Kihle et al. 2010; Kato et al. 2011). However, there are numerous experiments reported, which were conducted under fluid rich to fluid saturated conditions that nevertheless yielded metastable corundum and quartz (see Fig. 1.2b, Bratton and Brindley 1962; Huang and Wyllie 1974; Day 1973; Brearley and Rubie 1990).

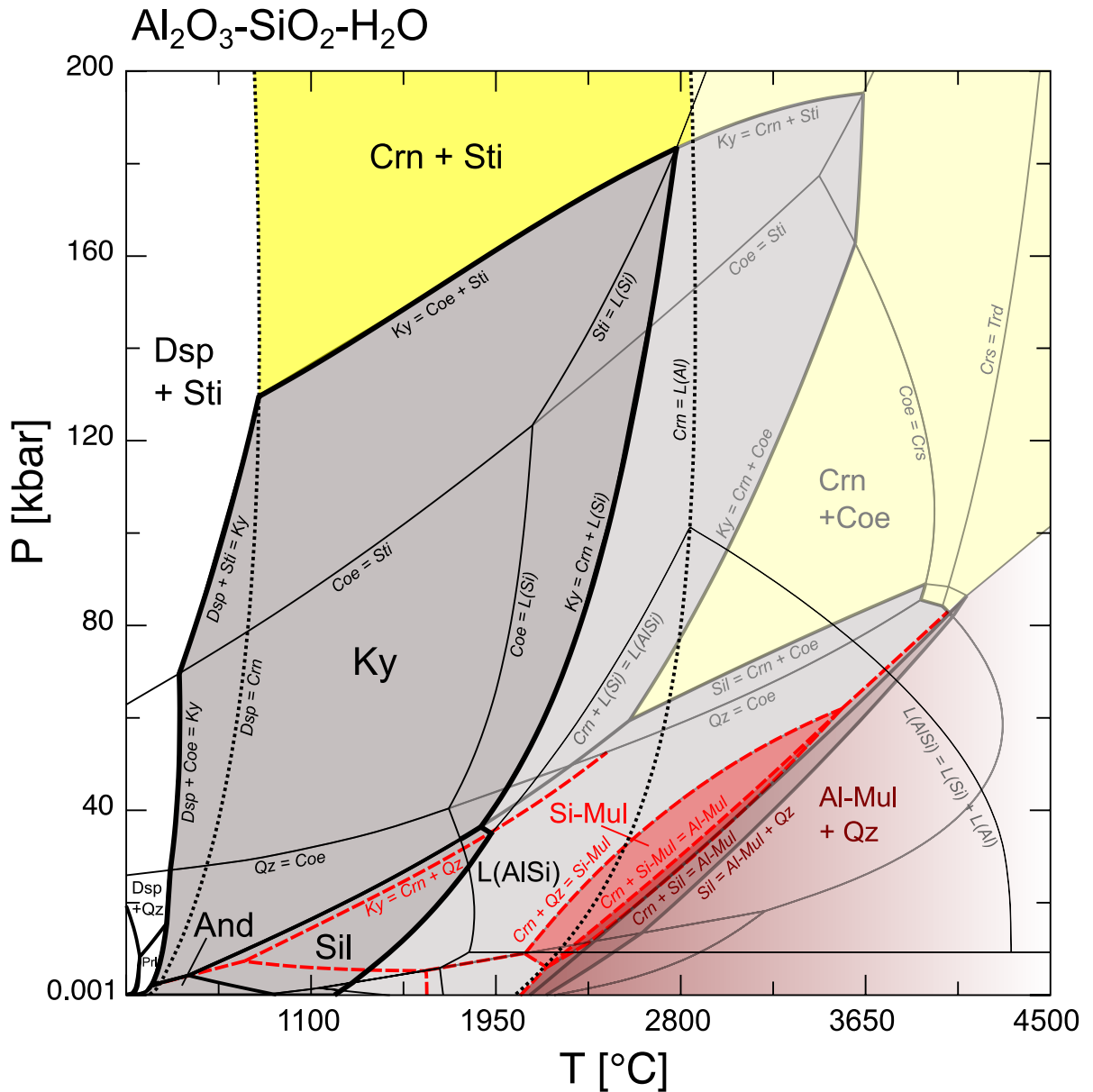


Fig. 1.1 Petrogenetic grid of the $\text{Al}_2\text{O}_3\text{-SiO}_2\text{-H}_2\text{O}$ (AHS) system calculated with the program Perplex_X (Connolly 2009), using the thermodynamic dataset of Holland & Powell (2011), mineral abbreviations after Whitney & Evans (2010). The stability fields of andalusite (And), sillimanite (Sil) and kyanite (Ky) are indicated in dark gray. The Ky stability is limited by the stability of corundum (Crn) and stishovite (Sti) to high pressures, and Ky and Sil stability are limited by the formation of silicate melt (L(Si)) plus Crn to higher temperatures. The Crn liquidus (Crn-L(Al)) is indicated with a black dotted line. The phase transitions of SiO_2 are indicated with thin black lines. Light gray stability fields represent melt absent conditions (extended Ky, Sil stability fields). According to the calculations Si-mullite (Si-Mul) is only stable if the formation of sillimanite (Sil) is suppressed (red lines) and Al-mullite (Al-Mul) is only stable in the absence of aluminium silicate melts (L(AlSi)).

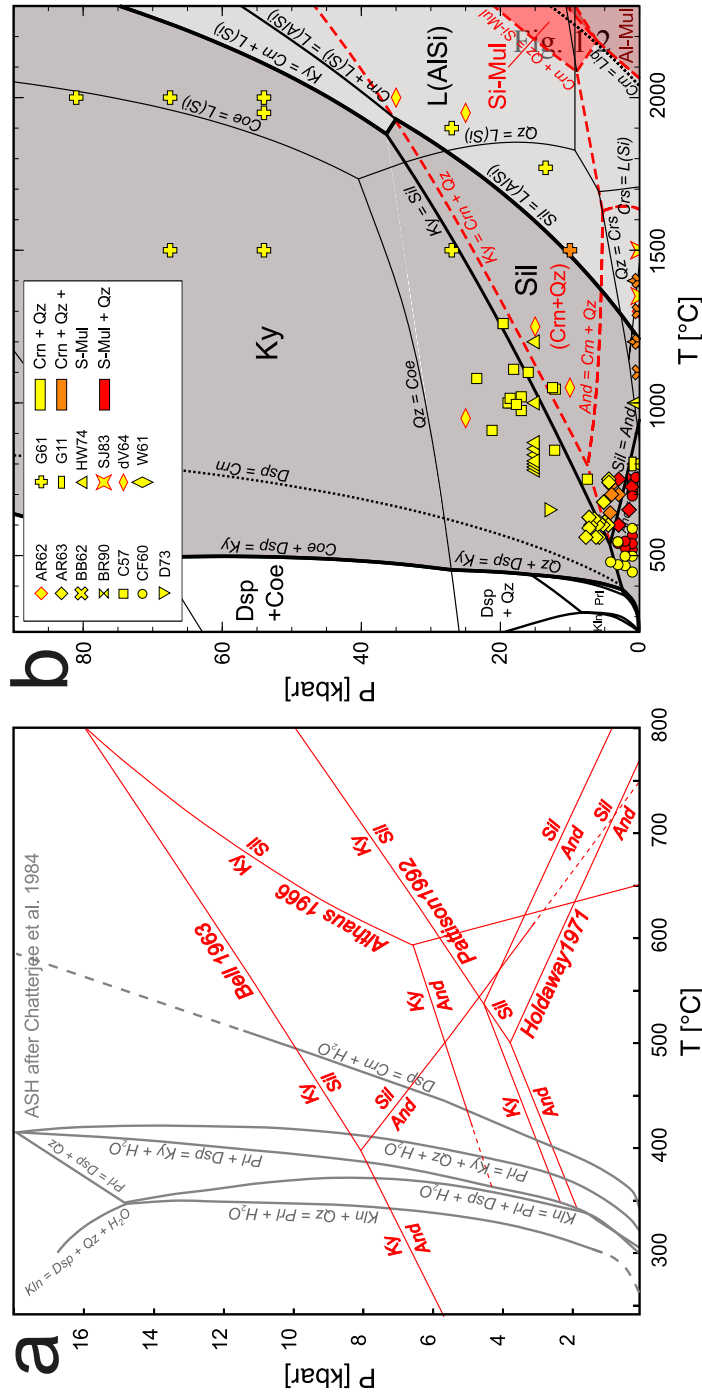


Fig. 1.2 a) Petrogenetic grid combining of the Al_2O_3 - SiO_2 - H_2O (AHS) system, modified after Chatterjee et al. (1984), with different experimentally determined Al_2SiO_5 polymorph triple points after Bell (1963), Althaus (1967), Holdaway (1971), and Pattison (1992) in red. b) The extent of the metastability of corundum (Crn) and quartz (Qz) in experiments in the petrogenetic grid of the system ASH (close up from Fig. 2.1 from 350–2300 °C and 0–90 kbar, see description Fig. 2.1). Included are experiments that yielded metastable Qz + Crn (yellow), Qz + Si-Mul, and Qz + Crn + Si-Mul (orange) from this study, Carr & Fyfe 1960 (CF60), Aramaki & Roy 1963 (AR63), Clark et al. 1957 (C57), Giardini et al. 1961 (G61), Grape 2011 (G11), Bratton & Brindley 1962 (BB62), Wahl et al. 1961 (W61), Huang & Wyllie 1974 (HW74), Day 1973 (D73), Brearley & Rubie 1990 (BR90), Aramaki & Roy 1962 (AR62), DeVries 1964 (dV64), Saalfeld & Junge 1983 (SJ83).

1.3 Fluid assisted mineral replacement reactions

Mineral coronas bear significant information about the geological history of a rock in that they preserve the transformation process of one phase into one or several others. Commonly, the reaction rate of corona-forming processes decreases and eventually stagnates with increasing width of the corona, the cause being limited transport of elements through the corona (Heimann et al. 2006; Keller et al. 2008; Ogilvie and Gibson 2017). As a result, both product and reactant phases of magmatic (Turner and Stüwe 1992; Claeson 1998; Grant et al. 2014), metamorphic (Brandt et al. 2003; Gallien et al. 2012; Ogilvie and Gibson 2017), and hydrothermal (Lucassen et al. 2012a, 2012b; Betkowski et al. 2016) reactions are preserved and can be used to reconstruct the rocks history.

The aim of this thesis was to investigate the processes involved in the generation of polycrystalline Al_2SiO_5 reaction coronas on a single crystal corundum precursor ($\alpha\text{-Al}_2\text{O}_3$) during the interaction with a mobile, silica-bearing phase (fluid or melt). In the present study as well as the previous work on titanite reaction coronas on rutile, the reaction rims in question form via a dissolution-precipitation process. During this process, the attacked precursor (reactant) is not just partly replaced by the substitution of components as in dissolution-re-precipitation reactions (Putnis 2002; Putnis and Putnis 2007; Putnis and Austrheim 2010; Pollok et al. 2011),

but is dissolved as a whole while a new, structurally unrelated mineral phase crystallizes, preferably at the surface of the reactant. The crystallographic relations between host grain and corona crystals are therefore much less clear than in dissolution-re-precipitation processes where pseudomorphic relations exist between precursor and product phase or the re-precipitated phase at least inherits crystallographic information of the precursor. The dissolution-precipitation reaction is mainly determined by surface dissolution along the host, and nucleation and growth behavior of the product phase. Corona growth under metamorphic conditions is mostly driven by grain boundary diffusion since the range of bulk diffusion through the existing reaction rim is limited (Lasaga 2014). Fluid enhances the effectivity of element transport along grain boundaries. However, even most efficient replacement reactions tend to halt at a certain point, when the element supply crucial for the product formation ceases due to insuperable transport ways. This means that the dissolution-precipitation reactions are preserved at a preliminary state of the investigated reaction. Thus both experimental and natural samples of corona growth, can be used as micro-laboratories for investigations of mineral reactions.

Titanite coronas on rutile frequently occur in natural samples and can be synthesized hydrothermally within only a few hours, due to the fact that titanite nucleates spontaneously at the rutile surface in contact with Ca and Si saturated fluid (Lucassen et al. 2010, 2011, 2012a, 2012b). In contrast, experimental attempts to synthesize the aluminium silicate polymorphs by reacting corundum with dissolved silica, at P-T conditions comparable to most natural examples (<1000°C; <15 kbar), have repeatedly been unsuccessful and indicate inhibited nucleation of Al_2SiO_5 (Carr and Fyfe 1960; Aramaki and Roy 1962, 1963; Carr 1963,

1968; Harlov and Milke 2002). Kyanite, sillimanite or andalusite coronas around corundum, as a natural equivalent of those experiments, are relatively rare (Outhuis 1989; Shaw and Arima 1998; Mouri et al. 2003, Raith and Schuhmacher 2012), despite the high abundance of Al and Si in the Earth's crust, whereas reaction rims of aluminium bearing silicates like mica, sapphirine, feldspar, and cordierite are more commonly found (Horrocks 1983; Ferguson and Al-Ameen 1985; Koshimoto et al. 2004; Heimann et al. 2006; Das and Mohanty 2014).

1.4 Mobility of Al and Si and precipitation of Al_2SiO_5 polymorphs

The aforementioned nucleation inhibition of Al_2SiO_5 in experiments posed a challenge in the design of experiments with the aim of Al_2SiO_5 corona formation through dissolution-precipitation mechanism. Detailed information about the heterogeneous nucleation of Al_2SiO_5 during the replacement of mica, staurolite etc., is available due to partly preserved reactants in natural samples. According to those, the formation of Al_2SiO_5 nuclei is structurally favored in cases where only small lattice adjustments in the precursor phase (muscovite, staurolite) are necessary to achieve an arrangement of isolated silica tetrahedra and chains of edge sharing Al-octahedra inherent to all three Al_2SiO_5 polymorphs (Chinner 1961; Wenk 1980; Lefebvre 1982; Cesare and Grob  ty 1995; Sanchez-Navas 1999).

What ultimately triggers the precipitation of Al_2SiO_5 from fluid or melt phase is unknown, since despite the abundance of natural examples, experimental verification is rarely possible (Heinrich 1955; McKie 1959; Vr  na 1973; Nyman et al. 1995; Widmer and Thompson 2001; Norlander et al. 2002; Harris et al. 2004; J  ns and Schenk 2004; Beitter et al. 2008; Bucholz and Ague 2010; Anenburg and Katzir 2014; Iaccarino et al. 2015). However, the solubility and molecular structure(s) of Al and Si in aqueous fluid and silicate melt has been investigated broadly and is summarized in the following.

Carmichael (1969) stated that the mobility of Al is very limited, based on the observation that Al dissolution experiments in superheated steam yielded a solubility of alumina three orders of magnitude smaller than that of silica (Morey 1957). The solubility of corundum in pure water is pressure dependent and very low over a broad range of temperatures (Morey 1957; Anderson and Burnham 1967; Burnham et al. 1973; Becker et al. 1983; Ragnarsdottir and Walther 1985; Walther 1997). At 10 kbar and 800  C a total Al concentration of only 1.2 ± 0.2 millimolal was reported (Tropper and Manning 2007). However, the aluminum solubility increases under certain conditions, due to, among other criteria, its ligand forming potential. Additional anions (Cl^- , F^- , OH^- , NH_2^-) or cations (Na^+ , K^+ , H^+ , NH_4^+) in solution form various aqueous complexes with dissolved Al that increase corundum solubility (Anderson and Burnham 1967; Pascal and Anderson 1989; Pokrovskii and Helgeson 1995; Pokrovski et al. 1996; Walter 2001; Tagirov and Schott 2001; Tagirov et al. 2002; Manning 2004, 2006; Newton and Manning 2006, 2008; Wohlers and Manning 2009). For this study the ligand formation of alumina and silica is of major importance, since molecular Al-Si-compounds in solution potentially provide precursor phases for Al_2SiO_5 nucleation. Quartz solubility in neutral aqueous fluid is high compared with corundum solubility and positively related to

temperature (Rimstidt et al. 1980). Al solubility increases drastically in quartz saturated fluid due to Al-Si-complex formation (Manning 2006, Manning 2007). An Al concentration of 0.013 molal at 800°C; 10 kbar has been attributed to the formation of the neutral $\text{AlSiO}(\text{OH})_5$ complex (Manning 2006, Manning 2007). Shifts in pH towards either acidic or alkaline conditions in a solution furthermore increases corundum solubility due to the fact that corundum reacts amphoteric (Gresens 1967; Vernon 1979; Carroll-Webb and Walther 1988; Nabelek 1997; Zraisky and Soboleva 1997; Salvi et al. 1998; McLelland et al. 2002). Aluminium in hydroxide monomers is mainly four-fold coordinated in fluids with alkaline pH and six-fold coordinated in acidic fluids. In silica-bearing aqueous fluids, $^{\text{VI}}\text{AlH}_3\text{SiO}_4^{2+}$ is likely the dominant species of complexes in acidic and quartz saturated solutions, with $\text{pH} < 3.5$, at 25 to 150°C, and $^{\text{IV}}\text{Al}(\text{OH})_3(\text{H}_3\text{SiO}_4)^-$ in quartz saturated solutions, with $\text{pH} > 3.5$, at 300 °C (Pokrovski et al. 1996, Salvi et al. 1998). In quartz undersaturated systems, Al- and Si-hydroxy monomers dominate in solution over Al-Si dimer species (Salvi et al. 1998). Mibe et

al. (2008) conducted hydrothermal diamond-anvil cell experiments in the $\text{KAlSi}_3\text{O}_8\text{-H}_2\text{O}$ system to simulate subduction zone fluids and showed that above 900°C and 23 kbar polymer chains of silica form that include a single Al-tetrahedral position (e.g. $\text{H}_8\text{Si}_3\text{AlO}_{12}^{1-}$). While the solubility of silica increased in the corresponding experiment, corundum plates precipitated. Continuous increase in silica polymerization in supercritical aqueous fluids finally approaches the transition to hydrous silicates melts (e.g. Shen and Keppler 1997), and the fact that Al is insulated in these silica polymer chains, suggests that the “aluminium avoidance principle” (de Jong et al. 1983), which applies to the molecular structure of silicate melts could be extended to the Al-Si hydrous complexes in fluids. The rule implies that Al is exclusively encompassed by and corner-sharing with Si tetrahedra and not allowed to form oxygen-bonds with other Al tetrahedra (or octahedra). To my knowledge, no conclusive evidence of an aqueous complex or silicate melt structure including dimer structures of Al-O-Al has been found to date.

2. Samples, experiments, and methods

Due to the large inconsistencies between nature and laboratory in the ASH system, the combination and detailed comparison of natural samples and experimental results with regard to aluminium silicate corona formation on corundum was considered essential. Observations made on natural examples, should help

determining the circumstances of corona growth in nature, and experimental approaches were designed to test individual corona formation parameters, as well as to determine characteristics and persistence of metastable mineral assemblages.

2.1 Natural samples

Two examples of kyanite coronas on corundum from different locations were used for the natural part of the study. Both samples were purchased by mineral retailers, one of them was kindly provided by Hans-Peter Schertl (University of Bochum). The exact sampling

location of the samples is unknown, but some information about the mining locations was provided. This information was used together with literature data to reconstruct the corresponding geological settings as good as possible.

2.1.1 Sample MI

Sample MI, a corundum-kyanite-muscovite-rock, commercially described as “ruby-kyanite-fuchsite rock”, was mined near the city of Mysore in the district of Karnataka (India) (Fig. A2.1, the letter A hereinafter indicates that the corresponding figures or tables is given in the electronic Appendix). Most mines of the area are located in the district of Karnataka, a region including parts of the Deccan Traps in the north and Archaean to Proterozoic basement of the Dharwar Craton in the south. The latter mainly

consists of Archean granitoids known as the Peninsular Gneiss (>3.0 Ga) that hosts several Archean greenstone belts associated with metapsamitic and metapelitic belts, the Dharwar Schist Belts (Jayananda et al. 2008, 2013; Sharma 2010; Mukherjee et al. 2012). The Dharwar Schist Belts along with the rest of the Archean basement of the Dharwar Craton experienced several metamorphic cycles. The latest event of the Dharwar orogenic cycle is older than 2.5 Ga (Mukhopadhyay 1986; Hanson et al. 1988). The oldest greenstone belts

(3.4-3.0 Ga) located around Mysore are subsumed under the name Sagur Group and comprise fuchsite-bearing (Cr-muscovite) rocks, banded iron formations, metapelites, metabasaltic amphibolites, metaperidotites and “gabbro-anorthosites” (Chadwick et al. 1997; Dey 2013). Sample MI was collected near the city of Mysore (Fig. A2.1) located on the east-west striking facies boundary from northern amphibolite (600 °C; 5-7 kbar) to southern

granulite facies rocks (700-750 °C; 7-9 kbar), within the partly migmatized Peninsular Gneiss of the Western Block of the Dharwar Supergroup (Pichamuthu 1935; Naqvi et al. 1988; Sharma 2010). The first accounts of ruby-kyanite-fuchsite rocks from southwest India were published in Milisenda (2003) and Raith and Schumacher (2012).

2.1.2 Sample KT

Sample KT is a light yellow, twinned corundum single crystal (2 cm diameter) with a colorless kyanite corona and small remnants of feldspar-biotite-muscovite-quartz host rock (Fig. A2.2). According to the mineral retailer the sample was collected at a mine in the subdistrict of Morogoro called Kilombero in South Tanzania. The sample was likely collected near Kilombero city, which is located where the Great Ruaha River enters the Kilombero plane after traversing the Udzungwa mountain range (Fig. A2.2). The specimen is smoothly rounded indicating its origin from a placer deposit. Yellow to colorless and short prismatic corundum megacrysts, very similar to the investigated sample, are also known from mining localities along highway A7 from Morogoro city to Iringa city, near Mbuyuni (Hughes et al. 2011), where the Great Ruaha River enters the Udzungwa Mountains, approximately 50 km WSW of Kilombero city. The

Western Granulites, including the Udzungwa Mountains, display predominantly Neoproterozoic peak metamorphic mineral assemblages dated at 640-620 Ma that coincide with the closure of Mozambique Ocean during the Pan African orogeny (Sommer et al. 2003). The rocks are mainly composed of migmatitic para- and orthogneisses, mafic to intermediate granulites, intercalated metapelitic units and locally occurring ultramafic rocks (Sommer et al. 2003, 2005a, 2005b, 2008, Fritz et al. 2005, 2009; Vogt et al. 2006). Metapelitic units within the strongly deformed orthogneisses from the Kidatu region, including the first 20 km of the Udzungwa Mountain range west of Kilombero city (Fig. A2.2 detail), show high-pressure metamorphic mineral assemblages of quartz-plagioclase-biotite-garnet-kyanite (Sommer et al. 2003). Peak metamorphic conditions for these rocks were estimated at 13-14 kbar and 750-800°C (Appel et al. 1998; Sommer et al. 2003, 2008; Fritz et al. 2005, 2009).

2.2 Experiments

2.2.1 Experimental approach

To investigate the response of the corundum single crystal to attacking silica-rich fluid and dehydrating phyllosilicates, as well as to discern the factors controlling or inhibiting the Al_2SiO_5 formation from fluid, different experimental approaches were used (see Tab. 2.1). All experiments were carried out under quartz saturated conditions, to ensure sufficiently fast reaction kinetics. P-T conditions were chosen close to common formation conditions of natural kyanite and sillimanite, specifically below 1000 °C and 20 kbar. Although kyanite synthesis is known to succeed best at >20 bar and $\geq 900^\circ\text{C}$ (Coes 1955; Huang and Wyllie 1974; Harlov and Milke 2002), the P-T range of all experiments, with the exception of run 4 (at 1200 °C; 20 kbar), was deliberately set lower to have a better correlation with natural occurrences. To be able to investigate the interaction of corundum and silica-bearing fluid explicitly, the solid reactants were in some experiments prevented from interacting by shielding the corundum grains with a perforated inner Pt-capsule from the silica source. These runs are denoted with “i.c.” in table 2.1. Mineral abbreviations used hereinafter in tables, figures, and figure captions are according to Whitney and Evans (2010).

In a first set of experiments (run 1-30, Tab. 2.1) corona growth on corundum single crystals in silica-rich aqueous fluid was simulated; the results to those experiments are presented in chapter 3. The interaction of corundum and silica saturated aqueous fluid, which should theoretically proceed according to: $\text{Al}_2\text{O}_3 + \text{SiO}_2 \text{ aq} \rightarrow \text{Al}_2\text{SiO}_5$, was simulated in pure deionized water (run 1-4) and at 500 – 1200 °C and 5 – 20 kbar. In piston cylinder experiments at conditions of 800 – 1200 °C and 10 – 20 kbar corundum single crystals were embedded in a matrix of amorphous SiO_2 powder or quartz and water was added. Because the solubility of Al in aqueous metamorphic fluid of near neutral pH is extremely low (Anderson and Burnham 1967; Burnham et al. 1973; Becker et al. 1983; Ragnarsdottir and Walther 1985; Walther 1997; Mookherjee et al. 2014), which could affect the nucleation of Al_2SiO_5 , additional experiments with variable pH (Carroll-Webb and Walther 1988; Pokrovski et al. 1996; Salvi et al. 1998) were conducted. pH neutral experiments contained deionized water and amorphous SiO_2 , whereas in variably acidic (down to pH < 0) experiments either BH_3O_3 or HCl was added (run 5-18, Tab. 2.1). Acidic conditions favor the formation of octahedrally coordinated Al-complexes (e.g. Salvi et al. 1998), factors that should support the formation of molecular structures predominantly composed of six fold aluminium as in the aluminium silicates. In

some of the experiments, the corundum grains were coated with fine grained natural kyanite in order to see whether kyanite coronas would establish, if the well known nucleation inhibition was bypassed by providing a nucleation surface. Kyanite seeded experiments are indicated with “Ky-s.” in table 2.1.

In order to evaluate the general potential of corundum single crystals to establish silicate coronas as a result of fluid interaction, experiments were conducted in a range of 400-700°C and 2-5.15 kbar with different additional cations in solution (K^+ , Na^+ , Mg^{2+} , NH_4^+) by adding varying amounts of either NaCl, KCl, NaOH, NH_3OH , or MgO (run 19-30, Tab. 2.1). Anticipated reaction products were muscovite, orthoclase, paragonite, albite, clinocllore, and buddingtonite.

The fluid used in the aforementioned experiment (runs 1-18) is a simplified approximation of a natural metamorphic fluid (Beitter et al. 2008; Fusswinkel et al. 2014; Rauchenstein-Martinek et al. 2014; Yardley and Cleverley 2015). To monitor whether the silica-saturated aqueous fluid unfavorably influenced the precipitation of silicate products on oxide crystals in general, one experiment for the reaction baddeleyite plus silica saturated fluid \rightarrow zircon at 650°C at 5 kbar was performed (Tab. 2.1). The similarities of the systems Al_2O_3 - SiO_2 and ZrO - SiO_2 make them ideal for comparison; both corundum and baddeleyite have a very low solubility in aqueous fluids (Migdisov et al. 2011), the Al_2SiO_5 polymorphs

and zircon are both orthosilicates, thus when precipitating from fluids the silica components are required not to polymerize, and oxides of both systems have different crystallographic structures than their silicates. This difference does not allow epitactic replacement, as for example during albitization of feldspars (or dissolution-reprecipitation reactions, see Putnis, 2002; Putnis and Austrheim, 2010) but require dissolution-precipitation mechanisms (Lucassen et al. 2010).

A second set of experiments was conducted with corundum single grains embedded in a matrix of dehydrating phyllosilicates (run 32-34) in order to closely approximate aluminium silicate generating processes in nature (Read 1932; Carmichael 1969; Kerrick 1972, 1990; García-Casco et al. 1993; Hicks and Secco 1997; Ter Heege and Renner 2007). In run 32 the corundum single crystals were embedded in a matrix of natural muscovite and quartz (molar ratio $Ms:Qz = 2:3$), without added fluid. This run was conducted at 690 °C; 4.75 kbar (Tab. 2.1), analogue to sillimanite growth during muscovite breakdown according to the reaction; $2KAl_3Si_3O_{10}(OH)_2 + 3SiO_2 + Al_2O_3 \rightarrow 3Al_2SiO_5 + 2KAlSi_3O_8 + 2H_2O$.

In order to promote sillimanite corona growth on corundum during the dehydration of pyrophyllite via the reaction; $Al_2Si_4O_{10}(OH)_2 + Al_2O_3 \rightarrow Al_2SiO_5 + SiO_2 + H_2O$, corundum single crystals without fluid were placed in fine

grained natural pyrophyllite and treated at 650 °C; 5 kbar for run 33 (Tab. 2.1).

In run 34 diasporite was used as aluminium and fluid source embedded in a matrix of amorphous silica powder and heated to 800 °C at 10 kbar to achieve reaction; $2\text{AlOOH} + \text{SiO}_2 \rightarrow \text{Al}_2\text{SiO}_5 + \text{H}_2\text{O}$. The diasporite structure is composed of Al-octahedra double chains that potentially provide the required molecular Al precursor structures to nucleate Al_2SiO_5 . The dehydration reaction to corundum should take place at around 470 °C at 5 kbar according Hemley et al. (1980).

The third set of experiments comprised cooling (run 35-39) and decompression experiments (run 40-43), to answer the question, whether aluminium silicates would precipitate from fluid due to a sudden supersaturation of dissolved Al and Si with respect to Al_2SiO_5 (Fig. 2.1). According to Beitter et al. (2008) kyanite-quartz veins from the Alpe Sponda (Swiss Alps) are produced by overstepping the saturation of Al-Si-complexes in the vein fluid. The super-

saturation is supposedly triggered by a decrease in temperature and/or variations in pH of the fluid (Fig. 2.1). Since Al solubility in aqueous fluids is increasing with increasing pressure (Becker et al. 1983; Manning 2007), decompression experiments were additionally conducted (Tab. 2.1). Fluid was equilibrated with excess silica and alumina for several days at a constant starting P-T and then a decrease in either temperature or pressure (at constant P or T respectively) was induced. Cooling experiments in most cases included several steps in order to support the growth of larger Al_2SiO_5 crystals over high nucleation rate and small crystals. A mixture of amorphous $\gamma\text{-Al}_2\text{O}_3$ or ground, natural diasporite powder and amorphous SiO_2 powder was used with deionized water. Run 39 was doped with TiO_2 powder in order to produce rutile crystals within the Al-Si-mixture with the aim of providing potential nucleation seeds for Al_2SiO_5 crystals to grow.

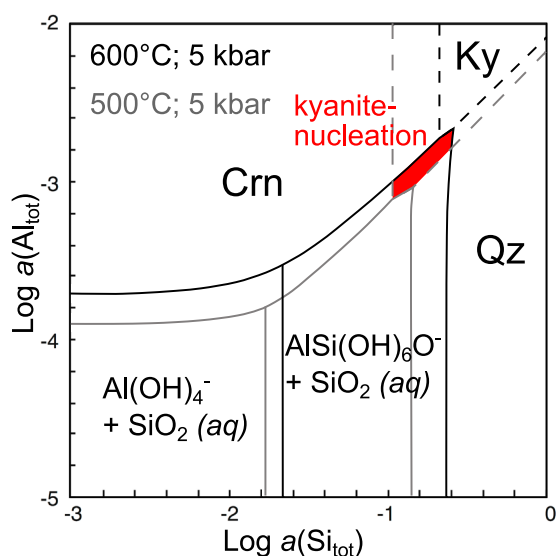


Fig. 2.1 Solubility diagram dependent of Al and Si activities and calculated AlSi-complex stability at neutral pH and constant 5kbar (modified after Beitter et al. (2008)). Predicted kyanite precipitation (in red) by AlSi-complex oversaturation during temperature decrease from 600-500°C.

2.2.2 Starting Materials

Chemical analyses for crystalline starting materials (natural minerals and synthetic crystals) used in the experiments listed in table 2.1 are given in table 2.2. Natural and of synthetic corundum single crystals were used in most experiments to check if Fe content and possible defects would influence the reactions. Trace element-free Czochralski grown synthetic corundum was obtained from Crystal GmbH Berlin and consisted of 1x10x10 mm chips, with polished basal planes. The chips were cut into approximately 1x1x2 mm cubes in order to fit into the capsules. Natural gem quality pale yellow corundum from Sri Lanka was crushed to < 1.5 mm and hand-picked for the experiments to avoid inclusions. Besides small amounts of Fe (0.05 wt% Fe_2O_3) the natural corundum is trace element free, no Ti, Cr, V or other trace elements typical for corundum could be detected in electron microprobe analysis

(Tab. 2.2). Natural and synthetic corundum grains were free of twins or parting planes. Gem quality kyanite crystals from Zimbabwe were used as crystallization seeds in setup 2. Baddeleyite from Serra Pocos de Caldas, (Minas Gerais, Brazil) was used in setup 4 (Tab. 2.2), Muscovite from the Münchberg Massiv, Bavaria (Germany) in setup 5, and pyrophyllite from North Carolina (USA) in setup 6 (Tab. 2.2). Both pyrophyllite and muscovite show trace contents of Fe and Mg (Tab. 2.2).

Analytic-grade chemicals NaCl, NaOH, KCl, MgO (Merck Millipore), H_3BO_3 (Alfa Aesar) and solutions NH_4OH (25%), HCl (25%) (Merck Millipore), were used as additional solvents in setup 1, 2, and 3. As silica source in setup 1, 2, 3, and 4, amorphous SiO_2 powder with 0.5 μm grain size (Alfa Aesar) was used. The powder was analyzed with XRD in order to exclude minor crystalline components. Natural inclusion-free quartz grains (< 30 μm) were used in setup 5.

2.2.3 Apparatus, conditions, preparation

Hydrothermal experiments: Experiments ≤ 5.15 kbar were conducted in externally heated cold-seal vessels in a hydrothermal apparatus using water as pressure medium at Technische Universität Berlin. For higher pressures a non-endloaded piston cylinder press was used at the GeoForschungs Zentrum Potsdam. The temperature was set with an accuracy of ± 10 °C, and pressure with an accuracy of ± 0.1 kbar. Gold capsules were loaded with the starting materials and fluid (see Tab. 2.1), the capsules were then welded, and impermeability was

controlled by checking for weight loss after heating the capsules to 100 °C for half an hour. To prevent direct contact of corundum crystals and the silica reactant and to assure interaction of the corundum with the silica bearing fluid only, the corundum grains in some experiments were enclosed in perforated inner gold or platinum capsules (1 mm outer diameter, 5 mm length, indicated with “ic” in Tab. 2.1). The duration of the experiments was variable between 6 days and 5 weeks at P-T-conditions of 400 to 700 °C and 2.0 to 5.15 kbar (Tab. 2.1).

Piston cylinder press: The Au or Pt capsules were loaded with amorphous silica powder embedding corundum or diaspore grains and water. The variable high-pressure assemblies consisted of single or double capsule arrangements, described in the following and in detail in Schilling and Wunder (2004):

For run 15 the capsules were embedded in sodium chloride (40 mm length, 12.7 mm in diameter) as pressure conducting medium, and included in a metal furnace, with a Ni-CrNi-thermocouple (K-type) comparable to assembly 6 in Schilling and Wunder (2004). Due to the top-position of the thermocouple, the temperature accuracy is about ± 20 °C, and a temperature gradient of ~ 30 °C is expected (Schilling and Wunder 2004). For NaCl, no pressure correction was necessary.

A second assembly with CaF_2 as pressure medium (40 mm length, 22 mm in diameter) was used to conduct run 2 (Tab. 2.1), in a graphite furnace, with a Ni-CrNi thermocouple. Comparable to the first assembly the thermocouple was in the top position in this assembly as well. A pressure correction of 10% was applied.

Runs 3, 34, 40 and 41 were conducted in a double-capsule (each 10 mm in length, 3 mm in diameter) CaF_2 assembly (dimensions as in the first assembly), in a graphite furnace, using a Ni-CrNi thermocouple. The design is comparable with assembly 5 in Schilling and Wunder (2004). The thermocouple is positioned between the two capsules. The accuracy is ± 10 °C and the T-gradient is about 10°C. A pressure correction of 10% was applied.

An assembly with talc-pyrex glass as pressure medium (40 mm length, 12.7 mm in diameter), in a graphite furnace, with a Pt-PtRh thermocouple, was used for run 4 (Tab. 2.1). The sample consisted of one small Pt capsule (4 mm length, 3 mm in diameter), and the thermocouple was located at the top of the capsule (about the design 4 in Schilling and Wunder 2004). Due to the small length of the Pt capsule

temperature accuracy and gradient are smaller than 10 °C. However, a large friction correction of about 15 % was applied.

Preparation: At the end of the hydrothermal experiments, the vessels were quenched in an air stream to < 100 °C within approximately 5 min. The capsules were then weighed to detect potential fluid loss. Capsules from experiments with added fluid were opened, pH values of the extracted fluids were determined and the corundum, kyanite, or baddeleyite grains along with additional solid run products were dried. Single crystals were mounted along with the

fine-grained powder products on specimen holders for scanning electron microscopy analyses (SEM). The capsules from phyllosilicate or SiO₂ powder matrix experiments from both hydrothermal and piston cylinder experiments were entirely embedded in epoxy, cut into slices and mounted directly on thin section glasses in order to preserve experimental textures.

Table 2.1. Summary of experiments referred to in chapters 4 and 5. Experiments with pressure > 5.15 kbar were conducted in a piston cylinder press, ≤ 5.15 kbar in a hydrothermal apparatus. The abbreviation "i.c." refers to the use of a perforated internal capsule, run with kyanite seeds are indicated with "Ky-s.". Starting materials: amorp. γ - Al_2O_3 , corundum single crystals (Crn), diaspore (Dsp), amorp. SiO_2 , quartz (Qz), or as indicated in additional reactants. Run 1-30; corona growth experiments on corundum in Qz saturated H_2O or in SiO_2 matrix plus H_2O . Run 31; corona growth experiments on baddeleyite (Bdy) in Qz saturated H_2O . Run 32-34 Al_2SiO_5 (corona) growth from dehydration reactions in muscovite (Ms) + Qz, pyrophyllite (Prl), and diaspore (Dsp) + Qz. Run 35-39; experiments on Al_2SiO_5 precipitation due to cooling of Al and Si saturated fluid. Run 40-43; experiments on Al_2SiO_5 precipitation due to decompression of Al and Si saturated fluid.

| Run number | Notes | Crn [mg] | SiO_2 [mg] | H_2O [mg] | Additional reactants [mg] | | P [kbar] | T [°C] | t [d] |
|------------|-------|----------|---------------------|---------------------------|---|-------------|-----------|-----------------------|-------------------|
| 1 | | 14.21 | 12.04 | 16.34 | - | | 5 | 500 | 26 |
| 2 | i.c. | 6.24 | 23.16 | 2.94 | - | | 10 | 800 | 10 |
| 3 | | 6.90 | 27.48 | 1.92 | - | | 10 | 800 | 20 |
| 4 | | 4.94 | 19.75 (Qz) | 0.50 | - | | 20 | 1200 | 1 |
| 5 | | 7.67 | 8.44 | 22.81 | BH_3O_3 | 5.54 | 5 | 500 | 26 |
| 6 | i.c. | 1.95 | 3.85 | 7.98 | HCl | 2.66 | 4.65 | 500 | 14 |
| 7 | i.c. | 2.84 | 1.56 | 9.95 | HCl | 3.32 | 4.7 | 500 | 33 |
| 8 | i.c. | 1.84 | 0.47 | 2.56 | HCl | 0.85 | 4.7 | 500 | 7 |
| 9 | i.c. | 8.83 | 1.20 | 1.62 | HCl | 0.54 | 4.8 | 500 | 23 |
| 10 | i.c. | 10.45 | 2.07 | 1.92 | HCl | 0.64 | 4.8 | 600 | 23 |
| 11 | i.c. | 8.61 | 1.76 | 47.54 | HCl | 15.85 | 5 | 500 | 31 |
| 12 | i.c. | 9.34 | 2.34 | 10.31 | HCl | 3.44 | 5 | 500 | 13 |
| 13 | | 8.05 | 10.55 | 13.28 | HCl | 4.43 | 5 | 500 | 24 |
| 14 | | 14.18 | 3.54 | 8.14 | HCl | 2.71 | 5 | 500 | 14 |
| 15 | Ky-s. | 5.34 | 20.51 | 6.46 | - | | 10 | 800 | 5 |
| 16 | Ky-s. | 6.91 | 1.92 | 9.05 | HCl | 3.02 | 4.7 | 500 | 33 |
| 17 | Ky-s. | 2.21 | 1.62 | 2.27 | HCl | 0.76 | 4.7 | 500 | 7 |
| 18 | Ky-s. | 8.19 | 2.70 | 10.12 | HCl | 3.37 | 5 | 500 | 13 |
| 19 | i.c. | 3.54 | 2.13 | 10.12 | NaCl | 0.26 | 5.15 | 500 | 6 |
| 20 | i.c. | 4.93 | 1.97 | 11.30 | NaCl | 0.29 | 5.15 | 500 | 6 |
| 21 | i.c. | 1.87 | 2.65 | 11.20 | NaCl | 4.03 | 3.8 | 700 | 21 |
| 22 | i.c. | 6.03 | 4.87 | 4.20 | NaCl | 0.11 | 5 | 500 | 31 |
| 23 | i.c. | 1.29 | 3.01 | 11.20 | KCl | 0.01 | 4.7 | 500 | 14 |
| 24 | i.c. | 1.84 | 2.87 | 11.19 | KCl | 0.07 | 4.7 | 500 | 14 |
| 25 | i.c. | 2.26 | 2.10 | 12.33 | KCl | 0.76 | 4.9 | 500 | 21 |
| 26 | i.c. | 12.00 | 2.74 | 11.35 | KCl | 0.70 | 3.8 | 700 | 21 |
| 27 | i.c. | 13.86 | 4.64 | 11.00 | NaOH | 0.44 | 4.9 | 500 | 21 |
| 28 | | 8.27 | 3.23 | 12.71 | NaOH | 0.50 | 4.9 | 500 | 21 |
| 29 | | 6.71 | 25.90 | 11.20 | NH_3OH | 3.73 | 5 | 650 | 21 |
| 30 | | 8.46 | 2.99 | 12.15 | MgO | 3.28 | 2 | 650 | 12 |
| 31 | | | 12.84 | 12.2 | Bdy | 3 | 5 | 650 | 21 |
| 32 | | 21.56 | 16.17 | - | Ms | 71.54 | 4.75 | 690 | 13 |
| 33 | | 10.30 | - | - | Prl | 55.99 | 5 | 650 | 14 |
| 34 | | - | 20.39 | - | Dsp | 13.82 | 10 | 800 | 20 |
| 35 | | - | 17.92 | 17.80 | γ - Al_2O_3 | 0.84 | 5 | 500-->490-->480 | 5-->5-->14 |
| 36 | | - | 3.37 | 17.60 | γ - Al_2O_3 | 1.03 | 5 | 600-->550-->500 | 13-->1-->1 |
| 37 | | - | 3.57 | 17.41 | γ - Al_2O_3 | 1.01 | 5 | 650-->636-->625-->615 | 7-->1-->0.5-->0.5 |
| 38 | | - | 27.31(Qz) | 20.25 | Dsp | 8.4 | 5 | 650-->636-->625-->615 | 7-->1-->0.5-->0.5 |
| 39 | | 4.03 | 3.24 | 13.09 | γ - Al_2O_3 / TiO_2 | 1.66 / 1.68 | 5 | 650-->550 | 5-->7 |
| 40 | | 2.63 | 17.42 | - | Dsp | 2.71 | 18-->5 | 550 | 1-->7 |
| 41 | | 9.31 | 20.94 | 2.46 | - | | 18-->5 | 550 | 1-->7 |
| 42 | | - | 31.96 | 38.15 | γ - Al_2O_3 | 12.54 | 4.5-->2.5 | 650 | 14-->14 |
| 43 | Ky-s. | - | 24.33 | 25.40 | γ - Al_2O_3 | 9.55 | 4.5-->2.5 | 650 | 14-->14 |

Table 2.2. Crystalline experimental starting material; corundum, kyanite, baddeleyite, pyrophyllite, muscovite, and diaspore (selected representative data, WDS results EMP in oxide wt%, detection limits „D.L.“ in element wt ppm)

| Corundum | synthetic | natural | D.L. | Kyanite | | D.L. |
|--------------------------------|-----------|---------|-------|--------------------------------|--------|------|
| SiO ₂ | 0.058 | 0.089 | 25 | SiO ₂ | 37.01 | 9 |
| Al ₂ O ₃ | 99.94 | 99.95 | 50 | Al ₂ O ₃ | 62.40 | 18 |
| Fe ₂ O ₃ | b.d. | 0.053 | 60 | Fe ₂ O ₃ | 0.580 | 18 |
| Total | 100.00 | 100.09 | - | Total | 100.00 | - |
| Pyrophyllite | | | D.L. | Baddeleyite | | D.L. |
| SiO ₂ | 66.82 | 66.86 | 96 | SiO ₂ | 0.60 | 148 |
| Al ₂ O ₃ | 28.10 | 28.03 | 93 | TiO ₂ | 0.65 | 221 |
| Fe ₂ O ₃ | 0.074 | 0.106 | 195 | ZrO ₂ | 96.50 | 264 |
| MgO | 0.033 | 0.033 | 70 | HfO ₂ | 1.00 | 810 |
| Total | 95.03 | 95.03 | - | FeO | 1.27 | 314 |
| | | | | Total | 100.02 | - |
| Muscovite | | | | | | D.L. |
| SiO ₂ | 45.96 | 45.58 | 45.66 | 45.86 | 46.19 | 370 |
| Al ₂ O ₃ | 38.16 | 36.80 | 37.44 | 37.43 | 37.38 | 360 |
| MgO | 0.541 | 0.569 | 0.547 | 0.547 | 0.574 | 470 |
| FeO | 1.434 | 1.528 | 1.567 | 1.566 | 1.599 | 450 |
| Na ₂ O | 0.551 | 0.589 | 0.555 | 0.569 | 0.580 | 500 |
| K ₂ O | 9.636 | 9.837 | 9.459 | 9.704 | 9.793 | 480 |
| H ₂ O | 4.336 | 4.300 | 4.308 | 4.327 | 4.358 | - |
| Total | 100.61 | 99.21 | 99.54 | 100.00 | 100.48 | - |
| Diaspore | | | D.L. | | | |
| SiO ₂ | 0.033 | 0.020 | 83 | | | |
| TiO ₂ | 0.029 | b.d. | 148 | | | |
| Al ₂ O ₃ | 83.86 | 83.59 | 93 | | | |
| Fe ₂ O ₃ | 0.699 | 0.732 | 190 | | | |
| Total | 84.62 | 84.34 | - | | | |

2.3 Analytical methods

Powder X-ray diffraction analyses were carried out using a first generation D2 Phaser powder X-ray diffractometer (Bruker) in a range of 5 to 80 °2 θ , with 0.01 degree step width at a velocity of 0.4 seconds per step. The diffractometer is equipped with a Cu X-ray tube and the analyses were conducted at 30 kV voltage and 10 mA current.

Bulk rock X-ray fluorescence (XRF) major and trace element analysis of a powdered representative portion of sample MI was conducted using a wavelength dispersive Philips WDRFA PW 2400 machine at Technical University (TU) Berlin. Cation concentrations were determined in lithium borate beads (0.6 g sample, 3.6 g fluxana lithium borate flux), fluorine in pressed powder discs (6.0 g sample, 1.5 g fluxana Höchstwachs C bonding wax). In order to determine the weight loss on ignition (LOI) representing volatile contents, the powdered sample was heated to 1000°C.

SEM analyses were conducted at Technische Universität Berlin using a Hitachi S-520 SEM. Field emission electron microprobe analysis (EMPA) were conducted with a JEOL JXA-8530F instrument at Technische Universität Berlin at 15 kV and between 15 and 20 nA for all quantitative measurements. Measurement conditions for element mapping analyses required higher probe currents as well as increased dwell time and are given in the corresponding figure captions. Astimex

MINM25-53 natural and synthetic mineral standards were used for the majority of elements (Si, Ca, Mg, Fe, Ti, Mn, Cr, Ba, K, Na, Cl and F) except for Al and Cr, which were standardized to synthetic corundum doped with 0.45 wt % Cr₂O₃. For V an Astimex METM25-44 metal standard was used. Counting times for major elements were 20 s (peak) with 10 s on the background, for volatile major elements (K, Na, Cl) 10 s; 5 s, and for trace elements 50 to 100 s and 25 to 50 s background respectively. ZAF mode matrix corrections were applied. Detection limits for all presented analyses are given in the corresponding tables. Cathodoluminescence (CL) imaging was done with an optical cold cathode microscope (CITL Mk5) and 260 μ A beam current at 8 kV at the University of Helsinki, and with a SEM-CL at 20 nA and 10 kV at the GeoForschungsZentrum Potsdam.

For transmission electron microscopy (TEM), approximately 15x7x0.15 μ m large foils were cut from selected areas in thin sections by focused ion beam (FIB) milling method using a FEI FIB200 instrument at the GeoForschungs-Zentrum Potsdam. The foils were then placed on a perforated carbon film and analyzed with an electron microscope type FEI Tecnai G2 F20 X-Twin. The scanning transmission electron mode (STEM) was operated at 300 kV, and images in the high-angle annular dark field (HAADF) mode, or images in bright- and dark-field (BF,

DF) mode were acquired. TEM energy diffraction analyses were used to identify phases
dispersive analyses (EDS) and high-resolution at this scale.
TEM images (HRTEM) combined with electron

3. Kyanite corona formation on corundum (*natural samples*)

3.1 Summary

Detailed observation of natural aluminium silicate formation reactions in well defined chemical systems can be used as natural laboratories on geological timescales in order to better understand the relevant reaction pathways. Kyanite coronas around corundum are rare but provide an ideal case for such studies because the kyanite formation is localized and the reactants are preserved, which allows to reconstruct the Al_2O_3 and SiO_2 fluxes during corona growth. Furthermore, they are the closest natural equivalent to aforementioned poorly understood experiments.

Two geographically and geologically unrelated samples, of kyanite coronas on corundum from Mysore (India) and Kilombero (Morogoro, Tanzania) were investigated (see Fig. 3.1, and chapter 2.1). In both samples the corundum grains with associated corona are included in host rocks primarily composed of potassium bearing aluminium silicates. Corundum in sample MI (Mysore, India) is embedded in a muscovite matrix, and sample KT (Kilombero, Tanzania) consists of a large corundum grain with a remnant of mainly orthoclase (and minor albite). Both samples contain quartz in the host rocks surrounding the corundum porphyroblasts and since corundum is not stable with quartz, the rocks must have been silica undersaturated with respect to quartz at the time of corundum crystallization. The monocrystalline kyanite coronas in both samples thus could have formed during two different processes:

1) The infiltration of silica-bearing fluid into the host rocks and kyanite formation at the corundum interface according to the reaction;
 $\text{Al}_2\text{O}_3 + \text{SiO}_2 \text{ aq} \rightarrow \text{Al}_2\text{SiO}_5$, or

2) The decomposition of host rock silicate minerals adjacent to corundum and subsequent reaction to kyanite coronas.

Option 1 is undoubtedly intuitive and was formerly suggested for samples of similar composition and geographic origin as sample MI (Raith and Schuhmacher 2012). Reaction preserving features in the mineral coronas along with chemical signatures or petrological features in the surrounding host rocks in both samples MI and KT, however, strongly support the second option to be the process behind the formation of kyanite coronas. Most importantly, the kyanite grains preference to grow mainly along their grain boundaries, lead to the isolation and subsequent inclusion of the replaced phases inside the corona grains in both samples. As a result, inclusions of corundum and aluminosilicates (muscovite in MI and orthoclase plus albite in KT) not only preserve the corona forming reaction participants, but also allow to establish the original interfaces of corundum and aluminosilicates in the host rock.

3.2 Results

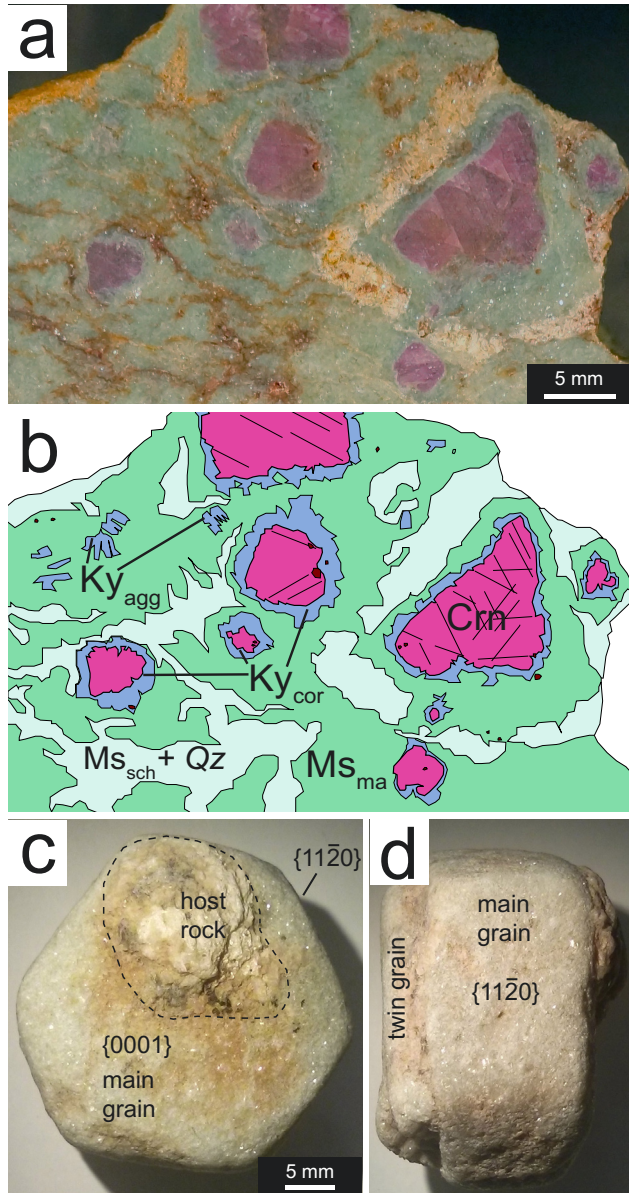


Fig. 3.1 Handspecimen of sample MI (a, b) and sample KT (c, d). a) Photograph of sample MI and b) schematic drawing of a), MI is composed of greenish Cr-muscovite (Ms_{ma}) matrix, porphyroblasts of corundum (Crn) covered with a kyanite corona (Ky_{cor}). Schlieren of colorless muscovite (Ms_{sch}) and quartz (Qz), and polycrystalline kyanite aggregates (Ky_{agg}) are distributed in the matrix. c) and d) photographs of sample KT in different orientations, the sample is composed of a 2.2 cm large corundum single crystal with prismatic habitus, with a twin individual in [0001]. Both main grain and twin are completely covered in a white kyanite corona. On the exposed pinacoid of the main grain a remnant of host rock is preserved.

3.2.1 Sample MI (Mysore, India)

Whole rock chemistry sample MI

Major and trace elements of whole rock are shown in table 3.1. Sample MI is mainly composed of Al_2O_3 (~ 45 wt%), SiO_2 (~ 40.5 wt %), and K_2O (~ 6 wt%). Loss on ignition (LOI) of 3.5% represents likely almost exclusively H_2O considering the mica dominated mineral composition of the sample. Only minor concentrations of Fe_2O_3 (1.08 wt%) and MgO were detected (0.63 wt%). TiO_2 contents of 0.87 wt% represents mostly accessory rutile in the sample. Among the trace elements Cr (1575 ppm) and Ba concentrations (1843 ppm) are the most pronounced. Zirconium and the light rare earth elements (LREE), especially La, Ce, and Nd show values that are well above 100 ppm, whereas Y contents are <20 ppm (Tab. 3.1). This reflects the general occurrence of accessory zircon and monazite grains, whereas xenotime is comparably rare. Nickel concentrations are below detection limit.

Table 3.1. Whole rock data (XRF) of sample MI, Crn-Ky-Ms rock; major elements [oxide wt%], trace elements [ppm]

| | sample MI | D.L. |
|--------------------------------|-----------|-------|
| SiO ₂ | 40.57 | 10.00 |
| TiO ₂ | 0.87 | 2.00 |
| Al ₂ O ₃ | 44.99 | 0.50 |
| Fe ₂ O ₃ | 1.08 | 0.01 |
| MnO | <0.01 | 0.03 |
| MgO | 0.63 | 0.30 |
| CaO | <0.30 | 0.10 |
| Na ₂ O | 0.5 | 0.10 |
| K ₂ O | 6.36 | 0.05 |
| P ₂ O ₅ | 0.08 | 0.02 |
| LOI | 3.59 | |
| Total | 99.28 | |
| ppm | | |
| F | <500 | 500 |
| V | 228 | 10 |
| Cr | 1575 | 500 |
| Ni | <3 | 3 |
| Cu | 33 | 7 |
| Zn | 89 | 10 |
| Ga | 35 | 3 |
| Ge | 2.1 | 1 |
| As | 6 | 4 |
| Rb | 103 | 10 |
| Sr | 77 | 10 |
| Y | 17.3 | 5 |
| Zr | 393.6 | 20 |
| Nb | 13.6 | 5 |
| Mo | 13.9 | 5 |
| Ag | <20 | 20 |
| Cd | <5.0 | 5 |
| Sn | <20 | 20 |
| Sb | 20.2 | 10 |
| Cs | <50 | 50 |
| Ba | 1843.9 | 50 |
| La | 241.4 | 10 |
| Ce | 353.6 | 20 |
| Pr | 46.7 | 10 |
| Nd | 125.9 | 10 |
| Sm | 26.9 | 3 |
| Hf | <10 | 10 |
| Pb | 25 | 5 |
| Bi | 20.3 | 20 |
| Th | 86 | 5 |
| U | 12.5 | 10 |

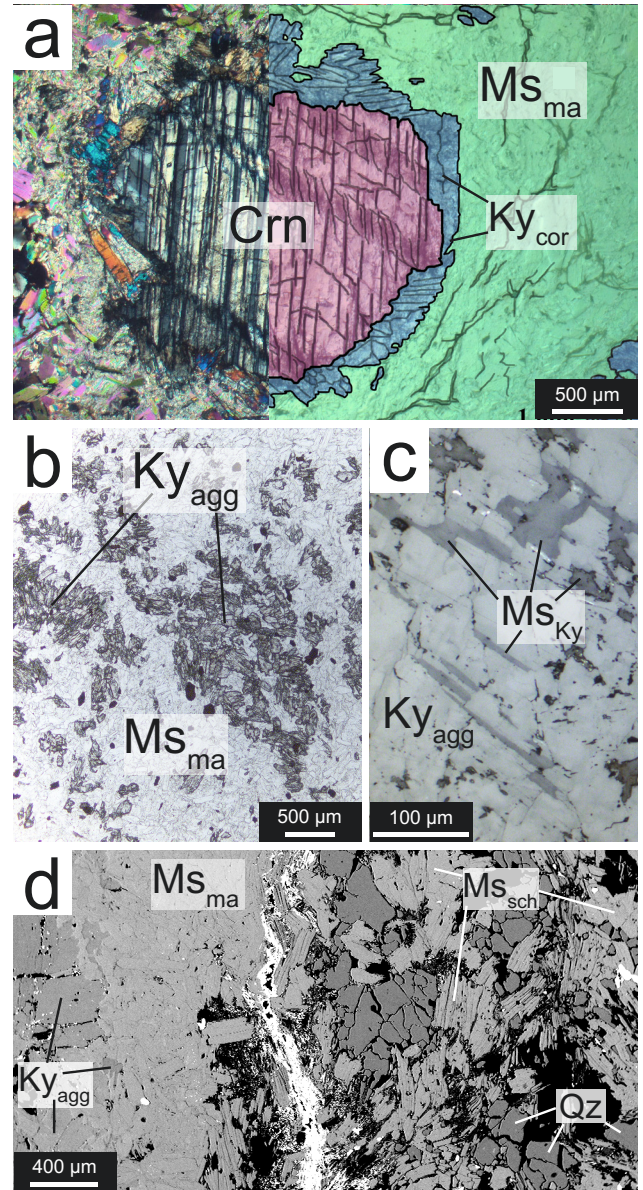


Fig. 3.2 a) Half-colored, half crossed polarized microphotograph of a corundum porphyroblast with kyanite coronae (Ky_{cor}) in Cr-muscovite matrix (Ms_{ma}) of sample MI. The porphyroblast displays two sets of parting planes (with boehmite, see Fig. A3.1). b) Microphotograph of kyanite aggregates (Ky_{agg}) distant from corundum porphyroblasts. c) Microphotograph (reflected light) of muscovite inclusions (Ms_{Ky}) in a Ky_{agg} grain. d) Backscattered electron (BSE) image of a schlieren feature composed of coarse grained, colorless, and mainly Cr-free muscovite (Ms_{sch}) together with quartz (Qz) adjacent to matrix muscovite (Ms_{ma}) and Ky_{agg} grains.

Petrography

Sample MI is composed of around 75 vol% of fine grained, light green muscovite matrix (Ms_{ma} , variety “fuchsite”) with around 10 vol% of corundum porphyroblasts (Crn , variety “ruby”) that are surrounded by monomineralic kyanite coronas (Ky_{cor}) (Figs. 3.1a, b, Fig. 3.2a). In addition to the corona grains, kyanite occurs as polycrystalline aggregates (Ky_{agg}) in the muscovite matrix without connection to the corundum porphyroblasts (Fig. 3.1b, Fig. 3.2b). Aggregate kyanite appears heterogeneously distributed in the matrix generally as intergrowth of several anhedral individuals with random orientation and of highly variable size (5 to 1000 μm) and rarely as single grains (Fig. 3.2b). Both Ky_{agg} and Ky_{cor} grains are intergrown with or contain inclusions of muscovite (Ms_{Ky} ; Fig. 3.2c, Fig. 3.3). The muscovite inclusions in kyanite aggregate grains often match the host grains crystallography in that they are elongated parallel to the kyanite cleavage (Fig. 3.2c). Besides muscovite, Fe-oxides and gahnite inclusions are found in Ky_{agg} grains.

The grain size of the greenish matrix muscovite (Ms_{ma}) does not exceed 300 μm in diameter and no systematic foliation was observed. Distributed within the muscovite matrix are up to 5 vol% of rutile (grain size 50 to 500 μm) and zircon (< 50 μm) in a ratio of ca. 2:1, and accessory monazite (up to 200 μm) and chalcopyrite. Locally, schlieren features comprised exclusively of colorless muscovite

(Ms_{sch}) and quartz, appear in the matrix (Fig. 3.1a, b, Fig. 3.2d). The schlieren often form halos around the corundum porphyroblasts and coronas. However, both corundum with kyanite coronas but without schlieren, and schlieren without associated corundum occur. Therefore the schlieren structures are not considered part of the coronas here. Figure 3.3d shows a cross-section (left to right) from the rock matrix including aggregate kyanite into the schlieren features. The texture of the latter is distinctly coarse grained in comparison with the matrix and hosts several cavities (some of which formed during preparation). The border between Ms_{ma} and Ms_{sch} is outlined by fine-grained iron-hydroxide (Fig. 3.2d).

Coronas in sample MI

The corundum contains randomly distributed fluid-solid inclusion trails (inclusion size < 10 μm) that end at the corundum surface. The solids are mostly mica, rarely large rutile or zircon inclusions are found (> 50 μm). The corundum grains often show a set of polysynthetic twins that is crosscut by parting planes, creating a distinctive rhombohedral network (Fig. 3.1a, b, Fig. 3.2a, Fig. A3.1). Along these planes as well as along twin boundaries, a 1-50 μm wide layer of differently oriented boehmite grains (Bhm) is found (Fig. A3.1b). The phase boundaries of boehmite and corundum are partially open. Less than 10 μm thick layers are generally straight, whereas wider layers consist of several conjoint

branches that enclose corundum remnants (Fig. A3.1).

The width of the kyanite corona is independent of the diameter of the corundum grain and the orientation of the subhedral kyanite grains is apparently random showing no clear correlation with crystallographic features in the corundum. Along the phase boundary of corona and corundum, the kyanite hosts variable quantities of solid inclusions especially iron-oxides (probably magnetite), gahnite with significant hercynite component, and chalcopyrite. Gahnite crystals vary in size but are always oriented parallel to a kyanite cleavage (Fig. A3.2). The phase boundary of corundum and kyanite is irregularly shaped, resembling a “valley-and-hill” topography, where valleys represent depressions and hills represent elevations along the corundum surface (Fig. 3.3a). Valleys are commonly associated with a kyanite-kyanite-grain boundary in the corona, indicating enhanced kyanite growth beneath the corona grain boundaries (Fig. 3.3a, b, d). Occasionally, valleys are associated with a pronounced (open) cleavage plane of individual kyanite crystals. Hills typically form under single kyanite individuals (Fig. 3.3a, b). They get gradually isolated and finally incorporated into the kyanite grain as the neighboring kyanite grain boundaries (valleys) penetrate the corundum surface (see Fig. 3.3b, d). As a result, rounded corundum remnants are preserved as inclusions in the corona grains near the kyanite-corundum phase boundary. Also, muscovite inclusions

(Ms_{Ky}) of variable shape (elongated and rounded) are observed in corona kyanite grains (Fig. 3.3a, c).

The corundum-kyanite phase boundary, like parting planes and twin boundaries inside the corundum porphyroblasts, hosts nanometer wide boehmite layers as TEM investigations reveal (Fig. 3.3e). Also along kyanite-kyanite grain boundaries and between kyanite and corundum inclusions boehmite layers are observed. Furthermore, kyanite-kyanite-grain boundaries are often connected to the rhombohedral boehmite hosting network in the corundum by a small channel ($< 1 \mu m$ wide) that enters the corundum starting at the tip of valley structures (Fig. 3.3d).

Mineral chemistry sample MI

Major and trace element concentrations of corundum, boehmite and kyanite as well as of muscovite from sample MI are given in table 3.2 and 3.3 respectively. Corona- and aggregate-kyanite show very comparable composition with Cr_2O_3 contents of 0.25-0.45 wt%, and Fe_2O_3 contents of 0.05-0.1 wt% (see Tab. 3.2). The Cr-distribution between corundum and kyanite corona crystals appears almost homogeneous in element mappings (Fig. 3.3a map) and measured trace amounts are essentially identical (compare Cr_n and Ky_{cor} , Tab. 3.2). Iron contents of corundum are, however, twice as high as in the adjacent corona kyanite. Titanium contents are very low in corundum (0.02 wt%) and often below

detection limit in kyanite (Tab. 3.2), although TiO₂ concentration is relatively high in the bulk rock at almost 1 wt% due to significant accessory rutile (Tab. 3.1). The outermost parts of the corundum porphyroblasts within the first 40 µm from the corundum-corona contact show a slight but systematic increase in SiO₂, from <0.03 wt% in the center of the porphyroblasts to 0.065 wt% along the phase boundary and in corundum inclusions in corona kyanite (Tab. A3.1).

It is possible to distinguish three types of muscovite (Fig. 3.4, Tab. 3.3, Tab. A3.2). The green matrix muscovite (Ms_{ma}) shows the highest Cr contents among all mica phases with up to 0.5 wt% Cr₂O₃, in that being comparable with Cr-concentrations in kyanite and corundum (Tab. 3.2). Colorless muscovite (Ms_{sch}) within quartz bearing schlieren shows the lowest Cr content among the muscovite types with concentrations below detection limit. Between the Cr maxima and minima in Ms_{ma} and Ms_{sch} respectively, a range of intermediate Cr-concentrations was measured in Ms_{ma} grains located in the selvage of the schlieren features (see Tab. A3.2). These analyses displays a gradual Cr depletion from Ms_{ma} distant from the schlieren features to Ms_{sch} included in the

schlieren (Fig. 3.4), and are not considered an independent muscovite type. Muscovite that is intergrown or included in kyanite (Ms_{Ky} in Ky_{cor} and Ky_{agg}) has distinctly higher Al content than Ms_{ma} and Ms_{sch}, whereas Cr concentrations are comparable with Ms_{ma}. Among all muscovite analyses a positive correlation of Al and Na can be observed with a Na₂O maxima of 1.4 wt% in Ms_{Ky}, whereas Mg and Fe correlate negatively with Al and are lowest in Ms_{Ky} (Fig. 3.4). Titanium concentrations are generally highest in the matrix muscovite, however, strong fluctuations in Ti contents in Ms_{sch} and Ms_{Ky} do not display a clear trend (Tab. 3.3, Table A3.2). Halogen concentrations are generally low in all three muscovite types (F < 0.4 wt%, Cl < 0.07 wt%). The Al:Si (apfu) ratio of the schlieren muscovite is lowest (0.84) compared with Ms_{ma} and Ms_{Ky} (0.87 and 0.93 respectively).

Semiquantitative analyses (EDS) of the accessory mineral phases rutile, zircon, monazite, and chalcopyrite, as well as solid inclusions of gahnite exclusively found in kyanite are given in Table S3. Rutile grains are Cr and Nb bearing. Monazite grains show ThO₂ concentrations of around 6 wt%, which is also reflected in the Th trace element content of whole rock chemistry (Tab. A3.3, Tab. 3.1).

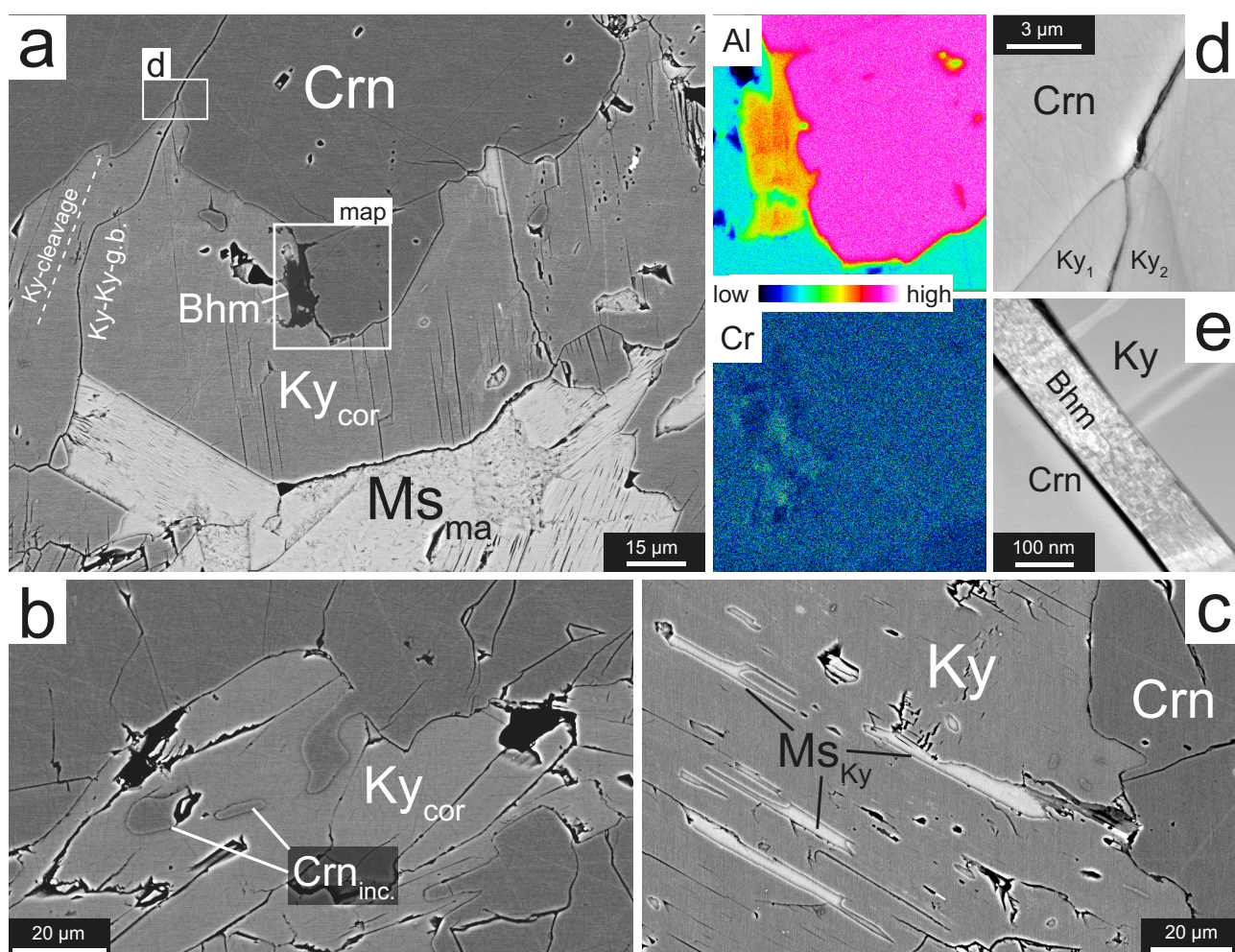


Fig. 3.3 Detailed petrography of the kyanite corona in sample MI. a) Backscattered electron (BSE, EMP) image of a valley-and-hill shaped Crn-Ky corona phase boundary. On the right are two element maps of Al (top) and Cr (bottom) attached (mapping area is indicated in BSE image). The Cr distribution between Crn, Ky, and Ms is homogeneous. b) BSE image of isolated corundum inclusions ($\text{Crn}_{\text{inc.}}$) within kyanite individuals due to enhanced Ky_{cor} growth along Ky-Ky grain boundaries. c) Elongated muscovite inclusions (Ms_{Ky}) in Ky_{cor} grain (BSE image). d) Secondary electron (SE) image displaying a valley structure related to a Ky-Ky grain boundary that is connected to a channel inside the corundum. e) High angle annular dark field (HAADF, TEM) image of boehmite (Bhm) layer located along Crn-Ky phase boundary.

Table 3.2. Chemical composition of corundum (Crn), kyanite (Ky_{cor} , Ky_{agg}), and boehmite (Bhm) in sample MI (WDS analyses, entire dataset see Table A3.1).

| wt% | Crn | | Ky_{cor} | | Ky_{agg} | | Bhm | | D.L. [wt%] |
|-------------------------|--------|---------|--------------------------|---------|--------------------------|--------|--------|--------|------------|
| | 1 | 2 | 1 | 2 | 1 | 2 | 1 | 2 | |
| SiO_2 | b.d. | 0.015 | 37.130 | 37.380 | 37.330 | 37.280 | 0.018 | 0.020 | 0.008 |
| TiO_2 | 0.037 | 0.034 | b.d. | b.d. | 0.052 | b.d. | b.d. | 0.044 | 0.015 |
| Al_2O_3 | 99.260 | 99.500 | 62.220 | 62.580 | 62.700 | 62.100 | 83.850 | 83.840 | 0.052 |
| V_2O_3 | 0.027 | b.d. | b.d. | b.d. | 0.045 | 0.023 | b.d. | b.d. | 0.009 |
| Cr_2O_3 | 0.385 | 0.268 | 0.402 | 0.353 | 0.265 | 0.358 | 0.270 | 0.248 | 0.007 |
| Fe_2O_3 | 0.169 | 0.204 | 0.078 | 0.054 | 0.136 | 0.110 | 0.377 | 0.148 | 0.012 |
| Total | 99.881 | 100.021 | 99.838 | 100.367 | 100.528 | 99.876 | 84.529 | 84.300 | - |

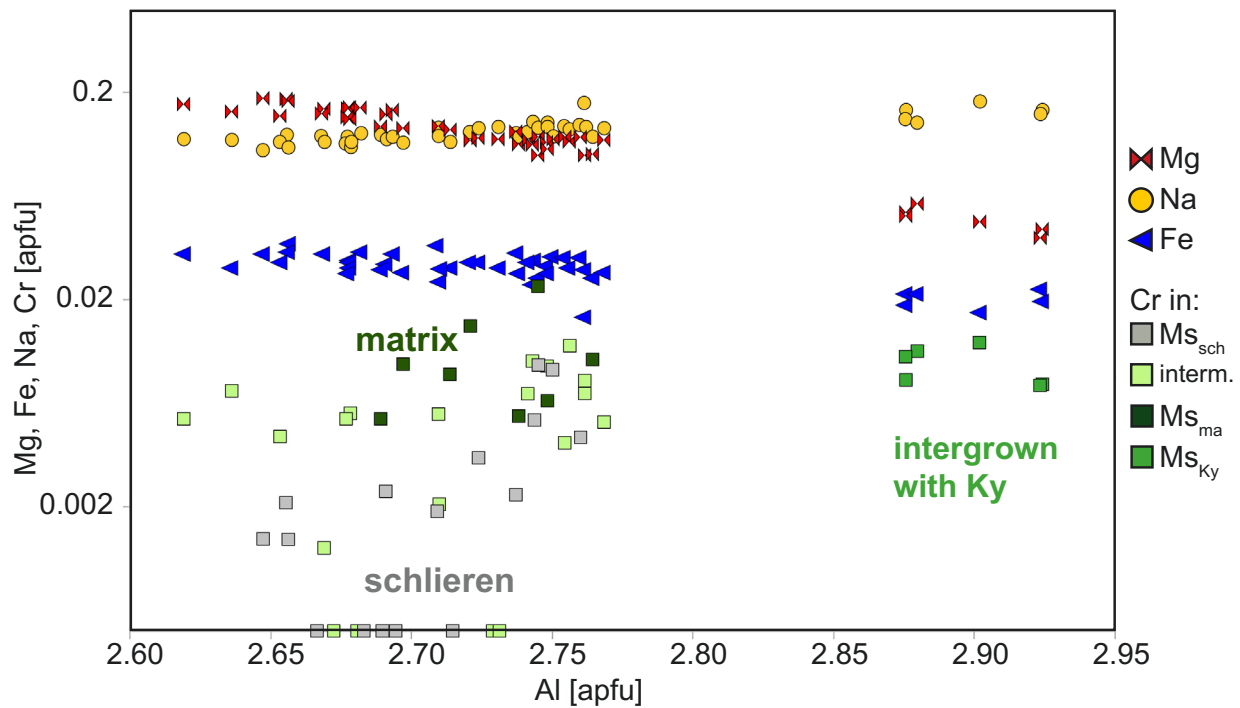


Fig. 3.4 Mineral chemistry of muscovite in sample MI (Al, Na, Mg, Fe, Cr concentration in atoms per formula unit [apfu] normalized to a cation sum of 7, EMP results WDS, Table 3.3 and Table A3.2). According to Al contents and optical differences caused by Cr contents three types of muscovite are determined; matrix muscovite (Ms_{ma}), muscovite intergrown with kyanite (Ms_{Ky}) and schlieren muscovite (Ms_{sch}), the first and the latter show a chemical overlap (intermediate composition) in the selvage of the schlieren features (light green squares).

Table 3.3. Muscovite mineral chemistry (WDS, EMP) of the different muscovite types in sample MI: Ms_{sch} = schlieren muscovite, Ms_{Ky} = muscovite intergrown with Ky, Ms_{ma} = matrix muscovite (see Table A3.2 for solid solution between Ms_{ma} and $Ms_{sch} = Ms_{mix}$). Atom per formula units (apfu) calculated on the basis of 7 cations.

| | Ms_{mx} | | Ms_{sch} | | Ms_{Ky} | |
|--------------------------------|-----------|---------|------------|--------|-----------|--------|
| | 1 | 2 | 1 | 2 | 1 | 2 |
| <i>wt%</i> | | | | | | |
| SiO ₂ | 46.989 | 47.510 | 47.607 | 47.341 | 46.946 | 46.434 |
| TiO ₂ | 0.702 | 0.728 | 0.056 | 0.201 | 0.122 | 0.082 |
| Al ₂ O ₃ | 34.888 | 34.936 | 33.548 | 33.854 | 37.062 | 36.783 |
| Cr ₂ O ₃ | 0.438 | 0.286 | 0.040 | b.d. | 0.157 | 0.215 |
| CaO | 0.040 | 0.011 | b.d. | b.d. | b.d. | b.d. |
| MgO | 0.998 | 1.190 | 1.846 | 1.675 | 0.534 | 0.583 |
| FeO | 0.456 | 0.542 | 0.600 | 0.598 | 0.386 | 0.380 |
| MnO | b.d. | b.d. | 0.018 | 0.029 | b.d. | 0.028 |
| BaO | 0.155 | 0.214 | 0.513 | 0.431 | 0.256 | 0.440 |
| Na ₂ O | 1.022 | 1.011 | 0.950 | 0.967 | 1.288 | 1.103 |
| K ₂ O | 9.348 | 9.561 | 9.165 | 9.161 | 9.223 | 9.283 |
| F | b.d. | 0.383 | b.d. | 0.132 | 0.175 | b.d. |
| Cl | b.d. | b.d. | b.d. | 0.037 | 0.013 | 0.024 |
| H ₂ O | 4.491 | 4.356 | 4.462 | 4.389 | 4.468 | 4.508 |
| Total | 99.527 | 100.728 | 98.813 | 98.815 | 100.632 | 99.866 |
| <i>apfu</i> | | | | | | |
| Si ⁴⁺ | 3.137 | 3.139 | 3.198 | 3.182 | 3.091 | 3.084 |
| Ti ⁴⁺ | 0.035 | 0.036 | 0.003 | 0.010 | 0.006 | 0.004 |
| Al ³⁺ | 2.745 | 2.721 | 2.656 | 2.682 | 2.876 | 2.880 |
| Cr ³⁺ | 0.023 | 0.015 | 0.002 | 0.000 | 0.008 | 0.011 |
| Ca ²⁺ | 0.003 | 0.001 | 0.000 | 0.000 | 0.000 | 0.000 |
| Mg ²⁺ | 0.099 | 0.117 | 0.185 | 0.168 | 0.052 | 0.058 |
| Fe ²⁺ | 0.025 | 0.030 | 0.034 | 0.034 | 0.021 | 0.021 |
| Mn ²⁺ | 0.000 | 0.000 | 0.001 | 0.002 | 0.000 | 0.002 |
| Ba ²⁺ | 0.004 | 0.006 | 0.013 | 0.011 | 0.007 | 0.011 |
| Na ⁺ | 0.132 | 0.129 | 0.124 | 0.126 | 0.164 | 0.142 |
| K ⁺ | 0.796 | 0.806 | 0.785 | 0.786 | 0.775 | 0.787 |
| F ⁻ | 0.000 | 0.080 | 0.000 | 0.028 | 0.036 | 0.000 |
| Cl ⁻ | 0.000 | 0.000 | 0.000 | 0.004 | 0.001 | 0.003 |
| OH ⁻ | 2.000 | 1.920 | 2.000 | 1.968 | 1.962 | 1.997 |
| O ²⁺ | 10.092 | 10.076 | 10.075 | 10.077 | 10.069 | 10.070 |

3.2.2 Sample KT (Kilombero, Tanzania)

Petrography

Host rock portions in sample KT were insufficient to produce whole rock XRF data, because it consists mainly of a 2.5 cm large, euhedral corundum megacryst with a smaller twin grain at its base surrounded by a kyanite corona and only a small remnant of host rock (Fig. 3.1c, d, Fig. 3.5). The latter is composed of perthitic orthoclase (size >5 mm), with minor albite and biotite, as well as muscovite and quartz (Fig. 3.5a, b, Fig. A3.3a, b). Almost every single perthite lens includes F and Cl bearing apatite of less than 10 µm grain size (Fig. A3.3b detail). Coarse-grained biotite (>1 mm) is partially replaced by chlorite, rutile and iron-oxides and shows kink-bands. Muscovite and interstitial quartz apparently replace orthoclase, since remnants of strongly altered orthoclase are included in up to 1 mm large muscovite grains (Fig. A3.3a) and quartz fills the cracks in fragmented orthoclase. Both feldspar and mica phases are locally replaced by kaolinite mainly along their phase boundaries.

Corona in sample KT

The pale yellowish corundum is a flat hexagonal prism with 2.4 cm diameter and 1.0 cm height, whereas the smaller twin individual with the twin law {0001} is 1.7x0.2 cm large (Fig. 3.5). For the thin section the prism was cut parallel to {11-20} (Fig. 3.5). A rhombohedral network of boehmite hosting parting planes comparable to

sample MI (Fig. A3.1) crosscuts both corundum individuals (Fig. 3.5). A second set of such planes with a different crystallographic orientation is observed in a few places.

The colorless kyanite corona is 2.0 – 3.0 mm wide on the *a*-faces of the prism, whereas it is generally <1.5 mm wide on the basal pinacoid (Fig. 3.5). The corona crystals show a highly variable grain size of 50 – 700 µm in diameter and are anhedral with rounded surfaces in a crystal assemblage that is mainly defined by equilibrium grain boundary contacts (Fig. 3.5). Sample KT shows valley-and-hill shaped phase boundaries between corundum and kyanite corona but also between kyanite corona and feldspar in the host rock (Fig. 3.6a, b, c, d). As in sample MI, preferred kyanite growth along the kyanite-kyanite grain boundaries during corona formation creates this type of phase boundary towards the corundum grain and also towards the host rock (Fig. 3.6a, d, compare Fig. 3.3). In sample KT isolation and incorporation of corundum hill structures into kyanite crystals due to an enhanced kyanite growth along corona grain boundaries resulted in kyanite crystals that occasionally enclose several rounded and up to 300 µm large corundum inclusions (Fig. 3.6a, d). Kyanite crystals grown parallel to the corundum basal plane {0001}, located on one of the *a*-faces are generally elongated with up to 700 µm length and less than 200 µm width (Fig. 3.7a). Crystals grown perpendicular to the corundum base are blocky, can reach a width of up to 500 µm and are not longer than 500 µm

(Fig. 3.7b). Both elongated kyanite grains on the a-faces of the corundum prism and blocky kyanite grains on the basal pinacoid host elongated corundum inclusions that are oriented with their elongation approximately parallel to the corundum base (Fig. 3.7a, b). The shape of corundum inclusions and host kyanite grains indicates preferential growth of kyanite along {0001} of the corundum. However, in contrast to the shape-preferred orientation, there is no lattice-preferred orientation of the corona crystals.

The kyanite corona expands also along the twin plane of the two corundum twin individuals (Fig. 3.5, Fig. A3.4). The corona between the twins is around 1 mm wide in the center and increases towards the prisms faces (up to 3 mm). The corona along the twin contact can be divided into three areas, according to the orientation of the kyanite grains. The middle part, with maximum distance to the corundum consists of randomly oriented kyanite grains that are generally free of corundum inclusions (Fig. A3.4 6), whereas the upper and lower part of the corona represent the growth of the kyanite reaction front towards the two twin individuals, characterized by kyanite-kyanite grain boundaries that are oriented approximately perpendicular to the twin plane, and kyanite crystals with corundum inclusions. Chains of kyanite without corundum inclusions are occasionally located inside the corundum oriented along the parting planes (Fig. 3.7c, see Fig. 3.5 detail). These kyanite chains are

connected to the corona. Both kyanite growth between the two (0001) twin individuals and the occurrence of oriented kyanite chains inside the corundum indicate that crystallographic features like twin planes and parting planes provided nucleation sites for kyanite inside the corundum during the corona growth.

Adjacent to the host rock, kyanite crystals include remnants of orthoclase and albite instead of corundum (Fig. 3.6a, b, c). These solid inclusions are less abundant than the corundum inclusion and found only in close vicinity within less than 500 μm distance to the host rock (Fig. 3.6a, c). Rarely both feldspar and corundum inclusions are found in the same kyanite grain, but kyanite grains with either solid inclusions type appear as direct neighbors in the corona. The change from corundum inclusions to feldspar inclusions is located around 300 – 500 μm away from the present corona-host rock contact (Fig. 3.6a). The portion of the corona containing corundum inclusions constitutes 2/3 of the corona volume, approximately 1/3 of the volume consists of kyanite with feldspar inclusions. Other solid inclusions in the corona crystals apart from feldspar and corundum are rare gahnite, and Cl-F-apatite. Kyanite lacks fluid inclusions. Muscovite and quartz are found only in the host rock and muscovite partly replaces kyanite when the two phases occur adjacent along the host-corona contact (Fig. A3.5a, b).

Along the corona grain boundaries (Crn-Ky, and Ky-Ky), a network of boehmite and kaolinite

layers occurs (Fig. A3.6) that is connected to the rhombohedral network inside the corundum host. Boehmite is located mainly along the rhombohedral planes of the corundum but extends occasionally into the corona grain boundaries (Fig. A3.6, A1 map), whereas kaolinite is found exclusively along the grain boundaries in the kyanite corona. Transmission electron microscopy showed that the corundum-kyanite phase boundaries are composed of boehmite or kaolinite layers and no immediate phase contacts or phase boundaries are observed.

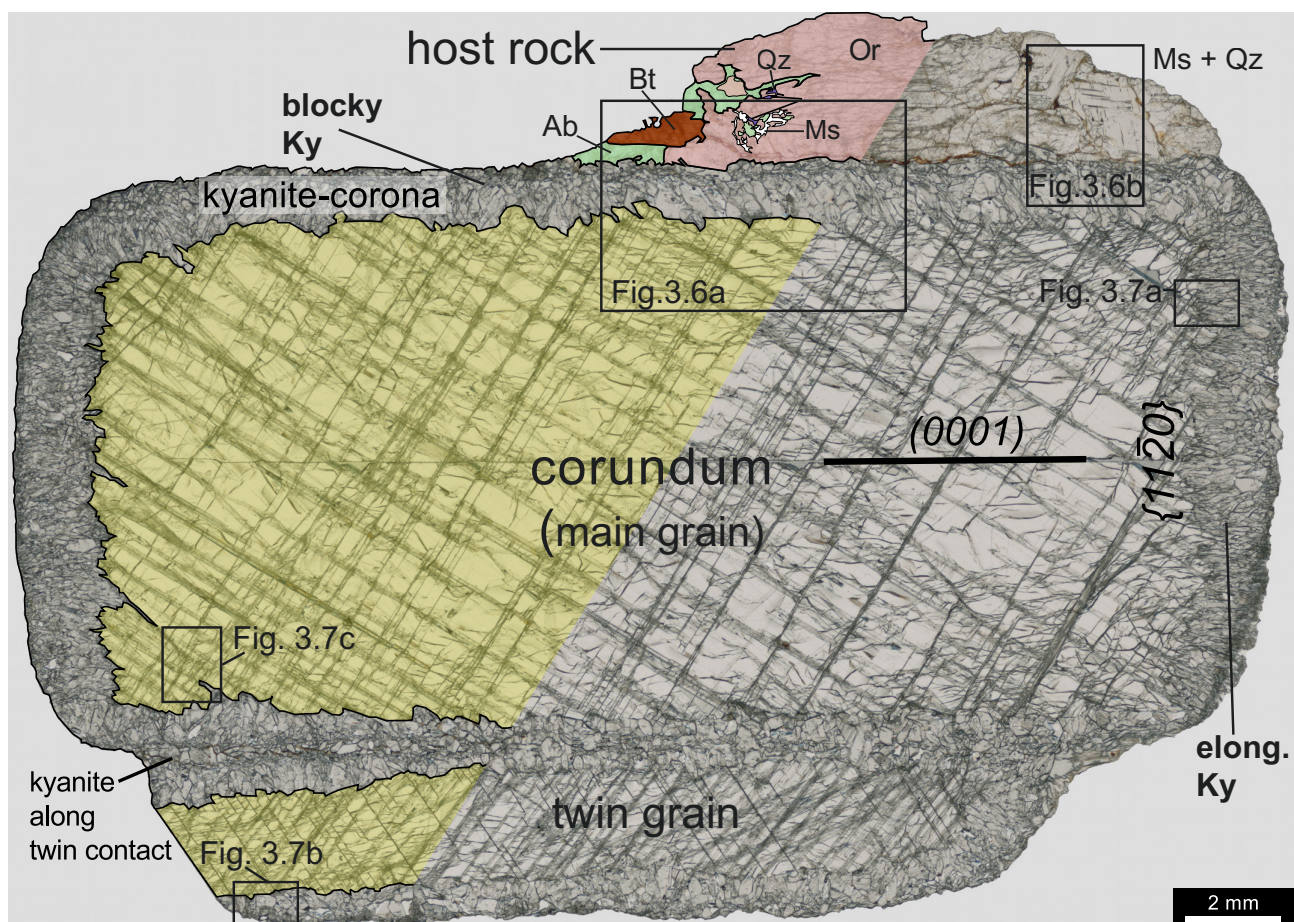


Fig. 3.5 Partly colored photograph of the thin section of sample KT including the main corundum grain (line of sight in $[10\bar{1}0]$) with twin grain (bottom) and complete kyanite corona cover. The corundum displays four different sets of parting planes, along which boehmite layers are located. Elongated kyanite grains are found on faces in $\{11\bar{2}0\}$, blocky kyanite on the basal pinacoid. The host rock remnant is mainly composed of orthoclase (Or) and additional albite (Ab), biotite (Bt), muscovite (Ms), and quartz (Qz). The position of the following figures 3.6 and 3.7 are indicated.

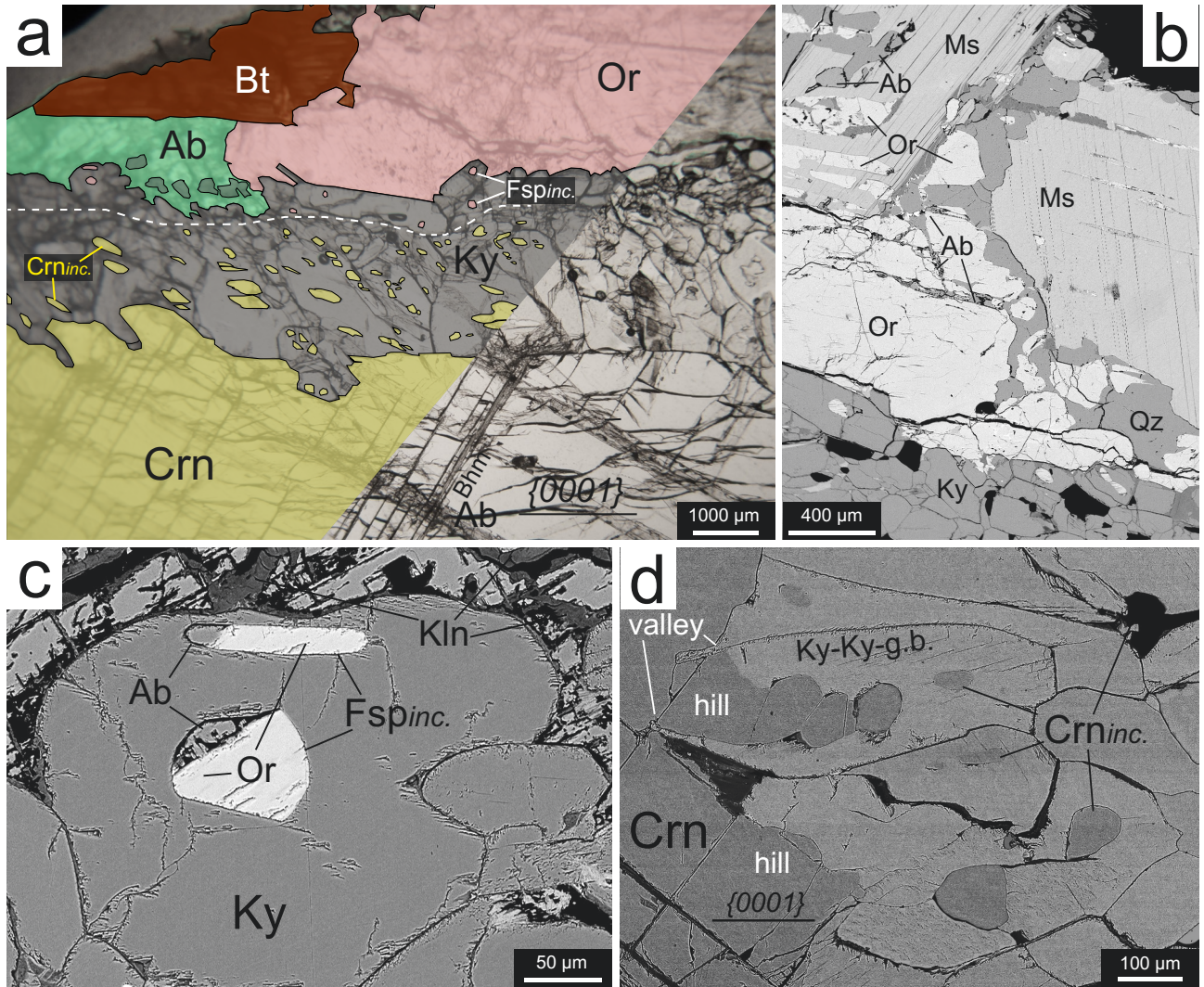


Fig. 3.6 Detailed petrography of the kyanite corona in sample KT. a) Partly colored microphotograph of the contact between Crn main grain (yellow) and Ky-corona (gray), as well as Ky-corona and host rock (Or, Ab, Bt). Kyanite grains include inclusions of Fsp (Fsp_{inc.}) within the outward grown part of the corona and corundum inclusions (Crn_{inc.}) within the inward grown part. The approximate original Crn-host (Fsp) contact is indicated with a dashed white line. The phase boundary of Crn and Ky-corona displays a valley-and-hill topography. b) BSE image of the Ky-corona-host rock contact with Or replacement features composed of Ms and Qz. c) BSE image (EMP) of Fsp inclusions (combined Ab and Or) in Ky crystal. d) BSE image (EMP) of preserved Crn inclusion formation along two highly evolved valleys (deep into Crn grown Ky-Ky-grain boundaries).

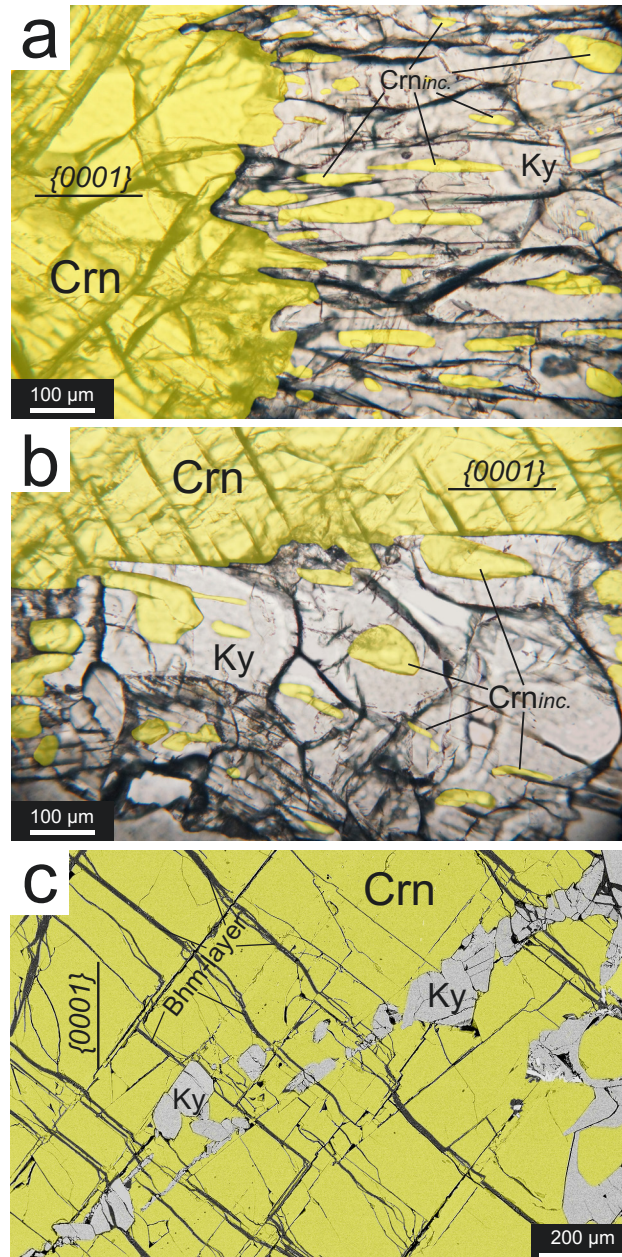


Fig. 3.7 The growth of kyanite corona crystals in dependence of the Crn orientation and crystallographic features (sample KT). a) Colored microphotograph (Crn indicated in yellow) of elongated kyanite individuals grown perpendicular to $[0001]$ into the Crn grain. b) Ky grains grown parallel to $[0001]$ into the Crn grain are blocky and the detachment of Crn islands from the main grain appear to happen mainly parallel to the basal plane of the main grain (indicating inhibited Crn dissolution in $[0001]$). c) Colored BSE image (EMP) of a row of Ky individuals, which is located along a parting plane inside the main grain and is connected to the Ky-corona.

Mineral chemistry sample KT

Both kyanite and corundum contain up to 0.9 wt % Fe_2O_3 , whereas Ti, V, Cr, and Nb concentrations are near or below detection limit of microprobe analyses (Tab. 3.1). Iron distribution is homogeneous throughout the corundum grain and the corona crystals (Fig. A3.6, Fig. A3.7). Neither corundum nor kyanite show any chemical zonation pattern. However, iron is heterogeneously distributed along the grain boundary layers in boehmite and kaolinite (Fig. A3.6).

A systematic increase in silica can be observed in corundum near the corona contact and in corundum inclusions inside the corona crystals (Fig. A3.7). The bulk of the corundum has a SiO_2 content near detection limit of averaged 0.009 wt% (d.l. 0.005), whereas corundum within less than 100 μm distance to the phase boundary shows an increased silica content of 0.039 wt% on average (Tab. 3.1, Tab. A3.4, Fig.

A3.7). Furthermore, the corundum inclusions in kyanite contain an average of 0.077 wt% of SiO_2 . Element profiles through kyanite including corundum fragments and through the reaction front of kyanite and corundum show a homogeneous distribution of Fe among the two phases (Fig. A3.7a, b). On average the Fe_2O_3 content of the corundum inclusions is around 0.05 wt% lower than in the bulk corundum (Fig. A3.7 c, Tab. A3.4).

Mineral chemistry of host rock phases and solid inclusions is given in Tab. A3.5 (EDS results). Feldspars have orthoclase ($\text{Or}_{90}\text{Ab}_{10}$) and albite ($\text{Ab}_{90}\text{An}_{10}$) composition, whether occurring as perthitic lens or coarse grained host rock mineral. The small apatite inclusions associated with the perthitic lenses in orthoclase contain around 1.1 wt% Cl, 3.3 wt% F, and traces of Fe (Tab. A3.5).

Table 3.4. Chemical composition of corundum, kyanite, boehmite, and kaolinite in samples KT (WDS results EMP, entire dataset in Table A3.4) (n = number of analyses, \pm = Std of 1 sigma)

| Table 1. Chemical composition of the sample (wt%) | | | | | | | | | | | | | |
|---|--------------------------|-------|---------------------------------|-------|-------------------------------|-------|--------------|-------|-----------------|-----------------|---------|------------|----|
| wt% | Corundum (Crn) | | | | | | Kyanite (Ky) | | Kaolinite (Kln) | Boehmite (Bhm) | | D.L. [ppm] | |
| | Crn grain center (n = 3) | | Crn < 100µm from ph.b. (n = 35) | | Crn inclusions in Ky (n = 29) | | (n = 79) | | Fe poor | Fe poor Fe rich | | | |
| | Average | ± | Average | ± | Average | ± | Average | ± | | Fe poor | Fe rich | | |
| | | | | | | | | | | | | | |
| SiO ₂ | 0.009 | 0.005 | 0.039 | 0.012 | 0.077 | 0.011 | 36.527 | 0.214 | 47.207 | 0.011 | 0.763 | Si | 28 |
| Al ₂ O ₃ | 99.370 | 0.215 | 99.210 | 0.339 | 99.275 | 0.245 | 62.572 | 0.256 | 39.947 | 82.059 | 82.293 | Al | 49 |
| Fe ₂ O ₃ | 0.833 | 0.056 | 0.821 | 0.033 | 0.772 | 0.037 | 0.797 | 0.029 | 0.382 | 0.762 | 1.997 | Fe | 53 |
| Total | 100.212 | - | 100.070 | - | 100.124 | - | 99.896 | - | 87.550 | 82.766 | 84.853 | | |

3.3 Discussion

Two distinct samples of kyanite corona growth on corundum in quartz bearing rocks are presented (Fig. 3.2, Fig. 3.5). The presence of large porphyroblasts of corundum indicates quartz under-saturation in both rock units prior to kyanite formation. Therefore, the present-day disequilibrium assemblage not only raises the question under what circumstances the reaction corona grew, but also what caused the SiO_2 activity in the rock to increase to the point of formation of kyanite and subsequently quartz.

Introducing external silica via fluid to the corundum bearing rock would be undoubtedly the most intuitive explanation for the occurrence of kyanite reaction rims and quartz precipitates and has been proposed for a rock type similar to sample MI (Raith and Schumacher 2012). Furthermore, the reaction of Al_2O_3 with silica to aluminium silicates is supposed to succeed as long as sufficient fluid flux is present (Shaw and Arima; Kihle et al. 2010). An assumption, however, that is contradictory to failed attempts to synthesize aluminium silicates from Al and Si saturated aqueous fluids under P-T conditions, relevant for most metamorphic crustal rocks (Carr and Fyfe 1960; Aramaki and Roy 1963; Harlov and Milke 2002; Schultze and Franz 2014; Schultze et al. 2014).

The reaction $\text{Crn} + \text{SiO}_2(\text{aq}) = \text{Ky}$ would cause a 74% volume gain per mol Al_2O_3 (Crn: 42.257 $\text{\AA}^3/\text{f.u.}$; Ky: 73.365 $\text{\AA}^3/\text{f.u.}$; f.u. = formula unit at

standard state conditions) if Al is assumed to be immobile. If indeed a net silica influx would be the driving force behind the kyanite corona formation, this would cause a considerable inflation of the rock while it is still under the relatively high pressure conditions of kyanite stability. Considering ductile behavior of the rock matrix at given P-T conditions a volume increase could be partly absorbed. In this case clear signs of deformational stress should be preserved in the mineral assemblage, which are absent in both samples. Excess SiO_2 would need to come from unknown neighboring rock units given that both samples were originally quartz-free rocks.

An alternative option of kyanite corona formation involves the breakdown of matrix phases around and subsequent reaction with the corundum porphyroblasts. An option that not only is more reasonable with respect to the molar volume budget but also is supported by textural evidence found in both samples coronas. Enhanced kyanite growth along kyanite-kyanite grain boundaries in samples MI and KT resulted in isolation of corundum fragments and their incorporation into the corona as corundum inclusions. This allows tracing the original outline of the corundum crystal before inward growth of the kyanite corona. Additionally, inclusions of muscovite (sample MI) and feldspar (sample KT) are

preserved along the outer portions of the kyanite coronas, which allow to reconstruct the outward corona growth (Fig. 3.3, Fig. 3.6). Abundance and textures of the host rock mineral inclusions in the kyanite corona and the contact between the kyanite and the adjacent matrix mineral grains strongly suggest that the kyanite forming reaction consumed the host rock minerals

(muscovite and K-feldspar, respectively) in both samples. In the following corona growth events for both samples are reconstructed based on the textural and chemical observations (Fig. 3.8a, b).

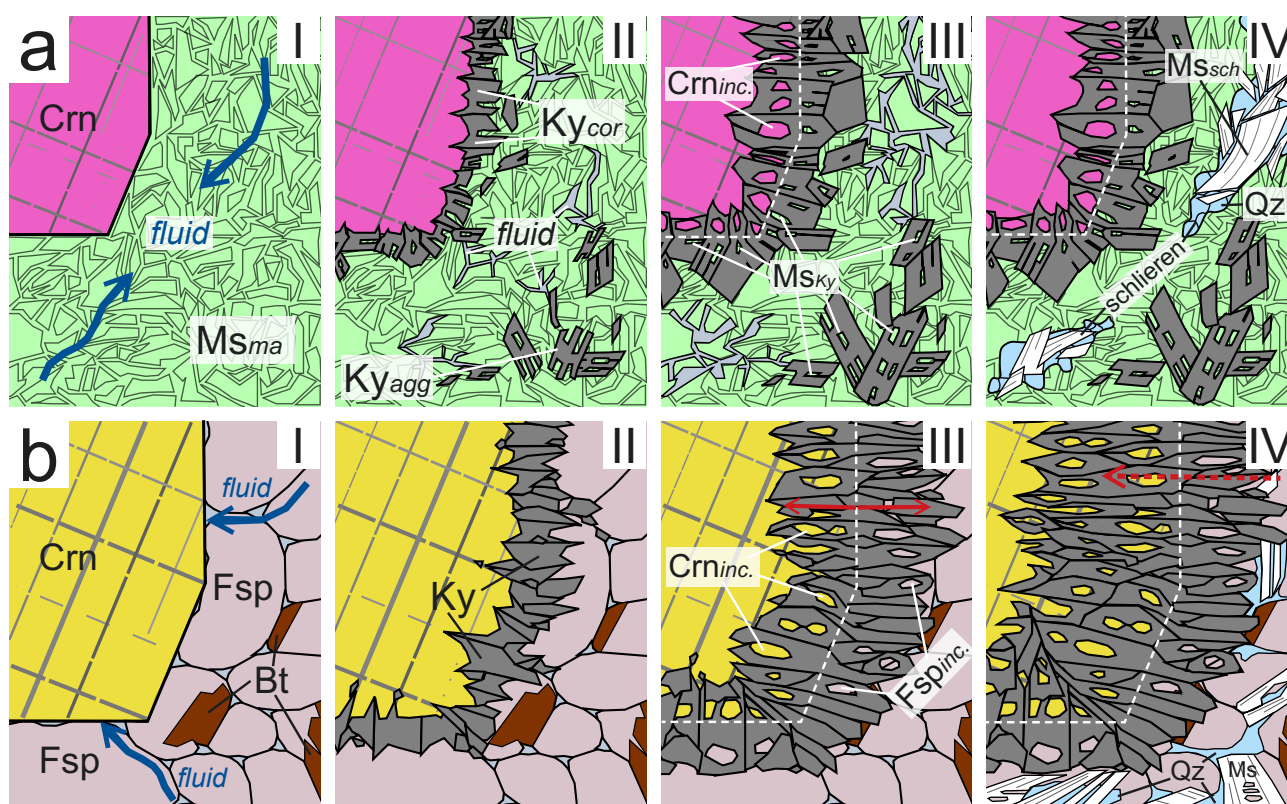


Fig. 3.8 Corona growth-sketches in samples MI (a) and KT (b). a) I) Original paragenesis of sample MI, Crn in Ms_{ma} dominated matrix, is infiltrated by fluid. II) Equilibration processes between fluid and rock triggers both aggregate kyanite growth (Ky_{agg}) inside Ms_{ma} according to reaction *MI1* (see text) at the expense of Ms_{ma} , and corona kyanite growth (Ky_{cor}) along the Crn- Ms_{ma} interfaces according to reaction *MI2* (see text). III) Educts of reaction *MI1* and *MI2* are preserved as Crn and Ms_{Ky} inclusions in Ky_{cor} and Ky_{agg} grains. IV) Later Ms_{ma} recrystallizes along schlieren shaped areas in the rocks matrix distant from Ky-rich areas, forming Cr-free muscovite (Ms_{sch}) together with quartz (Qz). b) I) The original assemblage of sample KT, Crn main grain in feldspar (Fsp) dominated host rock is introduced to an external fluid that dissolves Fsp and Crn. II) Kyanite forms along the Crn-Fsp interface and the Ky growth front of reaction *KT1* (see text) proceeds inwards towards Crn and outwards towards Fsp. III) Crn and Fsp (Or + Ab) inclusions form in Ky due to promoted Ky growth along Ky-Ky grain boundaries. IV) Low Al solubility limits the proceeding of reaction *KT1*, a corona comprised of around 2/3 vol.% of Ky with Crn inclusions and 1/3 vol.% Ky with Fsp inclusions is preserved. At lower temperatures Fsp reacts to Ms and Qz according to reaction *KT2* (see text).

3.3.1 Corundum and kyanite formation

Sample MI

Assemblage prior to corona growth:

The formation of chromium-aluminium-potassium rich, silica undersaturated rock domains like sample MI is still not completely understood, but their appearance is commonly linked to ultramafic rocks (Schreyer et al. 1981; Schreyer 1982; Kerrich et al. 1987; Upadhyaya et al. 1992). The question whether these rocks represent laterites, bauxites or alunites associated with greenstone belts or hydrothermally desilicified komatiites has been controversially debated (Schreyer et al. 1981; Kerrich et al. 1987, 1988; Schreyer 1988). The corundum-muscovite rocks described by Raith and Schumacher (2012) were sampled in small mines in near Mercara in the Kodagu District and are geographically closest to the mining location of sample MI (< 100 km west of Mysore). They are described as enclaves of Cr-enriched high-alumina metabauxites, within units of biotite-garnet schists, surrounded by Peninsular Gneiss (Raith and Schumacher 2012). The whole rock Al_2O_3 and SiO_2 contents of sample MI are typical for metabauxites or metalaterites (Beukes et al. 2002). Compared to common soils the sample is, however, strongly depleted in Fe, Mg, Ni, Mn, Ca, and Na, and enriched in Cr and Ti, which suggests a redox-induced fractionation during weathering (Davies et al. 1989). Under reducing conditions ferrous iron is mobile and likely removed along with

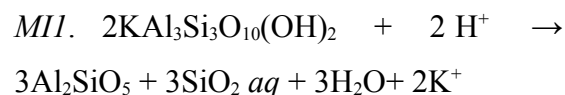
Ni, Co, Mn, and Mg. Chromium on the other hand, is normally mobile under oxidizing conditions as Cr^{6+} and immobile under reducing conditions as Cr^{3+} (Klein-BenDavid Ofra et al. 2011; Watenphul et al. 2012). It is worth mentioning that modern day lateritic weathering cannot explain the absence of FeO (1.08 wt%) in sample MI (Davies et al. 1989), but strongly Fe-deficient paleosols are known to have formed prior to the Great Oxidation Event (GOE) during the Paleoproterozoic (Golani 1989; Murakami et al. 2001; Kanzaki and Murakami 2016). Assuming sample MI derived from a former laterite, the corundum-muscovite rock is most likely the product of a prograde metamorphic decomposition of typical soil minerals, e.g. illitic mica and gibbsite to muscovite and corundum (Fig. 3.8a I). The large corundum porphyroblasts could also represent sedimentary deposits in the former soil. However, considering the fairly homogenous Cr distribution between muscovite and corundum, a scenario where the two minerals stem from different sources seems less likely.

Corona growth:

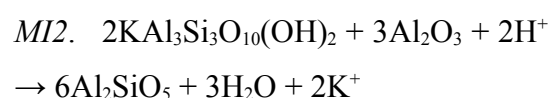
Kyanite corona crystals (Ky_{cor}) contain both corundum and muscovite inclusions occasionally within the same grain, whereas the kyanite crystals in the matrix aggregates (Ky_{agg}) contain only muscovite inclusions and no corundum (Fig. 3.2b, c, Fig. 3.3a, b, c). The corundum and muscovite inclusions indicate that kyanite growth included the replacement of

either one or both phases. Since aggregate and corona kyanite are chemically identical (Tab. 3.2), a concurrent formation appears very likely. For aggregate kyanite the only plausible formation process involves the decomposition of muscovite since the system lacks other Al sources besides corundum and muscovite. Muscovite that is closely associated or intergrown with kyanite (Ms_{Ky}) shows increased Al and decreased Si, Mg, and Fe contents compared with the matrix muscovite (Ms_{ma}), Cr contents are similar (see Tab. 3.3, Fig. 3.4). García-Casco et al. (1993) described almost identical trends for Al, Si, Mg, and Fe from primary muscovite to recrystallized muscovite in an andalusite-producing muscovite dehydration reaction, which suggests recrystallization of Ms_{ma} and formation of Ms_{Ky} during aluminium silicate growth. The replacement of muscovite by kyanite liberates substantial amounts of K^+ and silica and since neither quartz nor feldspar is found along with aggregate or corona kyanite the reaction must have been accompanied by the removal of K^+ and silica from the reaction site (kyanite bearing areas of the sample). This strongly suggests that a metamorphic fluid induced and catalyzed the muscovite replacement by removing K^+ and silica (see reaction *MII*; and Wintsch 1975). The fluid- and quartz-absent muscovite dehydration requires temperatures of around 800°C (Huang and Wyllie 1974; Spear et al. 1999). Considering an open system, the introduction of a fluid not only decreases the required tem-

perature for muscovite dehydration, it is also the only plausible explanation for substantial K^+ and silica removal from the reaction site (reaction *MII*, see Wintsch 1975; Weinberg and Hasalová 2015). For formation of kyanite aggregates distributed in the muscovite matrix of sample MI, reaction *MII* is proposed (Fig. 3.8a II):



Incompletely replaced corundum and muscovite inclusions (Fig. 3.3) in corona kyanite grains indicate involvement of corundum and muscovite as reactants during kyanite corona formation. Around the porphyroblasts and possibly aided by the pressure contrast imposed by the rigid corundum, muscovite can react with corundum and fluid directly to form kyanite without the release of silica (reaction *MI2*; Fig. 3.8a II, III):



Chromium contents in Cr-rich muscovite (Ms_{ma} and Ms_{Ky}), kyanite and corundum are comparable, which indicates immobile behavior of Cr during kyanite growth. At temperatures relevant for kyanite formation, Cr is most likely trivalent and relatively immobile (Klein-BenDavid et al. 2011; Watenphul et al. 2013) and substitutes for Al^{3+} without much fractionation in reactions *MII* and *MI2*. It is

therefore assumed that the Cr-free muscovite and quartz in the schlieren (Fig. 3.2d) formed during a chronologically separate event (Fig. 3.8a IV). Since schlieren muscovite (Ms_{sch}) occasionally shows Cr-rich core regions and matrix muscovite in vicinity of the schlieren tends to have lower Cr-contents than grains within greater distance to the schlieren, it is concluded that Ms_{sch} represents locally recrystallized matrix muscovite (Ms_{ma}). The low Al:Si (apfu) ratio of the schlieren muscovite compared with Ms_{ma} and Ms_{Ky} (Tab. 3.3) reflects the growth of Ms_{sch} under silica saturated conditions and supports a concurrent growth of Ms_{sch} and quartz in the schlieren features. The silica and K^+ -bearing and Cr-free fluids produced during the formation of the kyanite aggregates (reaction *III*) may have precipitated quartz and Cr-free muscovite in extension fractures during the uplift of the unit at lower temperatures as a result of decreasing mineral solubility, forming the schlieren structures (Fig. 3.8a IV).

The mineral assemblage of sample MI and the reconstructed reaction sequence MI suggest P-T formation conditions of around 9 kbar and 750 °C (Spear et al. 1999), which coincide with the upper limit of P-T estimates of 600 – 750 °C and 5 – 9 kbar for an approximate sampling location along the E-W striking facies boundary of amphibolite (N) and granulite terrains (S) in the partly migmatized Peninsular Gneiss units of the Dharwar Supergroup and the estimated P-T conditions of kyanite corona growth in sam-

ples from Mercara (Pichamuthu 1935; Raith et al. 1982; Srikantappa et al. 1985; Naqvi et al. 1988; Chadwick et al. 1997; Sharma 2010; Raith and Schuhmacher 2012; Fig. 2.1). The formation of kyanite at the expense of muscovite is generally associated with a prograde metamorphic evolution, although in sample MI an increase in temperature is neither evident nor necessary for the reaction.

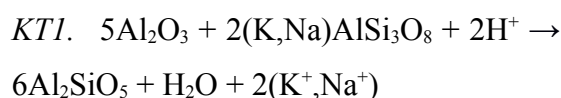
Sample KT

Assemblage prior to corona growth:

The kyanite corona evolved between corundum and feldspar implying the original rock consisted of large corundum grains in a feldspar (mainly orthoclase) dominated gneiss. Such an assemblage can occur as a result of quartz undersaturated muscovite dehydration (Huang and Wyllie 1974). The Udzungwa mountains (sampling location of sample KT) consist of different ortho- and paragneisses. Migmatization and partial anatexis of Si-deficient metapelitic rocks in the area have been described and likely affected sample KT (Vogt et al. 2006; Sommer et al. 2008; Fig. 3.8b I). Kyanite is common in these granulite facies rocks, however, corundum has not been mentioned. Ferric iron contents of corundum in sample KT indicates growth temperatures of >700 °C (Feenstra et al. 2005) consistent with the predicted peak metamorphic temperatures of the region (Sommer et al. 2003, 2008).

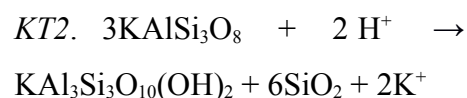
Corona growth:

The corona in sample KT includes corundum and feldspar inclusions and the systematic distribution of those in the corona crystals provides evidence that the reaction proceeded both inward and outward from the original interface (Fig. 3.6a). One reaction front developed in direction of the host rock and is represented by a single row of kyanite grains containing exclusively feldspar (Or and Ab) inclusions (Fig. 3.6a, b, c). The other front, in which kyanite includes only corundum and constitutes approximately 2/3 of the corona volume, evolved inward into the corundum grain (Fig. 3.6a, d, Fig. 3.7). This indicates that kyanite formed via reaction *KT1* (Fig. 3.8b II):



The reaction involves alkali loss from the system and therefore requires the participation of a fluid or liquid phase (Fig. 3.8b I, II, III) and requires a volume ratio corundum to feldspar (orthoclase) of around 63 to 37, which corresponds well with the approximately 2/3 volume portion of corona containing corundum inclusions and around 1/3 volume portion of corona with feldspar inclusions. Therefore, reaction *KT1* theoretically accounts for the entire corona formation process and no additional silica input is required. Although muscovite and quartz occur as replacement products of orthoclase in the host rock remnant

(Fig. 3.6b), no muscovite or quartz inclusions are found inside the corona. Instead, wherever kyanite and muscovite occur adjacent to each other, kyanite is partly replaced by muscovite (Fig. A3.5). Those features support a first occurrence of kyanite that predates the precipitation of muscovite and quartz and likely proceeds outside the muscovite stability field. The replacement of feldspar by muscovite and quartz probably proceeded at lower temperatures than reaction *KT1* as reaction *KT2*:



The isolation of corundum inside the kyanite corona and limited Al dissolution and transport in metamorphic fluids prevent the participation of corundum as chemical component in reaction *KT2* (Fig. 3.8b III). Hence, the precipitation of quartz only several hundreds of micrometer away from corundum is possible. However, since the fluid phase involved in *KT2* is clearly saturated with respect to quartz, silica transport through the corona towards corundum can be expected. Although the major corona growth event is texturally recorded as replacement reaction *KT1*, and kyanite is locally replaced by muscovite, which contradicts simultaneous growth of both minerals (Fig. A3.5), a kyanite growth sequence induced by silica bearing fluid (from *KT2*) that proceeded exclusively towards corundum cannot be ruled out completely (Fig. 3.8b IV). Muscovite growth at the expense of

kyanite could represent a separate muscovite generation postdating *KT2*.

Sample KT displays kyanite corona growth at the expense of feldspar and corundum induced and catalyzed by fluid input (reaction *KT1*, Fig. 3.8b) and the subsequent formation of muscovite and quartz at decreasing temperatures (reactions *KT2*). The reaction sequence points to a retrograde P-T evolution with an initial

decompressive stage that enables fluid infiltration (*KT1*) followed by cooling (*KT2*), which is consistent with a clockwise metamorphic path with peak metamorphic conditions of around 800°C, 13 kbar and a subsequent approximately isothermal decompression to 10 kbar and 750°C for the Western Granulites (Sommer et al. 2003, 2008).

3.3.2 Comparison of samples MI and KT

Corona growth features

The corona growth in both samples is controlled by mineral replacement reactions involving one or more reactant phases that are preserved as inclusions in kyanite (reactions *M11*, *M12* and *KT1*). These reactions necessarily involve a fluid, which mobilizes K⁺. A pronounced and characteristic interface morphology, the valley-and-hill structured corundum-kyanite phase boundary indicates that in both samples element transport through the corona happened mainly along kyanite-kyanite grain boundaries (Fig. 3.3, Fig. 3.6) comparable with the growth of titanite coronas on rutile (Lucassen et al. 2010, 2012a, 2012b). The presence of a fluid will enhance grain boundary diffusion. A possible role of the kyanite cleavage as diffusion pathway during kyanite growth is probable for sample MI, since occasionally valley structures also appear at the end of open cleavage planes.

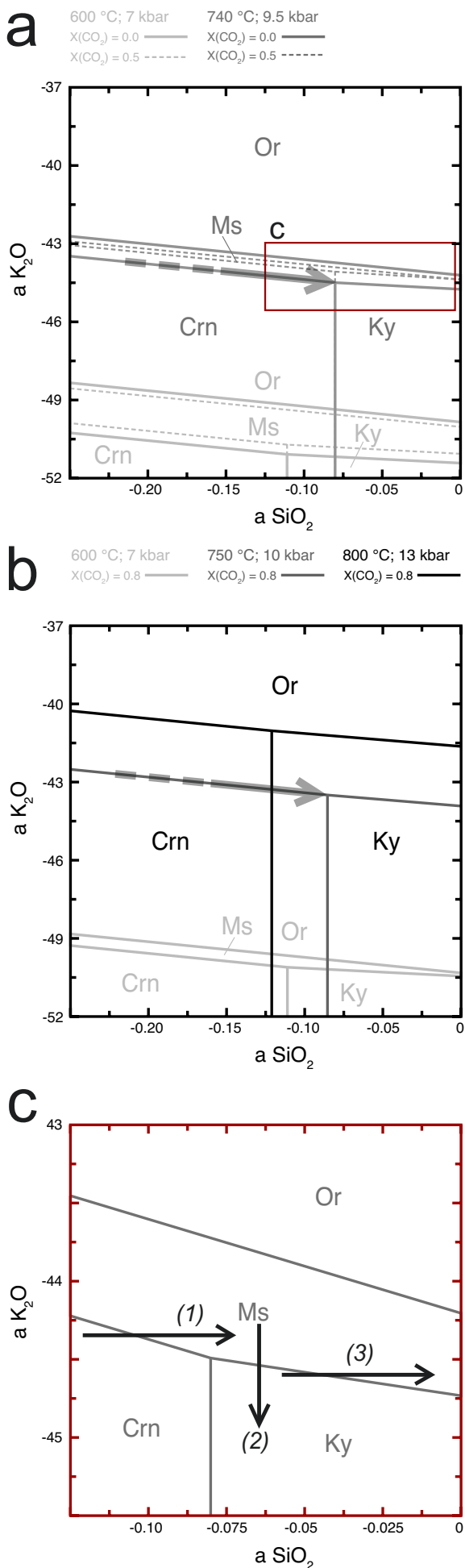
The elongation of corundum inclusions and kyanite grains in the corona of sample KT indicate enhanced corundum dissolution parallel to the basal plane, whereas dissolution perpendicular to faces in (0001) appears reduced (Fig. 3.7a, b). This crystallographic growth dependence of kyanite is only observed in sample KT, whereas the corona crystals in sample MI display random shape, independent of their location on corundum. The orientation relationship between kyanite grains and muscovite remnants (Fig. 3.3a, c) suggests that the corona kyanite in sample MI adopted the crystallographic orientation of muscovite rather than that of corundum (as in sample KT). This may indicate that the corona growth was at least partially initiated by pure muscovite breakdown without involvement of corundum (reaction *M11*) before corundum started to be consumed as well (*M12*). Also, the distinctly different shape of kyanite corona crystals in sample MI (subhedral to euhedral) and KT (anhedral) are likely reflecting the different reactions involved

in the kyanite formation (Fig. 3.3a, Fig. 3.6, Fig. 3.7).

The majority of grain boundaries within the corona of sample MI is filled with boehmite, whereas in sample KT, boehmite is mainly found inside corundum and instead kaolinite occurs along the corona grain boundaries (Fig. 3.3, Fig. A3.1, Fig. A3.6). The presence of hydroxides indicates the presence of a hydrous fluid along partly open grain boundaries that re-equilibrates at temperatures $< 300\text{ }^{\circ}\text{C}$ with the surrounding kyanite and corundum (Kennedy 1959; Bratton and Brindley 1962; Scott and Carruthers 1969; Chatterjee et al. 1984). The variable shape and appearance of boehmite in corundum (layers along twins and parting planes and patchy inclusions) indicates a transformation of corundum with locally preserved fluid along cracks, parting and twin planes and fluid inclusion trails. Whether the opening of corona grain boundaries is mainly the result of thermal contraction during cooling and exhumation of the rock and the presence of fluid is caused by subsequent weathering, or boehmite and kaolinite evolve along fluid pathways and from fluids that were directly involved in the growth process of the corona cannot be determined definitively. The same accounts for boehmite along the rhombohedral network inside corundum in both samples. The fact that boehmite clearly appears in corundum during late stages of the rocks' geological cycle at lower temperatures (Kennedy 1959) does not necessarily imply that the stage of crystal-

lographic deformation responsible for the formation of parting planes in corundum happened simultaneously. In sample KT kyanite grains are found aligned parallel to the parting planes inside the corundum and between corundum twins in (0001), apparently placing the formation of these crystallographic features prior or during corona formation. Depressions in the corundum surface ("valleys") created by Ky-Ky grain boundaries are often connected to parting planes suggesting that the formation of the planes might play a role in Al-dissolution and transport during corona growth.

Fig. 3.9 Page 50; Activity diagrams of $a\text{K}_2\text{O}$ vs. $a\text{SiO}_2$, calculated with the program Perplex_X using the thermodynamic dataset of Holland and Powell (1998). a) Diagram for sample MI calculated with variable XCO_2 and at two distinct P-T conditions, $740\text{ }^{\circ}\text{C}$; 9.5 kbar was suggested by Raith and Schuhmacher (2012)(gray arrow indicates fluid evolution leading to corona formation). b) Diagram for sample KT at P-T conditions proposed for the Western Granulites with peak metamorphic conditions of $800\text{ }^{\circ}\text{C}$; 13 kbar (see text) and a fluid composition of 0.8 XCO_2 (gray arrow indicates fluid evolution leading to corona formation). c) Detailed area in a (rectangle) displaying the influence of compositional changes in the fluid on the mineral paragenesis in sample MI (Crn-Ms-Ky): (1) pure SiO_2 influx at constant K_2O activity leads to Ms growth at the expense of Crn and (3) Ky, whereas (2) K^+ removal at constant SiO_2 leads to Ky growth at the expense of Ms (equivalent trends can be applied to b, sample KT).



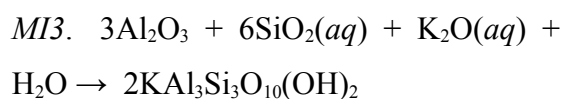
Fluid-mineral interaction and element distribution

For the kyanite producing reactions *MI1*, *MI2* and *KT1*, fluid acts as crucial agent and triggers the mineral replacement. In order to do so infiltration of external fluid is required and the source of external fluid is likely located in the surrounding rocks. Considering that no fluids (no fluid inclusions) are preserved in MI and KT, some basic insight into potential fluid compositions can only be gained by looking at mineral assemblages and the metamorphic grades of the samples. According to Crawford and Hollister (1986) and Olsen (1987) fluids in metapelites show a compositional progression characterized by increasing $X\text{CO}_2$ in mixed $\text{H}_2\text{O}-\text{CO}_2$ fluids with increasing metamorphic grade. Whereas fluids are composed of ~70 to >99 mol% H_2O above the pyrophyllite isograd, >60 mol% CO_2 can be observed in fluids above the staurolite isograd (Crawford and Hollister 1986; Stout et al. 1986). The appearance of muscovite and absence of feldspar in reactions reconstructed for sample MI indicates that the participating fluid was likely aqueous with $X\text{CO}_2 < 0.5$ (Fig. 3.9a).

Sample KT originates from an area of migmatized metasediments and according to Crawford and Hollister (1986) fluids tend to enrich in CO_2 with the onset of melting due to removal of H_2O into the melt phase (> 0.85 $X\text{CO}_2$ at > 950 °C; >5 kbar). Therefore, and due to the absence of water-bearing products during kyanite growth, the fluid in sample KT is

assumingly CO₂ rich and water activity is limited (Fig. 3.9b). With XCO₂ of 0.8, muscovite stability is reached at lower temperatures coinciding with the retrograde metamorphic path reported for the Western Granulites (Fig. 3.9b; Sommer et al. 2003, 2008).

Analysis of the reaction textures of kyanite and remnants of reactants preserved in kyanite has shown that kyanite replaced muscovite (reaction *MII*) or muscovite plus corundum (*MI2*) in sample MI. In sample KT, kyanite replaced K-feldspar plus corundum (*KTI*). In simplified aK₂O vs. aSiO₂ diagrams in the system K₂O-Al₂O₃-SiO₂-H₂O-CO₂, for both samples the fluids involved prior to kyanite precipitation lie somewhere on the univariant curve between corundum and muscovite, and corundum and feldspar respectively (Fig. 3.9a, b). In sample MI the phase equilibrium along this curve involves only corundum and muscovite as solids and SiO₂ and K₂O in solution (*MI3*):



This equilibrium shows that silica influx into sample MI of a fluid that is muscovite buffered with respect to aK₂O would lead to muscovite growth at the expense of corundum (path 1 in Fig. 3.9c), while simultaneously reducing aK₂O in the fluid until the system reaches the invariant point Crn-Ky-Ms. Conversely, a reduction of aK₂O under constant aSiO₂ would

push equilibrium *MI3* to the left side, forming corundum at the expense of muscovite until the invariant point is reached. There is no textural evidence for either of these processes and both may contribute. Once the invariant point is reached, kyanite can form via reactions *MII* or *MI2*. The reactions both release potassium, and path 2 in figure 3.9c shows that potassium activity needs to be decreased and silica activity increased to move into the kyanite stability field. Therefore, potassium removal from the system is a prerequisite for the formation of kyanite. The pure addition of silica at constant aK₂O at the invariant point would keep transforming corundum to muscovite (*MI3*) and not into kyanite. After a kyanite corona has formed around the corundum, effectively shielding the latter from the rest of the system due to a low Al solubility in most metamorphic fluids (Manning 2006, 2007), the fluid is in equilibrium only with kyanite and muscovite (reaction *MII*). Increase of silica at constant aK₂O would now produce muscovite at the expense of kyanite (path 3 in Fig. 3.9c). This was not observed in the samples. The reaction that was indeed observed at this interface, kyanite formation at the expense of muscovite (*MII*), can only take place if potassium activity decreases. Silica activity may or may not increase during this reaction. The univariant curve between muscovite and kyanite describes the maximum ratio of aSiO₂ increase to aK₂O decrease that would still allow the kyanite producing reaction to proceed. However,

isolation of corundum inside kyanite coronas prevents corundum from participating as Al buffer in the system, which potentially leads to a disproportionate increase in silica in the fluid during muscovite dissolution and even quartz saturation (*MII*), if potassium continues to be removed (Fig. 3.9a, b).

For sample KT, this discussion is essentially the same except that orthoclase needs to be substituted for muscovite, because the topologies of the activity diagrams are qualitatively very similar. This shows that in the two investigated samples, the main kyanite-forming reactions are controlled by potassium loss and not silica influx. The breakdown of K-bearing phases provides all necessary silica for kyanite. Since there is no evidence for K-consuming reactions concurrent with the kyanite formation, the only way to lower potassium activity in the fluid is removal from the system via a mobile fluid. A stagnant fluid would halt the reactions in an early stage. Whether or not additional silica influx does occur is inconsequential for the corona formation, contrary to that, a continuous removal of potassium not only explains the formation of kyanite but also the presence of quartz in both samples.

Alkali (K or Na) loss often accompanies the formation of Al_2SiO_5 polymorphs and has been reported from numerous localities and geological settings (Vernon 1979; Wintsch and Andrews 1988; Nyman et al. 1995; Nabelek 1997; McLelland et al. 2002; Verma et al. 2005). Kyanite rich domains representing “hydro-

thermally potassium-leached” feldspathic metarhyolites have been described by Gresens (1971) from New Mexico. Sillimanite-quartz assemblages in high-grade metapelitic gneisses and migmatites of the Cooma Complex (New South Wales, Australia) are explained as a result of feldspar and mica being exposed to “hydrogen metasomatism or base-leaching” (Vernon 1979). The mineral replacement of feldspar and mica is driven by K^+ , Ca^{2+} , Na^+ , Mg^{2+} , and Fe^{2+} removal from the rock. Widmer and Thompson (2001) described the formation of kyanite quartz veins in metabasaltic eclogite facies rocks from the Zermatt-Saas Zone (Switzerland) as result of fluid induced paragonite replacement, in which sodium is dissolved and removed by fluid flow through the veins. On the microscopic scale andalusite formation in partly decomposed muscovite was described from the Torrox orthogneiss complex (Spain) (Sanchez-Navas 1999). The dehydration reaction culminating in andalusite growth inside the large muscovite grains can only be explained with K diffusion out of the muscovite into the rocks matrix. Mobilized alkali components also appear to aid the non-seeded aluminium silicate synthesis, however, the role of additional H_2O seems controversial (Coes 1955; Huang and Willey 1974; Brearley and Rubie 1990). To my knowledge, this study presents the first two cases of aluminium silicate corona formation on corundum by a comparable alkali-leaching process.

Although probably not accounting for the major silica mass transfer during the formation of kyanite coronas in samples MI and KT, SiO_2aq clearly plays a role in the silica distribution along the coronas (Anderson and Burnham 1967; Manning 2004). Silica mobility along grain boundaries limits the corona growth rate, once direct contact of the reactants (Crn-Ms, Crn-Or) is prevented by a kyanite reaction rim. A systematic increase of Si in corundum near the corona phase boundary contact and in corundum inclusions in kyanite in both samples indicates silica bulk diffusion several tens of μm into the corundum lattice (Tab. A3.1, Fig. A3.7). Besides Al, Si, and K, the relevant trace elements for sample MI and KT respectively are Cr and Fe. The homogeneity of Cr and Fe distribution between corundum and corona

crystals, distinguishes the coronas of the present study clearly from other coronas, e.g. titanite rims on rutile (Lucassen et al. 2010, 2011). Kyanite is known to form and preserve specific trace element zonation pattern over the course of its geological appearance (Müller et al. 2012, 2016), which indicates slow internal chemical re-equilibration by bulk diffusion. Both Cr and Fe are mainly incorporated as trivalent cations for Al^{3+} in kyanite, in which state they show limited solubility in metamorphic fluids. The homogeneous Cr and Fe distribution in samples MI and KT, therefore, points to an immobile or stationary distribution of the trace elements during kyanite growth comparable with Al, mainly driven by surface interactions during mineral replacement.

3.4 Conclusion

Using systematically preserved mineral inclusions in monomineralic kyanite coronas on corundum single crystals from two different locations, mineral replacement reactions responsible for the corona formation were reconstructed. In both samples the reactions are triggered by the infiltration of external fluid and the subsequent replacement of corundum and adjacent host rock aluminosilicates. No clear evidence is found in either of the two samples that kyanite precipitated substantially as result of a net influx of SiO_2 into the corundum bearing rocks. This observation agrees with known experimental constraints in the synthesis of aluminium silicates (Carr 1968; Hemingway 1992; Harlov and Milke 2002; Schultze and Franz 2014; Schultze et al. 2014). The replacement textures indicate that for both corona forming events an external silica source is unlikely, or at least unnecessary. On the contrary, potassium leaching from feldspar or muscovite and removal of K^+ along with the metamorphic fluid appears to be the critical requisite for kyanite formation in both samples. This seems to be the only hypothesis compatible with all observations in the samples as well as established knowledge about kyanite formation in much more common regional metamorphic

metapelitic rocks (Read 1932; Carmichael 1969; Kerrick 1972, 1990; García-Casco et al. 1993).

Moreover, the replacement reactions leading to corona formation potentially allow the initially silica deficient rocks to saturate in quartz. The transition from quartz undersaturated to quartz saturated systems is achieved not by silica input but by the loss of potassium from the system via fluid and by shielding a substantial Al_2O_3 portion from the system as an effect of corona formation.

The involved host-rock mineral in sample MI (India) is muscovite, which breaks down to form kyanite. Because muscovite dehydrates, this reaction can be viewed as nominally prograde, although it may in fact be triggered by fluid migration alone without major changes in P or T. In sample KT (Tanzania), mainly K-feldspar reacts with corundum to kyanite. Since the original (almost) water-free assemblage subsequently forms muscovite, kyanite formation likely takes place on a retrograde path in this case. The case study of those two samples therefore indicates that kyanite corona formation on corundum as a result of potassium leaching happens both on prograde and retrograde pathways in rocks of the KASH system.

4. How Si diffusion into corundum promotes the metastable coexistence of corundum and quartz over the formation of Al_2SiO_5 - an experimental study (*experiments part 1*)

4.1 Summary

In the previous chapter investigations on natural kyanite corona formation on corundum showed that kyanite was at least partially produced by fluid-induced mineral replacement reactions in aluminosilicates (mica, feldspar) surrounding the corundum. While corundum acts as Al source to the growing corona, flow through of alkali deficient fluid triggers the decomposition of muscovite or feldspar, which ultimately provides silica. Under experimental conditions of Al_2SiO_5 formation the removal of fluid mid-experiment is not possible. Instead, different experiments were conducted in order to establish whether Al_2SiO_5 coronas would form on corundum as a result of the interaction of corundum with silica saturated fluid, in direct contact with quartz and fluid, or as a result of dehydrating phyllosilicates adjacent to corundum at 400 – 800 °C and 2 – 20 kbar. To determine the parameters influencing the corona formation on corundum some of these experiments were seeded with fine grained kyanite and several comparative experiments, under similar conditions but in other systems (with variable reactants) were conducted. A better understanding of the transformation mechanisms captured at the corundum surface, would hopefully shed light on the complex and often thermodynamically inconsistent reactions in the system Al_2O_3 - SiO_2 - H_2O .

Corundum showed to be a suitable precursor phase for corona formation. However, coronas only formed

in experiments with additional components Na, K, N, and Mg (yielding feldspar or sheet silicates). In experiments with pure water and with low pH neither kyanite nor sillimanite formed, indicating that the nucleation and growth of Al_2SiO_5 are obstructed even in experiments including seed crystals despite sufficiently high reaction rate and the presence of reaction-triggering fluids. In contrast, an unusual fluid-aided silica diffusion process of silica into corundum is documented that lead to the precipitation of quartz in corundum. Nanometer-wide silica layers structurally similar to single tetrahedral-octahedral layers as in dioctahedral phyllosilicates formed along the basal plane of the corundum crystal in an up to 50 μm wide rim. These nano-layers enhance the silica diffusion rate drastically and provoke silica supersaturation in corundum with precipitation of quartz. Insufficiently high reaction kinetics in the system Al_2O_3 - SiO_2 - H_2O can thus be ruled out as an explanation for the absence of aluminium silicates in many experimental studies. The metastable assemblage of quartz and corundum sometimes observed in rocks is furthermore not necessarily the result of dry or fluid absent conditions as postulated in the literature. The aqueous fluid in experiments does not promote Al_2SiO_5 formation, but rather seems to support the prevalence of the metastable assemblage.

4.2 Results

No Al_2SiO_5 polymorphs formed in unseeded experiments or grew in kyanite-seeded experiments. Instead, various other features of interaction between Al_2O_3 and SiO_2 were observed in different stages at different experimental times. The corundum's response to the attacking silica-rich agent was documented on the nanometer scale, providing detailed insight into the interactions of all involved components. The observations will be presented sorted by experiments of similar design that are summarized under the term "setup".

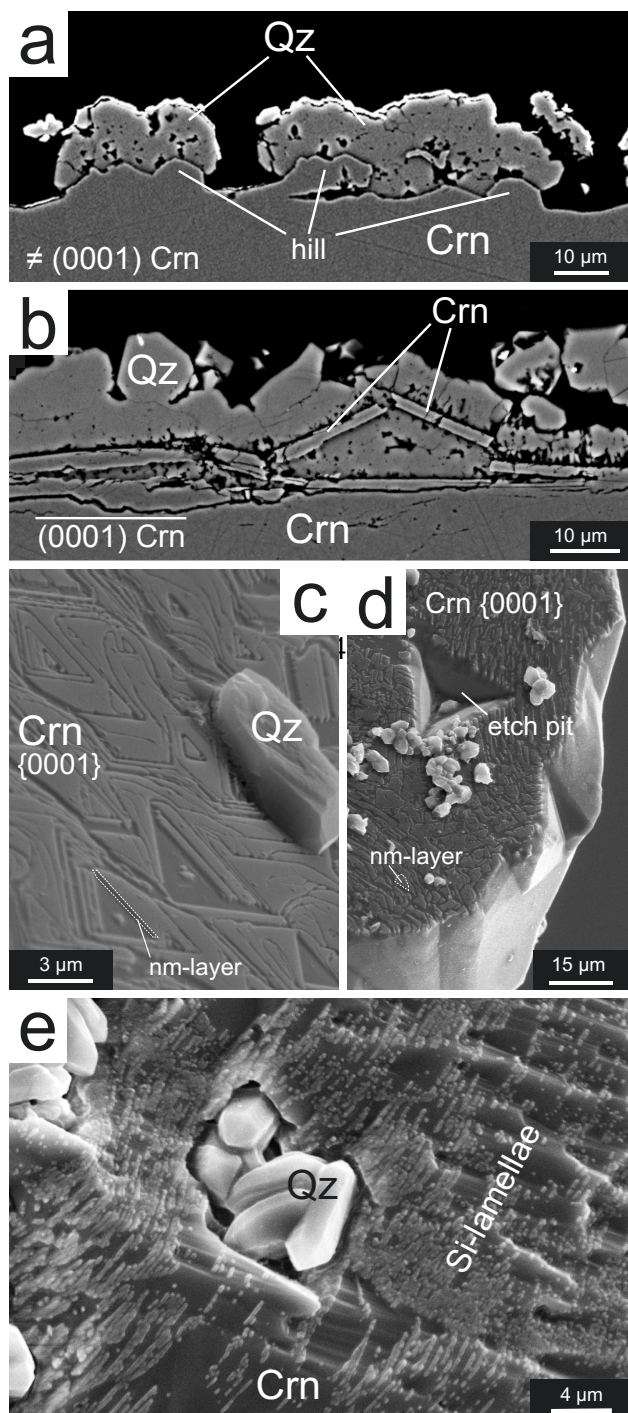
Setup 1) Corundum + SiO_2 + H_2O \pm HCl \pm BH_3O_3

(Runs 1 to 14)

The interaction of corundum with neutral, silica-saturated water (run 1; Tab. 2.1) resulted in a complete, yet porous quartz cover on the corundum grains (Fig. A4.1). With decreasing pH the quartz cover on corundum became increasingly incomplete and intense etch pit formation was observed at the corundum surface (Fig. 4.1). In experiments with neutral or moderately low pH (runs 1 to 5) the dissolution features at the corundum surface appeared to be mainly influenced by fluid paths provided by the covering quartz crystals (Fig. 4.1a, b, Fig. A4.1a). Numerous trails of fluid inclusions along the quartz grain boundaries

within the cover were found by TEM analysis (Fig. A4.1b). Quartz grains and corundum have an open phase boundary, whereas the quartz grain boundaries are partly closed (Fig. A4.1b). Topographic depressions in the corundum are situated either at the contact of the corundum surface with quartz-quartz grain boundaries (Fig. 4.1b, Fig. A4.1a) or between neighboring quartz grains in an incomplete quartz cover (Fig. 4.1a). Sections through the quartz-corundum contact show that corundum dissolution was promoted and etch pits were formed between adjacent quartz grains on the corundum surface (grain boundary or interstice), while the dissolution of corundum at positions covered by quartz appear limited and form hill-like features (Fig. 4.1a). Moreover, the covered parts of corundum were occasionally enclosed and isolated by quartz and eventually detached from the large single crystal (Fig. 4.1a).

Fig. 4.1 Page 59; Altered corundum from setup 1 and 2, with low pH (a, b H_3BO_3 added run 5; c, d, e HCl added runs 7, 15, 6). a) and b) BSE images (EMP) of dissolution features along the corundum (Crn) surface; a) Crn face oblique to $\{0001\}$ shows a valley-and-hill-morphology evolved beneath an incomplete quartz (Qz) cover, with detached Crn inclusions in Qz grains. b) Qz cover grown on $\{0001\}$ face of Crn without valley and hill morphology, instead plates of Crn are detached parallel to $\{0001\}$. c) SE image of shallow etch pits formation on $\{0001\}$ faces indicates limited Crn dissolution in $[0001]$. d) Only one prominent etch pit with dissolution planes in $\{10\bar{1}2\}$ is found on $\{0001\}$ (SE image). In both c) and d) a silica bearing, ~ 200 nm wide layer is displayed on the Crn basal plane (Fig. A4.2, Table A4.1). Shallow etch pits are carved into this layer. e) SE images of etched Crn surface, covered in < 1 μm thick, strictly parallel oriented, Si-bearing lamellae (brighter than Crn surface). Qz is grown into the Crn surface.



Dissolution features observed on synthetic corundum grains reveal that the corundum dissolution rate varied on different faces (Fig. 4.1a, b). The polished basal plane rarely shows etch pits but instead is detached as entire plates by enclosing quartz (Fig. 4.1b). Only experimental runs of more than 14 days with HCl (runs 7, 9, 10, 11, 13) show characteristic triangular, generally shallow ($< 1 \mu\text{m}$ deep) etch pits on $\{0001\}$ (Fig. 4.1c, d). These etch pits are depressions in an up to 500 nm wide, Si-rich (0001) surface layer on strongly etched grains (Fig. 4.1c, d, Fig. A4.2, Tab. A4.1). SiO_2 and Al_2O_3 values obtained by EMPA along the layers are highly variable due to edge effects caused by uneven grain boundaries (Tab. A4.1). Corundum faces $\{10\bar{1}2\}$ and occasionally $\{\bar{1}014\}$ formed prominent dissolution planes during those runs (Fig. 4.1d, Fig. A4.2). Independent of the intensity of etch features the precipitation of Al_2SiO_5 was not observed. Aluminum- and Cl-bearing quench products associated with quartz grains were found in HCl added runs instead. The quartz grains show unsystematically elevated Al concentrations of up to 0.5 wt% Al_2O_3 in both neutral and acidic experiments.

Experiments carried out for ≤ 14 days produced etched corundum grains (synthetic and natural) interspersed with single quartz grains grown several μm into the corundum surface (Fig. 4.1e). The corundum surface was furthermore systematically covered with up to 1 μm thick,

parallel oriented, Si-bearing lamellar and planar features (Fig. 4.1e). Cross sections through natural corundum single grains of those experiments show an up to 50 μm wide, altered area in the margin of the grains (visible in both CL and BSE images), where the Si content of the corundum increases substantially to up to 5000 ppm (Fig. 4.2a, b, c). Highest Si contents were measured along the reaction front of the rim (Fig. 4.2c, profile *A-B* see Tab. 4.1). Within the altered rim and towards the corundum surface, Si concentrations decrease continuously, while in average still exceeding the concentration of the non-altered grain (Fig. 4.2c, Tab. 4.1). The profile pattern resembles a steep ramp (Fig. 4.2c). The Si distribution in the rim is heterogeneous, with maximum Si concentrations along parallel, up to one μm thick layers within the grain (Fig. 4.2c), which presumably correspond to the lamellar and planar Si-rich features observed at the corundum surface (Fig. 4.1e). Iron contents of 0.05 ± 0.02 wt% Fe_2O_3 in unaltered corundum were depleted in the reaction rims to < 0.03 wt % or show values below detection limit (Tab. 4.1, Fig. 4.2c). Reaction rims on natural corundum crystals are significantly wider than those on synthetic grains. The latter are generally not more than one μm wide and cover grains less comprehensively than natural grains, making it difficult to investigate the rims on synthetic grains.

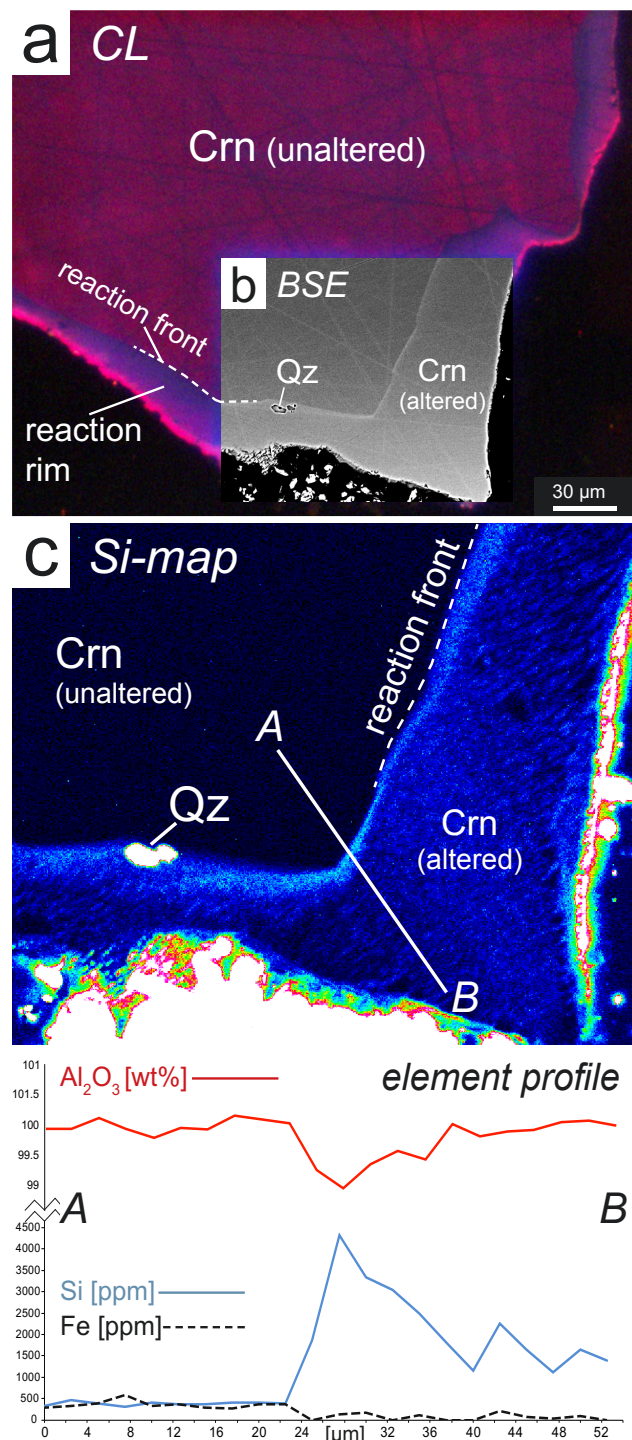


Fig. 4.2 a) Optical cathodoluminescence (CL) image of an altered natural corundum (Crn) grain from run 6 with a marginal, up to 50 μm wide, reaction rim (reaction front indicated with white dashed line). b) Detail BSE image of the reaction rim (brighter than the unaltered Crn) containing two quartz (Qz) inclusions. c) Element mapping of Si (produced at 20 kV, 100 nA, 500 ms dwell time) of the area in b) combined with an element profile *A-B* (Tab. 4.1). The map displays Si increase and heterogeneous Si distribution (stripe pattern) in the rim compared with the unaltered Crn grain. Al and Si trends in the profile are inverse, Si-maxima are measured in the reaction front, and the rim is depleted in Fe (Al₂O₃ in wt%, Si, and Fe in ppm).

TEM investigations carried out along an element profile (Fig. 4.2c) show that the Si increase in the altered corundum rim is caused by silicate nano-layers (SNLs) located along the basal plane (Fig. 4.3). The first 200 nm of the reaction front are enriched in Si (measurable with TEM-EDS) but no specific features in bright field images or HRTEM indicates the cause for the enrichment (Fig. 4.3a). Behind the 200 nm front homogeneously distributed single SNLs were found (Fig. 4.3a). Throughout the rest of the alteration rim starting 200 nm away from the reaction front and ending at the corundum surface, however, the SNLs appear gradually organized or accumulated in restricted, parallel oriented areas separated by SNL-free areas (Fig. 4.3b). In these accumulated areas, the single SNLs occur together with double layers (Fig. 4.3b). In BF images and in Si element mappings the accumulated layers are visible as a stripe pattern (Fig. 4.2c, Fig. 4.3b). Diffraction patterns of altered corundum, which shows SNLs in HAADF images, display a weak additional diffraction peak halfway between (0000) and (0006), indicating double lattice plane distance (Fig. A4.3). Electron diffraction patterns display the SNLs as streak pattern in [0001] (Fig. A4.3). Quantitative results of an EDS profile through the SNLs and SNL-free corundum (Fig. 4.3c) lie within the range of error of the analytical method of $\leq 5\%$ for elements with an atomic mass number > 8 . An inverse trend is observed between the Si- and Al-profile with on average ca. 4 atom % less Al

in the SNLs compared with the layer free corundum and ca. 2 atom % more Si (Fig. 4.3c).

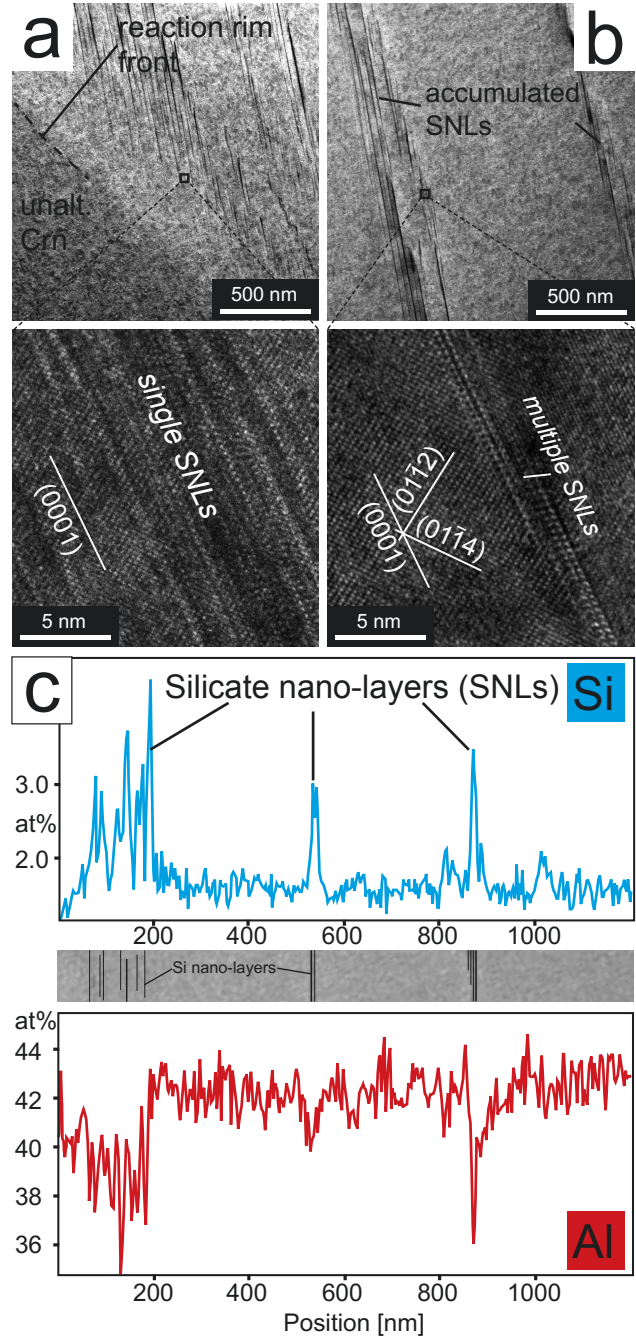
Despite this intense interaction of corundum and silica, Al_2SiO_5 precipitation was not observed. Instead, up to 10 μm large quartz inclusions were occasionally found inside the altered corundum rim, distant from the single crystal's surface (Fig. 4.2b, c). Furthermore, the SNL-bearing corundum areas disappeared in experiments of prolonged duration (> 21 days). Altered areas were also found around fluid inclusion trails inside the corundum grain after ≤ 14 days of experiment (Fig. 4.4a, profile *AA-AB*, Tab. A4.2). Similar inclusion trails hosted numerous quartz grains and fluid after longer experiments, while no increase in Si or other signs of alteration could be detected in areas enclosing the trail (Fig. 4.4b, c).

Runs 2, 3, and 5 were unfortunately contaminated and are not reproducible thus not included in this chapter.

Table 4.1. Element profile A-B (1 analysis point per 2.5 μm) through Si-enriched reaction rim in corundum single grain in run 6: 500°C; 4.65 kbar, see Fig. 4.2c (WDS results EMP)

| wt% | 0 | 2.5 | 5 | 7.5 | 10 | 12.5 | 15 | 17.5 | 20 | 22.5 | 25 | 27.5 |
|--------------------------------|--------|--------|--------|--------|-------|--------|--------|--------|--------|--------|-------|-------|
| SiO ₂ | 0.069 | 0.098 | 0.084 | 0.066 | 0.086 | 0.078 | 0.080 | 0.088 | 0.085 | 0.084 | 0.397 | 0.925 |
| Al ₂ O ₃ | 99.93 | 99.93 | 100.11 | 99.93 | 99.79 | 99.95 | 99.93 | 100.15 | 100.08 | 100.03 | 99.26 | 98.95 |
| Fe ₂ O ₃ | 0.041 | 0.047 | 0.054 | 0.083 | 0.046 | 0.052 | 0.042 | 0.038 | 0.052 | 0.051 | 0.000 | 0.020 |
| Total | 100.04 | 100.07 | 100.25 | 100.08 | 99.92 | 100.08 | 100.05 | 100.28 | 100.22 | 100.17 | 99.66 | 99.90 |
| Si ppm | 323 | 458 | 393 | 309 | 402 | 365 | 374 | 411 | 397 | 393 | 1856 | 4324 |
| Fe ppm | 288 | 326 | 381 | 583 | 319 | 365 | 295 | 264 | 365 | 358 | 0 | 140 |

| wt% | 30 | 32.5 | 35 | 37.5 | 40 | 42.5 | 45 | 47.5 | 50 | 52.5 | D.L. |
|--------------------------------|--------|--------|-------|--------|--------|--------|--------|--------|--------|--------|-------|
| SiO ₂ | 0.715 | 0.652 | 0.534 | 0.384 | 0.248 | 0.482 | 0.354 | 0.240 | 0.351 | 0.296 | 0.020 |
| Al ₂ O ₃ | 99.35 | 99.56 | 99.42 | 100.02 | 99.80 | 99.89 | 99.92 | 100.04 | 100.07 | 99.99 | 0.023 |
| Fe ₂ O ₃ | 0.023 | b.d. | 0.016 | b.d. | b.d. | 0.031 | 0.009 | b.d. | 0.014 | b.d. | 0.005 |
| Total | 100.09 | 100.21 | 99.97 | 100.40 | 100.05 | 100.40 | 100.28 | 100.28 | 100.44 | 100.29 | - |
| Si ppm | 3342 | 3048 | 2496 | 1795 | 1159 | 2253 | 1655 | 1122 | 1641 | 1384 | - |
| Fe ppm | 163 | 0 | 109 | 0 | 0 | 218 | 62 | 31 | 101 | 0 | - |



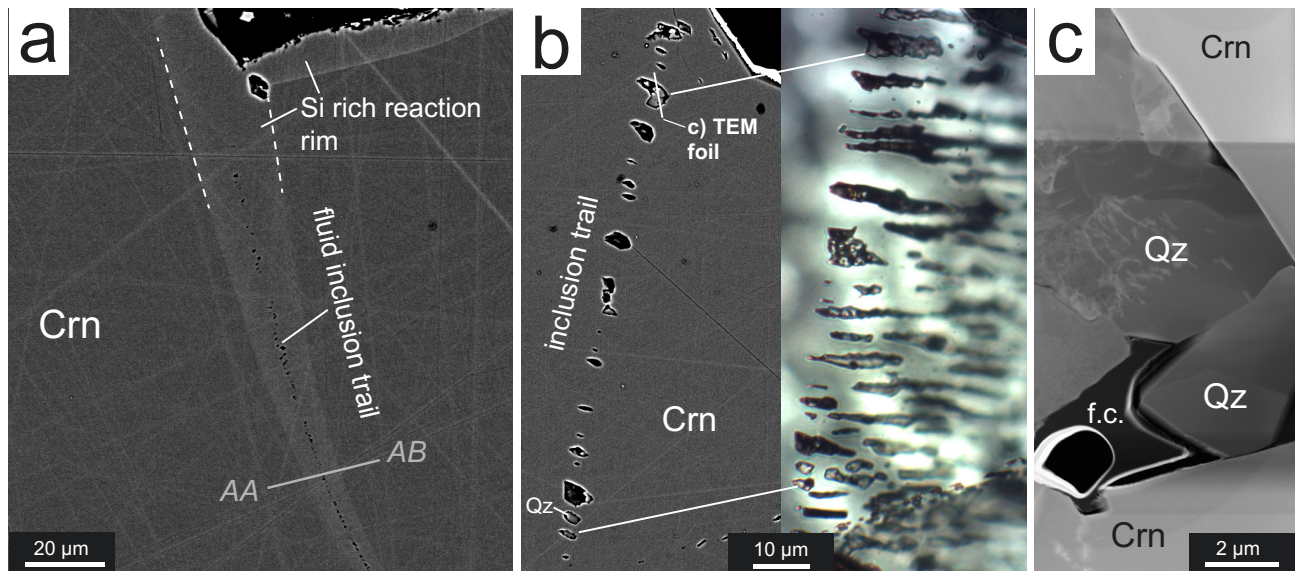


Fig. 4.4 Natural corundum single crystals after a) 14 days (run 6) and b), c) 33 days of runtime (run 7, setup 1, HCl added). a) After 14 days of experiment Si rich reaction rims are found along fluid trails in Crn (BSE image). A chemical profile AA-AB through the altered area around the fluid trail is indicated and data is given in Table A4.2. b) After 33 days of experiment, quartz grains are found along former fluid inclusion trails (left: BSE image and right: microphotograph of the Qz hosting trail). The Crn adjacent to the inclusions appears unaltered (no Si-rich reaction rim). c) HAADF image of a TEM foil cutting through Qz hosting inclusion (indicated in b). Several Qz individuals are associated with a fluid cavity (f.c.).

Setup 2) Corundum + SiO₂ + H₂O + kyanite ± HCl

(Runs 15 to 18)

Kyanite seeds placed on the corundum show no sign of growth, specifically not towards the corundum grains (Fig. A4.4a, b). Besides clear signs of deformation, e.g. kink features, resulting from the compressional stress during the experiment, no clear evidence of (re-) crystallization or dissolution of the kyanite could be observed. However, the fact that kyanite did not grow was not due to a lack of interaction between silica-bearing fluid, kyanite and corundum, since fluid inclusion trails in

corundum clearly showed increased Si in EMPA element maps. Furthermore, the perforated Pt-capsule used in run 12 partly dissolved and left clear evidence of fluid transport through the kyanite grain boundaries and into the corundum by re-precipitating Pt along the way (Fig. A4.4b). Kyanite seeded experiments with added HCl (runs 16-18, Tab. 2.1) show dissolution features predominantly along the kyanite cleavage. The features become more pronounced with increasing run time.

The piston cylinder experiment with pure water (run 15; 800°C; 10 kbar) resulted in synthetic and natural corundum grains with clear signs of dissolution at the surface often associated with the formation of twins, which only occurred at

higher pressure, in matrix supported experiments presumably due to non-hydrostatic pressure. Along these twins oriented fluid trails penetrate the corundum grain starting at the grain surface (Fig. 4.5a, b). The fluid inclusions are located at the contact of twin individuals and host corundum (Fig. 4.5b). HRTEM images of the twin lamellae showed that those are actually composed of nanometer wide polysynthetic twins (Fig. 4.5b, detail).

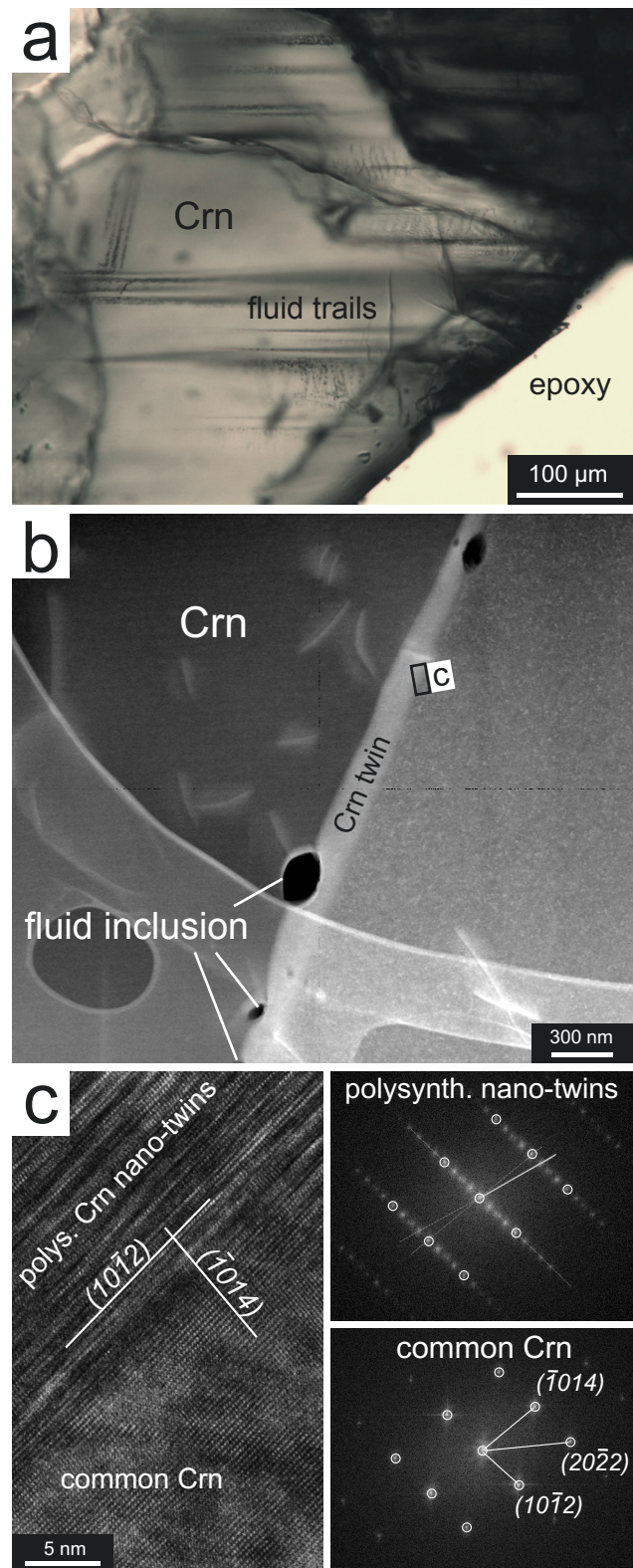


Fig. 4.5 Synthetic corundum after run 15 in SiO₂ powder matrix plus pure water at 800 °C; 10 kbar; 5 days. a) Microphotograph of a Crn including oriented fluid trails that penetrate the grain from the surface. b) TEM investigations showed that fluid inclusions are often found along twin contact planes with the adjacent Crn (HAADF images on the left). c) The twins are composed of polysynthetic nanometer wide twins. On the left; HRTEM image of twins and adjacent common Crn, and on the right; electron diffraction pattern of polysynthetic twins (top) and common Crn (bottom).

Setup 3) Corundum + SiO₂ + H₂O + additional cations

(Runs 19 to 30)

The interaction of corundum single crystals and fluids containing additional cations K⁺, Na⁺, Ca²⁺, Mg²⁺, and NH₄⁺ resulted in moderate dissolution features on the corundum surface at lower concentrations of the solutes (e.g. KCl < 0.08 molal; run 23). The addition of NaCl did not result in the formation of solids independent of NaCl concentration, instead the experiments contained Si- and Na-bearing quench products with highly variable amounts of Al and Cl. At higher concentrations of KCl, NaOH, NH₃OH, and MgO (runs 24-30) and depending on the temperature of the experiments, phyllosilicates muscovite, paragonite, and clinochlore (Fig. A4.5a, b) and/or feldspars orthoclase, albite, and buddingtonite (Fig. A4.5c) were synthesized. Among the alkali-bearing products, muscovite and orthoclase readily formed complete or almost complete coronas, while the sodium-bearing equivalents paragonite and albite were found loosely adhering to the corundum surface or within greater distance to the strongly etched single crystals. MgO-bearing experiments produced complete clinochlore coronas, and forsterite in the rest of the capsule (Fig. A4.5a, b).

The formation of a corona is entirely defined by the products. While phyllosilicates form coronas (Ms, Clc), which are fine grained, porous and occasionally with pseudomorphic replacement

features (Fig. A4.5a, b), buddingtonite forms fewer large, euhedral grains that enclose corundum and quartz remnants without visible crystallographic connection between the reactants and the product (Fig. A4.5c). Also, the morphology of the phase boundary between phyllosilicate coronas and corundum is entirely different to the phase boundary between feldspar and corundum. The contact between corundum and feldspars is even the phase boundaries with phyllosilicates on the contrary appear frayed (Fig. A4.5). A common observation in nearly all three types of experiments, however, is that the polished basal plane of synthetic corundum single crystals barely displays etch pits or at least distinctively less pronounced than other areas of the crystal. Also, the basal plane is generally corona-free, even though the rest of a given grain might be entirely covered.

Setup 4) Baddeleyite + SiO₂ + H₂O

(Run 31)

After 21 days an up to 5 µm wide, continuous zircon corona in silica-saturated deionized water was formed (Tab. 2.1; Fig. A4.6a, b). Porous aggregates of anhedral to subhedral zircon crystals (up to 5 µm in size) and scattered quartz grains (< 2 µm) are located along open cleavage planes or cracks in baddeleyite (Fig. A4.6a, b). The zircon corona is covered by an up to 20 µm thick quartz coat, the quartz grains of which

were occasionally grown directly on the baddeleyite surface (Fig. A4.6b).

Setup 5) Corundum + muscovite + quartz

(Run 32)

After a run time of 2 weeks (run 32, Tab. 2.1) the products are composed of interstitial silicate glass, orthoclase, corundum, euhedral quartz, and minor biotite between partly decomposed muscovite and strongly etched quartz grains, (Fig. 4.6a, Fig. A4.7). The chemical composition of the glass is highly heterogeneous and locally the glass contains orthoclase according to chemical analyses (Tab. 4.2). Optically, however, no distinction between glass and orthoclase could be made (Fig. 4.6a). The chemistry of glass areas appears to be mainly influenced by closely associated solids; near ($< 5 \mu\text{m}$) the surface of corundum single grains the glass is often enriched in SiO_2 and depleted in Al_2O_3 and newly grown quartz is commonly associated with this Si-rich glass, whereas near quartz grains the glass composition showed the opposite chemical trend with Si depletion and Al increase (Fig. 4.6a, Tab. 4.2). No sillimanite was produced, instead thin plates of corundum ($< 1 \mu\text{m}$ width, $< 3 \mu\text{m}$ in diameter) are dispersed in the silicate glass and occasionally in contact with quartz (Fig. 4.6a, Fig. A4.7a, b). Biotite was found as $< 0.5 \mu\text{m}$ thin plates, thus chemical data could not be obtained.

The glass is commonly associated with the corundum single crystals and appears to have accumulated around the crystals during the experiment. The corundum surface and cracks within the grains display reaction rims strongly resembling the altered margins of run products from setup 1 at low pH (Fig. 4.2, Fig. 4.4). The rims are enriched in SiO_2 (up to 4 wt%) compared to the non-altered corundum ($< 0.1 \text{ wt} \%$) and the highest concentrations in the rim were measured along the reaction front (Fig. 4.6b, Si map, Tab. 4.3). An element profile (Fig. 4.6b; C-D, with additional single point measurements along the reaction rims; Tab. 4.3) shows that Fe_2O_3 is enriched in the reaction rims (up to 1 wt%) compared with the unaltered corundum and thus shows an opposite trend as observed in reaction rims of setup 1 experiments, which are depleted in Fe (Fig. 4.2c, Tab. 4.3). Also, in contrast to products of setup 1, quartz inclusions were much more frequently found along the reaction rims in run 32, and the rims are rich in parallel cracks up to a point where the rims look comb-like (Fig. 4.6b, Fig. 4.7a). Natural single crystals differ from synthetic ones; their reaction rims are generally wider (up to $20 \mu\text{m}$) and less interspersed with cracks (Fig. 4.6, Fig. 4.7), whereas the rims along synthetic grains are less than $10 \mu\text{m}$ wide and basically composed of individual comb teeth due to numerous cracks. The polished basal plane of synthetic grains showed no visible alteration features.

TEM investigations revealed that the Si increase in the reaction rims was caused by parallel oriented SNLs along (0001) planes that also corresponded to the parallel, comb-like cracks (Fig. 4.7a, b). Due to the almost parallel position of the TEM foil to these planar rim features, the SNLs are poorly visible in figure 4.7b. In addition to SNLs, numerous kidney shaped, silica rich inclusions, between 50 nm and one μm in size were observed in the foremost front of the reaction rim (Fig. 4.7b). Accounting for the considerable increase in Si along the reaction front, these inclusions likely represent the origin of the larger quartz grains that precipitated in the rim (Fig. 4.6b, Fig. 4.7a).

Table 4.2. Run 32 (setup 5) glass and/or orthoclase formed after muscovite dehydration (WDS results, EMP), ordered by SiO_2 content. A/NK = $\text{Al}_2\text{O}_3/\text{Na}_2\text{O}+\text{K}_2\text{O}$ (molar)

| wt% | glass near Crn | glass/Or? distant fr. Crn | Or | Or | Or | glass | glass | glass | glass near Qz |
|-------------------------|-------------------|------------------------------|--------|---------|---------|-------|--------|--------|------------------|
| SiO_2 | 79.86 | 67.09 | 65.25 | 64.257 | 63.937 | 61.57 | 61.645 | 55.768 | 51.19 |
| Al_2O_3 | 8.71 | 18.97 | 18.52 | 19.744 | 19.498 | 17.44 | 18.839 | 26.035 | 27.11 |
| Na_2O | 0.00 | 1.32 | 1.44 | 1.597 | 1.520 | 1.31 | 1.663 | 1.455 | 0.97 |
| K_2O | 0.00 | 13.44 | 14.99 | 14.768 | 14.975 | 13.71 | 14.649 | 13.444 | 9.70 |
| FeO | b.d. | b.d. | b.d. | 0.042 | 0.058 | b.d. | b.d. | 0.104 | b.d. |
| Total | 88.57 | 100.82 | 100.19 | 100.442 | 100.061 | 94.03 | 96.862 | 96.873 | 88.98 |
| A/NK | - | 1.13 | 1.00 | 1.06 | 1.04 | 1.03 | 1.01 | 1.54 | 2.24 |

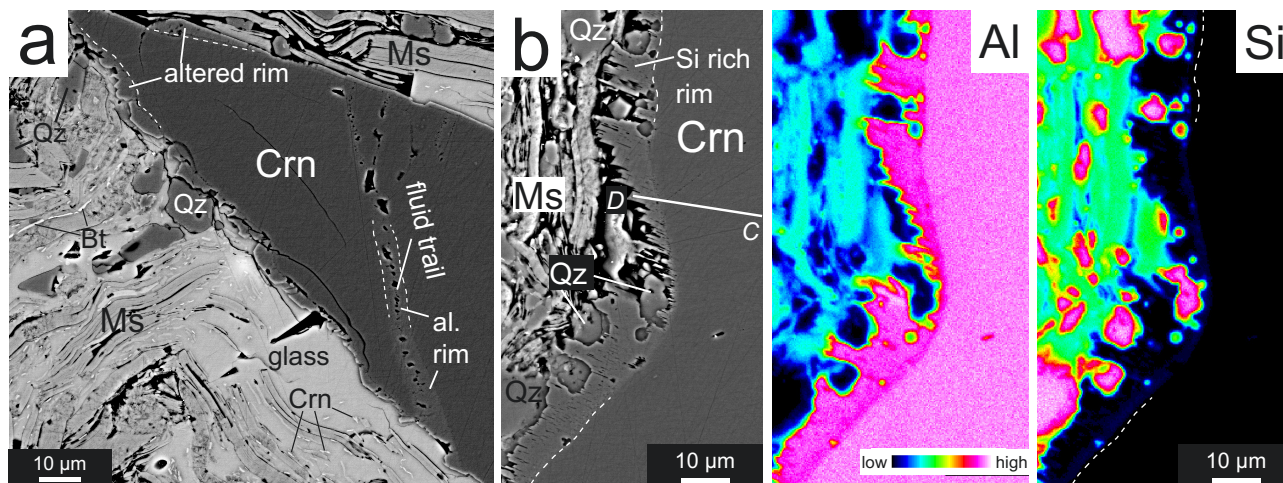


Fig. 4.6 Experimental product of setup 5 (run 32): natural corundum (Crn) grain in muscovite-quartz matrix. a) After two weeks of experiment the muscovite (Ms) is partly decomposed forming a heterogeneous glass with local orthoclase (Tab. 4.2) that is mainly located around the Crn single crystals and contains rounded Qz grains and tiny Crn plates (bright in BSE). Si rich reaction rims are developed at the Crn surface and along fluid trails. b) Left: BSE images of a Si rich reaction rim in Crn at the Crn-matrix interface (chemical profile C-D through rim and unaltered corundum is indicated, data is given in Table 4.3), with corresponding Al and Si element mappings on the right (conducted at 20 kV, 50 nA, 100 ms dwell time). The comb-structured rim locally contains up to 4 wt% SiO_2 whereas Al contents are slightly decreased (see Al and Si mappings, and Tab. 4.3).

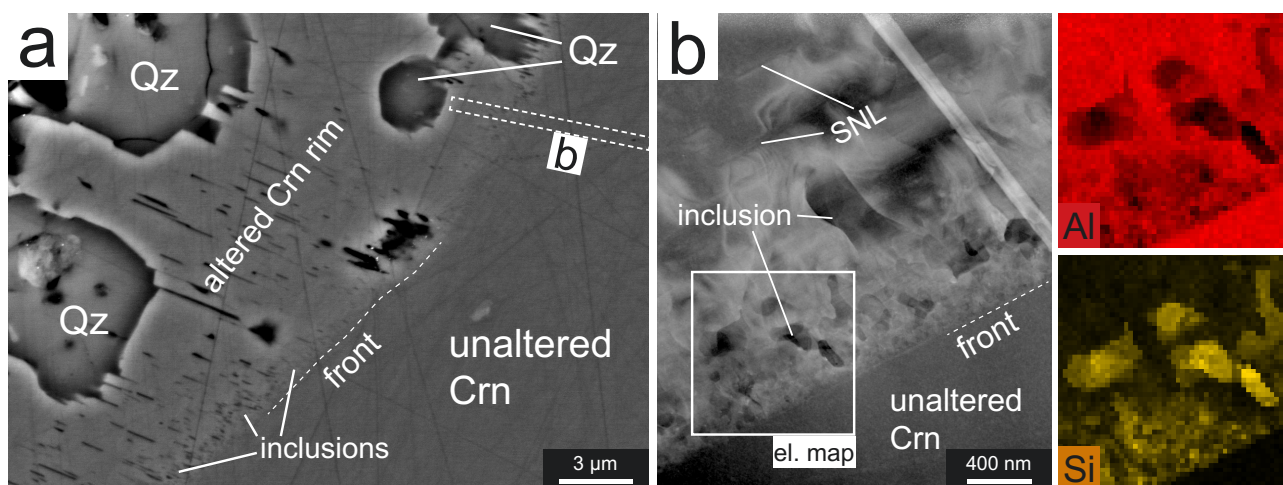


Fig. 4.7 Investigations on the Si reaction rim in natural Crn from setup 5 (run 32) show that a) the comb shaped, altered Crn rim (see Fig. 4.6b for overview) shows an accumulation of nanometer sized inclusions along reaction front (or at the contact with unaltered Crn, marked with dashed white line; BSE image). Numerous larger Qz grains are located inside the rim. b) TEM investigations along the contact between reaction front of comb Crn rim and unaltered Crn single crystal (indicated in a), HAADF (TEM) image displays parallel oriented SNLs and a high concentration of nano-inclusion and lattice defects at the reaction front. TEM EDS element mappings of Al (upper right) and Si (lower right) show that the inclusions contain high amounts of Si and are completely depleted in Al. The inclusions tend to enlarge with increasing distance to the front.

Table 4.3.Element profile C-D (1 analysis point per 4 μm) through an Si-rich reaction rim in a natural corundum single crystal in run 32; 690°C; 4.75 kbar (Fig. 4.6b) unreacted corundum areas in *gray* and *italic* (WDS results EMP)

| wt% | 0 | 4 | 8 | 12 | 16 | 20 | 24 | 28 | 32 | 36 | D.L. |
|--------------------------------|-------------|-------------|-------------|-------------|-------------|-------------|-------------|-------------|-------------|---------|-------|
| SiO ₂ | <i>b.d.</i> | <i>b.d.</i> | <i>b.d.</i> | <i>b.d.</i> | <i>b.d.</i> | <i>b.d.</i> | <i>b.d.</i> | 4.139 | 0.699 | 2.236 | 0.056 |
| Al ₂ O ₃ | 100.042 | 99.579 | 100.482 | 100.513 | 99.790 | 100.849 | 100.542 | 99.328 | 99.828 | 96.868 | 0.151 |
| Fe ₂ O ₃ | 0.075 | 0.064 | 0.047 | 0.066 | 0.069 | 0.059 | 0.072 | 0.249 | 0.927 | 0.957 | 0.039 |
| K ₂ O | <i>b.d.</i> | <i>b.d.</i> | <i>b.d.</i> | <i>b.d.</i> | <i>b.d.</i> | <i>b.d.</i> | <i>b.d.</i> | <i>b.d.</i> | <i>b.d.</i> | 0.245 | 0.111 |
| Total | 100.116 | 99.643 | 100.528 | 100.579 | 99.858 | 100.908 | 100.614 | 103.716 | 101.455 | 100.306 | |

| Single point measurements in corundum reaction rims | | | | D.L. [wt%] | |
|---|--------|--------|--------|------------|-------|
| SiO ₂ | 0.650 | 1.845 | 0.209 | 0.675 | 0.006 |
| Al ₂ O ₃ | 98.44 | 95.80 | 95.82 | 99.27 | 0.007 |
| Fe ₂ O ₃ | 0.804 | 0.624 | 0.837 | 0.850 | 0.011 |
| K ₂ O | b.d. | b.d. | b.d. | b.d. | 0.111 |
| Total | 99.893 | 98.269 | 96.866 | 100.796 | - |

Setup 6) Corundum + pyrophyllite

(Run 33)

After two weeks, (run 33, Tab. 2.1) products showed a completely reacted former pyrophyllite matrix composed of approximately 30 vol% of long prismatic mullite crystals, and around 10 vol% of very thin $< 1\ \mu\text{m}$ wide, and up to $10\ \mu\text{m}$ in diameter, corundum plates in a porous quartz groundmass (Fig. 4.8a, b). Both, mullite crystals and corundum plates appeared preferably in separated areas as clusters or layers of several individuals and were associated with a large volume of void or glass-filled interstice (Fig. 4.8a, b). The interstitial glass, composed of $\sim 85\ \text{wt}\%$ SiO_2 and $\sim 10\ \text{wt}\%$ Al_2O_3 , was also found in spherical inclusions in quartz and mullite together with a vesicle containing a fluid and vapor phase (Fig. 4.8c). The composition of mullite ranges from approximately ideal 3:2 mullite (molar ratio $\text{Al}_2\text{O}_3:\text{SiO}_2$) to strongly silica-oversaturated mullite with a composition of $(^{\text{VI}}\text{Al}_{1.98}\text{Fe}_{0.02})_2(^{\text{IV}}\text{Al}_{2.28}\text{Si}_{1.71}\text{Mg}_{0.01})\text{O}_{9.85}$ (Tab. 4.4). According to the molar ratio $\text{Al}_2\text{O}_3:\text{SiO}_2$, the silica-rich mullite could be addressed as 5:4 mullite.

Despite the presence of mullite in the matrix, not a single mullite crystal was found grown on the surface of the corundum single crystals. Instead, both synthetic and natural corundum single crystals had developed Si-enriched reaction rims towards the matrix, similar to experiments from setup 1 and 5 (Fig. 4.9a, b, c; Tab. 4.5). The polished crystal faces (0001) of

synthetic grains appear unaltered (Fig. 4.8d). As in products of run 32, the reaction rims on synthetic grains on other faces than (0001) are smaller ($< 5\ \mu\text{m}$) than on natural grains (up to $30\ \mu\text{m}$; compare Fig. 4.6c and Fig. 4.8a). Seemingly composed of individual, parallel oriented corundum plates, the rims on synthetic grains resemble the comb features in setup 5 (compare Fig. 4.8c and Fig. 4.6b). The reaction rims on natural corundum are best distinguished from the unaltered single crystals by CL (Fig. 4.9a) because reflected light or BSE investigation sometimes failed to depict the rim-grain contact entirely (Fig. 4.9a), due to a locally lower inclusion density than for the rims on synthetic grains (Fig. 4.8c). In CL images crushed single crystal fragments (strong luminescence in nat. Crn) show no clear sign of marginal decomposition or dissolution, instead the reaction rims enclose sharp edged and pointed corundum shards and quartz grains (Fig. 4.9a).

Two element profiles through a natural grain (Fig. 4.9a, b, *E-F*) and associated reaction rim and through a synthetic grain (Fig. 4.9a, c, *G-H*; Tab. 4.5) show a pronounced Si maximum at the contact of the single grains and their rims. The content of Fe in both natural and synthetic corundum is also increased in the reaction rims, however, Fe concentration gradually decreases towards the contact of rim and single grain, converging to the concentration in the single grain, and not showing a maximum con-

centration at the contact (Fig. 4.9 b, c; unreacted syn. Crn = Fe-free, nat. Crn = ~ 0.05 wt% Fe_2O_3 , see Tab. 4.5).

TEM investigations across the contact of natural corundum to the reaction rim (Fig. 4.10a) show that the rims are composed of densely stacked corundum plates (Fig. 4.10b, c, d) with well-developed basal pinacoids and smaller crystal faces $\{01\bar{1}2\}$ (Fig. 4.10c, e). The contact of the plates and the corundum shard (Fig. 4.10d) is

defined by an abrupt lack of cavities between the plates. The crystallographic orientation of the plates and the corundum single crystal is identical (Fig. 4.10e). Furthermore, the corundum plates include numerous nanometer-wide silica-bearing layers grown parallel to the basal plane (0001) (Fig. 4.10e). Electron diffraction patterns taken inside the reaction rim display a similar streak pattern in $[0001]$ as observed in experiments of setup 1 (Fig. A4.3).

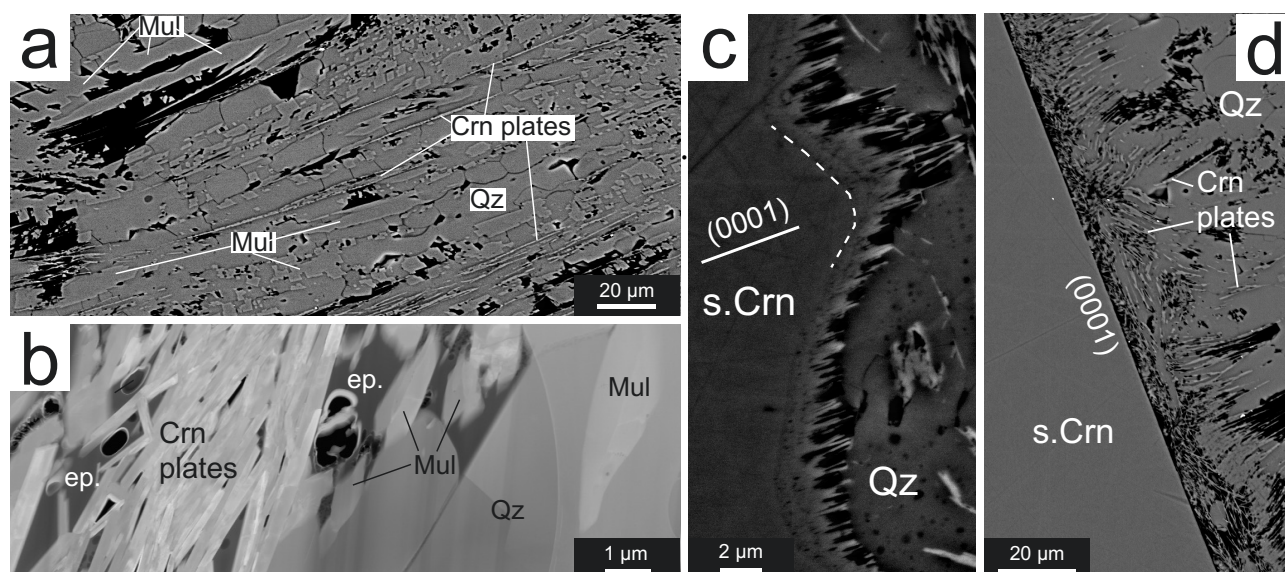


Fig. 4.8 a) Completely decomposed former pyrophyllite in run 33 (setup 6) produced mullite (Mul) and thin corundum plates (Crn) in a porous quartz (Qz) matrix (BSE image, mullite chemistry is given in Table 4.4). b) TEM foil of run products in HAADF mode, epoxy (ep.) fills the interstitial cavities. c) A comb-like reaction rim composed of parallel to the single crystals (0001) oriented and Crn plates grown on a synthetic Crn (s.Crn) surface oblique to $\{0001\}$ (BSE image). The dashed white line indicates the contact between unaltered corundum and reaction rim, the adjacent Qz is interspersed with numerous fluid-glass inclusions. d) The polished (0001) face of s. Crn grains are unaltered. Numerous Crn plates are accumulated along the s. Crn surface but not grown onto the single crystal (BSE).

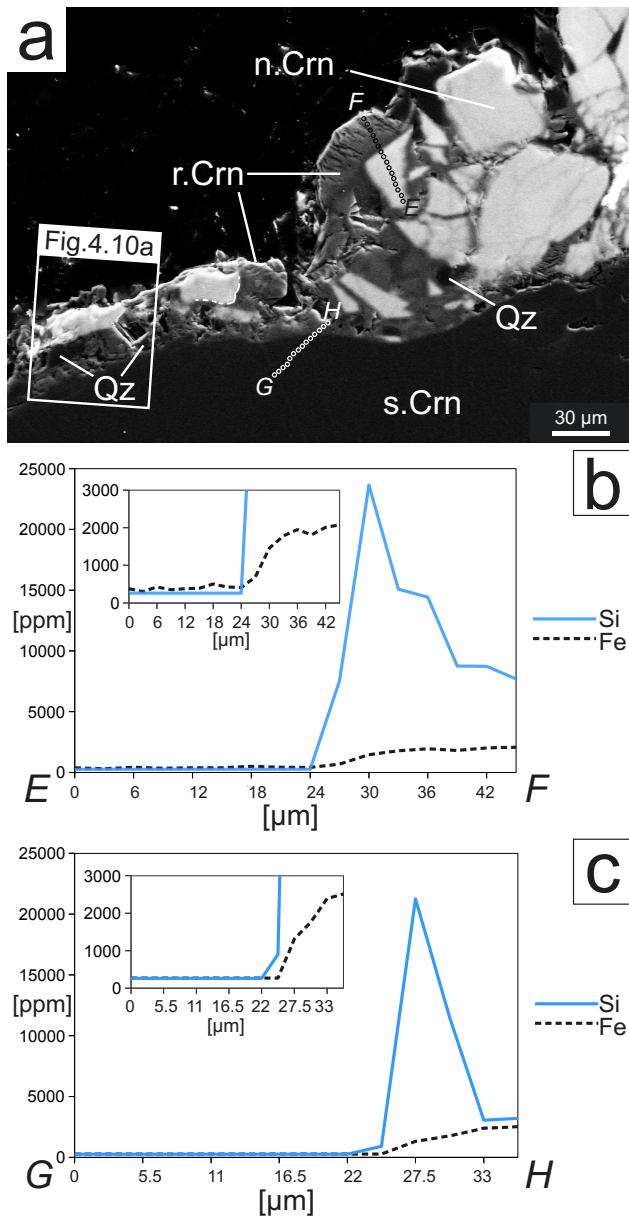


Fig. 4.9 Products of run 33, setup 6: a) Reaction rims „r.“ of corundum (gray) around natural „n.“ (bright gray) and synthetic „s.“ (dark gray) corundum single crystals in a SEM-CL image. Chemical profiles through rim and unaltered natural (E-F) and synthetic (G-H) corundum are indicated (see Tab. 4.5). The n.Crn grain is crushed and the shards are connected with reacted Crn rims (gray). b) Chemical profile E-F of Si and Fe through a natural grain (in wt ppm). Insets show the transition at the rim at larger scale (up to 3000 ppm). Values of <260 and <270 for Si and Fe respectively are below detection limit of the EMP analyses. c) Chemical profile G-H of Si and Fe through a synthetic grain (in wt ppm).

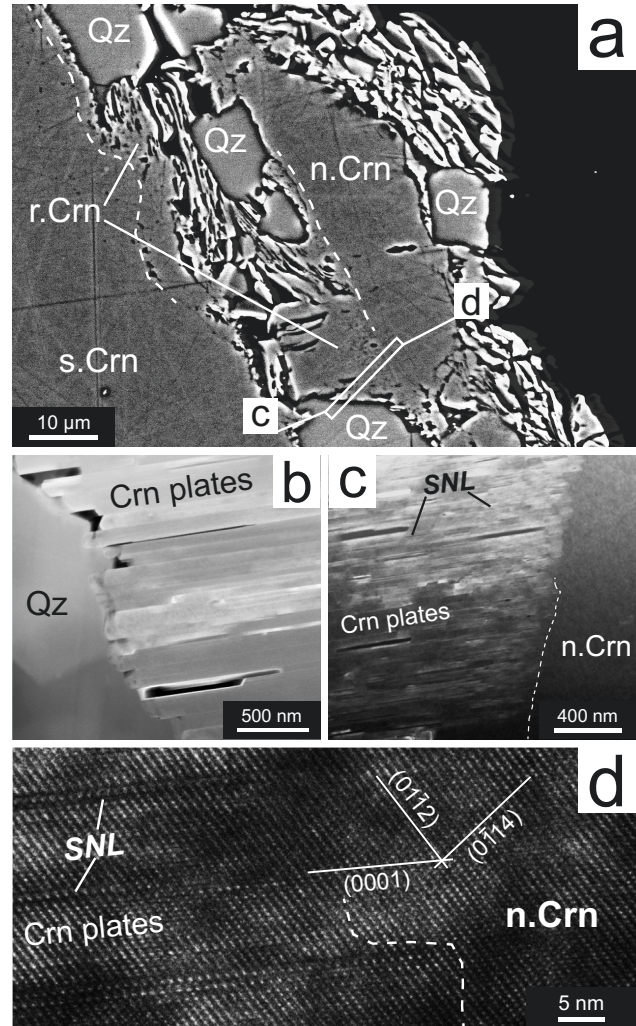


Fig. 4.10 a) Detail indicated in figure 4.9a of a n.Crn fragment with reaction rim intergrown with Qz grains (BSE image). b) HAADF image of the contact between Crn reaction rim and Qz, the rim is composed of numerous thin and identically oriented and strictly separated Crn plates. c) HAADF image of the reaction front between Crn rim and unaltered n.Crn. Parallel cracks or inclusions appear between the thin Crn plates in the rim. d) HRTEM image of contact between the reaction front rim and the single crystal in d) displaying SNLs parallel to (0001). The orientation of Crn plates and n.Crn grain is identical. The plates are separated by SNLs, otherwise they would grow together.

Table 4.4. Run 33 mullite chemistry according to the formula ${}^{\text{VI}}\text{Al}_2({}^{\text{VI}}\text{Al}_{2+2x}\text{Si}_{2-2x})\text{O}_{10-x}$ (WDS results EMP); Si-saturation of mullite is indicated ($x=0$ Sil, $x=0.25$ 3:2-Mullite, $x=0.4$ 2:1-Mullite)

| wt% | strongly Si-rich | strongly Si-rich | Si-rich | Si-rich | Si-rich 3:2 mullite | Si-rich 3:2 mullite | Si-rich 3:2 mullite | Si-rich 3:2 mullite | Si-rich 3:2 mullite | Si-rich 3:2 mullite | Si-rich 3:2 mullite | Si-rich 3:2 mullite | D.L. wt% |
|--------------------------------|---------------------|---------------------|---------|---------|------------------------|------------------------|------------------------|------------------------|------------------------|------------------------|------------------------|------------------------|----------|
| SiO_2 | 31.86 | 31.60 | 29.62 | 29.66 | 28.58 | 28.58 | 28.65 | 28.64 | 28.42 | 28.45 | 28.43 | 28.29 | 0.020 |
| Al_2O_3 | 67.41 | 68.23 | 68.63 | 69.31 | 69.81 | 69.81 | 70.20 | 70.46 | 70.12 | 70.19 | 70.24 | 70.69 | 0.035 |
| Fe_2O_3 | 0.566 | 0.530 | 0.749 | 0.476 | 0.493 | 0.493 | 0.423 | 0.366 | 0.511 | 0.554 | 0.339 | 0.517 | 0.064 |
| MgO | 0.075 | 0.033 | 0.080 | 0.054 | 0.052 | 0.043 | 0.039 | 0.042 | 0.053 | 0.051 | 0.047 | 0.039 | 0.012 |
| Total | 99.91 | 100.39 | 99.08 | 99.50 | 98.93 | 99.02 | 99.31 | 99.51 | 99.10 | 99.24 | 99.06 | 99.54 | - |
| apfu | | | | | | | | | | | | | |
| Si^{4+} | 1.709 | 1.684 | 1.598 | 1.591 | 1.540 | 1.539 | 1.538 | 1.534 | 1.529 | 1.529 | 1.529 | 1.514 | |
| ${}^{\text{IV}}\text{Al}^{3+}$ | 2.283 | 2.307 | 2.395 | 2.402 | 2.453 | 2.458 | 2.459 | 2.463 | 2.467 | 2.467 | 2.467 | 2.481 | |
| ${}^{\text{VI}}\text{Al}^{3+}$ | 1.977 | 1.979 | 1.970 | 1.981 | 1.980 | 1.984 | 1.983 | 1.985 | 1.979 | 1.978 | 1.986 | 1.979 | |
| Fe^{3+} | 0.023 | 0.021 | 0.030 | 0.019 | 0.020 | 0.016 | 0.017 | 0.015 | 0.021 | 0.022 | 0.014 | 0.021 | |
| Mg^{2+} | 0.006 | 0.003 | 0.006 | 0.004 | 0.004 | 0.003 | 0.003 | 0.003 | 0.004 | 0.004 | 0.004 | 0.003 | |
| $x = (2-\text{Si})/2$ | 0.146 | 0.158 | 0.201 | 0.204 | 0.230 | 0.231 | 0.231 | 0.233 | 0.235 | 0.236 | 0.235 | 0.243 | |
| O10-x | 9.854 | 9.842 | 9.799 | 9.796 | 9.770 | 9.769 | 9.769 | 9.767 | 9.765 | 9.764 | 9.765 | 9.757 | |

Table 4.5. Element profiles E-F (Fig.4.9b) and G-H (Fig.4.9c) through an Si-rich reaction rim in a natural and synthetic corundum single crystal respectively in run 33; 650°C; 5 kbar (Fig. 4.8) unreacted corundum areas in *gray* and *italic* (WDS results EMP in oxide wt%; analysis points indicated in Fig.4.9a).

| E-F (through natural corundum grain) | | | | | | | | | | | | | | | | |
|--------------------------------------|--------------|--------------|--------------|--------------|--------------|--------------|--------------|--------------|--------------|--------------|--------------|--------------|--------------|--------------|--------------|--------------|
| μm | 0 | 3 | 6 | 9 | 12 | 15 | 18 | 21 | 24 | 27 | 30 | 33 | 36 | 39 | 42 | 45 |
| SiO ₂ | <i>b.d.</i> | <i>b.d.</i> | <i>b.d.</i> | <i>b.d.</i> | <i>b.d.</i> | <i>b.d.</i> | <i>b.d.</i> | <i>b.d.</i> | <i>b.d.</i> | 1.611 | 5.059 | 3.227 | 3.085 | 1.873 | 1.869 | D.L. |
| Al ₂ O ₃ | 99.647 | 99.969 | 99.561 | 99.744 | 99.939 | 99.759 | 100.002 | 100.216 | 100.579 | 100.655 | 93.762 | 97.404 | 99.353 | 99.434 | 99.260 | 1.646 |
| Fe ₂ O ₃ | <i>0.054</i> | <i>0.043</i> | <i>0.061</i> | <i>0.050</i> | <i>0.054</i> | <i>0.056</i> | <i>0.072</i> | <i>0.061</i> | <i>0.059</i> | <i>0.099</i> | <i>0.208</i> | <i>0.255</i> | <i>0.279</i> | <i>0.259</i> | <i>0.288</i> | <i>0.151</i> |
| Total | 99.701 | 100.012 | 99.622 | 99.795 | 99.993 | 99.815 | 100.074 | 100.276 | 100.637 | 102.365 | 99.030 | 100.886 | 102.717 | 101.567 | 101.416 | 102.890 |
| Si ppm | <i>b.d.</i> | <i>b.d.</i> | <i>b.d.</i> | <i>b.d.</i> | <i>b.d.</i> | <i>b.d.</i> | <i>b.d.</i> | <i>b.d.</i> | <i>b.d.</i> | 7530 | 23648 | 15083 | 14422 | 8756 | 8735 | 7694 |
| Fe ppm | 191 | 152 | 213 | 176 | 190 | 195 | 251 | 213 | 205 | 346 | 191 | 152 | 213 | 176 | 1006 | 1039 |

| G-H (through natural corundum grain) | | | | | | | | | | | | | | | | |
|--------------------------------------|-------------|-------------|-------------|-------------|-------------|-------------|-------------|-------------|-------------|-------------|---------|--------|---------|---------|-------|-------|
| μm | 0.00 | 2.75 | 5.50 | 8.25 | 11.00 | 13.75 | 16.50 | 19.25 | 22.00 | 24.75 | 27.50 | 30.25 | 33.00 | 35.75 | D.L. | D.L. |
| SiO ₂ | <i>b.d.</i> | <i>b.d.</i> | <i>b.d.</i> | <i>b.d.</i> | <i>b.d.</i> | <i>b.d.</i> | <i>b.d.</i> | <i>b.d.</i> | <i>b.d.</i> | 0.192 | 4.546 | 2.457 | 0.653 | 0.685 | 0.056 | 0.056 |
| Al ₂ O ₃ | 100.456 | 100.274 | 100.750 | 100.716 | 100.094 | 99.936 | 99.078 | 99.901 | 98.796 | 98.690 | 98.889 | 95.731 | 99.033 | 99.566 | 0.151 | 0.151 |
| Fe ₂ O ₃ | <i>b.d.</i> | <i>b.d.</i> | <i>b.d.</i> | <i>b.d.</i> | <i>b.d.</i> | <i>b.d.</i> | <i>b.d.</i> | <i>b.d.</i> | <i>b.d.</i> | <i>b.d.</i> | 0.187 | 0.251 | 0.341 | 0.359 | 0.039 | 0.039 |
| Total | 100.456 | 100.274 | 100.750 | 100.716 | 100.094 | 99.936 | 99.078 | 99.901 | 98.796 | 98.882 | 103.623 | 98.439 | 100.028 | 100.611 | | |
| Si ppm | <i>b.d.</i> | <i>b.d.</i> | <i>b.d.</i> | <i>b.d.</i> | <i>b.d.</i> | <i>b.d.</i> | <i>b.d.</i> | <i>b.d.</i> | <i>b.d.</i> | 899 | 21252 | 11484 | 3053 | 3202 | | |
| Fe ppm | <i>b.d.</i> | <i>b.d.</i> | <i>b.d.</i> | <i>b.d.</i> | <i>b.d.</i> | <i>b.d.</i> | <i>b.d.</i> | <i>b.d.</i> | <i>b.d.</i> | 0 | 655 | 879 | 1193 | 1256 | | |

4.3 Discussion

All experiments in this study were conducted well inside the stability field of kyanite or sillimanite (see Tab. 2.1) according to experimental data of (Holdaway 1971), internally consistent thermodynamic datasets (Holland and Powell 2011), as well as according to studies that combined several approaches (Holdaway and Mukhopadhyay 1993; Pattison 2001). Aqueous fluid was either added or provided by dehydrating phyllosilicates in all runs in order to assure sufficiently high reaction rates. However, none of the experiments produced the corresponding stable Al_2SiO_5 polymorph, and none of the used corundum single crystals developed an Al_2SiO_5 corona. Since the precipitation of Al_2SiO_5 from aqueous fluids seems impeded, independent of fluid composition, or Al solubility, other causes such as low

nucleation rates could be responsible for the inability to synthesize Al_2SiO_5 from fluids. But even when kyanite seeds were used, kyanite growth was not observed, which seems to imply that not only the nucleation of Al_2SiO_5 polymorphs, but also their growth in aqueous fluid is obstructed. The formation of quartz + corundum or any other phase seems to be favored over the nucleation of Al_2SiO_5 , even when seed crystals provide a way to bypass the nucleation barrier. This implies that Al_2SiO_5 polymorph formation was not merely thwarted by slow kinetics and too short experimental times but by more fundamental processes. Nonetheless, the results of the different experimental approaches provide crucial information about the factors controlling the corona-forming reactions and are discussed in the following.

4.3.1 Corona formation

In pure water plus silica experiments, a porous quartz coating formed on corundum single crystals. Underneath this coating, corundum dissolution is predominantly bound to grain boundary diffusion and due to the steep chemical gradient along the corundum-quartz phase boundary; the precipitation of Al_2SiO_5 was expected but not observed. Low dissolution rates of corundum and thus lack of Al saturation

in the fluid with respect to kyanite (Beitter et al. 2008) could have hindered its nucleation. However, the experiment conducted with baddeleyite instead of corundum (setup 4, identical fluid as in setup 1) produced a zircon corona after only 3 weeks. Baddeleyite has a very low solubility in aqueous fluid similar to corundum (Migdisov et al. 2011). Also, the higher corundum solubility in experiments with low pH (HCl or BH_3O_3 added, Fig. 4.1) as

evidenced by intensified etch pit formation on the corundum surface, did not result in the formation of Al_2SiO_5 . The intense dissolution of corundum in experiments containing additional K^+ , Na^+ , Ca^{2+} , Mg^{2+} , or NH_4^+ (setup 3) and the formation of orthoclase, albite, buddingtonite, paragonite or clinochlore, as corona or in separate clearly shows that corundum is in fact a very suitable and compliant reactant for corona growth processes and that the generally low Al solubility in metamorphic fluids does not control the nucleation and crystal-growth processes.

Dehydration reactions in muscovite (setup 5) are known to generate all three Al_2SiO_5 polymorphs in metamorphic rocks (García-Casco et al. 1993; Sanchez-Navas 1999). The approach of run 32 was to simulate these natural processes, but no sillimanite was found among the products of decomposed muscovite (glass, orthoclase, quartz, corundum). Instead fine-grained corundum plates are associated with the heterogeneous glass, and quartz precipitated in direct contact with the large corundum single crystals or inside their reaction rims. Chemical heterogeneities in a melt phase produced during dehydration reactions in pelitic rocks have been also reported, suggesting that Si-undersaturated domains allow corundum growth in quartz-saturated experiments (Kato et al. 2011). However, in run 32 quartz and corundum growth was often observed in Al-rich (e.g. on and in corundum) and Si-rich domains (Si rich

glass or near quartz) respectively (Fig. A4.7a). This experiment shows that the dehydration of muscovite does not suffice to trigger the formation of an Al_2SiO_5 polymorph (e.g. Huang and Wyllie 1974).

The dehydration of pyrophyllite (setup 6) was expected to generate sillimanite and quartz at the P-T conditions of run 33 (Tab. 2.1). The experiment produced large volumes of 3:2 and 5:4 Si-enriched mullite, compositionally close to sillimanite. Large portions of the completely reacted pyrophyllite produced corundum plates in quartz and these corundum plates also build up the reaction rims on corundum single crystals. Mullite as a close relative to the Al_2SiO_5 polymorphs did not grow on the corundum or at the expense of corundum.

It can be concluded that experimental corona formation on corundum is readily achieved at the P-T conditions of the experiments in this study, as long as the corona is not made of kyanite or sillimanite. Natural observations of kyanite corona growth on corundum in muscovite-bearing gneissic rocks (chapter 3) and numerous studies concerning Al_2SiO_5 polymorph formation in nature (Gresens 1971; Vernon 1979; Vernon et al. 1987; Wintsch and Andrews 1988; Widmer and Thompson 2001; Daniel et al. 2003) suggest that the formation of the Al_2SiO_5 polymorphs depends on a chemically open system where the fluid induced removal of alkalis plays an essential role.

4.3.2 Silica diffusion in corundum

Three different experimental setups (1, 5, 6) have shown that the interaction of corundum with silica provided by aqueous fluid or silicate melt results in the formation of rims that are characterized by SNLs parallel to (0001) (Fig. 4.3, Fig. 4.7, Fig. 4.10). Their formation may actually impede corona formation and thus, they are highlighted in the following. Two specific rim types could be distinguished. The first type is bound to the dissolution of corundum and was documented in setup 1 and setup 5 experiments, in which corundum and silica-rich fluid (1) or silicate melt (5) interacted. It displays clear dissolution features along the corundum surface (rounded grains, etch pits, alteration along cracks and fluid trails, Figs. 4.1, 4.2, 4.4a, 4.6, A4.2). The alteration rims in these runs strongly resemble fluid-mediated diffusion profiles with dissolution re-precipitation features (Putnis 2002; Putnis and Mezger 2004; Harlov et al. 2005; Putnis and Putnis 2007; Putnis and Austrheim 2010). It is therefore concluded that such rims form during the dissolution of corundum coupled with silica diffusion into the corundum lattice (Fig. 4.2, 4.4, Fig. 4.6).

The second type is dominated by the precipitation of corundum on corundum in setup 6. Run 33 produced significant volumes of thin corundum plates in a matrix of quartz and mullite after complete dehydration of pyrophyllite (Fig. 4.8). The reaction rims on corundum single crystals enclose undissolved

shards of crushed grains (Fig. 4.9). Therefore, the reaction rims in run 33 are interpreted to be mainly the result of corundum precipitation on corundum, instead of Si diffusion into a dissolving grain (setups 1, 5). However, a certain degree of interaction between the single crystals and dissolved silica cannot be excluded.

1) Dissolution rims: In order to get a complete picture of the dissolution processes involved in the rim formation, both surface features (etch pits etc.) and features inside the altered corundum are highlighted in the following.

Experiments with pH neutral aqueous fluid and silica showed a dissolution pattern on corundum that is mainly controlled by fluid pathways through the porous or incomplete quartz cover encasing the single crystals. However, with decreasing pH and increasing corundum solubility, dissolution features independent of the quartz cover displayed crystallographically controlled dissolution characteristics of the corundum. In theory the dissolution form of a crystal corresponds to the equilibrium form or “E-form” of the mineral (Lacmann et al. 1974). Equilibrium faces of corundum are $\{10\bar{1}2\}$, $\{11\bar{2}0\}$, $\{\bar{1}014\}$, and $\{0001\}$ (Siesmayer et al. 1975). Experimental dissolution faces, however, deviate from the E-faces depending on the attacking agent used (Siesmayer et al. 1975; Smirnov et al. 1981). Observations in this study indicate dissolution faces on corundum on the rhombohedral faces $\{10\bar{1}2\}$ and occasionally on

$\{\bar{1}014\}$, in agreement with the equilibrium form and observations made by Siesmayer et al. (1975), while dissolution faces on $\{11\bar{2}0\}$ are missing (Fig. 4.1c, d). The basal plane of corundum is free of etch pits after weeks of experiment and appears to show a strong resistance to dissolution (Fig. 4.1b, c, d). Literature data suggest slow dissolution along $[0001]$ but not completely passive behavior (Siesmayer et al. 1975; Smirnov et al. 1981). After several weeks of interaction with acidic, quartz-saturated fluid, a sub-micron wide, silica-enriched layer is found on the basal plane of synthetic corundum grains (Fig. A4.2). Shallow etch pits merely consist of areas where this layer was removed. The passivated dissolution in $[0001]$ is presumably caused by this silica-enriched layer, produced by a similar diffusion process as in experiments with shorter run time (Fig. 4.2). Since SNLs inside the up to 50 μm wide rims developed strictly parallel to (0001) , it can be speculated that Si-diffusion perpendicular to (0001) of the synthetic single grains is restricted by the formation of SNLs, and thus formed only a several hundred nanometer wide rim. At least, the SNLs increase the chemical potential of Si locally, which should reduce the diffusive Si flux into corundum through (0001) . In the same way $\{0001\}$ surfaces are potentially protected by SNL formation from the attacking fluid, by reducing the chemical gradient between corundum and the quartz-saturated fluid.

The several tens of micrometers wide, silicon-enriched rims (setups 1 and 5) represent the result of an unusual Si infiltration into the corundum single crystals. Unusual, because the Si and Al concentration profiles (e.g. Fig. 4.2) do not seem to follow Fick's law assuming that corundum and Si-bearing fluid are the only participating phases. The concentration profiles should resemble monotonically increasing or decreasing functions between two phases, whose shape and slope depend on the chemical gradient between the reactants and elapsed time of interaction (Ganguly 2002; Abart et al. 2004; Harlov et al. 2005). In contrast, the Fe trace concentrations along the reaction rim displays a typical diffusion pattern (Fig. 4.2c). In setup 1 the reaction rims are depleted in Fe because the attacking agent (HCl added water + silica) was Fe-free, whereas in setup 5 higher Fe contents were measured due to FeO contents of around 1.5 wt% in the muscovite starting material (compare Tab. 4.1, Tab. 4.3 and Tab. A4.2).

The Si concentration profile displays a distinct maximum Si content at the sharp contact of rim and unaltered single crystal (Fig. 4.2c, Tab. 4.1, Tab. A4.2). A complementary pattern is observed in the Al distribution along the rim, with a minimum Al concentration at the reaction front, which implies a substitution of Al by Si. Similar concentration profiles are known from uphill diffusion processes that can occur in systems including more than two diffusive components (Ganguly 2002; Kohn and Pen-

niston-Dorland 2017). The diffusion of a single component is then not solely controlled by its own concentration and chemical potential gradient, but is influenced by the other diffusing components (chemical interdiffusion). The substitution mechanism of Al and Si clearly connects Si and Al diffusion. However inside a single crystal, classical uphill diffusion processes cannot explain the observed concentration profile. Instead, the formation of SNLs must have an influence on the local chemical potential of both Si and Al since they are the only major difference between the silica-free and silica-rich domains in the corundum.

TEM investigations along the foremost 200 nm of reaction front show Si bulk diffusion into the crystal (Si increase without visible crystallographic features) and subsequent reorganization of Si behind this 200 nm reaction front, along SNLs parallel to (0001) (Fig. 4.3a, b). It is poorly understood how a substitution mechanism of Al by Si in corundum works and, to my knowledge, this study is the first one reporting pronounced Si diffusion into corundum. Trace concentrations of Si in natural corundum are generally ≤ 700 ppm according to the scarce literature data that is available on that matter (Harlow and Bender 2013; Sutherland et al. 2014). Concentrations above 700 ppm and up to 5000 ppm as measured in the rims are considered above the solubility limits of Si in corundum and were only reported from rubies that have been influenced by skarn formation

processes or metasomatic alteration in the Mogok metamorphic belt of Myanmar (Harlow and Bender 2013). Harlow and Bender (2013) proposed “fine-scale inclusions, not visible by optical or most electron microscopy” as possible source of the unusually high Si content.

Since a reduction of Si^{4+} to Si^{3+} for a simple Al-Si exchange in the experiments presented here is highly unlikely and the increase in Si along the rims coincides with both an increase and decrease in iron in different experiments (Fig. 4.2c, Tab. 4.3), which excludes coupled $2\text{Al}^{3+} \rightarrow \text{Si}^{4+} + \text{Fe}^{2+}$ substitution (e.g. Nassau 1981), the substitution of Al^{3+} by Si^{4+} more likely involves the formation of vacancies and/or the combination with charge balancing hydrogen. The corundum basal plane is structurally similar to the octahedral layer of dioctahedral kaolinite and pyrophyllite, and inserting a tetrahedral layer of silica parallel to (0001) is possible if at least two octahedral layers are removed from the corundum structure (Fig. 4.11). Si replaces Al in an approximate ratio of 1:2 (Fig. 4.3c) and a substitution of two octahedral layers would result in a single tetrahedral-octahedral layer pair and corresponding lattice gap as in kaolinite (Fig. 4.11). Only in this case the octahedral layer is connected to the corundum lattice. In addition, double silica layers were observed indicating a structure loosely related to pyrophyllite (Fig. 4.11). A possible substitution mechanism for the single layer could be described as $2\text{Al}^{3+} \rightarrow \text{Si}^{4+} + 2\text{H}^+$, for the double

layer as $3\text{Al}^{3+} \rightarrow 2\text{Si}^{4+} + \text{H}^+$. Nano-structures larger than silica double layers were not found, which is probably due to the structural mismatch between the corundum host and the nano-layers. The latter simply do not have enough space in $[0001]_{\text{cm}}$ to develop a proper dioctahedral phyllosilicate structure, since e.g. the distance between two neighboring Al-octahedral layers in pyrophyllite is 0.1 nm larger than that of the corresponding layers in corundum. The nano-layers induce an offset or stacking fault into the corundum perpendicular to the c axis, which is visible in a decrease in symmetry and the appearance of an additional peak in the electron diffraction pattern (Fig. A4.3).

The formation of SNLs creates nm-wide gaps in the corundum lattice (Fig. 4.11) that form a kind of nano-porosity similar to the increased porosity in dissolution-re-precipitation processes (Walker et al. 1995; Harlov et al. 2005; Putnis and Putnis 2007). Once formed, the SNLs allow for an accelerated mass transfer into and out of the corundum. Perpendicular to the SNLs, however, the corundum dissolution and Si diffusion is restricted due to a reduced chemical gradient (see above). The modified mass transfer enhances the Si transport through the rim and towards the reaction front, explaining the sharp profile of Si with a maximum concentration at the reaction front (Fig. 4.2c, Tab. 4.1, Tab. A4.2).

After the formation of the SNLs, most element transport happens along these layers, where the chemical potential of Si is locally elevated and transport is fast and anisotropic. The SNLs effectively shield the Si-poor corundum between them from the new incoming Si that is transported within the SNLs. Thus Si can diffuse quickly towards the unaltered corundum where its potential is distinctly lower. The chemical potential of Al, on the other hand, highest in the unaltered corundum, decreases significantly inside and along the SNL, and is lowest in the quartz-saturated fluid. The potential gradients of Si and Al thereby redirect the reaction front from the surface of the corundum towards the center of the grain, leading to a Si concentration profile in the corundum that resembles uphill diffusion.

Precipitated quartz grains are found in the rims, often specifically located along the diffusion front where the Si maximum was measured (Fig. 4.2, Fig. 4.7). In the first 500 nm of the reaction front in setup 5 numerous small, silica inclusions can be observed aside from SNLs (Fig. 4.7). These inclusions are interpreted as a supersaturation of silica with respect to the formation capacity of SNLs in the corundum. They are probably a result of the self-enhanced Si influx caused by the SNL formation. Behind these foremost 500 nm, fewer but larger quartz grains of up to 10 μm in diameter suggest continuous reorganization of excess silica within the reaction rim and an Ostwald ripening

process (Fig. 4.2, Fig. 4.6, Fig. 4.7). The disparity of quartz inclusions in different experiments likely reflects the different Si diffusion rates caused by different attacking agents in setups 1 and 5 (fluid and liquid/melt). The SiO_2 content of the rims in setup 5 can reach >4 wt%, whereas the maximum in setup 1 was 0.72 wt%. Cracks parallel to (0001) of reacted corundum in setup 5 suggest that the high Si content results in a volume expansion that is compensated by the formation of those cracks along SNLs, which represent areas of increased weakness. Fracturing of the rim further increases the permeability for fluids (Figs. 4.6, 4.7).

In summary, the process observed during corundum dissolution in silica-saturated fluid/melt appears to proceed in several overlapping intervals. Initially Al and Si bulk diffusion increases Si on and inside the corundum until the Si solubility is locally reached to form SNLs. They allow faster transport for the element exchange than bulk diffusion and the Si influx increases significantly. Locally the amount of influx exceeds the SNL saturation and quartz precipitates, whose formation is apparently facilitated by epitaxial nucleation along the SNLs. A conclusive reason why quartz forms inside corundum instead of Al_2SiO_5 , has yet to be found, although, based on the structures one could argue that a tetrahedral silica-layer is more closely related to the silica network in quartz

than to the isolated position of single silica tetrahedra in Al_2SiO_5 and thus less reorganization is locally required during quartz nucleation.

A combination of observations on shorter and longer experiments in setup 1 (runs 6 and 7) shows that the SNLs in the rims annealed during prolonged experiments, since no silica rich rims are preserved after more than two weeks. Al saturation is presumably reached after approximately two weeks in the HCl-added runs and most reactions come to a halt. Annealing inevitably leads to the removal of silica from the corundum lattice. On the corundum surface the excess silica would simply be redistributed in the fluid, along the fluid trails inside the grain; however, the only place for silica retreat would be inclusion cavities. It is concluded that quartz inclusions (Fig. 4.4b, c) are the result of annealed Si diffusion rims along former fluid inclusion trails or cracks.

2) *Precipitation rims*: In run 33 (setup 6) the rims are composed of very fine corundum plates, identically oriented as the corundum single crystal they grow on. They include similar SNLs as the rims in setups 1 and 5 (Fig. 4.10). Distinguishing corundum alteration (setup 1, 5) and corundum precipitation (setup 6) is difficult due the textural and chemical similarities of the reaction rims formed, but also due to a possible overlap of the second and the first process in setup 6. Intense dissolution of the corundum single crystals simultaneously to

corundum plate precipitation in the matrix is unlikely, but locally the chemical gradient between single crystals and quartz-saturated environment results in diffusive exchange of Si and Al ions. Circulating fluid released from dehydrating pyrophyllite likely assists the latter. Therefore, while corundum plates grow on the single crystals surface, silica-saturated fluid might also interact with the single crystals. Chemical profiles (Fig. 4.9) through unaltered parts and rims are very similar to the rim profiles in setup 1 and 5 (Fig. 4.2c, Tab. 4.3). A Si maximum at the contact between single crystal and corundum plates strongly resembles the ramp like pattern of the Si diffusion rim in figure 4.2c, a similarity that suggests a mechanism of Si transport through the corundum plates towards the single crystal. The plate rims provide porosity not only in the form of SNLs, but also as elongated inclusions between the individual corundum plates (Fig. 4.10b, c). Therefore, the similarity of the concentration profiles seems to be the result of Si influx from the matrix through existing SNLs and cracks (or inclusions) in the rims towards the single crystal, as described previously. In contrast to the ramp-like Si profile the Fe distribution resembles a normal diffusion profile with balancing slope between increased Fe contents in the rim and the contents of the single crystals (Fig. 4.9). In combination with the Fe profile in alteration rims (Fig. 4.2), this indicates independent diffusion mechanisms for Si and Fe in the experiments of this study.

The distribution of quartz in reaction rims of setup 6 is different than in setup 1 and 5 mainly regarding the size and position of the grains. Up to 40 μm large, isolated quartz grains are found enclosed in corundum plates. In contrast to setups 1 and 5, the grains are not associated with the contact of reaction rims and single crystals (or the reaction front or the rim). This indicates simultaneous growth of quartz and platy corundum.

The corundum plates have a disproportionately large basal pinacoid, besides which predominantly crystal faces of $\{01\bar{1}2\}$ are found indicating slow growth perpendicular to these faces. According to Wulff (1901), crystal faces grow at a rate inversely related to their reticular density, defined by the number of points per unit area in a two dimensional lattice. Since both the basal planes and faces of $\{01\bar{1}2\}$ are faces of highest possible reticular density in corundum, they should be the slowest growing faces (Bagdasarov et al. 1974). The slowest growing faces should also be the faces with the lowest dissolution rate in directions perpendicular to them and therefore disappear during etching. This holds true for $\{01\bar{1}2\}$, whereas $\{10\bar{1}2\}$ and occasionally $\{\bar{1}014\}$ with low reticular density appear during dissolution (setup 1). The behavior of the basal plane during dissolution however, is contradictory. Faces in $\{0001\}$ persist etching under very acidic silica-saturated conditions (Fig. 4.1). Wulff's theorem is therefore realized for dissolution of faces in

$\{01\bar{1}2\}$ and $\{10\bar{1}2\}$ in the experiments of this study, but not for $\{0001\}$. The passivation of the basal plane is the result of nano-silica coating on the basal planes that are exposed to the fluid, similar to the SNLs in corundum. This is evident when considering the fact that identically oriented corundum plates included in the rims are strictly separated and not intergrown among each other (Fig. 4.10b, c). Difference in width and porosity between synthetic and natural corundum rims indicate

that the epitactic growth or surface connectivity between corundum plates and natural corundum is more efficient than between corundum plates and synthetic grains (Figs. 4.8, 4.9, 4.10). The reason for this preference is unknown. On the other hand, no rim was found on the polished base of synthetic corundum, which is not surprising given the likely formation of nano-silica coating on the (0001) surface that does not allow for new corundum to grow on or to attach to the single grain.

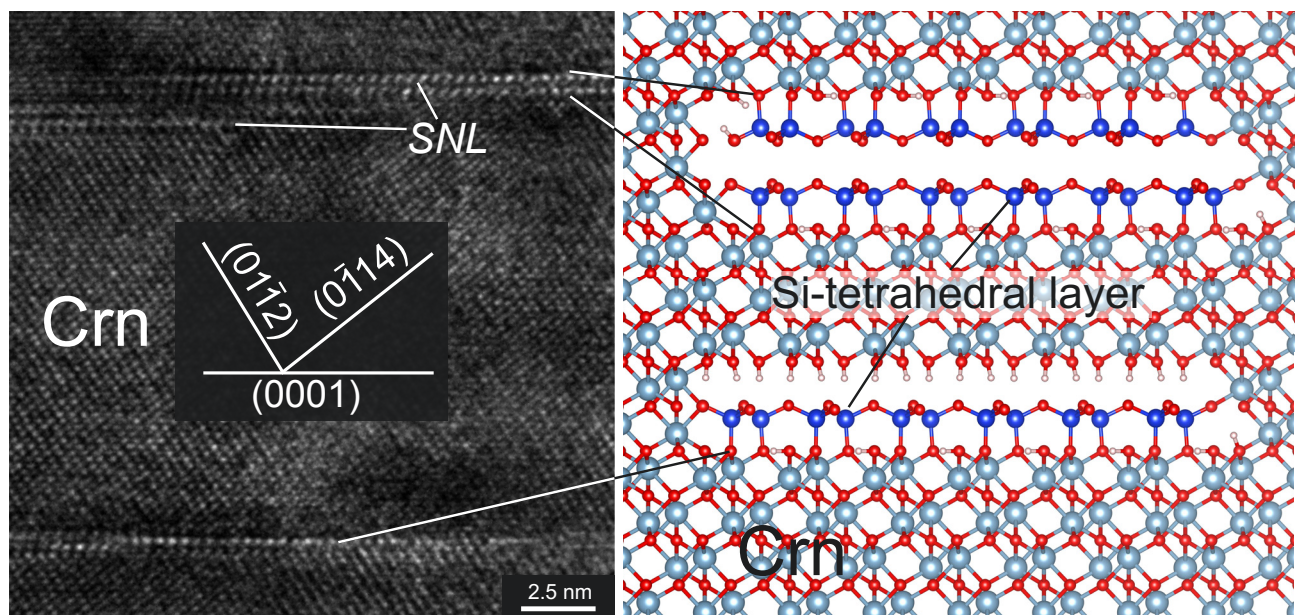


Fig. 4.11 On the left; HRTEM image inside the corundum reaction or Si diffusion rim around 1 μm away from the reaction front (run 6, setup 1). On the right; atomic model of the silicate nano-layers (SNLs): the layers are strictly parallel oriented to $\{0001\}$ in Crn and they appear as silica tetrahedral double (top) or single layers (bottom) comparable with molecular structures of pyrophyllite and kaolinite respectively (crystal structure models were made with the program VESTA „Visualization for Electronic and Structural Analysis“ by Momma & Izumi 2006)

4.3.3 Corundum plus quartz and H₂O

In rims of setups 1, 5, and 6, the formation process of SNLs in corundum (Fig. 4.11) depends significantly on participating and catalyzing aqueous species (H₂O, OH⁻, H⁺ from fluid or hydrous melt). Annealing processes of nano-layered corundum and recrystallization (Ostwald ripening) of silica inclusions eventually result in quartz inclusions inside single crystals of corundum (Fig. 4.2, 4.4, 4.7). The result of the fluid-saturated reaction thus is silica-free corundum with quartz inclusions (Fig. 4.4). The natural occurrences of metastably coexisting corundum and quartz and even quartz inclusions in corundum is usually explained with low H₂O activity and therefore slow reaction kinetics in the associated systems. For example, granulite facies metapelites of the Bamble Sector (SE Norway) contain quartz inclusions in corundum, which were interpreted as a feature of SiO₂ immiscibility in corundum at dry conditions (Kihle et al. 2010). According to Kato et al. (2011) a quartz-corundum assemblage within K-feldspar in the Kerala Khondalite Belt (S India) indicates corundum and subsequent quartz growth from a melt at low H₂O activity. Fluid-absent conditions as well as “sluggish diffusion rates of SiO₂ and Al₂O₃” during isobaric cooling were proposed as cause for a metastable reaction of spinel + quartz into corundum + orthopyroxene, instead

of spinel + quartz into garnet + sillimanite, in quartzites from the Napier Complex, Antarctica (Motoyoshi et al. 1990). Corundum and quartz in nature should reflect metamorphic or partly anatectic rocks under “extremely dry conditions” (Mouri et al. 2003; Kato et al. 2011). This study clearly shows that the presence of an aqueous fluid (aH₂O = 1) not necessarily catalyzes the formation of Al₂SiO₅ between corundum and quartz, but can even favor their metastable coexistence.

At pressures ≥ 10 kbar, layers composed of polysynthetic nano-twins developed in corundum (Fig 4.5) along which oriented fluid trails formed. Those fluid trail hosting twins could represent the precursor of the boehmite hosting parting planes in rhombohedral networks found in the natural corundum of chapter 3. The origin of the rhombohedral network of boehmite layers was debated in White (1979) who suggested that boehmite represents a product of hydrogen exsolution from corundum. White (1979) stated that the formation of boehmite was not a result of twinning or parting, but the cause for these features. With regard to the products of run 15, the crystallization of aqueous fluid inclusions along the nanometer wide polysynthetic twins at temperatures < 500 °C (for 10 kbar; Kennedy 1959), provides an alternative explanation for the boehmite network formation in corundum.

4.4 Conclusion

Neither the interaction of corundum with quartz-saturated fluid nor the interaction of corundum with silicate melt produced Al_2SiO_5 coronas in closed systems such as the presented hydrothermal and piston cylinder experiments.

Comparison with the spontaneous formation of coronas of other, more complex silicates, e.g. muscovite or feldspar around corundum as well as that of zircon around baddeleyite indicates that the limiting factor for an experimentally formed Al_2SiO_5 corona is not dissolution or transport kinetics. The presence of fluid, which should catalyze otherwise inhibited reactions like the Al_2SiO_5 formation (Motoyoshi et al. 1990; Kihle et al. 2010), has proven not to be the determining factor in the formation of Al_2SiO_5 coronas. Also, intense silica diffusion into the corundum single grains demonstrates that corundum is reactive and therefore time dependent reaction kinetics do not prevent the formation of a corona. It is also evident that the formation of Al_2SiO_5 polymorphs well within the kyanite or sillimanite stability field is not inhibited by transport kinetics. Instead, the nucleation of Al_2SiO_5 and its growth on seeds is obstructed by previously unknown factors.

Silicon diffusion results in the formation of silicate nano-layers (SNLs) parallel to the

corundum base in reaction rims along the surface of corundum crystals. The same nano-phase is discovered in precipitated corundum plates on corundum crystals. These SNLs allow the corundum to coexist with its quartz-saturated environment without producing an Al_2SiO_5 corona. Moreover, the SNL formation eventually results in quartz precipitation in the reaction rims, as a consequence of intensified Si infiltration along the SNLs or their annealing in the altered corundum in longer experiments. Dissolution and growth behavior of passivated $\{0001\}$ faces in quartz-saturated, fluid-rich experiments apparently contradicts Wulff's (1901) theorem, but $\{10\bar{1}2\}$ and $\{01\bar{1}2\}$ are in good agreement. This indicates strong influence of the SNLs on both dissolution and growth of corundum under the given circumstances.

Regarding the interpretation of natural, meta-stable occurrences of corundum and quartz, the findings of this study provide some additional and possibly alternative explanations. It clearly disproves that sufficient aqueous fluid necessarily promotes the reaction towards Al_2SiO_5 . On the contrary, nano-scale phenomena observed in this studies experiments suggest that under certain conditions an increased water activity promotes the metastability of corundum and quartz.

5. The influence of a nanometric phase on mineral equilibration in the system $\text{Al}_2\text{O}_3\text{-SiO}_2\text{-H}_2\text{O}$ (*experiments part 2*)

5.1 Summary

The metastable paragenesis of corundum and quartz is known from nature but occurs predominantly in experiments where according to thermodynamic predictions aluminium silicate polymorphs should form. The cause for obstruction of the reaction $\text{Al}_2\text{O}_3 + \text{SiO}_2 \rightarrow \text{Al}_2\text{SiO}_5$ was so far unknown but is often attributed to kinetic inhibitions. Often corundum and quartz (or other polymorphs of SiO_2) are produced from different starting materials well inside the stability fields of andalusite, sillimanite, and kyanite (Fig. 1.2b, Fig. 5.1a; yellow icons, for abbreviations see caption of Fig. 1.2b). An explanation for the broad experimental metastability has not been found, which is troubling since the interpretation of natural samples and thermodynamic modeling in the ASH system relies on experimental data that are affected by this phenomenon.

Metastable corundum products from several selected experiments (runs 2, 3, and 33-43; Tab. 2.1) were investigated in detail. All experiments were silica saturated with respect to quartz (and fluid rich), and thus the silica and alumina educts would be expected to only produce the Al_2SiO_5 polymorphs and quartz as solid products at given P-T, but no corundum. Runs 35 to 43 were cooling or decompression experiments, which according to Beitter et al. (2008) should precipitate sillimanite or kyanite due to supersaturation of mono- and dimer Al and Si complexes with respect to Al_2SiO_5 from the aqueous fluids. Supersaturation is achieved by either cooling or decompressing a fluid equilibrated at initially

higher P-T. Run 43 additionally contained kyanite seeds in order to provide a nucleation surface.

The results showed that localized phase assemblages with an Al-Si-H-bearing nanometer-sized phase on the corundum surface can explain the metastability plaguing experimental studies in this system without invoking further unknown kinetic factors. This nano-phase formed inside and on the corundum crystals, thereby controlling the growth behavior of its host. Less than 10 nm wide, this phase resembles an incomplete dioctahedral phyllosilicate structure that developed along the basal plane of corundum. Along the interface of corundum and quartz, the nano-phase effectively isolates the bulk phases and presumably prevents the reaction towards the stable Al_2SiO_5 polymorph. High temperatures and prolonged experimental duration lead to recrystallization or annealing of the corundum including the nano-phase and to the formation of quartz inclusions inside the host crystal. A process that increases the bulk phases volume and simultaneously reduces the phase boundary area between them, thereby providing further opportunity to expand their coexistence. Apart from its size, the transient nature of the nano phase makes it difficult to be detected both in experiments and even more in natural samples. The findings, however, emphasize how vastly the formation and modification of nano-phases influence and even control geochemical reactions and kinetics under metamorphic conditions in one of the most important chemical systems of the earth crust.

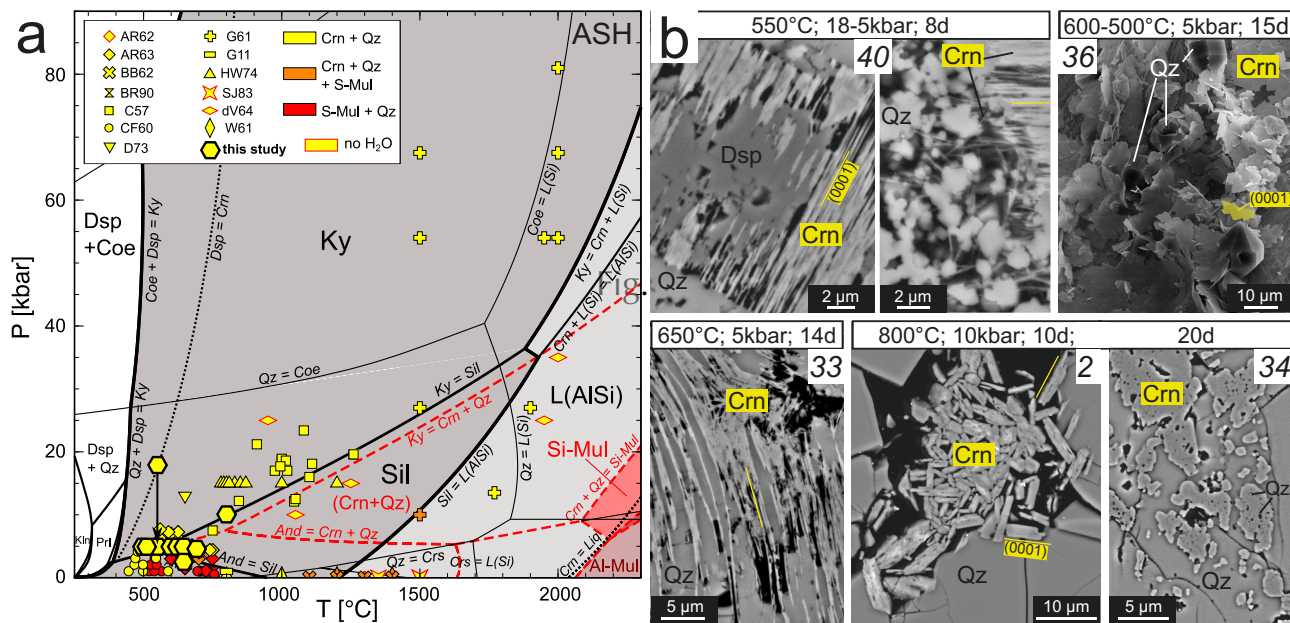


Fig. 5.1 Extent of the metastability of corundum (Crn) and quartz (Qz) in experiments. a) Petrogenetic grid of the system $\text{Al}_2\text{O}_3\text{-SiO}_2\text{-H}_2\text{O}$ (ASH) calculated with the program Perplex_X (Connolly 2009), using the thermodynamic dataset of Holland & Powell (2011), mineral abbreviations after Whitney & Evans (2010), for details see chapter 1 (Figs. 1.1 and 1.2). Included are experiments of this study that yielded metastable Qz + Crn (yellow; runs, Qz + Si-Mul, and Qz + Crn + Si-Mul (orange), for abbreviations of experiments from literature see Fig. 1.2b. b) Crn + Qz produced in experiments of this study (run numbers are indicated in the corresponding figures in italic) with increasing temperature from top to bottom and left to right (Dsp = diasporite). Note increasing width in [0001] of the Crn plates with increasing T, and the change of crystal habit at 800°C from flat prism after 10 days to porous rounded Crn grains after 20 days.

5.2 Results

All experiments produced corundum and quartz, and in one case corundum-quartz and mullite (Fig. 5.1a, data on Si-mullite, see chapter 4.2, Tab. 4.4). The quartz grains displayed equilibrium-growth textures when composing the matrix phase, which was the case for all piston cylinder experiments (runs 2, 3, 34, 40, 41). In hydrothermal experiments (runs 33, 35-39, 42, and 43) with high fluid content the phase developed euhedral single crystals (Fig. 5.1b). The aluminium content in quartz seems to depend mainly on the silica starting material.

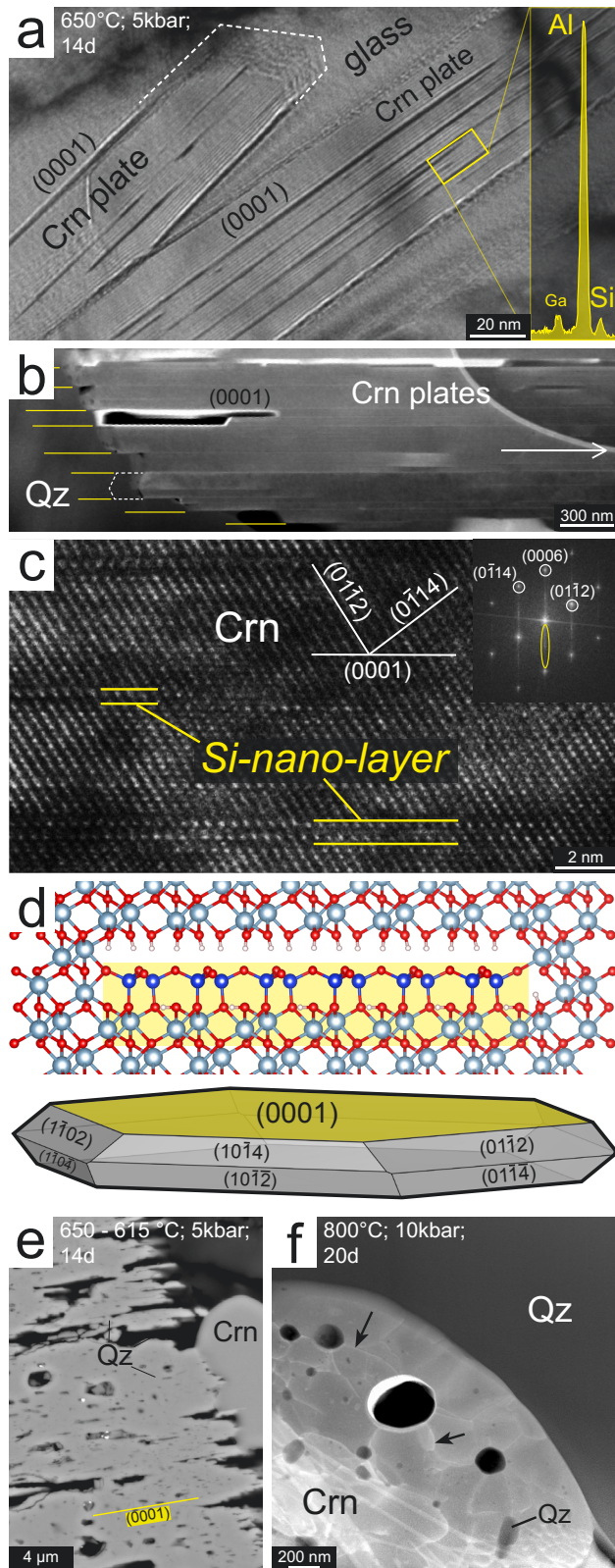
The highest Al_2O_3 wt% values of 0.73 were measured in quartz produced during pyrophyllite dehydration (run 33, Tab. A5.1). In experiments with high fluid contents, a positive temperature dependency of the Al concentration in quartz was observed (Tab. A5.1).

Corundum formed in all experiments > 500°C in direct contact with quartz, whereas Al_2SiO_5 polymorphs were not produced (Fig. 5.1a, b). In run 43, the kyanite seeds showed etch pit formation but corundum and quartz grew on the seed surface instead of sillimanite (Fig. A5.1).

Corundum crystallized as flat hexagonal prisms or plates characterized by a large basal pinacoid $\{0001\}$ and vanishingly small faces of $\{01\bar{1}2\}$ and $\{0\bar{1}14\}$ (see Fig. 5.1b). Independent of the alumina starting material ($\gamma\text{-Al}_2\text{O}_3$, or diaspore), the habit of synthesized corundum displayed a strong temperature dependence in that the area (or aspect) ratio of crystal faces $\{0001\}/(\{01\bar{1}2\}+\{0\bar{1}14\})$ decreased with increasing temperature (Fig. 5.1b). Corundum produced at 550 °C resembled phyllosilicate shaped flakes or plates with < 200 nm width (Fig. 5.1b; runs 40 and 35). At 650 °C the corundum crystals reached up to 300 nm in width, and at 800 °C, up to 5000 nm thick plates or prisms were produced (Fig. 5.1b; run 33). The influence of pressure on the habit of the corundum crystals seems to be negligible, however, at temperatures of 800 °C the duration of the experiments affected the shape of the crystals. While after 10 days the corundum occurred as flat prisms, an experiment of 20 days produced rounded corundum grains surrounded and included in quartz as well as corundum grains including up to 1 μm large, rounded quartz inclusions (Fig. 5.1b; runs 2 and 34). A series of experiments with diaspore as Al_2O_3 source produced less than 200 nm wide, pseudomorphic parallel piles of corundum plates at 550 °C (Fig. 5.1b; run 40, Fig. A5.2a). Corundum plates formed after diaspore at 615-650 °C are up to 3 μm thick and locally inter-grown with adjacent plates, and contain elongated quartz inclusions (Fig. A5.2b; run 38). At 800 °C the prism shape was only

poorly developed and the corundum mainly occurred in rounded, up to 50 μm large grains, with numerous often parallel elongated, rounded quartz inclusions (Fig. A5.2c; run 34). EMPA results of the corundum plates show variable SiO_2 wt% contents between 0.08 and 11.0 (Tab. A5.2). However, most analyses represent mix results of corundum grains, inclusions, and interstice, which likely contain quartz (especially those synthesized at lower T).

Fig. 5.2 Page 90; a) Bright field image of Crn plates (run 33) including silicate nano-layers (SNL) parallel to (0001), a TEM-EDX spectra of a nano-layered area is displayed in yellow (Ga contamination is caused during FIB preparation of TEM foils). b) HAADF image of identically oriented Crn plates grown on a large single crystal (connected along $10\bar{1}0$), position indicated with white arrow) but not inter-grown with each other. Si-anon-layers are visible as fine stripes inside and between the Crn plates (grain boundaries with SNLs indicated in yellow). c) HRTEM image of SNLs along (0001) with characteristic electron diffraction image showing a streak pattern parallel to $[0001]$ (yellow ellipse, upper right angle). d) Model of molecular structure of a single SNL, where one Si-tetrahedral layer is replacing two Al-octahedral layers in Crn, and the crystal model of a Crn plate with large basal pinacoid (0001), which presumably comprises a single SNL comparable with the molecular model (in yellow). e) Recrystallized Crn from 20 day long experiment (Run 34) including elongated and rounded Qz inclusions (and fluid). f) HAADF image of recrystallized Crn without SNLs but with rounded inclusions (Qz and fluid, see upper right detail HAADF image) that are connected with sub-grain boundaries (black arrows). The Crn-Qz bulk phase boundary is almost spherical and thus the bulk minerals surface area to volume ratio is at a minimum.



TEM investigations showed that the corundum plates comprise silica-bearing or silicate nano-layers (SNL) distributed along (0001) inside the grains (Fig. 5.2a, Fig. A5.3). In HRTEM mode these layers are only visible in foils cut roughly parallel to the corundum's c-axis (Fig. 5.2a, b, c). In experiments including corundum single crystals (up to 1 mm diameter) the precipitated corundum plates overgrew the single crystal surface epitactically with growth directions perpendicular to [0001] (Fig. 5.2b, Fig. A5.4a, b, c) but not inter-grown along (0001). The grain boundary between individual corundum plates is indistinguishable from the SNLs inside the individual plates indicating that SNLs on the basal pinacoids of the plates separate the individual grains from each other (Fig. 5.2b). No corundum plates were found grown on (0001) of the single crystals.

Similar SNLs to those in this study were also found in corundum single grains experimentally treated with silica rich aqueous fluid (chapter 4.2, Fig. 4.3). Synthetic corundum single crystals with polished (0001) faces included in these experiments showed a strong dissolution resistance in [0001] and developed a silica-bearing surface layer of ≤ 500 nm thickness in prolonged experiments (> 14 days) (Fig. A4.2). HRTEM images of the SNLs suggest that their structure resembles isolated Si-tetrahedral and Al-octahedral layers as in dioctahedral phyllosilicates, e.g. kaolinite or pyrophyllite (Fig. 5.2c, d, compare Kogure et al. 2006). The basal plane of corundum provides the Al-octahedral

layer (Fig. 5.2c, d) and the tetrahedral layers are incorporated as single layer substituting $2\text{Al}^{3+} \rightarrow \text{Si}^{4+} + 2\text{H}^+$ (see Fig. 5.2d) or double layer according to: $3\text{Al}^{3+} \rightarrow 2\text{Si}^{4+} + \text{H}^+$ (see also chapter 4.3; Fig. 4.11). In electron diffraction images of the Si-layered corundum the nano-phase is represented by a streak pattern in [0001] (Fig. 5.2c), which reflects offsets and stress in the corundum lattice induced by the nano-layers due to structural mismatches between nano-phase and host crystal. The octahedral layer in corundum is not identical to the octahedral layer in dioctahedral phyllosilicates regarding the position of Al ions in $(0001)_{\text{Cm}}$ and $(001)_{\text{Phy}}$ respectively (Lee and Guggenheim 1981; Lewis et al. 1982). However, the connecting basal layer of Al octahedra is very likely modified in contact with the tetrahedral layer. Eng et al. (2000) reported a displacement of the Al ions in the surface layer of hydrated (0001) corundum crystal faces

towards approximately the position the Al ions hold in boehmite. A similar approximation of the corundum basal plane to the octahedral layer in dioctahedral phyllosilicates can be expected in contact with a silica layer.

Rounded corundum produced within 20 days at 800 °C; 10 kbar, included no SNLs, but instead inclusions of silica or quartz and fluid (Fig. 5.2e, f). Numerous sub-grain boundaries connecting the inclusions indicate strong recrystallization and occasionally display an increase in Si compared with the Si-free rest of the grain (Fig. 5.2f).

In some of the XRD analyses, the corundum diffraction pattern displays a discrepancy between the measured relative peak intensities and standard spectra (e.g. Lewis et al. 1982). Specifically, increased intensities of the $(11\bar{2}0)$ peak relative to the intensity of the $(11\bar{2}3)$ peak were noted (Fig. A5.2d).

5.3 Discussion

Natural occurrences of corundum adjacent to quartz without visible reaction to Al_2SiO_5 are rare and generally interpreted as a metastable feature of fluid-free metamorphic reactions (Kihle et al. 2010; Kato et al. 2011). The missing reaction towards Al_2SiO_5 is usually interpreted to be caused low reaction kinetics due to lack of a catalyzing fluid phase. The results show that the presence of fluid not necessarily promotes the reaction of $\text{Al}_2\text{O}_3 + \text{SiO}_2 \rightarrow \text{Al}_2\text{SiO}_5$. Moreover, inside and on the surface of the synthesized corundum plates nano-layers of silica are inter-grown with the basal plane of the grain, forming phyllosilicate like structures (Al-octahedral with Si-tetrahedral layer, see Fig. 5.2d). Charge imbalances caused by the substitution of Al^{3+} by Si^{4+} or surface Al^{3+} are most likely compensated by free H^+ similar to real phyllosilicates or Al-hydroxides, which indicates that the presence of water in the experiments likely favors the formation of the nano-phase over the nucleation of the thermodynamically stable Al_2SiO_5 polymorphs rather than promoting the reaction towards the latter.

The nano-phase prevents adjacent, identically oriented corundum plates to coalesce and form a single crystal, an observation that indicates that the nano-layers are the cause of growth obstruction along [0001]. Suchanek and Garcés (2010) reported the formation of “corundum nano-sheets” (plate shaped corundum with large basal plane) from boehmite dehydration, with

additional 1 – 10 wt% of silica, in hydrothermal experiments at $\leq 450^\circ\text{C}$; 0.1 kbar. In the absence of silica, the corundum crystals developed a granular shape. Furthermore, X-ray photoelectron spectroscopy conducted on the (0001) surface of the sheets and 6 nm below the surface showed the highest intensities for Si-derived bands (both Si2p and Si2s) at the surface (Suchanek and Garcés 2010), which further supports the existence of a SNL on the (0001) surface. Silica-bearing features inside the corundum sheets were not reported. Broadening of XRD peak width of all peaks but $(11\bar{2}0)$ and $(30\bar{3}0)$ with increasing SiO_2 concentration could, however, represent nano-layers included in the corundum, at least an increase of the relative intensities of those two peaks compared with the rest of the pattern was also observed in the present study (Suchanek and Garcés 2010). Relative peak intensity changes might mainly result from the habit of the corundum, broadening of the reflexes oblique to $[11\bar{2}0]$ and $[10\bar{1}0]$ though indicates a disruption of the crystal lattice continuity and could be induced by the SNLs.

Si-rich surface layers are also known from experiments in quartz saturated systems where corundum dissolution is passivated in [0001] probably due to the shielding effect the surface layer provides towards the attacking agent (see chapter 4.2, Fig. A4.2). In case of corundum plates with a surface area predominantly

consisting of silica-nano-layered basal pinacoids, the interaction with adjacent quartz is very likely passivated for similar reasons. Nanometer-sized minerals theoretically have a higher surface energy (or zeta potential) than their bulk minerals due to a large ratio of surface area/volume and should react more rapidly than the bulk minerals (Madden et al. 2006). Thin corundum plates adjacent to quartz should hence react faster towards Al_2SiO_5 polymorphs than larger corundum grains with smaller surface area/volume ratio. However, the SNL on corundum potentially reduces the chemical potential gradient between the corundum and neighboring quartz drastically and thus prevents the two phases from interacting. Fisher et al. (2001) showed that the zeta potential difference of pure quartz and pure corundum in solution is about 85 mV at neutral pH. The addition of 2.7 vol% of silica to a corundum suspension decreases the zeta potential of corundum drastically and reduces the zeta potential difference of quartz and corundum to about 25 mV due to the absorption of nano-silica particles (85 nm size) to the corundum surface. Similarly, the surface reactivity of corundum plates in contact with quartz or silica-saturated fluid with respect to quartz is probably reduced due to the silicate nanometric surface layer. A minimized surface energy also results in a smaller critical nuclei-size of corundum plates, which supports the survival of newly formed corundum plates so that they grow and increase in size. Further-

more, the zeta potential of silica decreases (becomes less negative) with decreasing nanoparticle size (Diedrich et al. 2012), which could explain why the SNL does not react with the corundum to aluminium silicate.

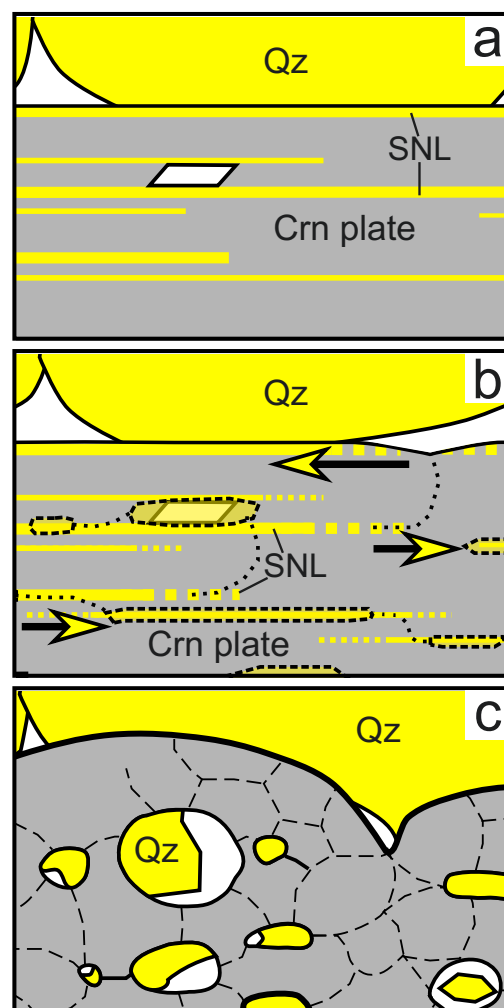


Fig. 5.3 a) Sketch of corundum plate with SNLs inside and at the (0001) face of the grain along the grain boundary with Qz, the nano-layer prevents Crn and Qz from reacting. b) Annealing of the Crn including SNL, Ostwald ripening of SiO_2 (+ H_2O) indicated by arrows, and nucleation of Qz inside the Crn, recrystallization of Crn. c) Recrystallized Crn is composed of numerous subgrain boundaries and near spherical fluid + Qz inclusions. The Crn-Qz phase boundary is continuously rounded and the interface between the two phases minimal, which prevents the reaction towards Al_2SiO_5 once again.

A series of experiments with diaspore starting material showed that at temperatures of 800 °C and prolonged run duration (>2 weeks) the corundum habit changes significantly and SNLs disappear. Sub-micron-wide platy corundum produced at 550°C yields to μm -wide corundum plates with quartz inclusions at >600°C and finally to anhedrally rounded corundum with elongated and rounded quartz inclusions. These findings are interpreted as a gradual Ostwald ripening of the corundum and the SNLs included in corundum with increasing temperature and experiment duration (Fig. 5.3). The SNLs are defects in the corundum structure that anneal when they become increasingly unstable at higher temperatures (compare Reich et al. 2006). Silica, formerly included in the SNLs, accumulates within the corundum as rounded, isolated quartz inclusions (Fig. 5.2e, f) (compare chapter 4.2, Figs. 4.4, 4.7). The annealing also enables neighboring plates to inter-grow and from larger crystals (especially in [0001]) that show likewise rounded phase boundaries towards surrounding quartz (Fig. 5.2 f). Nearly spherical phase boundaries reduce the surface area between quartz and annealed corundum and thus minimize the surface energy between the two phases, which probably preserves the metastability at higher temperatures (see Fig. 5.1b, Fig. 5.2f).

The features presented in this study are only directly visible and can only be identified conclusively with TEM in oriented corundum (basal plane $\sim\parallel$ incident beam). The SNLs

would be measurable with EMP analyses in large grains with low quartz inclusion density, however, since Si is not an expected trace element in corundum, analyses of corundum usually do not include Si (Harlow and Bender 2013). Furthermore, the layers tend to disappear in experiments with longer runtime (Fig. 5.3), all of which likely contributes to the phases being overlooked. However, the crystal shape of synthesized corundum, as well as μm to sub- μm sized quartz inclusions, give hints on whether SNLs might be, or have been, included in the grains and should be considered when interpreting experimental and possibly natural findings (e.g. Brearley 1986; Guiraud et al. 1996; Kihle et al. 2010; Grapes 2011; Karmakar and Schenk 2015). Although the amount of silica in and on the corundum plates is small, it needs to be taken into account, specifically if the precipitation of corundum is treated as an equilibrium feature and used for quantitative estimates (Manning 2007). The XRD-based interpretation of experiments in the ASH system at temperatures < 600°C can be influenced by the appearance of very thin, SNL-bearing corundum plates, depending on the detection limit of the X-ray diffractometer used. Intensity decrease and broadening of peak width can potentially prevent the identification of small amounts of corundum altogether. Thus the interpretation of experiments using only XRD to determine reaction pathways might be significantly biased.

The impact of nano-particles, or nano-minerals on environmental and biological processes (Waychunas et al. 2005; Hochella 2008; Wang 2014) but also on ore-forming processes (Reich et al. 2006, 2009) and occasionally extra-terrestrial materials (Navrotsky et al. 2008; Dai et al. 2010) is fairly well known. On the contrary, only little has been reported on the occurrence of nano-phases in magmatic (Reich et al. 2009, Xu et al. 2017) and even less in metamorphic rocks (Wu et al. 2002), which presumably results from fast reaction kinetics and/or long reaction timescales leading to the resorption of nano-phases in these settings prior to eruption or exhumation. Specifically for metamorphic systems, it seems therefore inevitable to combine natural findings with experiments that might preserve process controlling nano-phases.

5.4 Conclusion

After countless experiments in the ASH system Aramaki and Roy (1963) wrote: “It can easily be seen from the data that no structural prejudice is involved in the formation of quartz + corundum. Indeed, this is the strongest argument (in the absence of data) for the thermodynamic stability of this assemblage.” Now, several decades later it can be shown that there is in fact a structural parameter favoring the growth of corundum and quartz that is not part of the crystal structure of the bulk phases. The presence of SNLs in and on corundum, together with quartz in fluid-bearing experiments, formed well inside the stability fields of Al_2SiO_5 polymorphs provides an explanation for the persistent metastability of the two bulk phases. Influencing both growth and dissolution behavior of corundum the SNL stabilizes corundum next to quartz due to the fact that the bulk phases interface is reduced to a minimum

and both quartz and corundum are in contact with the SNL but not with each other. Consequently, the reaction to Al_2SiO_5 polymorphs is inhibited. Therefore, the extended metastability of quartz and corundum and suppression of Al_2SiO_5 polymorphs is not a problem of reaction kinetics but rather one of a transient and localized equilibrium on a time and space scale that is usually overlooked. Nanometric phases are known to influence various geological systems and control mineral phase stability and geochemical reaction kinetics due to very deviant physicochemical properties with respect to their bulk phases (Hochella 2008, Wang et al. 2014). The influence on processes in the system Al_2O_3 - SiO_2 - H_2O of the nano-phase presented in this study should be considered in both experimental and natural studies.

6. Concluding remarks

Natural kyanite corona formation on corundum in two geographically and geologically unrelated samples has shown to be a result of decomposing aluminosilicate phases (muscovite or feldspar) in contact with corundum. The mineral paragenesis of sample MI places the corona growth event on a prograde metamorphic path, whereas sample KT describes a retrograde path. Corona growth reactions for both samples could be estimated using inclusions of corundum and mica (MI) or feldspar (KT) in kyanite (Figs. 3.3, 3.6). No compelling evidence was found that suggests external silica influx into either one of the samples. A key component during aluminosilicate replacement, however, is the removal of potassium from the systems that is not included in solid reaction products in the samples and thus must be removed along with a fluid phase. Volume estimates of feldspar and corundum inclusions in the KT-corona showed that the amount of silica provided by decomposing feldspar and aluminium provided by the corundum would suffice the kyanite producing reaction. Thermodynamic modeling for the system KASH (representative for both MI and KT) indicates that for both samples kyanite precipitation requires K removal (Fig. 3.9).

Experimental setups for the simulation of open systems, including the removal of fluid (as observed in sample MI and KT) at P-T

conditions required for aluminium silicate formation are currently not available, and experiments of corundum single crystals interacting with quartz saturated aqueous fluid or silicate melt, did not produce Al_2SiO_5 coronas. On the contrary, fluid mediated Si-diffusion into corundum ultimately resulted in the precipitation of quartz inside the corundum grain (Figs. 4.2, 4.4). During these experiments, sluggish reaction kinetics, as are often held accountable for the preservation of metastable assemblages, could therefore not have been the factor that prevented the precipitation of Al_2SiO_5 and the corona formation. The formation of silicate nano-layers (SNL) inside and on corundum, parallel to (0001), as a reaction towards attacking silica bearing fluid/melt, indicates fast reaction kinetics. Similar SNLs were found also on the large basal pinacoid and inside precipitated, plate shaped corundum having phase boundaries with quartz. The presence of the SNL along the phase boundary of corundum and quartz is responsible for the persistence of the metastability of the bulk phases and the inhibited reaction towards stable Al_2SiO_5 . The phyllosilicate like structure of the SNLs furthermore features the possibility that aqueous components (in fluid and melt) might actually support the metastability of corundum next to quartz. This observation contradicts the conventional perception that fluid promotes

reactions into the direction of their stable assemblages (e.g. Kihle et al. 2010; Kato et al. 2011).

It is likely that the occurrence of SNLs also plays a role in the nucleation of corundum, quartz and Al_2SiO_5 . The basic molecular structure of corundum is that of an Al-octahedral plane, whereas kyanite, sillimanite, and andalusite are composed of Al-octahedral chain structures with (And, Sil) or without (Ky) singular, five or four fold Al, and with singular tetrahedral silica. In combination with polymerized silica the Al-plane seems to be favored over chain structures when forming in certain silica saturated aqueous fluids or silicate melts (see chapter 4 and 5). According to investigations on kyanite dissolution in aqueous fluid Al-O bonds are more easily broken than Si-O bonds (Oelkers and Schott 1999), which increases the probability of Al-O-Al instead of Si-O-Si connections being disrupted. The formation of an Al-plane connected to a Si-plane may stabilize the Al-plane structure in comparison with the Al-chain that connects to non polymerized Si-tetrahedra. This idea, although speculative and in need of further investigation, is supported by the formation of plate shaped corundum instead of Al_2SiO_5 in experiments in which Al-chain-bearing precursor phases decompose in the presence of quartz saturated fluid or melt phase (e.g. decomposing diaspore + quartz in this study, or staurolite in Grapes 2011) and the fact that corundum and quartz grow on decomposing

kyanite seeds instead of sillimanite (Fig. A5.1). SNLs are a transient phenomenon and are annealed by the host corundum at elevated temperature or prolonged experimental duration. Corundum and silica from the SNLs recrystallize, and Ostwald ripening subsequently precipitates rounded quartz inclusions in corundum. Approximately spherical phase boundaries also develop between corundum and surrounding bulk (matrix) quartz, in order to reduce the surface between both phases, thus providing another reason for the inhibition of Al_2SiO_5 nucleation.

It remains an unsolved question how Al_2SiO_5 nucleation proceeds in nature, and what the crucial difference between the natural samples and experiments is. The most striking discrepancy is the fact that the natural coronas developed in an open system, in which kyanite formation depends on the loss of alkalis via fluid, whereas experiments represent closed systems. The removal of alkali components from aluminosilicates and the subsequent decomposition of the latter next to corundum could allow heterogeneous nucleation of Al_2SiO_5 in the aluminosilicates. The crystal habit of kyanite composing the corona of sample MI was subhedral to euhedral with inclusions of muscovite occasionally parallel oriented to the kyanite main cleavage (Fig. 3.3), whereas kyanite in the KT-corona was completely anhedral (Figs. 3.6, 3.7). This difference likely displays the structural influence of the aluminosilicate precursor phases on the kyanite

growth. Detailed descriptions of mica replacement and approximate epitactic relations between Al_2SiO_5 and its precursor phases are given in Sanchez-Navas (1999) and Chinner (1961).

A distinct growth pattern of kyanite in the corona of sample KT, with elongated crystals parallel to, and blocky crystals perpendicular to (0001) of corundum is the result of different growth rates of kyanite on different faces of corundum (Fig. 3.7). The shape of kyanite indicates limited corundum dissolution in [0001], due to the fact that the growth of kyanite along kyanite-kyanite grain boundaries did not result in the formation of depressions in the corundum (0001) surface and instead grew parallel to (0001) (Fig. 3.7). The passivated dissolution of the corundum basal plane is also observed in experiments with quartz saturated fluid, which indicates related mechanisms during corundum dissolution in nature. In the presence of kyanite, however, corundum in the natural samples displays no sign of nano-phase enhanced Si-diffusion. Si bulk diffusion into corundum is moderate in contact with kyanite and does not exceed the Si solubility in corundum (Fig. A3.7).

A network of boehmite-bearing parting planes inside the corundum grains and boehmite or alternatively kaolinite layers along the phase boundary with kyanite are found in both natural samples. Both phases represent aqueous components in the corona structure, which re-equilibrated during cooling with the surrounding

kyanite and/or corundum (Kennedy 1959; Bratton and Brindley 1962; Scott and Carruthers 1969; Chatterjee et al. 1984). Sample KT, however, displayed kyanite growth along the rhombohedral parting planes and twin planes in corundum (Fig. 3.7c), which indicates that the crystallographic features preceding the boehmite formation existed at least since the corona growth event at P-T far above boehmite formation. The formation of these ultimately boehmite-bearing features in corundum can be explained with a process observed in experiments with pressures ≥ 10 kbar. At higher pressure the corundum single crystals develop pressure twins and exposure to aqueous fluid produced fluid inclusion trails along these pressure twins. TEM investigations furthermore showed that the twins associated with fluid trails were no simple twin individuals but an area composed of polysynthetic nano-twins (Fig. 4.5). It is therefore more likely that the boehmite represents fluid that re-equilibrated with these nano-pressure twins that represent areas of concentrated crystal defects and are thus prone to recrystallization.

I hope the findings of this thesis help to slightly widen our understanding of the system Al_2O_3 - SiO_2 - H_2O in all its peculiarity and eventually provide a starting point for future studies. The existence of nano-phases at high pressures and temperatures deserves particular attention, after all their impact on metamorphic processes seems to be vast.

7. Outlook and future directions

During the course of this study several additional natural and experimental examples of reactions involving corundum, quartz and some form of Al_2SiO_5 were investigated that were thought to potentially contribute to answering the main questions of the thesis. However, these turned out to go beyond or outside the scope of the thesis and were thus set aside. I will pursue the completion of these studies in the future and will outline them briefly in the following.

The most prominent obstacle to corona formation was the nucleation of the three aluminium silicate polymorphs. In order to gather information about this specific process, independent of the corona formation on corundum, a detailed field study and subsequent mineralogical investigation was conducted along the Greiner shear-zone at the Pfitscher Joch (Tauern window, Italian Alps). The Greiner shear-zone is a 200 km long and up to 250 m wide, strike-slip fault crosscutting metapelitic and metapsammitic units of the post variscan sedimentary cover (part of the Venediger duplex) that was tectonically squeezed between two branches of the Zentral-gneiss during collisional events of the alpine orogeny (Cole et al. 2007, Schmid et al. 2013). In the shear-zone these different metasediments were exposed to mylonitization and high fluid flux, which altered the protoliths beyond recognition. Kyanite-bearing shear-zone units are associated with

different protoliths and provide many different excellent opportunities to study kyanite formation. Six different sample points along the shear-zone were investigated and showed that kyanite formation is consistently linked to metasomatic reactions, in which muscovite is leached of volatile components (K, Na, Ba, Rb, Sr) in contact with shear-zone related fluid, comparable with observations in chapter 3 (Fig. 7.1, Vrána 1973; Grant 1986; Widmer and Thompson 2001). For all six sampling points the muscovite decomposition seems to be triggered due to K-undersaturation in the infiltrated fluid. Potassium undersaturated fluid reportedly stems from dehydrating ophiolite bodies that are dragged and deformed in the shear-zone (Barnes et al. 2004). The mass gain of elements usually associated with ultramafic rocks (Fe, Mg, Cr, Ni, Zn, Ca) in kyanite-quartz shear-zone units supports the ophiolite theory (Fig. 7.1, Tab. A7.1). Kyanite bearing quartz veins in the shear-zone represent areas of maximum protolith leaching and most intense fluid influx. The question whether kyanite trace element chemistry can be used as a fluid monitor and how the fluids involved in kyanite formation look like, is currently under investigation in different vein samples. Trace element concentrations of vein-kyanite (Fig. 7.2, Tab. A7.2) are compared with trace element contents in primary kyanite fluid inclusions

(measured by LA-ICPMS) in order to establish, which elements mirror the fluid composition and which reflect the precursor aluminosilicate minerals.

In one sampling point along the shear-zone kyanite microlites were found in the selvage of a porphyroblastic kyanite and quartz layer (Fig. 7.3). The trace element distribution in kyanite was used in combined CL and EMP studies to determine the growth of kyanite from microlite to porphyroblast. Due to trace element fractionation between three different growth sectors in the mineral, the growth pattern of a grain can be traced in detail, which showed that most porphyroblast are composed of numerous parallel grown kyanite individuals that may be displaying several intergrown former microlites (Fig. 7.4, Tab. A7.4).

The microlites in the Ky-Qz layer selvage are associated with a glass that is interpreted as the remnant of a transient melt phase formed during muscovite decomposition (Figs. 7.1, 7.3). The glass is alkali poor and composed mainly of silica and aluminium (Tab. A7.3). Dehydration melting and the formation of Al_2SiO_5 (mainly kyanite) was also inherent to some of the corona growth experiments. Hydrous silicate glass formed during muscovite dehydration in run 32 was rich in K and Na compared with the natural glass and the muscovite precursor (Fig. 7.5). The removal of alkalies seems to play a key role in the formation of Al_2SiO_5 from dehydrating muscovite and silicate melt, in that the presence of alkalies results in the precipitation of corundum in these melts in experiment (Fig. A3.6).

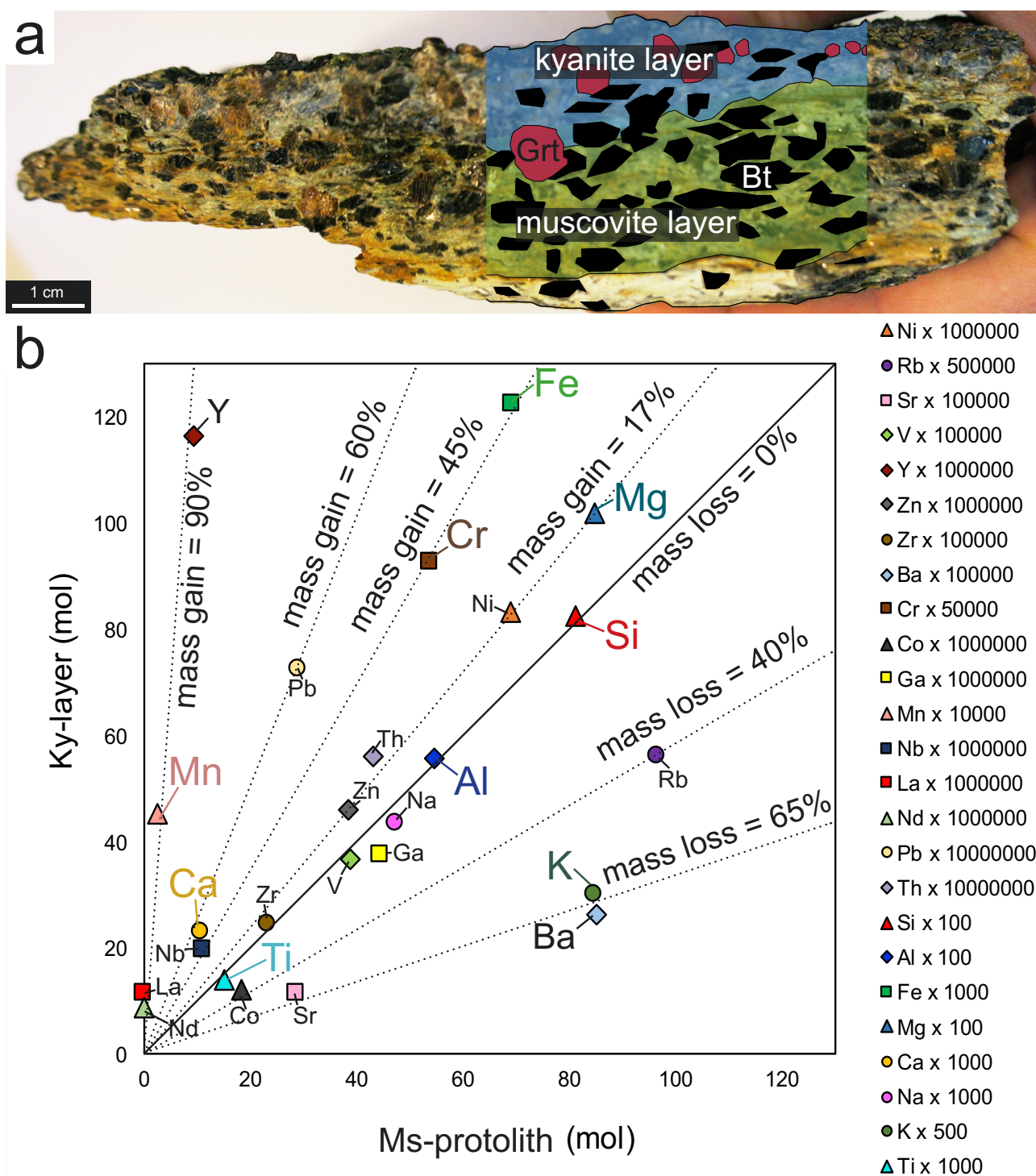


Fig. 7.1 a) Photograph of a hand specimen displaying the Ky-Qz layer (with garnet “Grt”) adjacent to the Ms-Qz protolith (meltapelite, Furttschagl-schist). b) Bulk rock analyses of Ky-bearing layer and Ms-dominated protolith plotted in a Grant diagram (after Grant 1986). Element concentrations of both domains (separately measured with XRF) are plotted against one another, in order to approximately quantify the mass gain or loss (in the Ky-domain with respect to the Ms domain) during Ky-Qz layer formation. All elements plotting above the iso-line of 0% mass loss or gain (black line) are enriched (Mg, Fe, Ca, Mn, Cr, Ni, Zn, Y, Th, Pb, Nb, La, Nd) in the Ky-rich layer and elements plotting below the 0%-iso-line are depleted (K, Ba, Sr, Rb, Ga). Data plotted in this figure are given in Tab. A7.1.

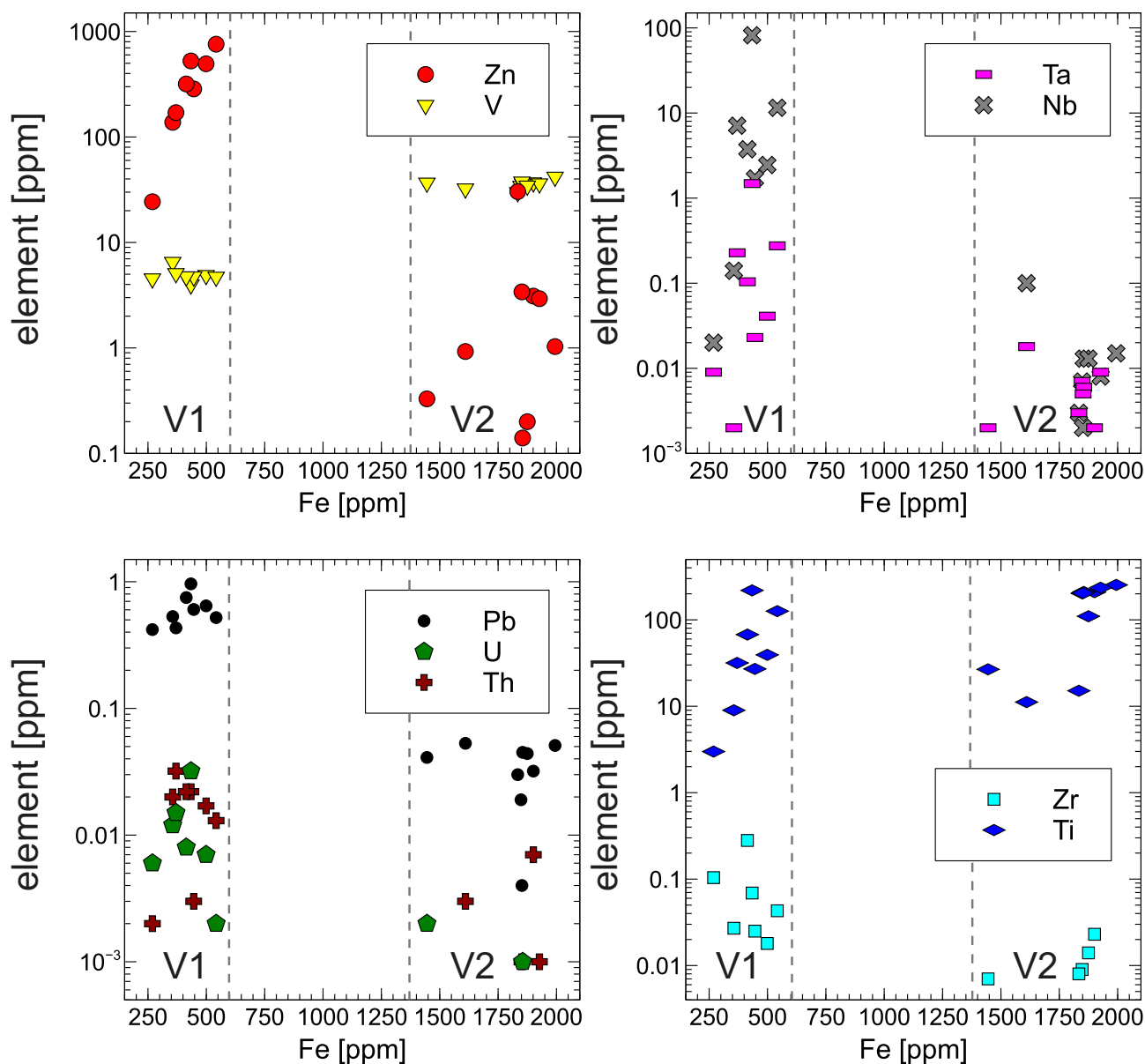


Fig. 7.2 Two different Ky-bearing Qz-vein types (V1 and V2) in the Greiner shear-zone, and their kyanite trace element chemistry (LA-ICPMS results). Trace elements in ppm are plotted against Fe (V1 and V2 data are separated with black dashed lines). V1 kyanite incorporates higher amounts of Zn, Nb, Ta, Zr, Pb, U, and Th than V2 kyanite, but shows lower concentrations of vanadium. The data are given in Tab. A7.2.

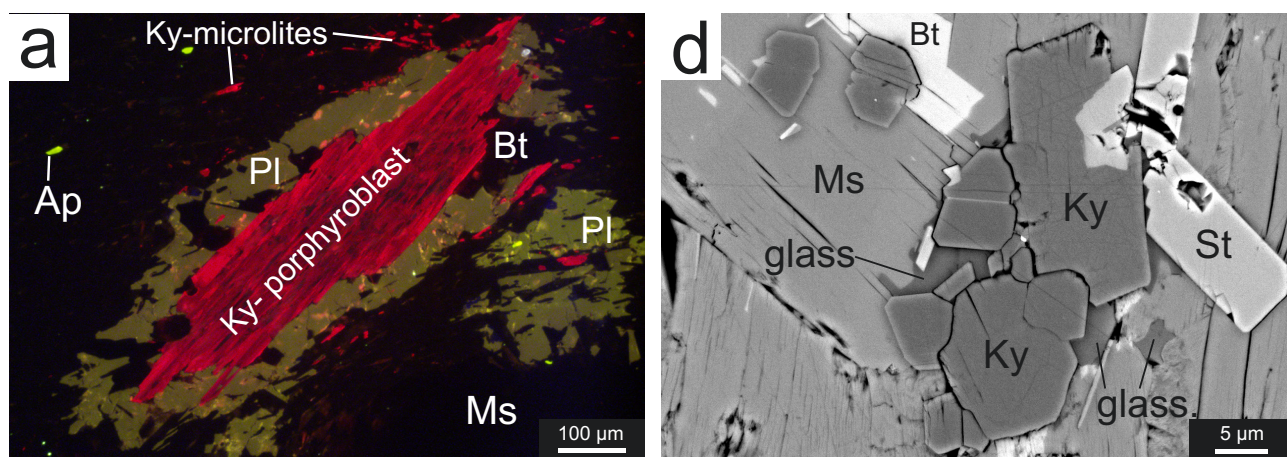


Fig. 7.3 Kyanite formation along the Ms-Qz and Ky-Qz layer selvage in Fig. 7.1. a) Optical CL image of a Ky-porphyroblast (intensely red due to Cr-traces) along the selvage, rimmed with anorthite rich plagioclase (Pl) and surrounded by numerous up to 100 µm long Ky-microlites (red) in muscovite (Ms). b) BSE image of a Ky microlite cluster grown along Ms grain boundaries. The interstice between the Ky microlites is filled with silicate glass; additionally staurolite (St) and biotite (Bt) are associated with Ky-microlites.

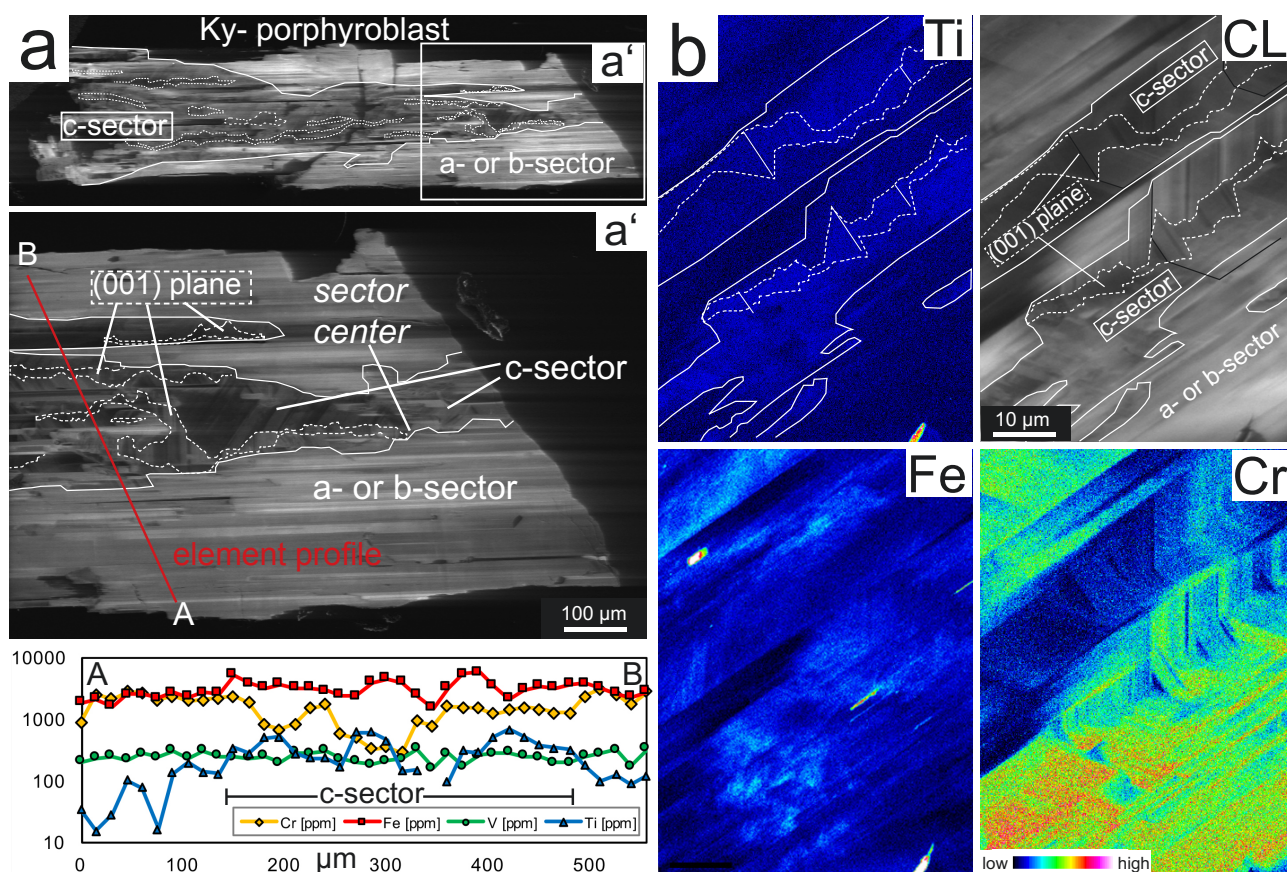


Fig. 7.4 Kyanite porphyroblasts growth pattern in the Ky-Qz layer (Greiner shear-zone). a) CL-SEM images combined with an element profile (A-B in red see Tab. A7.4, for Cr, Fe, V, Ti) through sectors a or b, and c. The c-sector is composed of several sub-grains or twins with their own sector zonation („sector forking“, indicated with white lines). The element profile shows an increase in Ti along the c-sector and a decrease in Cr content. b) Element mappings were combined with CL-SEM image to correlate intense luminescence and trace elements; bright glowing areas are rich in Cr, and the c-sectors are enriched in Ti.

The only experiment yielding Al_2SiO_5 was run 4 (1200 °C; 20 kbar) that was contaminated and is thus not reproducible. The unknown contaminant(s) produced different Al bearing silicate melts (glass) in the quartz-quartz or quartz-corundum interstice (Fig. 7.6). Kyanite was found exclusively in La and Ce silicate glasses with low alkali contents and with or without corundum contact, whereas in alkali rich glass no kyanite formed but corundum precipitated (Fig. 7.6d, e, Tab. A7.5). This indicates that Al_2SiO_5 formation is favored in melt with cations of charge $> 1+$. The influence of La and Y on aluminosilicate melts were investigated with NMR (nuclear magnetic resonance) spectroscopy by Schaller and Stebbins (1998) who stated that with increasing concentration of both components, Al in the melt tends to undergo coordination changes from four fold to five and six fold.

Alkali rich melts, on the other hand, charge balance and stabilize tetrahedrally coordinated Al in the silicate network (Mysen et al. 1985; Mysen 2007). Although speculative, the changes in Al coordination could be one of the reasons why kyanite precipitation in the experiment is only observed in La, Ce rich glasses and why the removal of alkalies (and possibly also the infiltration of Cr, Fe, Mg, Mn, Zn, Ni etc.) in the natural sample is essential. However, the observations regarding Al_2SiO_5 formation and transient melt phases clearly require further sampling and experimentation.

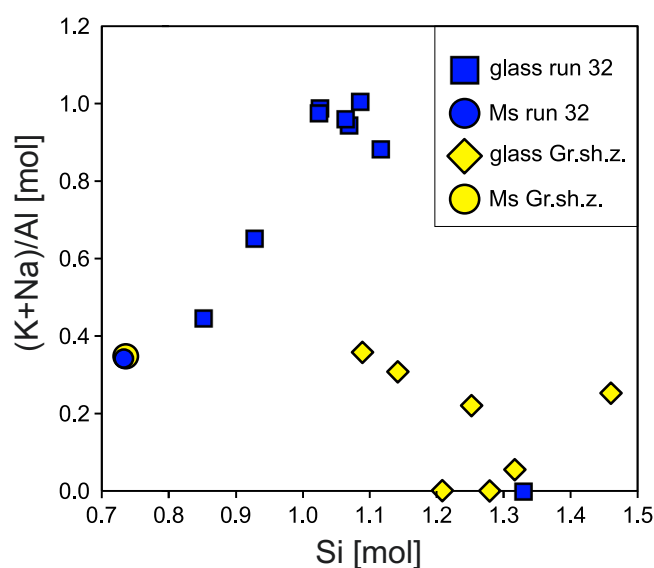


Fig. 7.5 Chemistry of glass phases produced during natural (Greiner shear-zone, Gr.sh.z.) and experimental (run 32) muscovite dehydration reactions. EDS (EMP) data acquired in glass phases (squares) and muscovite precursor (circles) of Gr.sh.z. (yellow) and products of run 32 (blue). The natural glass displays a significant loss in K, whereas the experimental glass is generally K-rich. An exception is documented in glass near or inside Crn single grains (one data point without measurable K). Data plotted in this figure are given in Tab. A7.3 (Gr.sh.z.) and Tab. 4.2 (run 32).

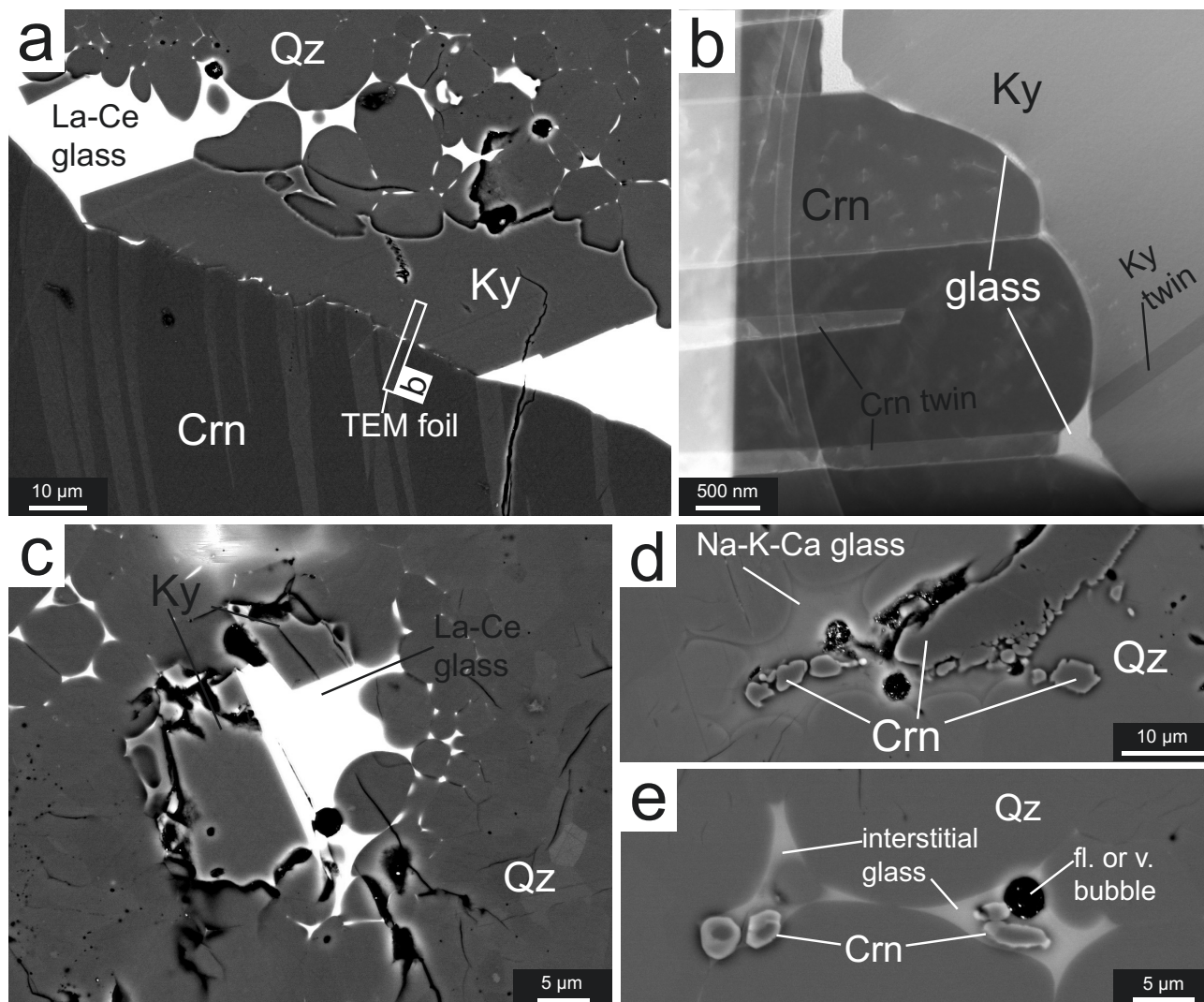


Fig. 7.6 Kyanite precipitation vs. corundum preservation (and potential precipitation) in run 5, at 1200 °C; 20 kbar; 1 day. a) BSE image (EMP) of Crn grain in Qz matrix with interstitial silicate La, Ce, Fe, Na, Mg and Cl bearing peraluminous glass; Ky grains are grown in this glass having phase boundaries with Qz or Crn. b) TEM-mode image of a foil cut along the Ky-Crn phase boundary (indicated in a). A valley and hill structure appears along the partly open Ky-Crn phase boundary; valleys in Crn are found along strongly dissolved twin individuals and often preserve glass (bright). c) BSE images (EMP) of Ky growth in La-Ce-rich glass interstice without contact to Crn, Ky grains are intergrown with highly rounded quartz grains and adapt the shape of the quartz grains. d) BSE image of Crn grains in Na, K, \pm Ca bearing peraluminous glass in Qz-Crn interstice, no Ky found in these glasses and small Crn grains appear to have been detached from the larger grain. e) BSE image of alkali glass interstice with Crn grains with no visible connection to larger grains (possible Crn precipitation). EDS results of glass analyses are given in Tab. A7.5.

With regard to Si concentrations in natural corundum and the question whether SNL formation plays any role in nature, a sample of kyanite-biotite-corundum rock from the island of Naxos (Greece) has been studied. The sample was kindly provided from the collection of Anne Feenstra at the GeoForschungs Zentrum Potsdam. Within partly decomposed kyanite, color-zoned corundum with a high inclusion density was found, which represents either corundum growth, or corundum alteration in silica-rich fluid (Fig. 7.7). Different corundum growth zones display not only Fe and Ti but also Si zonation with SiO₂ concentrations of > 0.3 wt % (Fig. 7.7, Tab. A7.6), and inclusions associated with the different zones are composed of muscovite, boehmite, fluid, and quartz (Fig. 7.7d). This study will complement the very few

other studies of silica rich natural corundum, such as hydrothermally altered quartz porphyry rocks from Tasmania containing plate shaped corundum instead of Al₂SiO₅, despite the obvious influence of fluid phases (Bottrill 1998), or the formation of hydrothermal corundum in advanced argillic alteration processes (western Thrace, Greece, Voudouris 2014).

... so in the spirit of “Science never solves a problem without creating ten more.” (G. B. Shaw) I will continue the search for new questions in this nasty system, which some justifiably won’t touch with a ten-foot pole.

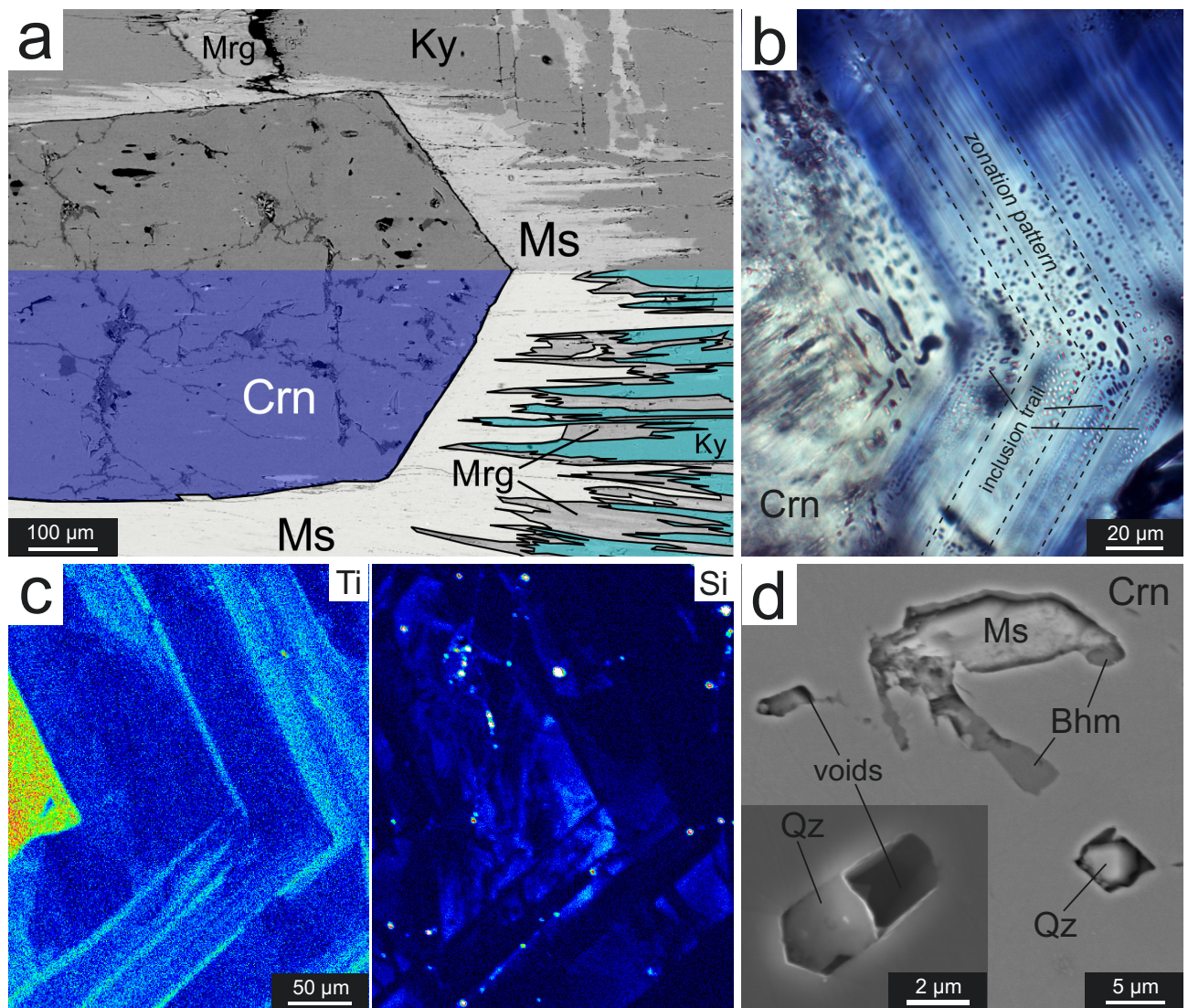


Fig. 7.7 Petrography of the corundum bearing kyanite-biotite rock from Naxos (Greece). a) Half colored BSE image of an euhedral Crn grain in muscovite (Ms), surrounded by kyanite (Ky), which is replaced by margarite (Mrg) and Ms. b) Microphotograph of the association of inclusions and blue and colorless zonation pattern in Crn. c) Element mappings of Ti and Si displaying Crn zonation pattern (mapping conditions; 20 kV, 20 nA, 100 ms dwell time). Tetravalent Ti shows an apparently reversed distribution trend with Si⁴⁺. Optically dark blue Crn zones represent areas with high TiO₂ concentrations, and colorless Crn is comparably Ti-poor. d) BSE image of Qz inclusions associated with inclusions of Ms, boehmite (Bhm) and fluid (voids). Inset shows a SE image of a Qz daughter crystal in a fluid inclusion.

“Scientifically traditions are an idiot thing!” (Rick Sanchez)

8. References

- Abart, R., Kunze, K., Milke, R., Sperb, R., and Heinrich, W. (2004) Silicon and oxygen self diffusion in enstatite polycrystals: The Milke et al. (2001) rim growth experiments revisited. *Contributions to Mineralogy and Petrology*, 147, 633–646.
- Abs-Wurmbach, I., and Langer, K. (1975) Synthetic Mn^{3+} -Kyanite and Viridine, $(Al_{2-x}Mn^{3+}_x)SiO_5$ in the System Al_2O_3 - MnO - MnO_2 - SiO_2 . *Contributions to Mineralogy and Petrology*, 49, 21–38.
- Althaus, E. (1966) Die Bildung von Pyrophyllit und Andalusit zwischen 2000 und 7000 Bar H_2O - Druck. *Naturwissenschaften*, 53, 105–106.
- Anderson, G.M., and Burnham, C.W. (1967) Reactions of quartz and corundum with aqueous chloride and hydroxide solutions at high temperatures and pressures. *American Journal of Science*, 265, 12–27.
- Anenburg, M., and Katzir, Y. (2014) Muscovite dehydration melting in Si-rich metapelites: Microstructural evidence from trondhjemitic migmatites, Roded, Southern Israel. *Mineralogy and Petrology*, 108, 137–152.
- Anovitz, L.M., Essene, E.J., Metz, G.W., Bohlen, S.R., Westrum, E.F., and Hemingway, B.S. (1993) Heat capacity and phase equilibria of almandine, $Fe_3Al_2Si_3O_{12}$. *Geochimica et Cosmochimica Acta*, 57, 4191–4204.
- Anovitz, L.M., Perkins, D., and Essene, E.J. (1991) Metastability in near-surface rocks of minerals in the system Al_2O_3 - SiO_2 - H_2O . *Clays and Clay Minerals*, 39, 225–233.
- Appel, P., Möller, A., and Schenk, V. (1998) High-pressure granulite facies metamorphism in the Pan-African belt of eastern Tanzania: P-T-t evidence against granulite formation by continent collision. *Journal of Metamorphic Geology*, 16, 491–509.
- Aramaki, S., and Roy, R. (1963) A new polymorph of Al_2SiO_5 and further studies in the system Al_2O_3 - SiO_2 - H_2O . *American Mineralogist*, 48, 1322.
- Aramaki, S., and Roy, R. (1963) A new polymorph of Al_2SiO_5 and further studies in the system Al_2O_3 - SiO_2 - H_2O . *The American Mineralogist*, 48, 1322–1347.
- Bagdasarov, H.S., Berezhkova, G. V, Govorkov, V.G., and Smirnov, A.E. (1974) Experimental investigation of the thermochemical dissolution of leucosapphire single crystals. *Journal of Crystal Growth*, 22, 61–64.
- Balconi, M. (1941) Esperienze di attacco su silicali di alluminio. *Rendiconti della Società Mineralogica Italiana*, 1, 77–82.
- Balconi, M. (1941) Sintesi della sillmanite. *Rendiconti della Società Mineralogica Italiana*, 1, 82–86.
- Barnes, J.D., Selverstone, J., and Sharp, Z.D. (2004) Interactions between serpentinite devolatilization, metasomatism and strike-slip strain localization during deep-crustal shearing in the Eastern Alps. *Journal of Metamorphic Geology*, 22, 283–300.
- Becker, K.H., Cemic, L., and Langer, K.E.O.E. (1983) Solubility of corundum in supercritical water. *Geochimica et Cosmochimica Acta*, 47, 1573–1578.
- Beitter, T., Wagner, T., and Markl, G. (2008) Formation of kyanite-quartz veins of the Alpe Sponda, Central Alps, Switzerland: Implications for Al transport during regional metamorphism. *Contributions to Mineralogy and Petrology*, 156, 689–707.
- Bell, P.M. (1963) Aluminum Silicate System: Experimental Determination of the Triple Point. *Science*, 139, 1055–1056.

- Betkowski, W.B., Harlov, D.E., and Rakovan, J.F. (2016) Hydrothermal mineral replacement reactions for an apatite-monazite assemblage in alkali-rich fluids at 300 – 600 °C and 100 MPa. *American Mineralogist*, 101, 2620–2637.
- Beukes, N.J., Dorland, H., Gutzmer, J., Nedachi, M., and Ohmoto, H. (2002) Tropical laterites life on land and the history of atmospheric oxygen in the Paleoproterozoic. *Geology*, 30, 491–494.
- Bottrill, R.S. (1998) A corundum-quartz assemblage in altered volcanic rocks, Bond Range, Tasmania. *Mineralogical Magazine*, 62, 325–332.
- Brandt, S., Klemm, R., and Okrusch, M. (2003) Ultrahigh-temperature metamorphism and multistage evolution of garnet ± orthopyroxene granulites from the proterozoic Epupa Complex, NW Namibia. *Journal of Petrology*, 44, 1121–1144.
- Bratton, R.J., and Brindley, G.W. (1962) Structure-controlled reactions in kaolinite - diaspore-boehmite clays. *Journal of the American Ceramic Society*, 45, 1689–1699.
- Brearley, A.J. (1986) An electron optical study of muscovite breakdown in pelitic xenoliths during pyrometamorphism. *Mineralogical Magazine*, 50, 385–397.
- Brearley, A.J., and Rubie, D.C. (1990) Effects of H₂O on the disequilibrium breakdown of muscovite + quartz. *Journal of Petrology*, 31, 925–956.
- Bucholz, C.E., and Ague, J.J. (2010) Fluid flow and Al transport during quartz-kyanite vein formation, Unst, Shetland Islands, Scotland. *Journal of Metamorphic Geology*, 28, 19–39.
- Burnham, C.W., Ryzhenko, B.N., and Schitel, D. (1973) Water solubility of corundum at 500–800 °C and 6 kbar. *Geochemistry International*, 10, 1374.
- Carmichael, D.M. (1969) On the mechanism of prograde metamorphic reactions in quartz-bearing pelitic rocks. *Contributions to Mineralogy and Petrology*, 20, 244–267.
- Carr, M., and Fyfe, W.S. (1960) Synthesis fields of some aluminium silicates. *Geochimica et Cosmochimica Acta*, 21, 99–109.
- Carr, R.M. (1968) The problem of quartz-corundum stability. *The American Mineralogist*, 53, 2092–2095.
- Carroll-Webb, S.A., and Walther, J. V (1988) A surface complex reaction model for the pH-dependences of corundum and kaolinite dissolution rates. *Geochimica et Cosmochimica Acta*, 52, 2609–2623.
- Cesare, B., and Grob  ty, B. (1995) Epitaxial replacement of kyanite by staurolite: a TEM study of the microstructures. *American Mineralogist*, 80, 78–86.
- Chadwick, B., Vasudev, V.N., and Hegdet, G. V (1997) The Dharwar craton, southern India, and its Late Archaean plate tectonic setting: current interpretations and controversies. *Earth and Planetary Science Letters*, 106, 249–258.
- Chatterjee, N.D., Johannes, W., and Leistner, H. (1984) The system CaO-Al₂O₃-SiO₂-H₂O: new phase equilibria data, some calculated phase relations, and their petrological applications. *Contributions to Mineralogy and Petrology*, 88, 1–13.
- Chesworth, W. (1994) Mineral metastability in the system Al₂O₃-SiO₂-H₂O: a Discussion. *Clays and Clay Minerals*, 42, 98–101.
- Chinner, G.A. (1961) The origin of sillimanite in Glen Clova, Angus. *Journal of Petrology*, 2, 312–323.
- Claeson, D.T. (1998) Coronas, reaction rims, symplectites and emplacement depth of the Rymmen gabbro, Transscandinavian Igneous Belt, southern Sweden. *Mineralogical Magazine*, 62, 743–757.
- Clark, S.P.J., Robertson, E.C., and Birch, F. (1957) Experimental determination of kyanite-sillimanite equilibrium relations at high temperatures and pressures. *American Journal of Science*, 255, 628–640.

- Coes, L. (1955) High-pressure minerals. *Journal of the American Ceramic Society*, 38, 298.
- Cole, J., Hacker, B., Ratschbacher, L., Dolan, J., Seward, G., Frost, E., and Frank, W. (2007) Localized ductile shear below the seismogenic zone: Structural analysis of an exhumed strike-slip fault, Austrian Alps. *Journal of Geophysical Research: Solid Earth*, 112.
- Connolly, J.A.D. (2009) The geodynamic equation of state: What and how. *Geochemistry Geophysics Geosystems*, 10, 1–19.
- Crawford, M.L., and Hollister, L.S. (1986) Metamorphic Fluids: The Evidence from Fluid Inclusions. In J. V Walther and B.J. Wood, Eds., *Fluid-rock interactions during metamorphism* pp. 1–35. Springer, New York, NY.
- Dai, Z.R., Bradley, J.P., Joswiak, D.J., Brownlee, D.E., Hill, H.G.M., and Genge, M.J. (2010) Possible in situ formation of meteoritic nanodiamonds in the early Solar System. *Nature*, 418, 157–159.
- Daniel, C.G., Hollister, L.S., Parrish, R.R., and Grujic, D. (2003) Exhumation of the main central thrust from lower crustal depths, eastern Buthan Himalaya, 21, 317–334.
- Das, S., and Mohanty, J.K. (2014) Characterisation of eluvial corundum (ruby) from Kermunda, Kalahandi district, Odisha, India. *Geology & Geosciences*, 3, 2–6.
- Davies, T.C., Friedrich, G., and Wiechowski, A. (1989) Geochemistry and mineralogy of laterites in the Sula Mountains greenstone belt, Lake Sonfon gold district, Sierra Leone. *Journal of Geochemical Exploration*, 32, 75–98.
- Day, H.W. (1973) The high temperature stability of muscovite plus quartz. *American Mineralogist*, 58, 255–262.
- de Jong, B.H.W.S., Schramm, C.M., and Parziale, V.E. (1983) Polymerization of silicate and aluminate tetrahedra in glasses, melts, and aqueous solutions-IV. Aluminum coordination in glasses and aqueous solutions and comments on the aluminum avoidance principle. *Geochimica et Cosmochimica Acta*, 47, 1223–1236.
- DeVries, R.C. (1964) The system Al_2SiO_5 at high temperatures and pressures. *Journal of American Ceramics Society*, 47, 230–237.
- Dey, S. (2013) Evolution of Archaean crust in the Dharwar craton: The Nd isotope record. *Precambrian Research*, 227, 227–246.
- Diedrich, T., Dybowska, A., Schott, J., Valsami-Jones, E., and Oelkers, E.H. (2012) The dissolution rates of SiO_2 nanoparticles as a function of particle size. *Environmental Science & Technology*, 46, 4909–4915.
- Essene, E.J., Anovitz, L.M., and Perkins, D. (1994) Mineral metastability in the system Al_2O_3 - SiO_2 - H_2O : A reply. *Clays and Clay Minerals*, 42, 102–105.
- Feenstra, A., Sämann, S., and Wunder, B. (2005) An experimental study of Fe-Al solubility in the system corundum-hematite up to 40 kbar and 1300 °C. *Journal of Petrology*, 46, 1881–1892.
- Ferguson, C.C., and Al-Ameen, S.I. (1985) Muscovite breakdown and corundum growth at anomalously low fH_2O : a study of contact metamorphism and convective fluid movement around the Omei granite, Connemara, Ireland. *Mineralogical Magazine*, 49, 505–514.
- Fisher, M.L., Colic, M., Rao, M.P., and Lange, F.F. (2001) Effect of silica nanoparticle size on the stability of alumina/silica suspensions. *Journal of American Ceramics Society*, 84, 713–718.
- Fritz, H., Tenczer, V., Hauenberger, C.A., Wallbrecher, E., Hoinkes, G., Muhongo, S., and Mogessie, A. (2005) Central Tanzanian tectonic map: A step forward to decipher proterozoic structural events in the East African Orogen. *Tectonics*, 24, 1–26.
- Fritz, H., Tenczer, V., Hauenberger, C., Wallbrecher, E., and Muhongo, S. (2009) Hot granulite nappes - Tectonic styles and thermal evolution of the Proterozoic granulite belts in East Africa. *Tectonophysics*, 477, 160–173.

- Fusswinkel, T., Wagner, T., Wenzel, T., Wälle, M., and Lorenz, J. (2014) Red bed and basement sourced fluids recorded in hydrothermal Mn-Fe-As veins, Sailauf (Germany): A LA-ICPMS fluid inclusion study. *Chemical Geology*, 363, 22–39.
- Gallien, F., Mogessie, A., Hauzenberger, C.A., Bjerg, E., Delpino, S., and De, B.C. (2012) On the origin of multi-layer coronas between olivine and plagioclase at the gabbro – granulite transition, Valle Fértil–La Huerta Ranges, San Juan Province, Argentina. *Journal of Metamorphic Geology*, 30, 281–301.
- Ganguly, J. (2002) Diffusion kinetics in minerals: Principles and applications to tectono-metamorphic processes. *EMU Notes in Mineralogy*, 4, 271–309.
- García-Casco, A., Sánchez-Navas, A., and Torres-Roldán, L. (1993) Disequilibrium decomposition and breakdown of muscovite in high P-T gneisses, Betic alpine belt (southern Spain). *American Mineralogist*, 78, 158–177.
- Giardini, A.A., Kohn, J.A., Eckart, D.W., and Tydings, J.E. (1961) The formation of coesite and kyanite from pyrophyllite at very high pressures and high temperatures. *The American Mineralogist*, 46, 976–982.
- Golani, P.R. (1989) Sillimanite-corundum deposits of Sonapahar, Meghalaya, India: a metamorphosed Precambrian paleosol. *Precambrian Research*, 43, 175–189.
- Grant, A. (1986) The isocon diagram - a simple solution to Gresens' equation for metasomatic alteration. *Economic Geology*, 81, 1976–1982.
- Grant, T.B., Milke, R., Wunder, B., Wirth, R., and Rhede, D. (2014) Experimental study of phlogopite reaction rim formation on olivine in phonolite melts: Kinetics, reaction rates, and residence times. *American Mineralogist*, 99, 2211–2226.
- Grapes, R. (2011) Experimental breakdown of staurolite + inclusions of albite and muscovite at 800 °C and 0.1 GPa. *Mineralogical Magazine*, 75, 117–133.
- Gresens, R.L. (1967) Composition–volume relations of metasomatism. *Chemical Geology*, 2, 47–65.
- Gresens, R.L. (1971) Application of hydrolysis equilibria to the genesis of pegmatite and kyanite deposits in Northern New Mexico. *The Mountain Geologist*, 8.
- Guiraud, M., Kienast, J.R., and Ouzegane, K. (1996) Corundum-quartz bearing assemblage in the Ihouhaouene area (In Ouzal, Algeria). *Journal of Metamorphic Geology*, 14, 754–762.
- Hanson, G.N., Krogstad, E.J., and Rajamani, V. (1988) Tectonic setting of the Kolar schist belt, Karnataka, India. *Geological Society of India*, 31, 40–42.
- Hariya, Y., and Arima, M. (1975) Kyanite-sillimanite Transition with Excess Quartz and Corundum. *Journal of the Faculty of Science, Hokkaido University*, 16, 357–366.
- Harlov, D.E., and Newton, R.C. (1993) Reversal of the metastable kyanite + corundum + quartz and andalusite + corundum + quartz equilibria and the enthalpy of formation of kyanite and andalusite. *American Mineralogist*, 78, 594–600.
- Harlov, D.E., and Milke, R. (2002) Stability of corundum + quartz relative to kyanite and sillimanite at high temperature and pressure. *American Mineralogist*, 87, 424–432.
- Harlov, D.E., Milke, R., and Gottschalk, M. (2008) Metastability of sillimanite relative to corundum and quartz in the kyanite stability field: Competition between stable and metastable reactions. *American Mineralogist*, 93, 608–617.
- Harlov, D.E., Wirth, R., and Förster, H.J. (2005) An experimental study of dissolution-reprecipitation in fluorapatite: Fluid infiltration and the formation of monazite. *Contributions to Mineralogy and Petrology*, 150, 268–286.
- Harlow, G.E., and Bender, W. (2013) A study of ruby (corundum) compositions from the Mogok Belt, Myanmar: Searching for chemical fingerprints. *American Mineralogist*, 98, 1120–1132.

- Harris, N.B.W., Caddick, M., Kosler, J., Goswami, S., Vance, D., and Tindle, A.G. (2004) The pressure-temperature-time path of migmatites from the Sikkim Himalaya. *Journal of Metamorphic Geology*, 22, 249–264.
- Heimann, A.D., and Spry, P.A.U.L.G. (2006) Coronas, symplectitic textures, and reactions involving aluminous minerals in gedrite-cordierite-garnet gneiss from Evergreen, Front Range, Colorado. *the Canadian Mineralogist*, 44, 1025–1044.
- Heinrich, E.W. (1955) Cordierite in pegmatite near Micanite, Colorado. *American Mineralogist*, 35, 173–184.
- Hemingway, B.S. (1992) On the Al_2SiO_5 triple point and the natural occurrence of two Al_2SiO_5 polymorphs under the same P-T conditions. Open-file report, U.S. Geological Survey.
- Hemley, J.J., Montoya, J.W., Marinenko, J.W., and Luce, R.W. (1980) Equilibria in the system $\text{Al}_2\text{O}_3\text{-SiO}_2\text{-H}_2\text{O}$ and some general implications for alteration/ mineralization processes. *Economic Geology*, 75, 210–228.
- Hicks, T.L., and Secco, R.A. (1997) Dehydration and decomposition of pyrophyllite at high pressures: electrical conductivity and X-ray diffraction studies to 5 GPa. *Canadian Journal of Earth Sciences*, 34, 875–882.
- Hochella, M.F.J. (2008) Nanogeoscience: From origins to cutting-edge applications. *Elements*, 4, 373–380.
- Holdaway, M.J. (1971) Stability of andalusite and the aluminum silicate phase diagram. *American Journal of Science*, 271, 97–131.
- Holdaway, M.J., and Mukhopadhyay, B. (1993) A reevaluation of the stability relations of andalusite: Thermochemical data and phase diagram for the aluminum silicates. *American Mineralogist*, 78, 298–315.
- Holland, T.J.B., and Powell, R. (2011) An improved and extended internally consistent thermodynamic dataset for phases of petrological interest, involving a new equation of state for solids. *Journal of Metamorphic Geology*, 29, 333–383.
- Horrocks, P.C. (1983) A corundum and sapphirine paragenesis from the Limpopo Mobile Belt, southern Africa. *Journal of Metamorphic Geology*, 1, 13–23.
- Huang, W.L., and Wyllie, P.J. (1974) Melting relations of muscovite with quartz and sanidine in the $\text{K}_2\text{O-Al}_2\text{O}_3\text{-SiO}_2\text{-H}_2\text{O}$ system to 30 kilobars and an outline of paragonite melting relations. *American Journal of Science*, 274, 378–395.
- Hughes, R.W., Pardieu, V., Soubiraa, G., Rogers, M., Chitty, W., Chitty, M., and Brunot, P. (2011) Downtown: Gem hunting in central & southern Tanzania. <http://www.ruby-sapphire.com/tanzania-ruby-sapphire-spinel.htm>.
- Iaccarino, S., Montomoli, C., Carosi, R., Massonne, H.-J., Langone, A., and Visonà, D. (2015) Pressure–temperature–time–deformation path of kyanite-bearing migmatitic paragneiss in the Kali Gandaki valley (Central Nepal): Investigation of Late Eocene–Early Oligocene melting processes. *Lithos*, 231, 103–121.
- Jayananda, M., Kano, T., Peucat, J.J., and Channabasappa, S. (2008) 3.35 Ga komatiite volcanism in the western Dharwar craton, southern India: Constraints from Nd isotopes and whole-rock geochemistry. *Precambrian Research*, 162, 160–179.
- Jayananda, M., Peucat, J.J., Chardon, D., Rao, B.K., Fanning, C.M., and Corfu, F. (2013) Neoarchean greenstone volcanism and continental growth, Dharwar craton, southern India: Constraints from SIMS U-Pb zircon geochronology and Nd isotopes. *Precambrian Research*, 227, 55–76.
- Jöns, N., and Schenk, V. (2004) Petrology of whiteschists and associated rocks at Mautia Hill (Tanzania): Fluid infiltration during high-grade metamorphism? *Journal of Petrology*, 45, 1959–1981.
- Kanzaki, Y., and Murakami, T. (2016) Estimates of atmospheric O_2 in the Paleoproterozoic from paleosols. *Geochimica et Cosmochimica Acta*, 174, 263–290.

- Karmakar, S., and Schenk, V. (2015) Neoproterozoic UHT Metamorphism and Paleoproterozoic UHT Reworking at Uweinat in the East Sahara Ghost Craton, SW Egypt: Evidence from Petrology and Texturally Controlled in situ Monazite Dating. *Journal of Petrology*, 56, 1703–1742.
- Kato, M., Hiroi, Y., Harlov, D.E., Satish-Kumar, M., and Hokada, T. (2011) Metastable corundum + quartz + andalusite association in pelitic granulite from the Kerala Khondalite Belt, southern India. *Journal of Mineralogical and Petrological Sciences*, 106, 195–203.
- Keller, L.M., Wirth, R., Rhede, D., Kunze, K., and Abart, R. (2008) Asymmetrically zoned reaction rims: Assessment of grain boundary diffusivities and growth rates related to natural diffusion-controlled mineral reactions. *Journal of Metamorphic Geology*, 26, 99–120.
- Kennedy, G.C. (1959) Phase relations in the system $\text{Al}_2\text{O}_3\text{-H}_2\text{O}$ at high temperatures and pressures. *American Journal of Science*, 257, 563–573.
- Kerrick, R., Fyfe, W.S., Barnett, R.L., Blair, B.B., and Willmore, L.M. (1988) Reply to: “A discussion of corundum, Cr-muscovite rocks at O’Briens, Zimbabwe: the conjunction of hydrothermal desilicification and LIL-element enrichment-geochemical and isotopic evidence.” *Contributions to Mineralogy and Petrology*, 100, 555–559.
- Kerrick, R., Fyfe, W.S., Barnett, R.L., Blair, B.B., and Willmore, L.M. (1987) Corundum, Cr-muscovite rocks at O’Briens, Zimbabwe: the conjunction of hydrothermal desilicification and LIL-element enrichment - geochemical and isotopic evidence. *Contributions to Mineralogy and Petrology*, 95, 481–498.
- Kerrick, D.M., Ed. (1990) *The Al_2SiO_5 Polymorphs*, Volume 22., 406 p. Mineralogical Society of America.
- Kerrick, D.M. (1972) Experimental determination of muscovite + quartz stability with $P_{\text{H}_2\text{O}} < P_{\text{total}}$. *American Journal of Science*, 272, 946–958.
- Kihle, J., Harlov, D.E., Frigaard, O., and Jamtveit, B. (2010) Epitaxial quartz inclusions in corundum from a sapphirine-garnet boudin, Bamble Sector, SE Norway: $\text{SiO}_2\text{-Al}_2\text{O}_3$ miscibility at high P-T dry granulite facies conditions. *Journal of Metamorphic Geology*, 28, 769–784.
- Klein-bendavid, O., Pettke, T., and Kessel, R. (2011) Chromium mobility in hydrous fluids at upper mantle conditions. *Lithos*, 125, 122–130.
- Kogure, T., Ilge, M., Kameda, J., Yamagishi, A., Miyawaki, R., and Kitagawa, R. (2006) Stacking structures in pyrophyllite revealed by high-resolution transmission electron microscopy (HRTEM). *American Mineralogist*, 91, 1293–1299.
- Kohn, M.J., and Penniston-Dorland, S.C. (2017) Diffusion: obstacles and opportunities in petrochronology. In *Reviews in Mineralogy & Geochemistry Vol. 83*, pp. 103–152. Mineralogical Society of America.
- Koshimoto, S., Tsunogae, T., and Santosh, M. (2004) Sapphirine and corundum bearing ultrahigh temperature rocks from the Palghat Cauvery Shear System, southern India. *Journal of Mineralogical and Petrological Sciences*, 99, 298–310.
- Lacmann, R., Franke, W., Heimann, R., and Freien, D. (1974) The dissolution forms of single crystal spheres 1. Theory for the molecular-kinetics interpretation. *Journal of Crystal Growth*, 26, 107–116.
- Lasaga, A.C. (2014) *Kinetic theory in the earth sciences*, 822 p. Princeton University Press.
- Lee, J.H., and Guggenheim, S. (1981) Single crystal X-ray refinement of pyrophyllite-1Tc. *American Mineralogist*, 66, 350–357.
- Lefebvre, A. (1982) Lattice Defects in Three Structurally Related Minerals: Kyanite, Yoderite and Staurolite. *Physics and Chemistry of Minerals*, 8, 251–256.
- Lewis, J., Schwarzenbach, D., and Flack, H.D. (1982) Electric field gradients and charge density in corundum, $\alpha\text{-Al}_2\text{O}_3$. *Acta Crystallographica*, A38, 733–739.

- Lucassen, F., Franz, G., Dulski, P., Romer, R.L., and Rhede, D. (2011) Element and Sr isotope signatures of titanite as indicator of variable fluid composition in hydrated eclogite. *Lithos*, 121, 12–24.
- Lucassen, F., Dulski, P., Abart, R., Franz, G., Rhede, D., and Romer, R.L. (2010) Redistribution of HFSE elements during rutile replacement by titanite. *Contributions to Mineralogy and Petrology*, 160, 279–295.
- Lucassen, F., Franz, G., and Rhede, D. (2012) Small-scale transport of trace elements Nb and Cr during growth of titanite: An experimental study at 600 °C, 0.4 GPa. *Contributions to Mineralogy and Petrology*, 164, 987–997.
- Lucassen, F., Franz, G., Wirth, R., Weise, M., and Hertwig, A. (2012) The morphology of the reaction front of the dissolution-precipitation reaction rutile + wollastonite = titanite in time series experiments at 600 °C / 400 MPa. *American Mineralogist*, 97, 828–839.
- Madden, A.S., Hochella, M.F.J., and Luxton, T.P. (2006) Insights for size-dependent reactivity of hematite nanomineral surfaces through Cu⁺² sorption. *Geochimica et Cosmochimica Acta*, 70, 4095–4104.
- Manning, C.E. (2007) Solubility of corundum + kyanite in H₂O at 700 °C and 10 kbar: evidence for Al-Si complexing at high pressure and temperature. *Geofluids*, 7, 258–269.
- Manning, C. (2004) Polymeric silicate complexing in aqueous fluids at high pressure and temperature, and its implications for water-rock interaction. *Water-Rock Interaction*, 45–49.
- Manning, C.E. (2006) Mobilizing aluminum in crustal and mantle fluids. *Journal of Geochemical Exploration*, 89, 251–253.
- McKie, D. (1959) Yoderite, a new hydrous magnesium iron aluminosilicate from Mautia Hill, Tanganyika. *Mineralogical Magazine*, 32, 282–307.
- McLelland, J., Morrison, J., Selleck, B., Cunningham, B., Olson, C., and Schmidt, K. (2002) Hydrothermal alteration of late- to post-tectonic Lyon Mountain Granitic Gneiss, Adirondack Mountains, New York: Origin of quartz-sillimanite segregations, quartz-albite lithologies, and associated Kiruna-type low-Ti Fe-oxide deposits. *Journal of Metamorphic Geology*, 20, 175–190.
- Mibe, K., Chou, I.-M., and Bassett, W.A. (2008) In situ Raman spectroscopic investigation of the structure of subduction-zone fluids. *Journal of Geophysical Research*, 113, 1–8.
- Michel-Levy, M.C. (1950) Reproduction artificielle de la sillimanite. *Comptes Rendus Chimie*, 230, 2213.
- Migdisov, A.A., Williams-Jones, A.E., van Hinsberg, V., and Salvi, S. (2011) An experimental study of the solubility of baddeleyite (ZrO₂) in fluoride-bearing solutions at elevated temperature. *Geochimica et Cosmochimica Acta*, 75, 7426–7434.
- Milisenda, C.C. (2003) Gemmologie Aktuell: Ruby-fuchsite-kyanite rock from India. *Zeitschrift der Deutschen Gemmologischen Gesellschaft*, 52, 124–125.
- Momma, K., and Izumi, F. (2011) VESTA 3 for three-dimensional visualization of crystal, volumetric and morphology data. *Journal of Applied Crystallography*, 44, 1272–1276.
- Mookherjee, M., Keppler, H., and Manning, C.E. (2014) Aluminum speciation in aqueous fluids at deep crustal pressure and temperature. *Geochimica et Cosmochimica Acta*, 133, 128–141.
- Morey, G.W. (1957) The solubility of solids in gases. *Economic Geology*, 52, 225–251.
- Motoyoshi, Y., Hensen, B.J., and Matsueda, H. (1990) Metastable growth of corundum adjacent to quartz in a spinel-bearing quartzite from the Archaean Napier Complex, Antarctica. *Journal of Metamorphic Geology*, 8, 125–130.
- Mouri, H., Andreoli, M.A.G., Kienast, J.R., Guiraud, M., and de Waal, S.A. (2003) First occurrence of the rare “corundum + quartz” assemblage in the high-grade zone from the Namaqualand Metamorphic Complex, South Africa: evidence for higher-P, T metamorphism? *Mineralogical Magazine*, 67, 1015–1021.

- Mouri, H., Guiraud, M., and Osanai, Y. (2004) Review on “corundum + quartz” assemblage in nature: Possible indicator of ultra high temperature conditions? *Journal of Mineralogical and Petrological Sciences*, 99, 159–163.
- Mukherjee, R., Mondal, S.K., Frei, R., Rosing, M.T., Waight, T.E., Zhong, H., and Kumar, G.R.R. (2012) The 3.1Ga Nuggihalli chromite deposits, Western Dharwar craton (India): Geochemical and isotopic constraints on mantle sources, crustal evolution and implications for supercontinent formation and ore mineralization. *Lithos*, 155, 392–409.
- Mukhopadhyay, D. (1986) Structural pattern in the Dharwar craton. *Journal of Geology*, 94, 167–186.
- Müller, A., van den Kerkhof, A.M., and Broekmans, M.A.T.M. (2011) Trace element content and optical cathodoluminescence of kyanite. In 10th International Congress for Applied Mineralogy (ICAM) pp. 453–461. Trondheim, Norway.
- Müller, A., van den Kerkhof, A.M., Selleck, B., and Broekmans, M.A.T.M. (2016) Trace element composition and cathodoluminescence of kyanite and its petrogenetic implications. *Contributions to Mineralogy and Petrology*, 171, 1–17.
- Murakami, T., Utsunomiya, S., Imazu, Y., and Prasad, N. (2001) Direct evidence of late Archean to early Proterozoic anoxic atmosphere from a product of 2.5 Ga old weathering. *Earth and Planetary Science Letters*, 184, 523–528.
- Mysen, B.O., Virgo, D., and Seifert, F.A. (1985) Relationships between properties and structure of aluminosilicate melts. *American Mineralogist*, 70, 88–105.
- Mysen, B.O. (2007) The solution behavior of H₂O in peralkaline aluminosilicate melts at high pressure with implications for properties of hydrous melts. *Geochimica et Cosmochimica Acta*, 71, 1820–1834.
- Nabelek, P.I. (1997) Black Hills, South Dakota: A perspective on the mobility of Al in high-grade metamorphic rocks, 995–998.
- Naqvi, S.M., Sawkar, R.H., Subba Rao, D. V, Govil, P.K., and Ganeswar Rao, T. (1988) Geology, geochemistry and tectonic setting of Archaean greywackes from Karnataka nucleus, India. *Precambrian Research*, 39, 193–216.
- Nassau, K. (1981) Heat treating ruby and sapphire: technical aspects. *Gems & Gemology*, 121–131.
- Navrotsky, A., Mazeina, L., and Majzlan, J. (2008) Size-driven structural and thermodynamic complexity in iron oxides. *Science*, 319, 1635–1638.
- Newton, R.C. (1969) Some high-pressure hydrothermal experiments on severely ground kyanite and sillimanite. *American Journal of Science*, 267, 278–284.
- Newton, R.C., and Manning, C.E. (2008) Solubility of corundum in the system Al₂O₃-SiO₂-H₂O-NaCl at 800 °C and 10 kbar. *Chemical Geology*, 249, 250–261.
- Newton, R.C., and Manning, C.E. (2006) Solubilities of corundum, wollastonite and quartz in H₂O-NaCl solutions at 800°C and 10 kbar: Interaction of simple minerals with brines at high pressure and temperature. *Geochimica et Cosmochimica Acta*, 70, 5571–5582.
- Norlander, B.H., Whitney, D.L., Teyssier, C., and Vanderhaeghe, O. (2002) Partial melting and decompression of the Thor-Odin dome, Shuswap metamorphic core complex, Canadian Cordillera. *Lithos*, 61, 103–125.
- Nyman, M.W., Pattison, D.R.M., and Ghent, E.D. (1995) Melt extraction during formation of K-feldspar plus sillimanite migmatites, West of Revelstoke, British-Columbia. *Journal of Petrology*, 36, 351–372.
- Oelkers, E.H., and Schott, J. (1999) Experimental study of kyanite dissolution rates as a function of chemical affinity and solution composition. *Chemical Geology*, 63, 785–797.
- Ogilvie, P., and Gibson, R.L. (2017) Arrested development – a comparative analysis of multilayer corona textures in high-grade metamorphic rocks. *Solid Earth*, 8, 93–135.

- Olsen, S.N. (1987) The composition and role of the fluid in migmatites: a fluid inclusion study of the Front Range rocks. *Contributions to Mineralogy and Petrology*, 96, 104–120.
- Outhuis, J.H.M. (1989) Hydrothermal andalusite and corundum in a potassic alteration zone around a proterozoic gabbro-tonalite-granite intrusion NE of Persberg, Central Sweden. *Mineralogy and Petrology*, 40, 1–16.
- Pascal, M.L., and Anderson, G.M. (1989) Speciation of Al, Si, and K in supercritical solutions; Experimental study and interpretation. *Geochimica et Cosmochimica Acta*, 53, 1843–1855.
- Pattison, D.R.M. (2001) Instability of Al_2SiO_5 “triple-point” assemblages in muscovite plus biotite plus quartz-bearing metapelites, with implications. *American Mineralogist*, 86, 1414–1422.
- Pichamuthu, C.S. (1935) The Conglomerates and grits of Kaldurga, Kadur District, Mysore. *Proceedings of the Indian Academy of Sciences - Section B*, 2, 254–279.
- Pokrovski, G.S., Schott, J., Harrichoury, J.C., and Sergeev, A.S. (1996) The stability of aluminum silicate complexes in acidic solutions from 25 to 150°C. *Geochimica et Cosmochimica Acta*, 60, 2495–2501.
- Pollok, K., Putnis, C. V, and Putnis, A. (2011) Mineral replacement reactions in solid solution-aqueous solution systems: Volume changes, reactions paths and end-points using the example of model salt systems. *American Journal of Science*, 311, 211–236.
- Putnis, A. (2002) Mineral replacement reactions: from macroscopic observations to microscopic mechanisms. *Mineralogical Magazine*, 66, 689–708.
- Putnis, A., and Austrheim, H. (2010) Fluid-induced processes: metasomatism and metamorphism. *Geofluids*, 10, 254–269.
- Putnis, A., and Putnis, C. V (2007) The mechanism of reequilibration of solids in the presence of a fluid phase. *Journal of Solid State Chemistry*, 180, 1783–1786.
- Putnis, C. V., and Mezger, K. (2004) A mechanism of mineral replacement: Isotope tracing in the model system $\text{KCl-KBr-H}_2\text{O}$. *Geochimica et Cosmochimica Acta*, 68, 2839–2848.
- Ragnarsdottir, K. V, and Walther, J. V (1985) Experimental determination of corundum solubilities in pure water between 400–700 °C and 1–3 kbar. *Geochimica et Cosmochimica Acta*, 48, 159–176.
- Raith, M., Raase, P., Ackermann, D., and Lal, R.K. (1982) The Archean Craton of Southern India: Metamorphic evolution and P-T conditions. *Geologische Rundschau*, 71, 280–290.
- Raith, M.M., and Schumacher, R. (2012) Ruby-fuchsite rocks from the Kodagu District, Southern India. In *International Conference on Mineralogy and Museums p. PS1-P04*.
- Rauchenstein-Martinek, K., Wagner, T., Wälle, M., and Heinrich, C.A. (2014) Gold concentrations in metamorphic fluids: A LA-ICPMS study of fluid inclusions from the Alpine orogenic belt. *Chemical Geology*, 385, 70–83.
- Read, H.H. (1932) On quartz-kyanite-rocks in Unst, Shetland Islands, and their bearing on metamorphic differentiation. *Mineralogical Magazine*, 23, 317–328.
- Reich, M., Satoshi, U., Kesler, S.E., Wang, L., Ewing, R.C., and Becker, U. (2006) Thermal behavior of metal nanoparticles in geologic materials. *Geology*, 34, 1033–1036.
- Reich, M., Zúñiga, A., Amigo, Á., Vargas, G., Morata, D., Palacios, C., Parada, M.Á., and Garreaud, R.D. (2009) Formation of cristobalite nanofibers during explosive volcanic eruptions. *Geology*, 37, 435–438.
- Rimstidt, J.D., and Barnes, H.L. (1980) The kinetics of silica-water reactions. *Geochimica et Cosmochimica Acta*, 44, 1683–1699.
- Roy, D.M. (1954) Hydrothermal synthesis of andalusite. *American Mineralogist*, 39, 140–143.

- Saalfeld, H., and Junge, W. (1983) Thermal decomposition of kyanite single crystals. *Tschermaks Mineralogische und Petrographische Mitteilungen*, 26, 17–26.
- Salvi, S., Pokrovski, G.S., and Schott, J. (1998) Experimental investigation of aluminum-silica aqueous complexing at 300°C. *Chemical Geology*, 151, 51–67.
- Sanchez-Navas, A. (1999) Sequential kinetics of a muscovite-out reaction: A natural example. *American Mineralogist*, 84, 1270–1286.
- Schaller, T., and Stebbins, J. (1998) The Structural Role of Lanthanum and Yttrium in Aluminosilicate Glasses : A ^{27}Al and ^{17}O MAS NMR Study. *J. Phys. Chem. B*, 102, 10690–10697.
- Schilling, F., and Wunder, B. (2004) Temperature distribution in piston-cylinder assemblies: Numerical simulations and laboratory experiments. *European Journal of Mineralogy*, 16, 7–14.
- Schmid, S.M., Scharf, A., Handy, M.R., and Rosenberg, C.L. (2013) The Tauern Window (Eastern Alps, Austria): A new tectonic map, with cross-sections and a tectonometamorphic synthesis. *Swiss Journal of Geosciences*, 106, 1–32.
- Schmidt, M.W., Poli, S., Comodi, P., and Zanazzi, P.F. (1997) High-pressure behavior of kyanite: Decomposition of kyanite into stishovite and corundum. *American Mineralogist*, 82, 460–466.
- Schneider, H., and Komarneni, S. (2005) *Mullite*, 487 p. Wiley VCH.
- Schreyer, W. (1982) Fuchsite-aluminium silicate rocks in archaean greenstone belts: Are they metamorphosed alunite deposits? *Geologische Rundschau*, 71, 347–360.
- Schreyer, W. (1988) A discussion of: “Corundum, Cr muscovite rocks at O’Briens, Zimbabwe: the conjunction of hydrothermal desilicification and LIL-element enrichment-geochemical and isotopic evidence ” by Kerrich et al.”. *Contributions to Mineralogy and Petrology*, 100, 552–554.
- Schreyer, W., Werding, G., and Abraham, K. (1981) Corundum-fuchsite rocks in greenstone belts of Southern Africa: Petrology, geochemistry, and possible origin. *Journal of Petrology*, 22, 191–231.
- Schultze, D., Loges, A., and Franz, G. (2014) Conditions of kyanite formation from fluid in an alpine shear zone. In *Geophysical Research Abstracts*, EGU General Assembly Vol. 16, p. 15190.
- Schultze, D., and Franz, G. (2014) Incorporation of quartz into corundum via aqueous fluids: experimental and natural examples (FLU-T08). In *Annual Meeting Deutsche Mineralogische Gesellschaft*, Jena p. 283.
- Scott, B., and Carruthers, T.G. (1969) Hydrothermal reactions and crystallographic relationships found during the reactive hot pressing of kaolinites. *Clay Minerals*, 8, 21–28.
- Sharma, R. (2010) *Cratons and Fold Belts of India*, 263-290 p. *Lecture Notes in Earth Sciences* Vol. 127.
- Shaw, R.K., and Arima, M. (1998) A corundum – quartz assemblage from the Eastern Ghats Granulite Belt, India: evidence for high P – T metamorphism? *Journal of Metamorphic Geology*, 16, 189–196.
- Shen, A.H., and Keppler, H. (1997) Direct observation of complete miscibility in the albite–H₂O system. *Nature*, 385, 710–712.
- Siesmayer, B., Heimann, R., and Franke, W. (1975) The dissolution forms of single crystal spheres. *Journal of Crystal Growth*, 28, 157–161.
- Smirnov, A.E., Urusovskaya, A.A., Govorkov, V.G., and Berezhkova, G. V (1981) Thermochemical dissolution of corundum. *Journal of Materials Science*, 16, 1071–1080.
- Sommer, H., Kröner, A., Hauzenberger, C., Muhongo, S., and Wingate, M.T.D. (2003) Metamorphic petrology and zircon geochronology of high-grade rocks from the central Mozambique Belt of Tanzania: crustal recycling of

- Archean and Palaeoproterozoic material during the Pan-African orogeny. *Journal of metamorphic Geology*, 21, 915–934.
- Sommer, H., Hauzenberger, C., Kröner, A., and Muhongo, S. (2008) Isothermal decompression history in the “Western Granulite” terrain, central Tanzania: Evidence from reaction textures and trapped fluids in metapelites. *Journal of African Earth Sciences*, 51, 123–144.
- Sommer, H., Kröner, A., Hauzenberger, C., and Muhongo, S. (2005) Reworking of archaean and Palaeoproterozoic crust in the Mozambique belt of central Tanzania as documented by SHRIMP zircon geochronology. *Journal of African Earth Sciences*, 43, 447–463.
- Sommer, H., Kröner, A., Muhongo, S., and Hauzenberger, C. (2005) SHRIMP zircon ages for post-Usagaran granitoid and rhyolitic rocks from the Palaeoproterozoic terrain of southwestern Tanzania. *South African Journal of Geology*, 108, 247–256.
- Spear, F.S., Kohn, M.J., and Cheney, J.T. (1999) P-T paths from anatectic pelites. *Contributions to Mineralogy and Petrology*, 134, 17–32.
- Srikantappa, C., Raith, M., and Ackermann, D. (1985) High-grade regional metamorphism of ultramafic and mafic rocks from the archaean Sagur terrane, Karnataka, South India. *Precambrian Research*, 30, 189–219.
- Stout, M.Z., Crawford, M.L., and Ghent, E.D. (1986) Pressure-temperature and evolution of fluid compositions of Al_2SiO_5 -bearing rocks, Mica Creek, B.C., in light of fluid inclusion data and mineral equilibria. *Contributions to Mineralogy and Petrology*, 92, 236–247.
- Suchanek, W.L., and Garcés, J.M. (2010) Hydrothermal synthesis of novel alpha alumina nano-materials with controlled morphologies and high thermal stabilities. *CrystEngComm*, 2996–3002.
- Sutherland, F., Zaw, K., Meffre, S., Yui, T.-F., and Thu, K. (2014) Advances in Trace Element “Fingerprinting” of Gem Corundum, Ruby and Sapphire, Mogok Area, Myanmar. *Minerals*, 5, 61–79.
- Tagirov, B., and Schott, J. (2001) Aluminum speciation in crustal fluids revisited. *Geochimica et Cosmochimica Acta*, 65, 3965–3990.
- Tagirov, B., Schott, J., Harrichourry, J.C., and Salvi, S. (2002) Experimental study of aluminum speciation in fluoride-rich supercritical fluids. *Geochimica et Cosmochimica Acta*, 66, 2013–2024.
- Ter Heege, J.H., and Renner, J. (2007) In situ impedance spectroscopy on pyrophyllite and CaCO_3 at high pressure and temperature: Phase transformations and kinetics of atomistic transport. *Physics and Chemistry of Minerals*, 34, 445–465.
- Tkalcec, E., Ivankovic, H., Nass, R., and Schmidt, H. (2003) Crystallization kinetics of mullite formation in diphasic gels containing different alumina components. *Journal of the European Ceramic Society*, 23, 1465–1475.
- Tropper, P., and Manning, C.E. (2007) The solubility of corundum in H_2O at high pressure and temperature and its implications for Al mobility in the deep crust and upper mantle. *Chemical Geology*, 240, 54–60.
- Turner, S.P., and Stüwe, K. (1992) Low-pressure corona textures between olivine and plagioclase in unmetamorphosed gabbros from Black Hill, South Australia. *Mineralogical Magazine*, 56, 503–509.
- Van Santen, R.A. (1984) The Ostwald Step Rule. *Journal of Physical Chemistry*, 88, 5768–5769.
- Verma, P., Sengupta, S., Chaddha, D.K., and Pant, N.C. (2005) Dehydration melting studies in a “Kyanite terrain”, Manali, NW Himalayas. *Journal of Asian Earth Sciences*, 25, 345–366.
- Vernon, R.H. (1979) Formation of late sillimanite by hydrogen metasomatism (base-leaching) in some high-grade gneisses. *Lithos*, 12, 143–152.

- Vernon, R.H., Flood, R.H., and D'Arcy, W.F. (1987) Sillimanite and andalusite produced by base-cation leaching and contact metamorphism of felsic igneous rocks. *Journal of Metamorphic Geology*, 5, 437.
- Vogt, M., Kröner, A., Poller, U., Sommer, H., Muhongo, S., and Wingate, M.T.D. (2006) Archaean and Palaeoproterozoic gneisses reworked during a Neoproterozoic (Pan-African) high-grade event in the Mozambique belt of East Africa: Structural relationships and zircon ages from the Kidatu area, central Tanzania. *Journal of African Earth Sciences*, 45, 139–155.
- Voudouris, P.C. (2014) Hydrothermal corundum, topaz, diaspore and alunite supergroup minerals in the advanced argillic alteration lithocap of the Kassiteres-Sapes porphyry-epithermal system, western Thrace, Greece. *Neues Jahrbuch für Mineralogie - Abhandlungen: Journal of Mineralogy and Geochemistry*, 191, 117–136.
- Vrána, S. (1973) A model of aluminium silicate accretion in metamorphic rocks. *Contributions to Mineralogy and Petrology*, 41, 73–82.
- Wahl, F.M., Grim, R.E., and Graf, R.B. (1961) Phase transformation in silica-alumina mixtures as examined by continuous X-ray diffraction. *American Mineralogist*, 46, 1064–1076.
- Walker, F.D.L., Lee, M.R., and Parsons, I. (1995) Micropores and micropermeable texture in alkali feldspars: geochemical and geophysical implications. *Mineralogical Magazine*, 59, 505–534.
- Walter, J. V (2001) Experimental determination and analysis of the solubility of corundum in 0.1 and 0.5 m NaCl solutions between 400 and 600 °C from 0.5 to 2.0 kbar. *Geochimica et Cosmochimica Acta*, 65, 2843–2851.
- Walther, J. V (1997) Experimental determination and interpretation of the solubility of corundum in H₂O between 350 and 600 °C from 0.5 to 2.2 kbar. *Geochimica et Cosmochimica Acta*, 61, 4955–4964.
- Wang, Y. (2014) Nanogeochemistry: Nanostructures, emergent properties and their control on geochemical reactions and mass transfers. *Chemical Geology*, 378–379, 1–23.
- Watenphul, A., Schmidt, C., and Scholten, L. (2012) First insights into Cr³⁺ solubility in aqueous fluids at elevated P and T by μ -XRF. *European Mineralogical Conference*, Vol. 1, 1, EMC2012-544.
- Waychunas, G.A., Kim, C.S., and Banfield, J.F. (2005) Nanoparticulate iron oxide minerals in soils and sediments: unique properties and contaminant scavenging mechanisms. *Journal of Nanoparticle Research*, 7, 409–433.
- Weinberg, R.F., and Hasalová, P. (2015) Water- fluxed melting of the continental crust: A review. *Lithos*, 212–215, 158–188.
- Wenk, H.-R. (1980) Defects along kyanite-staurolite interfaces. *American Mineralogist*, 65, 766.
- White, J.S. (1979) Boehmite exsolution in corundum. *American Mineralogist*, 64, 1300.
- Whitney, D.L., and Evans, B.W. (2010) Abbreviations for names of rock-forming minerals. *American Mineralogist*, 95, 185–187.
- Widmer, T., and Thompson, A.B. (2001) Local origin of high pressure vein material in eclogite facies rocks of the Zermatt-Saas zone, Switzerland. *American Journal of Science*, 301.
- Wintsch, R.P. (1975) Solid-fluid equilibria in the system KAlSi₃O₈-NaAlSi₃O₈-Al₂SiO₅-SiO₂-H₂O-HCl. *Journal of Petrology*, 16, 57–79.
- Wintsch, R.P., and Andrews, M.S. (1988) Deformation induced growth of sillimanite: “stress” minerals revisited. *Journal of Geology*, 96, 143–161.
- Wohlert, A., and Manning, C.E. (2009) Solubility of corundum in aqueous KOH solutions at 700 °C and 1 GPa. *Chemical Geology*, 262, 326–333.
- Wu, X., Han, Y., Meng, D., and Li, D. (2002) Discovery and implication of P2₁/n crystal structure on a nano-scale in single jadeite crystals, 197, 165–169.

- Wulff, G. (1901) Zur Frage der Geschwindigkeit des Wachstums und der Auflösung der Krystallflächen. *Zeitschrift der Kristallographie*, 29, 449–530.
- Xu, H., Lee, S., and Xu, H. (2017) Luogufengite: An Fe_2O_3 nanomineral with unique magnetic property. In Goldschmidt Conference.
- Yardley, B.W.D., and Cleverley, J.S. (2015) The role of metamorphic fluids in the formation of ore deposits. In G.R.T. Jenkin, P.A.J. Lusty, I. McDonald, M.P. Smith, A.J. Boyce, and J.J. Wilkinson, Eds., *Ore Deposits in an Evolving Earth* Vol. 393, pp. 117–134. Geological Society, London.
- Zaraisky, G.P., and Soboleva, Y. V (1997) Experimental determination of corundum solubility in aqueous HF solutions at 300 to 600 C° and 1 kbar. In: *Proceedings of the fifth international symposium on hydrothermal reactions*, Gatlinburg, Tennessee, 201–205.

Electronic Appendix

Appendix chapter 2

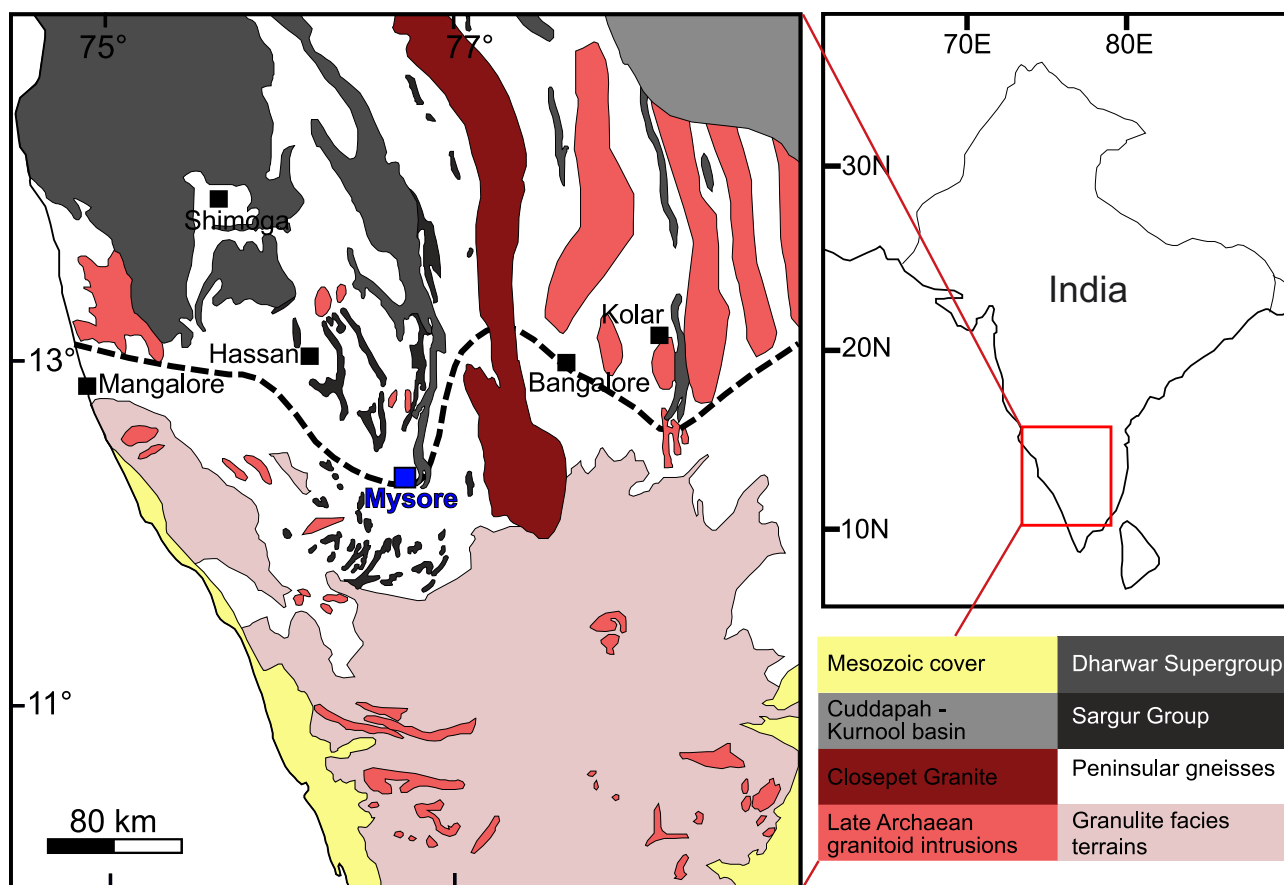


Fig. A2.1 Sampling location of sample MI near Mysore (blue) shown in the geological map of SW-India (province Karnataka), map modified after Jayananda et al. (2008). The facies boundary amphibolite (N) - granulite (S) is indicated with dashed line.

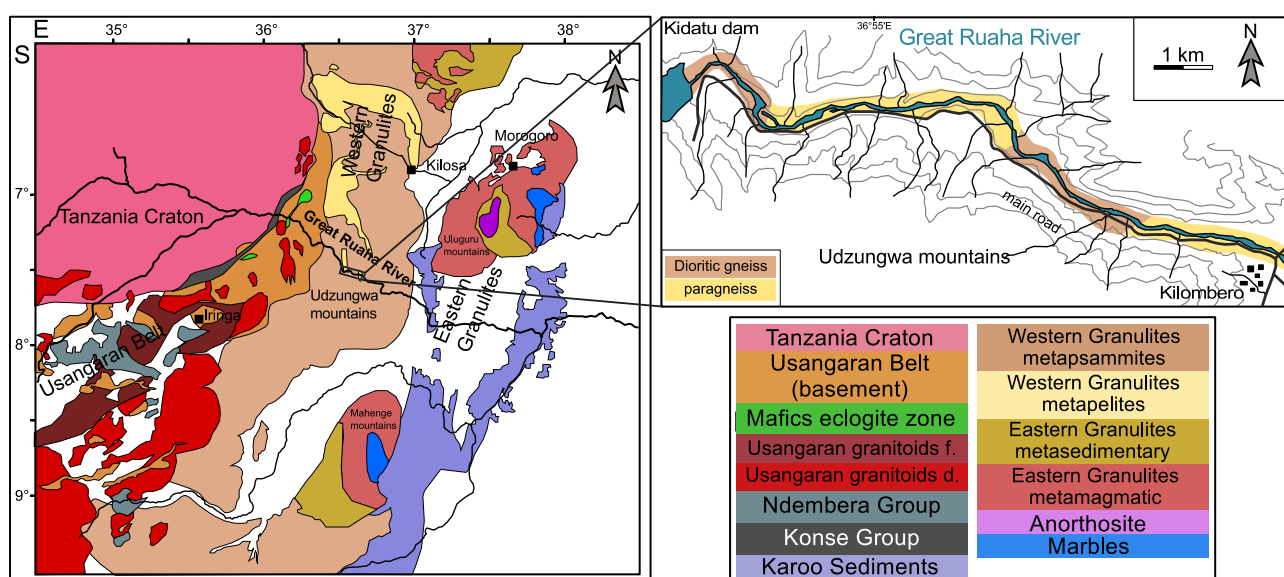


Fig. A2.2 Approximate sampling location of sample KT near Kilombero city in geological map of Tanzania modified after Fritz et al. (2005), and a detailed map of the river valley through the Udzungwa mountains (mod. after Vogt et al. 2006).

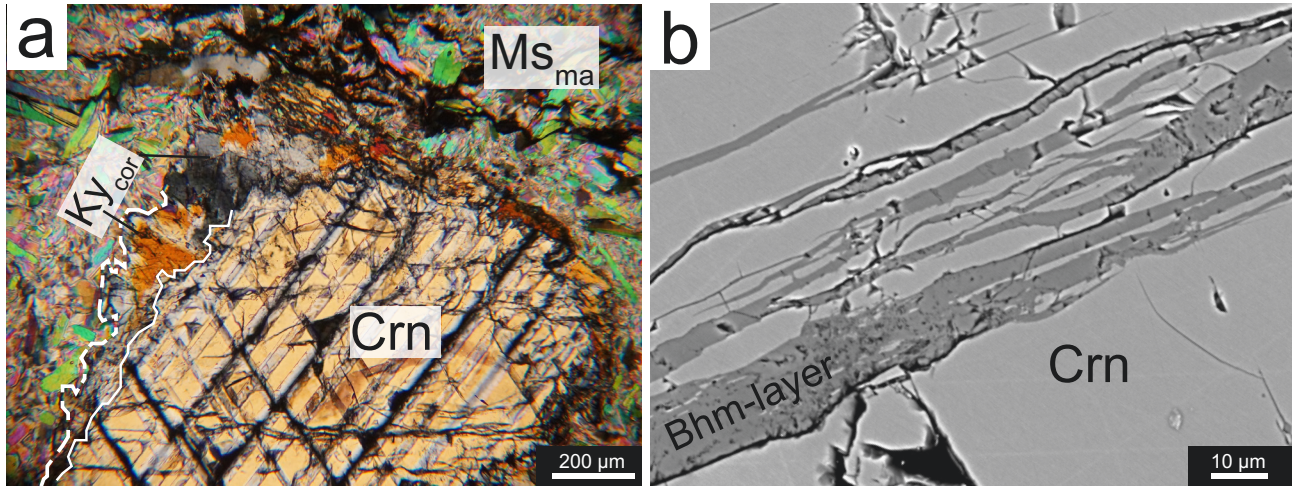


Fig. A3.1 Crystallographic features and in corundum porphyroblasts of sample MI. a) Crn grain with rhombohedral network of parting planes (microphotograph with crossed nicols). b) Backscattered electron image (EMP) of boehmite layers located along the parting planes of corundum (Tab. 3.2).

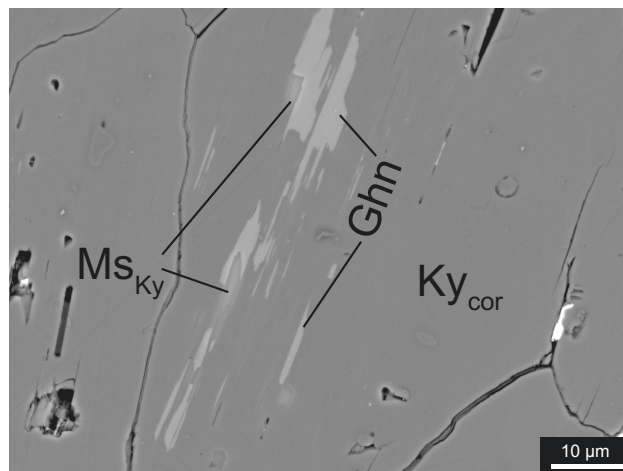


Fig. A3.2 BSE image (EMP) of kyanite including elongated gahnite (Ghn) and MsKy inclusions oriented parallel to the kyanite cleavage in sample MI, mineral chemistry is given in Table A3.3.

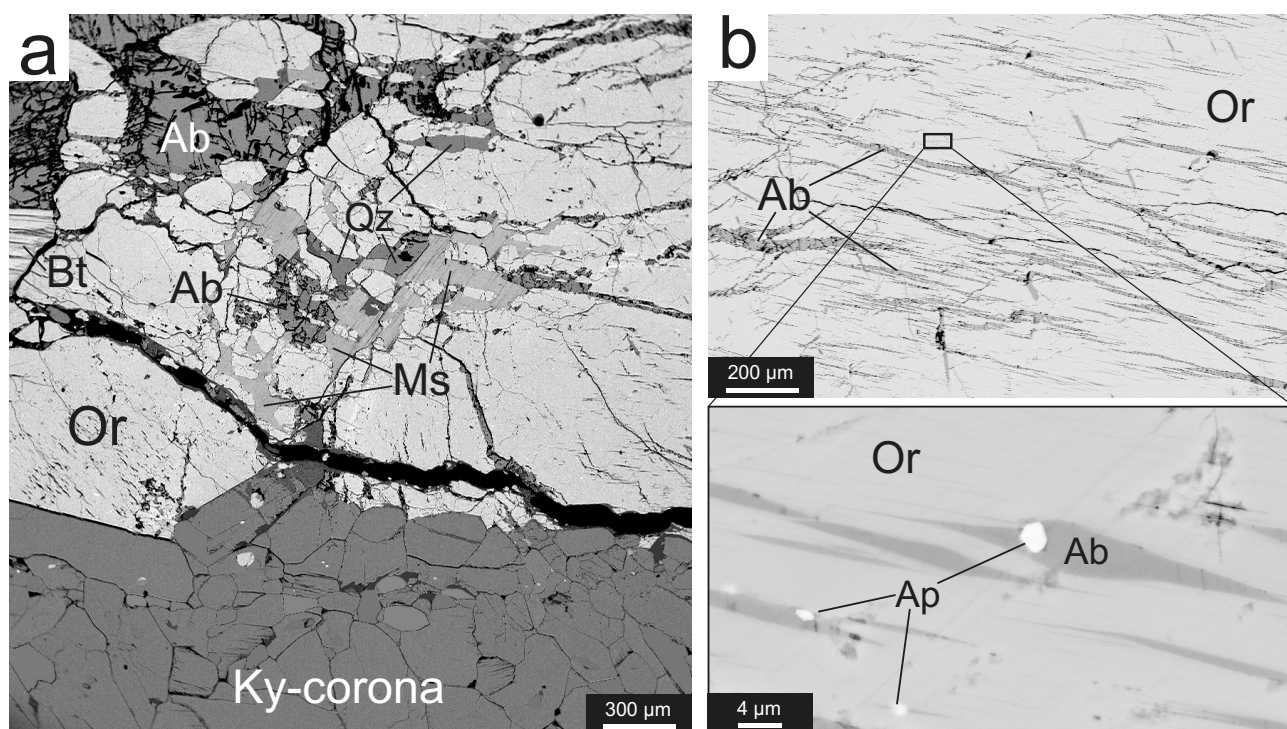


Fig. A3.3 Pertitic orthoclase (Or) with replacement features in sample KT (BSE image EMP). a) Orthoclase (Or) and albite (Ab) intergrowth, and Ms + Qz replacement of the feldspars in the center of the image. b) Ab lenses distributed in Or (upper image) and in detail pertites (Ab) with apatite (Ap) inclusions (lower image, detail). Mineral chemistry is given in Table A3.5.

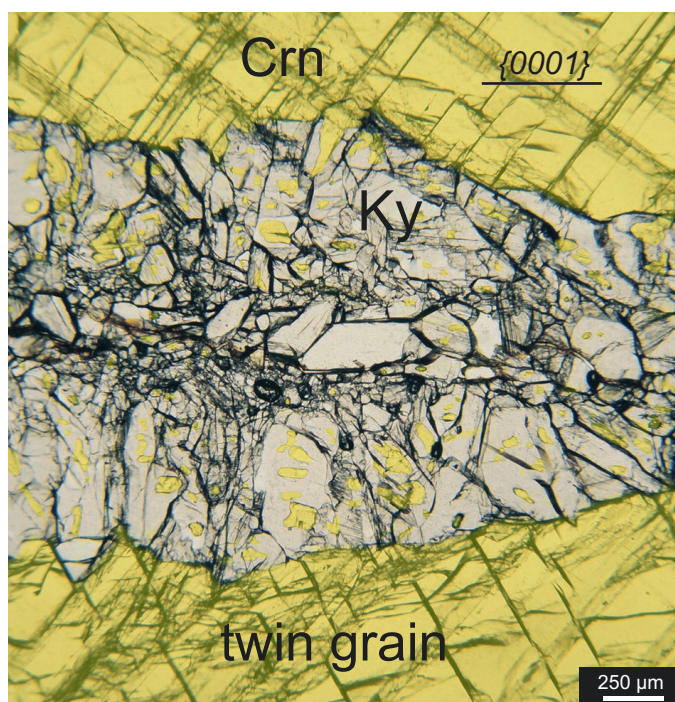


Fig. A3.4 Colored microphotograph of the Ky-corona between Crn main grain and the twin grain. Crn inclusions are only found in Ky individuals grown towards main grain and twin, whereas Ky grains in the middle part are Crn inclusion free.

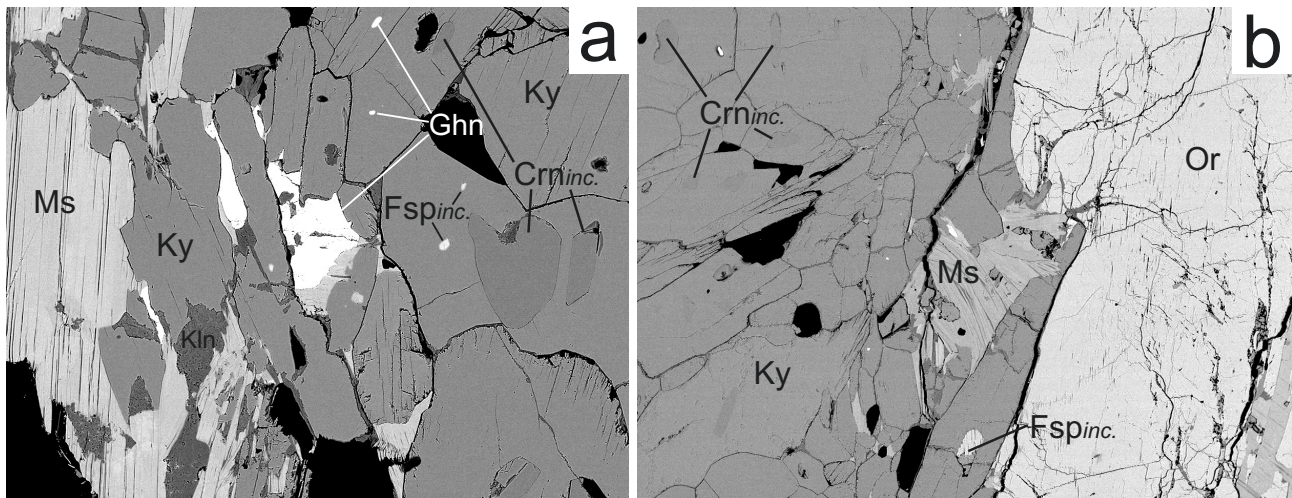


Fig. A3.5 a) and b) BSE images (EMP) of Ky replacement features in contact with Ms in sample KT. a) Kyanite includes Fsp, Crn, and Ghn inclusions.

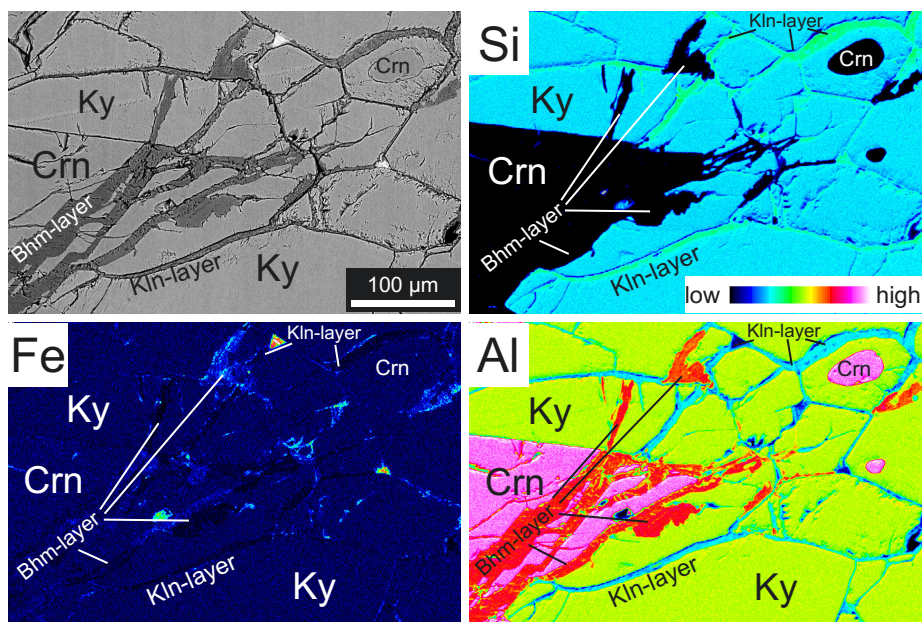


Fig. A3.6 BSE image (upper left) and corresponding element mapping images (Si, Fe, and Al) of the Crn-corona contact and the associated hydroxide layers found along the phase and grain boundaries in sample KT. Boehmite (Bhm) layers are mainly found inside the Crn grain, however, occasionally they expand into the corona. Kaolinite (Kln) layers are found along Ky-Ky grain boundaries mainly (see Tab. 3.4). Fe distribution among the non-hydroxides is very homogeneous, the hydroxides show highly heterogeneous concentrations.

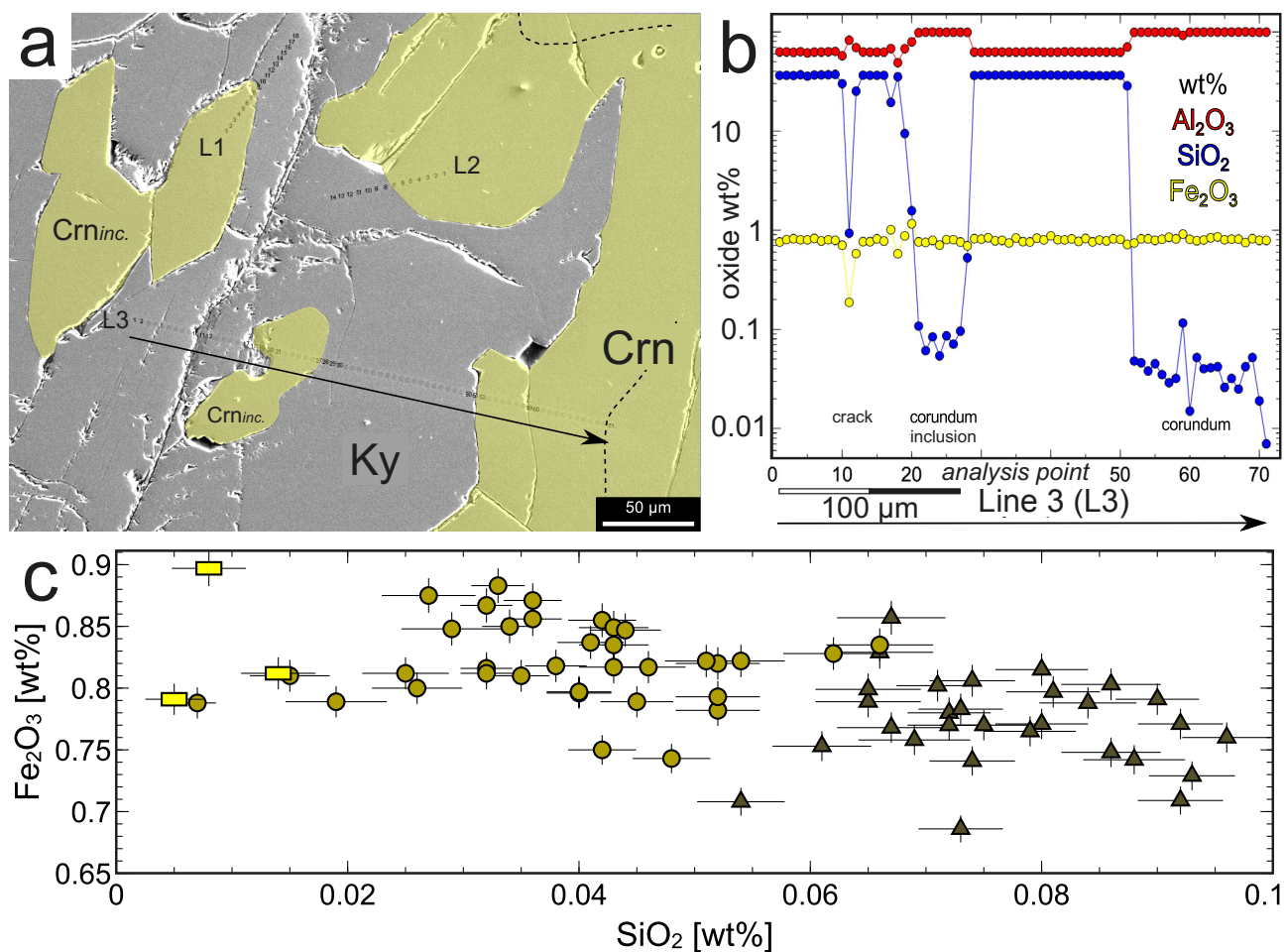


Fig. A3.7 Si-bulk diffusion into corundum along Ky-Crn interfaces (sample KT). a) Colored SE image (EMP) of the phase boundary between Crn main grain and Ky corona with Crn inclusions in two kyanite individuals. b) Element profile of Al_2O_3 , SiO_2 , Fe_2O_3 wt% through Ky corona grains, a Crn inclusion, and the first 70 μm of the Crn main grain (Profile position indicated by black arrow in a). Crn inclusions show elevated silica contents in comparison with the main grain. c) Chemical analyses of Crn inclusions (dark gray triangles), the first < 100 μm of the Crn grain in contact with Ky (dark yellow circles), and the interior of the main grain (bulk Crn) (yellow bars) show an increase in SiO_2 and slight average decrease in Fe_2O_3 with decreasing distance to the kyanite corona (error bars = 1 σ , EMP calculation). Entire dataset is given in Table A3.4_1 and A3.4_2.

Table A3.1. Chemical composition of corundum (Crn), kyanite (Ky_{cor}, Ky_{agg}), and boehmite (Bhm) in sample MI (WDS analyses) (data included in Table 3.2 are indicated bold and **bold & italic**) (distances of Crn analyses from Crn-Ky-phase boundary in dicated in µm).

| Corundum | | | | | | | | | | | | | | | | | | |
|--------------------------------|---------|---------------|--------|--------|--------|--------|--------|--------|--------|--------|---------|--------|--------|--------|---------|----------------|--------|---------------|
| | 1 | 2 | 3 | 4 | 5 | 6 | 7 | 8 | 9 | 10 | 11 | 12 | 13 | 14 | 15 | 16 | 17 | 18 |
| distance to ph.b. | 40 µm | 40 µm | 1 µm | 1 µm | 8 µm | 300 µm | 7 µm | 5 µm | 25 µm | 5 µm | 2 µm | 150 µm | 200 µm | 250 µm | 100 µm | 130 µm | 220 µm | Crn inclusion |
| SiO ₂ | 0.004 | 0.003 | 0.219 | 0.434 | 0.037 | 0.016 | 0.027 | 0.048 | 0.047 | 0.041 | 0.042 | 0.029 | 0.014 | 0.000 | 0.015 | 0.015 | 0.000 | 0.062 |
| TiO ₂ | 0.019 | 0.037 | 0.027 | 0.057 | 0.048 | 0.001 | 0.025 | 0.016 | 0.000 | 0.002 | 0.000 | 0.014 | 0.000 | 0.041 | 0.000 | 0.034 | 0.014 | 0.045 |
| Al ₂ O ₃ | 99.690 | 99.260 | 98.420 | 97.960 | 98.410 | 98.990 | 98.940 | 99.030 | 99.380 | 99.290 | 99.670 | 99.380 | 99.370 | 99.140 | 99.760 | 99.500 | 99.440 | 99.080 |
| V ₂ O ₃ | 0.029 | 0.027 | 0.045 | 0.000 | 0.056 | 0.000 | 0.020 | 0.036 | 0.013 | 0.013 | 0.023 | 0.000 | 0.000 | 0.006 | 0.033 | 0.000 | 0.000 | 0.001 |
| Cr ₂ O ₃ | 0.431 | 0.385 | 0.535 | 0.529 | 0.562 | 0.229 | 0.396 | 0.422 | 0.327 | 0.310 | 0.358 | 0.321 | 0.303 | 0.317 | 0.301 | 0.268 | 0.297 | 0.343 |
| Fe ₂ O ₃ | 0.057 | 0.169 | 0.233 | 0.148 | 0.144 | 0.093 | 0.162 | 0.140 | 0.180 | 0.119 | 0.097 | 0.164 | 0.137 | 0.127 | 0.101 | 0.204 | 0.127 | 0.156 |
| Total | 100.230 | 99.881 | 99.479 | 99.128 | 99.258 | 99.328 | 99.570 | 99.692 | 99.947 | 99.775 | 100.190 | 99.908 | 99.824 | 99.631 | 100.210 | 100.021 | 99.878 | 99.686 |

| Kyanite (Ky _{cor} = regular, Ky _{agg} = italic) | | | | | | | | | | | | Boehmite | | | | | | | |
|---|----------------|---------|---------|---------------|---------|---------------|--------|----------------|---------|---------|---------|--------------------------------|--------|--------|--------|--------|--------|---------------|---------------|
| | 1 | 2 | 3 | 4 | 5 | 6 | 7 | 8 | 9 | 10 | 11 | | 1 | 2 | 3 | 4 | 5 | 6 | 7 |
| SiO ₂ | 37.330 | 37.150 | 37.340 | 37.130 | 37.320 | 37.280 | 37.450 | 37.380 | 37.730 | 37.480 | 37.350 | SiO ₂ | 0.019 | 0.098 | 0.046 | 0.278 | 0.006 | 0.018 | 0.020 |
| TiO ₂ | 0.052 | 0.014 | 0.000 | 0.000 | 0.000 | 0.004 | 0.000 | 0.000 | 0.020 | 0.017 | 0.000 | TiO ₂ | 0.027 | 0.023 | 0.000 | 0.031 | 0.016 | 0.014 | 0.044 |
| Al ₂ O ₃ | 62.700 | 62.740 | 62.550 | 62.220 | 62.320 | 62.100 | 61.880 | 62.580 | 62.520 | 62.820 | 62.710 | Al ₂ O ₃ | 87.740 | 88.310 | 87.660 | 88.040 | 83.110 | 83.850 | 83.840 |
| V ₂ O ₃ | 0.045 | 0.035 | 0.019 | 0.007 | 0.018 | 0.023 | 0.093 | 0.000 | 0.000 | 0.000 | 0.013 | V ₂ O ₃ | 0.000 | 0.013 | 0.000 | 0.042 | 0.025 | 0.000 | 0.000 |
| Cr ₂ O ₃ | 0.265 | 0.398 | 0.332 | 0.402 | 0.419 | 0.358 | 0.211 | 0.353 | 0.331 | 0.345 | 0.442 | Cr ₂ O ₃ | 0.339 | 0.315 | 0.361 | 0.220 | 0.208 | 0.270 | 0.248 |
| Fe ₂ O ₃ | 0.136 | 0.023 | 0.083 | 0.078 | 0.162 | 0.110 | 0.126 | 0.054 | 0.082 | 0.105 | 0.099 | Fe ₂ O ₃ | 0.065 | 0.248 | 0.039 | 0.421 | 0.137 | 0.377 | 0.148 |
| Total | 100.528 | 100.360 | 100.324 | 99.838 | 100.239 | 99.876 | 99.760 | 100.367 | 100.683 | 100.767 | 100.613 | Total | 88.191 | 89.006 | 88.107 | 89.031 | 83.502 | 84.529 | 84.300 |

Table A3.2. Chemical composition of the different muscovite types in sample MI: matrix muscovite (Ms_{ma}), muscovite intergrown with kyanite (Ms_{Ky}), muscovite from quartz schlieren (Ms_{sch}), and Ms_{ma} in close vicinity to schlieren (Ms_{mix}), (EMP WDS analyses in oxide wt% and atom per formula unit [apfu] normalized to a cation sum of 7). Data from Table 3.3 indicated **bold**

| Ms _{ma} (matrix muscovite, variety „fuchsite“) | | | | | | | | | Ms _{mix} (Ms _{ma} near schlieren) | | | | | | | | | | | | | | | | | | |
|---|---------|---------|---------|---------|---------|---------|--------|---------|---|--------|---------|---------|---------|---------|---------------------------------------|--------|---------|---------|---------|--------|---------|--------|---------|---------|---------|---------|--|
| wt% | 48.340 | 48.498 | 48.150 | 47.327 | 48.415 | 47.858 | 46.989 | 47.510 | 47.919 | 47.694 | 48.169 | 48.237 | 48.031 | 47.355 | 47.129 | 46.788 | 48.680 | 47.660 | 48.344 | 47.844 | 48.067 | 47.484 | 48.542 | 48.289 | 47.590 | 49.213 | |
| SiO ₂ | 0.489 | 0.514 | 0.351 | 0.597 | 0.475 | 0.812 | 0.702 | 0.728 | 0.459 | 0.621 | 0.532 | 0.653 | 0.427 | 0.749 | 0.766 | 0.565 | 0.355 | 0.759 | 0.735 | 0.565 | 0.646 | 0.728 | 0.769 | 0.810 | 0.713 | 0.616 | |
| Al ₂ O ₃ | 35.443 | 34.681 | 34.919 | 35.444 | 34.835 | 35.631 | 34.888 | 34.936 | 35.765 | 34.623 | 34.348 | 34.318 | 35.734 | 35.080 | 35.416 | 35.193 | 34.450 | 35.346 | 34.068 | 33.317 | 35.389 | 35.185 | 34.550 | 35.060 | 35.001 | 34.018 | |
| Cr ₂ O ₃ | 0.105 | 0.102 | 0.167 | 0.197 | 0.189 | 0.126 | 0.438 | 0.286 | 0.157 | 0.107 | 0.000 | 0.102 | 0.079 | 0.133 | 0.229 | 0.097 | 0.024 | 0.184 | 0.084 | 0.136 | 0.195 | 0.134 | 0.109 | 0.040 | 0.009 | 0.103 | |
| CaO | 0.060 | 0.000 | 0.033 | 0.020 | 0.000 | 0.030 | 0.040 | 0.011 | 0.009 | 0.000 | 0.000 | 0.027 | 0.012 | 0.025 | 0.004 | 0.050 | 0.005 | 0.000 | 0.031 | 0.027 | 0.003 | 0.000 | 0.017 | 0.000 | 0.000 | 0.011 | |
| MgO | 1.151 | 1.389 | 1.340 | 1.020 | 1.366 | 1.094 | 0.998 | 1.190 | 1.027 | 1.370 | 1.612 | 1.520 | 1.244 | 1.194 | 1.179 | 1.182 | 1.696 | 1.167 | 1.557 | 1.611 | 1.143 | 0.988 | 1.517 | 1.301 | 1.197 | 1.801 | |
| FeO | 0.484 | 0.509 | 0.518 | 0.457 | 0.492 | 0.485 | 0.456 | 0.542 | 0.503 | 0.435 | 0.602 | 0.477 | 0.578 | 0.542 | 0.513 | 0.480 | 0.608 | 0.522 | 0.543 | 0.507 | 0.426 | 0.296 | 0.518 | 0.508 | 0.508 | 0.605 | |
| MnO | 0.000 | 0.021 | 0.031 | 0.006 | 0.000 | 0.000 | 0.000 | 0.000 | 0.000 | 0.000 | 0.000 | 0.000 | 0.033 | 0.029 | 0.000 | 0.012 | 0.000 | 0.000 | 0.000 | 0.005 | 0.031 | 0.000 | 0.000 | 0.000 | 0.000 | 0.025 | |
| BaO | 0.393 | 0.360 | 0.263 | 0.330 | 0.410 | 0.324 | 0.155 | 0.214 | 0.220 | 0.239 | 0.301 | 0.125 | 0.264 | 0.240 | 0.325 | 0.316 | 0.433 | 0.141 | 0.480 | 0.284 | 0.285 | 0.277 | 0.268 | 0.073 | 0.265 | 0.365 | |
| Na ₂ O | 0.934 | 0.982 | 0.910 | 0.946 | 0.896 | 1.061 | 1.022 | 1.011 | 1.078 | 0.964 | 0.961 | 0.875 | 1.078 | 1.000 | 1.039 | 1.046 | 0.906 | 1.108 | 0.905 | 0.901 | 1.124 | 1.374 | 0.872 | 1.060 | 1.056 | 0.934 | |
| K ₂ O | 9.472 | 9.411 | 9.484 | 9.554 | 9.595 | 9.523 | 9.348 | 9.561 | 9.542 | 9.404 | 9.627 | 9.462 | 9.351 | 9.316 | 9.451 | 9.199 | 9.371 | 9.168 | 9.458 | 9.339 | 9.128 | 8.640 | 9.406 | 9.435 | 9.402 | 9.506 | |
| F | 0.000 | 0.000 | 0.000 | 0.059 | 0.127 | 0.000 | 0.000 | 0.383 | 0.156 | 0.000 | 0.058 | 0.064 | 0.000 | 0.000 | 0.000 | 0.177 | 0.022 | 0.000 | 0.000 | 0.000 | 0.180 | 0.290 | 0.000 | 0.000 | 0.000 | 0.000 | |
| Cl | 0.024 | 0.000 | 0.018 | 0.035 | 0.022 | 0.006 | 0.000 | 0.000 | 0.046 | 0.022 | 0.000 | 0.023 | 0.018 | 0.001 | 0.002 | 0.006 | 0.044 | 0.003 | 0.000 | 0.000 | 0.022 | 0.000 | 0.051 | 0.009 | 0.000 | 0.004 | |
| H ₂ O | 4.568 | 4.558 | 4.543 | 4.495 | 4.499 | 4.580 | 4.491 | 4.356 | 4.491 | 4.510 | 4.522 | 4.494 | 4.580 | 4.522 | 4.541 | 4.407 | 4.540 | 4.544 | 4.537 | 4.466 | 4.468 | 4.365 | 4.546 | 4.569 | 4.529 | 4.589 | |
| Total | 101.462 | 101.024 | 100.728 | 100.486 | 101.320 | 101.530 | 99.527 | 100.728 | 101.373 | 99.988 | 100.731 | 100.378 | 101.431 | 100.187 | 100.592 | 99.517 | 101.135 | 100.601 | 100.743 | 99.000 | 101.108 | 99.761 | 101.164 | 101.152 | 100.270 | 101.789 | |
| apfu | | | | | | | | | | | | | | | | | | | | | | | | | | | |
| Si ⁴⁺ | 3.168 | 3.191 | 3.175 | 3.132 | 3.180 | 3.132 | 3.137 | 3.139 | 3.139 | 3.167 | 3.174 | 3.193 | 3.141 | 3.140 | 3.112 | 3.123 | 3.200 | 3.144 | 3.195 | 3.212 | 3.161 | 3.162 | 3.193 | 3.167 | 3.150 | 3.215 | |
| Ti ⁴⁺ | 0.024 | 0.025 | 0.017 | 0.030 | 0.023 | 0.040 | 0.035 | 0.036 | 0.023 | 0.031 | 0.026 | 0.033 | 0.021 | 0.037 | 0.038 | 0.028 | 0.018 | 0.038 | 0.037 | 0.029 | 0.032 | 0.036 | 0.038 | 0.040 | 0.035 | 0.030 | |
| Al ³⁺ | 2.738 | 2.689 | 2.714 | 2.764 | 2.697 | 2.748 | 2.745 | 2.721 | 2.761 | 2.710 | 2.668 | 2.677 | 2.754 | 2.741 | 2.756 | 2.768 | 2.669 | 2.748 | 2.653 | 2.636 | 2.743 | 2.761 | 2.678 | 2.710 | 2.731 | 2.619 | |
| Cr ³⁺ | 0.005 | 0.005 | 0.009 | 0.010 | 0.010 | 0.006 | 0.023 | 0.015 | 0.008 | 0.006 | 0.000 | 0.005 | 0.004 | 0.007 | 0.012 | 0.005 | 0.001 | 0.010 | 0.004 | 0.007 | 0.010 | 0.007 | 0.006 | 0.002 | 0.000 | 0.005 | |
| Ca ²⁺ | 0.004 | 0.000 | 0.002 | 0.001 | 0.000 | 0.002 | 0.003 | 0.001 | 0.001 | 0.000 | 0.000 | 0.002 | 0.001 | 0.002 | 0.000 | 0.004 | 0.000 | 0.000 | 0.002 | 0.002 | 0.000 | 0.000 | 0.001 | 0.000 | 0.000 | 0.001 | |
| Mg ²⁺ | 0.112 | 0.136 | 0.132 | 0.101 | 0.134 | 0.107 | 0.099 | 0.117 | 0.100 | 0.136 | 0.158 | 0.150 | 0.121 | 0.118 | 0.116 | 0.118 | 0.166 | 0.115 | 0.153 | 0.161 | 0.112 | 0.098 | 0.149 | 0.127 | 0.118 | 0.175 | |
| Fe ²⁺ | 0.027 | 0.028 | 0.029 | 0.025 | 0.027 | 0.027 | 0.025 | 0.030 | 0.028 | 0.024 | 0.033 | 0.026 | 0.032 | 0.030 | 0.028 | 0.027 | 0.033 | 0.029 | 0.030 | 0.028 | 0.023 | 0.016 | 0.028 | 0.028 | 0.028 | 0.033 | |
| Mn ²⁺ | 0.000 | 0.001 | 0.002 | 0.000 | 0.000 | 0.000 | 0.000 | 0.000 | 0.000 | 0.000 | 0.000 | 0.000 | 0.002 | 0.002 | 0.000 | 0.001 | 0.000 | 0.000 | 0.000 | 0.000 | 0.002 | 0.000 | 0.000 | 0.000 | 0.000 | 0.001 | |
| Ba ²⁺ | 0.010 | 0.009 | 0.007 | 0.009 | 0.011 | 0.008 | 0.004 | 0.006 | 0.006 | 0.006 | 0.008 | 0.003 | 0.007 | 0.006 | 0.008 | 0.008 | 0.011 | 0.004 | 0.012 | 0.007 | 0.007 | 0.007 | 0.007 | 0.002 | 0.007 | 0.009 | |
| Na ⁺ | 0.119 | 0.125 | 0.116 | 0.121 | 0.114 | 0.135 | 0.132 | 0.129 | 0.137 | 0.124 | 0.123 | 0.112 | 0.137 | 0.129 | 0.133 | 0.135 | 0.116 | 0.142 | 0.116 | 0.117 | 0.143 | 0.177 | 0.111 | 0.135 | 0.136 | 0.118 | |
| K ⁺ | 0.792 | 0.790 | 0.798 | 0.807 | 0.804 | 0.795 | 0.796 | 0.806 | 0.797 | 0.797 | 0.809 | 0.799 | 0.780 | 0.788 | 0.796 | 0.783 | 0.786 | 0.772 | 0.797 | 0.800 | 0.766 | 0.734 | 0.789 | 0.789 | 0.794 | 0.792 | |
| F ⁻ | 0.000 | 0.000 | 0.000 | 0.012 | 0.026 | 0.000 | 0.000 | 0.080 | 0.032 | 0.000 | 0.012 | 0.013 | 0.000 | 0.000 | 0.000 | 0.037 | 0.005 | 0.000 | 0.000 | 0.000 | 0.037 | 0.061 | 0.000 | 0.000 | 0.000 | 0.000 | |
| Cl ⁻ | 0.003 | 0.000 | 0.002 | 0.004 | 0.002 | 0.001 | 0.000 | 0.000 | 0.005 | 0.002 | 0.000 | 0.003 | 0.002 | 0.000 | 0.000 | 0.001 | 0.005 | 0.000 | 0.000 | 0.000 | 0.002 | 0.000 | 0.006 | 0.001 | 0.000 | 0.000 | |
| OH ⁻ | 1.997 | 2.000 | 1.998 | 1.984 | 1.971 | 1.999 | 2.000 | 1.920 | 1.962 | 1.998 | 1.988 | 1.984 | 1.998 | 2.000 | 2.000 | 1.962 | 1.990 | 2.000 | 2.000 | 2.000 | 1.960 | 1.939 | 1.994 | 1.999 | 2.000 | 2.000 | |
| O ²⁺ | 10.109 | 10.106 | 10.096 | 10.085 | 10.098 | 10.084 | 10.092 | 10.076 | 10.079 | 10.095 | 10.069 | 10.111 | 10.083 | 10.093 | 10.069 | 10.079 | 10.102 | 10.104 | 10.103 | 10.104 | 10.115 | 10.127 | 10.122 | 10.101 | 10.087 | 10.102 | |
| cation sum | 7.000 | 7.000 | 7.000 | 7.000 | 7.000 | 7.000 | 7.000 | 7.000 | 7.000 | 7.000 | 7.000 | 7.000 | 7.000 | 7.000 | 7.000 | 7.000 | 7.000 | 7.000 | 7.000 | 7.000 | 7.000 | 7.000 | 7.000 | 7.000 | 7.000 | 7.000 | |
| Ms _{sch} (schlieren) | | | | | | | | | | | | | | | Ms _{Ky} (intergrown with Ky) | | | | | | | | | | | | |
| wt% | | | | | | | | | | | | | | | | | | | | | | | | | | | |
| SiO ₂ | 46.363 | 46.621 | 47.607 | 46.951 | 47.067 | 47.341 | 46.764 | 46.784 | 47.276 | 45.854 | 46.021 | 45.951 | 46.546 | 46.355 | 46.506 | 46.755 | 46.946 | 46.855 | 45.781 | 47.178 | 46.434 | | | | | | |
| TiO _{Si} | | | | | | | | | | | | | | | | | | | | | | | | | | | |

Table A3.3 Accessory mineral phases in sample MI (EDS analyses EMP)

| Accessories distributed throughout the rock | | | | | | | | | | Solid inclusions in Ky | |
|---|--------|--------|------------------|--------|--------------------------------|----------|----------|-------|--------------|--------------------------------|---------|
| wt% | Rutile | Rutile | wt% | Zircon | wt% | Monazite | Monazite | wt% | Chalcopyrite | wt% | Gahnite |
| | | | SiO ₂ | 31.46 | SiO ₂ | 1.42 | 1.70 | | | SiO ₂ | 3.55 |
| TiO ₂ | 97.89 | 97.23 | ZrO ₂ | 68.54 | ZrO ₂ | 0.00 | 1.81 | O | 18.79 | Al ₂ O ₃ | 43.29 |
| V ₂ O ₃ | 0.00 | 1.37 | | | P ₂ O ₅ | 30.45 | 27.81 | S | 25.93 | Cr ₂ O ₃ | 1.71 |
| Cr ₂ O ₃ | 0.60 | 0.31 | | | La ₂ O ₃ | 20.27 | 20.03 | Fe | 25.17 | Fe ₂ O ₃ | 13.27 |
| ZrO ₂ | 0.25 | 0.00 | | | CeO ₂ | 32.25 | 31.68 | Cu | 30.10 | MgO | 1.75 |
| Nb ₂ O ₅ | 1.26 | 1.10 | | | Nd ₂ O ₃ | 9.88 | 10.20 | | | ZnO | 36.43 |
| | | | | | ThO ₂ | 5.73 | 6.78 | | | | |
| Total | 100 | 100 | Total | 100 | Total | 100 | 100 | Total | 100 | Total | 100 |

Table A3.4_1 SiO₂-contents in Sample KT corundum; Crn bulk, Crn in corona vicinity, and Crn inclusions in Ky-corona (WDS results EMP); D.L. are given in Table 4

| wt% | Bulk corundum (grain center) | | | | | | | | | |
|--------------------------------|---|---------|---------|---------|---------|---------|---------|---------|---------|---------|
| SiO ₂ | 0.014 | 0.005 | 0.008 | | | | | | | |
| Al ₂ O ₃ | 99.614 | 99.209 | 99.286 | | | | | | | |
| Fe ₂ O ₃ | 0.812 | 0.791 | 0.897 | | | | | | | |
| Total | 100.44 | 100.005 | 100.191 | | | | | | | |
| | | | | | | | | | | |
| wt% | Corundum <100 μm from Crn-Ky phase boundary | | | | | | | | | |
| SiO ₂ | 0.048 | 0.046 | 0.038 | 0.045 | 0.035 | 0.029 | 0.032 | 0.015 | 0.04 | |
| Al ₂ O ₃ | 98.836 | 99.104 | 99.159 | 99.055 | 99.284 | 98.995 | 99.311 | 99.127 | 99.203 | |
| Fe ₂ O ₃ | 0.743 | 0.817 | 0.818 | 0.789 | 0.81 | 0.848 | 0.816 | 0.81 | 0.797 | |
| Total | 99.627 | 99.967 | 100.015 | 99.889 | 100.129 | 99.872 | 100.159 | 99.952 | 100.04 | |
| | | | | | | | | | | |
| SiO ₂ | 0.052 | 0.04 | 0.041 | 0.042 | 0.026 | 0.032 | 0.025 | 0.042 | 0.033 | |
| Al ₂ O ₃ | 99.241 | 99.324 | 99.478 | 99.39 | 99.448 | 99.428 | 99.616 | 99.902 | 98.913 | |
| Fe ₂ O ₃ | 0.782 | 0.796 | 0.837 | 0.855 | 0.8 | 0.812 | 0.812 | 0.75 | 0.883 | |
| Total | 100.075 | 100.16 | 100.356 | 100.287 | 100.274 | 100.272 | 100.453 | 100.694 | 99.829 | |
| | | | | | | | | | | |
| SiO ₂ | 0.052 | 0.019 | 0.007 | 0.051 | 0.043 | 0.062 | 0.052 | 0.054 | 0.066 | |
| Al ₂ O ₃ | 99.335 | 99.041 | 99.442 | 99.55 | 99.664 | 99.818 | 99.397 | 99.817 | 98.719 | |
| Fe ₂ O ₃ | 0.82 | 0.789 | 0.788 | 0.822 | 0.835 | 0.828 | 0.793 | 0.822 | 0.835 | |
| Total | 100.207 | 99.849 | 100.237 | 100.423 | 100.542 | 100.708 | 100.242 | 100.693 | 99.62 | |
| | | | | | | | | | | |
| SiO ₂ | 0.036 | 0.032 | 0.043 | 0.043 | 0.044 | 0.036 | 0.027 | 0.034 | | |
| Al ₂ O ₃ | 98.968 | 98.756 | 98.923 | 99.131 | 98.716 | 98.758 | 98.911 | 98.586 | | |
| Fe ₂ O ₃ | 0.871 | 0.867 | 0.817 | 0.849 | 0.847 | 0.856 | 0.875 | 0.85 | | |
| Total | 99.875 | 99.655 | 99.783 | 100.023 | 99.607 | 99.65 | 99.813 | 99.47 | | |
| | | | | | | | | | | |
| wt% | Corundum inclusions in Ky | | | | | | | | | |
| SiO ₂ | 0.067 | 0.072 | 0.086 | 0.065 | 0.074 | 0.088 | 0.061 | 0.084 | 0.054 | 0.093 |
| Al ₂ O ₃ | 98.875 | 99.233 | 99.168 | 99.262 | 99.088 | 99.211 | 99.33 | 99.423 | 99.005 | 99.06 |
| Fe ₂ O ₃ | 0.768 | 0.78 | 0.748 | 0.789 | 0.741 | 0.742 | 0.753 | 0.788 | 0.708 | 0.729 |
| Total | 99.71 | 100.085 | 100.002 | 100.116 | 99.903 | 100.041 | 100.144 | 100.295 | 99.767 | 99.882 |
| | | | | | | | | | | |
| SiO ₂ | 0.086 | 0.071 | 0.096 | 0.073 | 0.08 | 0.079 | 0.069 | 0.092 | 0.081 | 0.092 |
| Al ₂ O ₃ | 98.965 | 99.169 | 99.132 | 100.182 | 99.536 | 99.295 | 99.217 | 99.446 | 99.314 | 99.345 |
| Fe ₂ O ₃ | 0.803 | 0.802 | 0.76 | 0.686 | 0.771 | 0.765 | 0.758 | 0.771 | 0.797 | 0.709 |
| Total | 99.854 | 100.042 | 99.988 | 100.941 | 100.387 | 100.139 | 100.044 | 100.309 | 100.192 | 100.146 |
| | | | | | | | | | | |
| SiO ₂ | 0.08 | 0.067 | 0.09 | 0.072 | 0.073 | 0.066 | 0.074 | 0.065 | 0.075 | |
| Al ₂ O ₃ | 99.585 | 99.307 | 99.443 | 99.391 | 98.961 | 99.124 | 99.306 | 99.289 | 99.324 | |
| Fe ₂ O ₃ | 0.815 | 0.857 | 0.791 | 0.77 | 0.783 | 0.829 | 0.806 | 0.799 | 0.77 | |
| Total | 100.48 | 100.231 | 100.324 | 100.233 | 99.817 | 100.019 | 100.186 | 100.153 | 100.169 | |

Table A3.4_2 Elemental line scans (L1, 2, 3 see Fig. SX, L 4, 5) along Ky, Crn inclusions in Ky, and into the Crn main grain in sample KT (WDS results EMP); D.L. are given in Table 4

| Line 1 | | | | | | | | | | | | | | | | | | |
|--------------------------------|--------|---------|---------|---------|--------|---------|---------|--------|--------|--------|--------|---------|--------|--------|---------|---------|---------|---------|
| wt% | 1 | 2 | 3 | 4 | 5 | 6 | 7 | 8 | 9 | 10 | 11 | 12 | 13 | 14 | 15 | 16 | 17 | 18 |
| SiO ₂ | 0.067 | 0.072 | 0.086 | 0.065 | 0.074 | 0.088 | 0.103 | 0.365 | 18.998 | 33.562 | 34.146 | 36.801 | 36.533 | 36.429 | 36.776 | 36.990 | 36.736 | 36.552 |
| Al ₂ O ₃ | 98.875 | 99.233 | 99.168 | 99.262 | 99.088 | 99.211 | 100.442 | 85.763 | 68.788 | 61.910 | 62.880 | 62.794 | 62.414 | 62.319 | 62.737 | 62.936 | 62.761 | 62.657 |
| Fe ₂ O ₃ | 0.768 | 0.780 | 0.748 | 0.789 | 0.741 | 0.742 | 0.756 | 0.453 | 0.652 | 0.734 | 0.781 | 0.799 | 0.782 | 0.776 | 0.791 | 0.860 | 0.792 | 0.800 |
| Total | 99.710 | 100.085 | 100.002 | 100.116 | 99.903 | 100.041 | 101.301 | 86.581 | 88.438 | 96.206 | 97.807 | 100.394 | 99.729 | 99.524 | 100.304 | 100.786 | 100.289 | 100.009 |

| Line 2 | | | | | | | | | | | | | | |
|--------------------------------|---------|---------|---------|---------|---------|---------|--------|--------|--------|--------|---------|---------|--------|---------|
| wt% | 1 | 2 | 3 | 4 | 5 | 6 | 7 | 8 | 9 | 10 | 11 | 12 | 13 | 14 |
| SiO ₂ | 0.051 | 0.043 | 0.062 | 0.052 | 0.054 | 0.071 | 0.231 | 33.864 | 33.890 | 33.933 | 36.616 | 36.729 | 36.569 | 36.677 |
| Al ₂ O ₃ | 99.550 | 99.664 | 99.818 | 99.397 | 99.817 | 99.412 | 99.077 | 62.740 | 62.375 | 62.665 | 62.841 | 62.736 | 62.675 | 62.675 |
| Fe ₂ O ₃ | 0.822 | 0.835 | 0.828 | 0.794 | 0.822 | 0.737 | 0.688 | 0.847 | 0.759 | 0.796 | 0.849 | 0.801 | 0.731 | 0.804 |
| Total | 100.423 | 100.542 | 100.708 | 100.243 | 100.693 | 100.220 | 99.996 | 97.451 | 97.024 | 97.394 | 100.306 | 100.266 | 99.975 | 100.156 |

| Line 3_1 | | | | | | | | | | | | | | | | | | |
|--------------------------------|--------|--------|--------|---------|--------|---------|---------|---------|---------|--------|--------|--------|---------|--------|--------|--------|--------|--------|
| wt% | 1 | 2 | 3 | 4 | 5 | 6 | 7 | 8 | 9 | 10 | 11 | 12 | 13 | 14 | 15 | 16 | 17 | 18 |
| SiO ₂ | 36.328 | 36.441 | 36.255 | 36.904 | 35.726 | 36.709 | 36.827 | 36.929 | 37.222 | 29.990 | 0.932 | 25.233 | 36.560 | 36.443 | 36.460 | 36.462 | 19.432 | 35.235 |
| Al ₂ O ₃ | 62.672 | 62.660 | 62.154 | 63.075 | 61.329 | 62.487 | 62.565 | 62.952 | 63.471 | 57.388 | 82.237 | 69.396 | 62.774 | 62.492 | 62.396 | 62.393 | 67.833 | 48.822 |
| Fe ₂ O ₃ | 0.760 | 0.804 | 0.820 | 0.800 | 0.799 | 0.825 | 0.778 | 0.800 | 0.790 | 0.705 | 0.187 | 0.580 | 0.767 | 0.766 | 0.818 | 0.776 | 1.010 | 0.578 |
| Total | 99.760 | 99.905 | 99.229 | 100.779 | 97.854 | 100.021 | 100.170 | 100.681 | 101.483 | 88.083 | 83.356 | 95.209 | 100.101 | 99.701 | 99.674 | 99.631 | 88.275 | 84.635 |

| Line 3_2 | | | | | | | | | | | | | | | | | | |
|--------------------------------|--------|--------|--------|---------|---------|--------|--------|---------|--------|---------|--------|--------|--------|---------|---------|--------|--------|--------|
| | 19 | 20 | 21 | 22 | 23 | 24 | 25 | 26 | 27 | 28 | 29 | 30 | 31 | 32 | 33 | 34 | 35 | 36 |
| SiO ₂ | 9.427 | 1.569 | 0.108 | 0.061 | 0.084 | 0.054 | 0.086 | 0.071 | 0.096 | 0.527 | 36.351 | 36.610 | 36.475 | 36.620 | 36.610 | 36.582 | 36.598 | 36.364 |
| Al ₂ O ₃ | 67.608 | 79.178 | 97.981 | 99.330 | 99.423 | 99.005 | 98.965 | 99.169 | 99.132 | 98.806 | 62.473 | 62.270 | 62.543 | 62.678 | 62.603 | 62.470 | 62.525 | 62.511 |
| Fe ₂ O ₃ | 0.876 | 1.159 | 0.764 | 0.754 | 0.788 | 0.708 | 0.804 | 0.802 | 0.760 | 0.696 | 0.821 | 0.812 | 0.838 | 0.781 | 0.789 | 0.744 | 0.834 | 0.767 |
| Total | 77.911 | 81.906 | 98.853 | 100.145 | 100.295 | 99.767 | 99.855 | 100.042 | 99.988 | 100.029 | 99.645 | 99.692 | 99.856 | 100.079 | 100.002 | 99.796 | 99.957 | 99.642 |

| Line 3_3 | | | | | | | | | | | | | | | | | | |
|--------------------------------|---------|---------|--------|--------|--------|---------|---------|--------|---------|--------|--------|--------|---------|--------|--------|--------|--------|---------|
| | 37 | 38 | 39 | 40 | 41 | 42 | 43 | 44 | 45 | 46 | 47 | 48 | 49 | 50 | 51 | 52 | 53 | 54 |
| SiO ₂ | 36.557 | 36.528 | 36.742 | 36.613 | 36.556 | 36.580 | 36.556 | 36.524 | 36.589 | 36.128 | 36.299 | 36.032 | 36.577 | 36.455 | 28.564 | 0.048 | 0.046 | 0.038 |
| Al ₂ O ₃ | 62.816 | 62.713 | 62.430 | 62.361 | 62.477 | 62.929 | 62.899 | 62.670 | 62.646 | 62.670 | 62.788 | 62.549 | 62.688 | 62.349 | 70.243 | 98.836 | 99.104 | 99.159 |
| Fe ₂ O ₃ | 0.761 | 0.830 | 0.798 | 0.877 | 0.800 | 0.798 | 0.816 | 0.770 | 0.825 | 0.764 | 0.796 | 0.780 | 0.818 | 0.809 | 0.717 | 0.744 | 0.817 | 0.818 |
| Total | 100.134 | 100.071 | 99.970 | 99.851 | 99.833 | 100.307 | 100.271 | 99.964 | 100.060 | 99.562 | 99.883 | 99.361 | 100.083 | 99.613 | 99.524 | 99.628 | 99.967 | 100.015 |

| Line 3_4 | | | | | | | | | | | | | | | | | | |
|--------------------------------|--------|---------|--------|---------|--------|--------|---------|---------|---------|---------|---------|---------|---------|---------|---------|--------|---------|--|
| | 55 | 56 | 57 | 58 | 59 | 60 | 61 | 62 | 63 | 64 | 65 | 66 | 67 | 68 | 69 | 70 | 71 | |
| SiO ₂ | 0.045 | 0.035 | 0.029 | 0.032 | 0.116 | 0.015 | 0.052 | 0.040 | 0.041 | 0.042 | 0.026 | 0.032 | 0.025 | 0.042 | 0.052 | 0.019 | 0.007 | |
| Al ₂ O ₃ | 99.055 | 99.284 | 98.995 | 99.311 | 92.168 | 99.127 | 99.241 | 99.324 | 99.478 | 99.390 | 99.448 | 99.428 | 99.616 | 99.902 | 99.335 | 99.041 | 99.442 | |
| Fe ₂ O ₃ | 0.789 | 0.810 | 0.848 | 0.816 | 0.912 | 0.810 | 0.782 | 0.796 | 0.837 | 0.855 | 0.800 | 0.812 | 0.812 | 0.750 | 0.820 | 0.789 | 0.788 | |
| Total | 99.889 | 100.129 | 99.872 | 100.159 | 93.196 | 99.952 | 100.075 | 100.160 | 100.356 | 100.287 | 100.274 | 100.272 | 100.453 | 100.694 | 100.207 | 99.849 | 100.237 | |

| Line 4_1 | | | | | | | | | | | | | | | | | | |
|--------------------------------|--------|--------|--------|--------|--------|--------|--------|--------|---------|--------|---------|---------|---------|---------|---------|---------|---------|---------|
| wt% | 1 | 2 | 3 | 4 | 5 | 6 | 7 | 8 | 9 | 10 | 11 | 12 | 13 | 14 | 15 | 16 | 17 | 18 |
| SiO ₂ | 36.429 | 36.498 | 36.463 | 36.511 | 36.530 | 36.579 | 36.441 | 36.601 | 36.708 | 36.700 | 36.584 | 21.024 | 0.073 | 0.080 | 0.079 | 0.069 | 0.092 | 0.081 |
| Al ₂ O ₃ | 62.550 | 62.483 | 62.635 | 62.373 | 62.482 | 62.323 | 62.425 | 62.383 | 62.547 | 62.500 | 62.921 | 82.095 | 100.182 | 99.536 | 99.295 | 99.217 | 99.446 | 99.314 |
| Fe ₂ O ₃ | 0.790 | 0.842 | 0.844 | 0.792 | 0.791 | 0.786 | 0.829 | 0.766 | 0.816 | 0.799 | 0.770 | 0.658 | 0.686 | 0.771 | 0.765 | 0.758 | 0.771 | 0.797 |
| Total | 99.769 | 99.823 | 99.942 | 99.676 | 99.803 | 99.688 | 99.695 | 99.750 | 100.071 | 99.999 | 100.275 | 103.777 | 100.941 | 100.387 | 100.139 | 100.044 | 100.309 | 100.192 |

| Line 4_2 | | | | | | | | | | | | | | | | | | |
|--------------------------------|---------|---------|---------|---------|--------|---------|---------|---------|---------|--------|---------|--------|---------|--------|--------|---------|--------|---------|
| | 19 | 20 | 21 | 22 | 23 | 24 | 25 | 26 | 27 | 28 | 29 | 30 | 31 | 32 | 33 | 34 | 35 | 36 |
| SiO ₂ | 0.080 | 0.067 | 0.090 | 0.072 | 0.073 | 0.066 | 0.074 | 0.065 | 0.075 | 0.093 | 0.092 | 23.720 | 36.614 | 36.565 | 36.310 | 36.489 | 36.039 | 36.617 |
| Al ₂ O ₃ | 99.585 | 99.307 | 99.443 | 99.391 | 98.961 | 99.124 | 99.306 | 99.289 | 99.324 | 99.060 | 99.345 | 73.925 | 62.609 | 62.404 | 62.442 | 62.681 | 62.619 | 62.656 |
| Fe ₂ O ₃ | 0.815 | 0.857 | 0.791 | 0.770 | 0.784 | 0.829 | 0.806 | 0.799 | 0.770 | 0.729 | 0.709 | 0.642 | 0.818 | 0.764 | 0.758 | 0.852 | 0.778 | 0.811 |
| Total | 100.480 | 100.231 | 100.324 | 100.233 | 99.818 | 100.019 | 100.186 | 100.153 | 100.169 | 99.882 | 100.146 | 98.287 | 100.041 | 99.733 | 99.510 | 100.022 | 99.436 | 100.084 |

| Line 4_3 | | | | | | |
|--------------------------------|--------|--------|--------|--------|---------|--------|
| | 37 | 38 | 39 | 40 | 41 | 42 |
| SiO ₂ | 36.446 | 36.436 | 36.385 | 36.379 | 36.596 | 36.404 |
| Al ₂ O ₃ | 62.411 | 62.563 | 62.557 | 62.669 | 62.662 | 62.580 |
| Fe ₂ O ₃ | 0.821 | 0.770 | 0.852 | 0.786 | 0.767 | 0.786 |
| Total | 99.678 | 99.769 | 99.794 | 99.834 | 100.025 | 99.770 |

| Line 5_1 | | | | | | | | | | | | | | | | | | |
|--------------------------------|--------|--------|--------|---------|--------|--------|--------|--------|---------|--------|--------|--------|--------|---------|--------|--------|--------|--------|
| wt% | 1 | 2 | 3 | 4 | 5 | 6 | 7 | 8 | 9 | 10 | 11 | 12 | 13 | 14 | 15 | 16 | 17 | 18 |
| SiO ₂ | 0.036 | 0.032 | 0.043 | 0.043 | 0.044 | 0.036 | 0.027 | 0.034 | 0.040 | 0.033 | 0.066 | 0.101 | 5.908 | 37.173 | 36.439 | 36.367 | 36.576 | 36.487 |
| Al ₂ O ₃ | 98.968 | 98.756 | 98.923 | 99.131 | 98.716 | 98.758 | 98.911 | 98.586 | 99.203 | 98.913 | 98.719 | 97.894 | 74.365 | 63.359 | 62.389 | 62.267 | 62.591 | 62.365 |
| Fe ₂ O ₃ | 0.871 | 0.867 | 0.817 | 0.849 | 0.847 | 0.856 | 0.875 | 0.850 | 0.797 | 0.884 | 0.835 | 0.854 | 0.529 | 0.705 | 0.766 | 0.779 | 0.756 | 0.786 |
| Total | 99.875 | 99.655 | 99.783 | 100.023 | 99.607 | 99.650 | 99.813 | 99.470 | 100.040 | 99.830 | 99.620 | 98.849 | 80.802 | 101.237 | 99.594 | 99.413 | 99.923 | 99.638 |

| Line 5_2 | | | | |
|--------------------------------|--------|--------|--------|--------|
| | 19 | 20 | 21 | 22 |
| SiO ₂ | 36.207 | 36.290 | 36.528 | 36.327 |
| Al ₂ O ₃ | 62.375 | 62.198 | 62.369 | 62.513 |
| Fe ₂ O ₃ | 0.817 | 0.775 | 0.741 | 0.802 |
| Total | 99.399 | 99.263 | 99.638 | 99.642 |

Table A3.5. Gneiss host rock mineral chemistry sample KT: muscovite in gneiss host (Ms_{Gn}), muscovite inclusion in corundum (Ms_{Cm}), plagioclase (Pl), orthoclase (Or) (EDS results EMP)

| wt% | Muscovite | | Biotite | | wt% | Feldspar | | | | wt% | Apatite |
|--------------------------------|------------------|------------------|---------|--|--------------------------------|----------|-------|-------|-------|-------------------------------|---------|
| | Ms _{Gn} | Ms _{Cm} | Bt | | | Pl | Pl | Or | Or | | in Or |
| SiO ₂ | 47.13 | 46.05 | 39.41 | | SiO ₂ | 64.78 | 65.25 | 64.62 | 64.03 | CaO | 56.03 |
| TiO ₂ | 0.00 | 0.00 | 1.74 | | Al ₂ O ₃ | 23.87 | 24.09 | 18.78 | 19.84 | FeO | 0.65 |
| Al ₂ O ₃ | 33.84 | 34.54 | 20.84 | | CaO | 2.48 | 2.38 | 0.00 | 0.00 | P ₂ O ₅ | 40.96 |
| Fe ₂ O ₃ | 1.56 | 3.14 | 11.42 | | Na ₂ O | 8.92 | 8.95 | 1.00 | 1.24 | Cl | 1.14 |
| MgO | 0.77 | 0.69 | 12.85 | | K ₂ O | 0.18 | 0.17 | 15.60 | 14.89 | F | 3.26 |
| FeO | 0.87 | 0.03 | 2.45 | | | | | | | -O | -2.05 |
| Na ₂ O | 0.40 | 0.85 | 0.00 | | | | | | | | |
| K ₂ O | 11.19 | 10.46 | 7.59 | | | | | | | | |
| BaO | 0.00 | 0.00 | 0.00 | | | | | | | | |
| OH ⁻ | 4.24 | 4.25 | 3.70 | | | | | | | | |
| Total | 100 | 100 | 100 | | Total | 100 | 100 | 100 | | Total | 100 |
| <i>apfu</i> | | | | | <i>apfu</i> | | | | | <i>apfu</i> | |
| Si ⁴⁺ | 3.138 | 3.065 | 3.010 | | Si ⁴⁺ | 3.231 | 3.006 | 2.989 | | Ca ²⁺ | 5.042 |
| Ti ⁴⁺ | 0.000 | 0.000 | 0.100 | | Al ³⁺ | 1.257 | 1.029 | 1.091 | | Fe ²⁺ | 0.046 |
| IVAl ³⁺ | 0.862 | 0.935 | 0.990 | | Ca ²⁺ | 0.129 | 0.000 | 0.000 | | P ⁵⁺ | 2.912 |
| VIAl ³⁺ | 1.794 | 1.775 | 0.885 | | Na ⁺ | 0.944 | 0.090 | 0.112 | | F ⁻ | 0.867 |
| Fe ³⁺ | 0.078 | 0.157 | 0.656 | | K ⁺ | 0.011 | 0.926 | 0.887 | | Cl ⁻ | 0.163 |
| Mg ²⁺ | 0.077 | 0.068 | 1.462 | | | | | | | charge + | 23.707 |
| Fe ²⁺ | 0.048 | 0.002 | 0.157 | | | | | | | O (-F) | -0.646 |
| Na ⁺ | 0.052 | 0.110 | 0.000 | | | | | | | | |
| K ⁺ | 0.951 | 0.888 | 0.740 | | | | | | | | |
| Ba ²⁺ | 0.000 | 0.000 | 0.000 | | | | | | | | |
| H ⁺ | 1.996 | 2.000 | 1.994 | | | | | | | | |

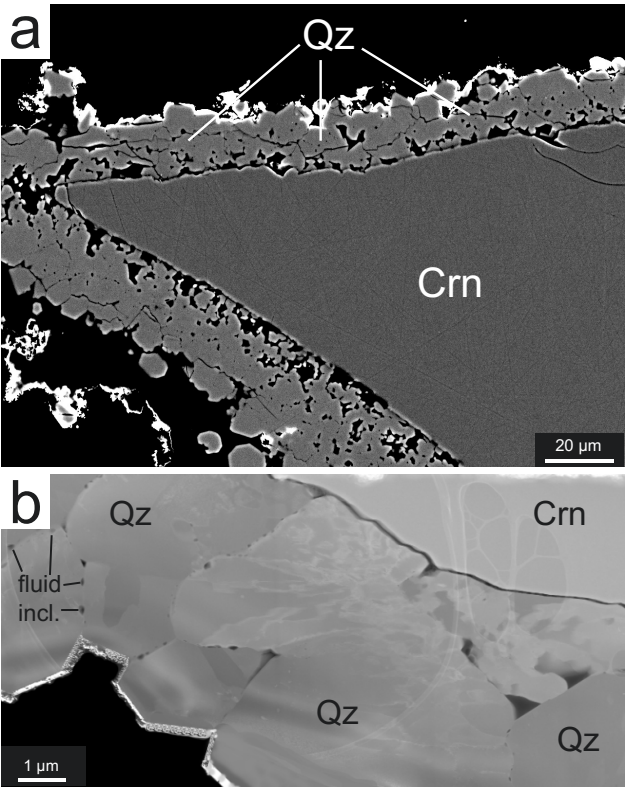


Fig. A4.1 a) BSE image of complete but porous quartz (Qz) cover on corundum (Crn) single crystal from run 1 at neutral fluid pH. b) High-angle annular dark field (HAADF) image (TEM) of a foil cut along the Crn-Qz-cover interface, showing favored fluid transport along the Qz-Qz grain boundary (preserved as fluid inclusions) and defect rich Qz in contact with the Crn surface.

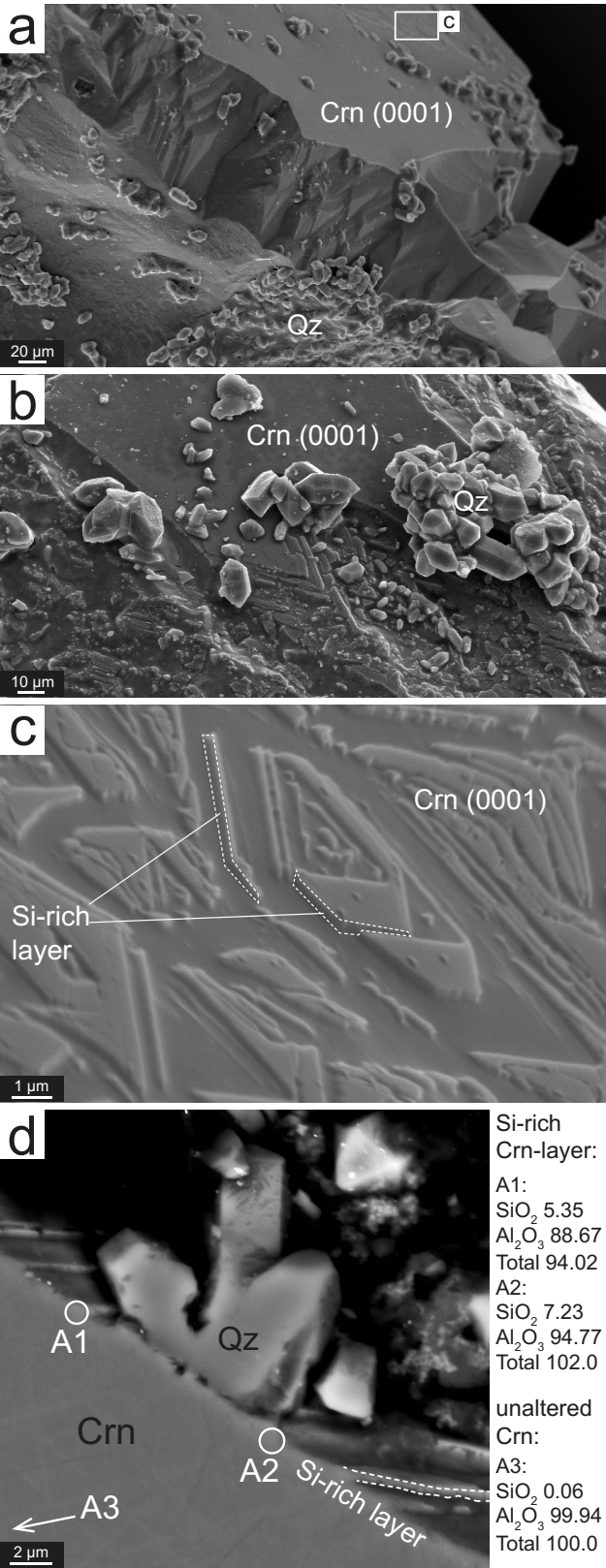


Fig. A4.2 Altered corundum (Crn) from setup 1, with low pH (HCl added; a, c = run 7, b run = 14, d = run 11). a), b), and c) SE images (SEM) of dissolution features on synthetic corundum grains (Crn). The (0001) shows a Si-rich Crn-surface layer of up to 500 nm width, including no etch pits or maximal shallow etch pits carved into the Si-rich layer. d) BSE image and corresponding chemical analyses of the Si-rich surface layer and unaltered Crn (EMP data of the layer are influenced by edge effects).

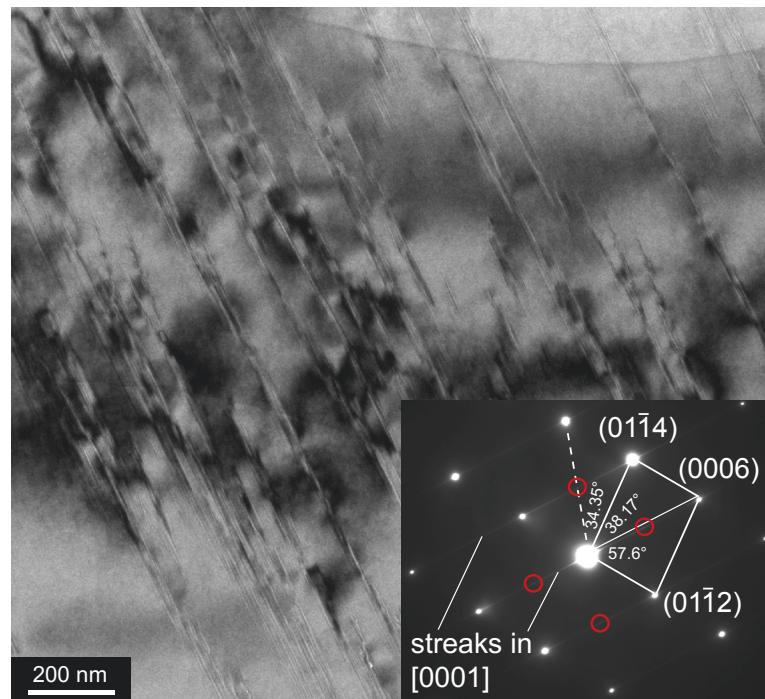


Fig. A4.3 HAADF image of Si rich nano-layers in Crn and their crystallographic influence on the lattice (run 6). The nano-layers appear in electron diffraction experiments (lower right) as distinct streak-features in [0001], furthermore the nano-layers cause an additional reflex (in red) in the normal Crn reflex pattern (in white) between (0006) and the incident beam.

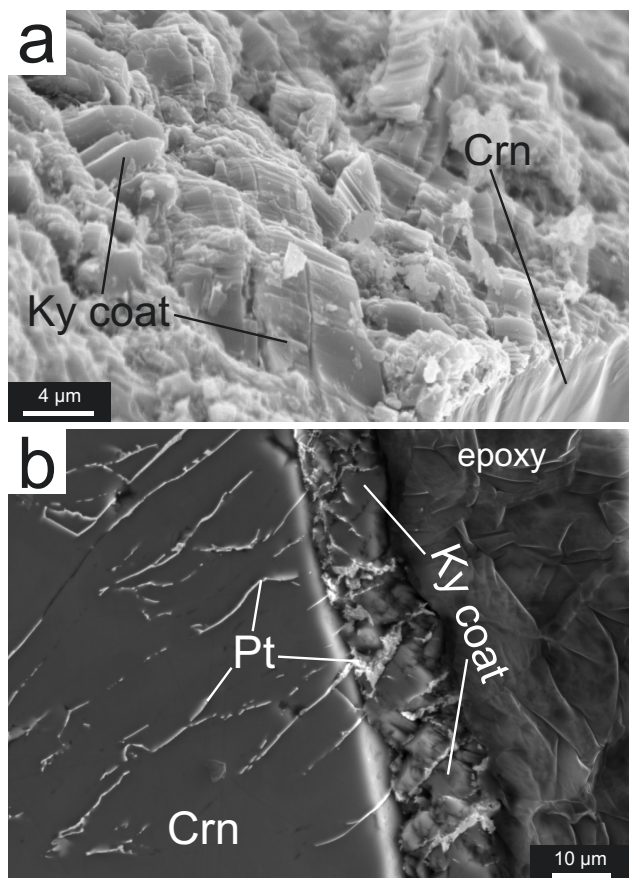


Fig. A4.4 Kyanite (Ky) coated experiment 15, setup 2 in pure water (800°C; 10 kbar); a) Ky seeds appear deformed, kinked (SE image SEM). b) Ky shows no signs of growth towards Crn single crystal, although, fluid was evidently transported through the Ky coat into the Crn (indicated by Pt inclusion trails; BSE image EMP).

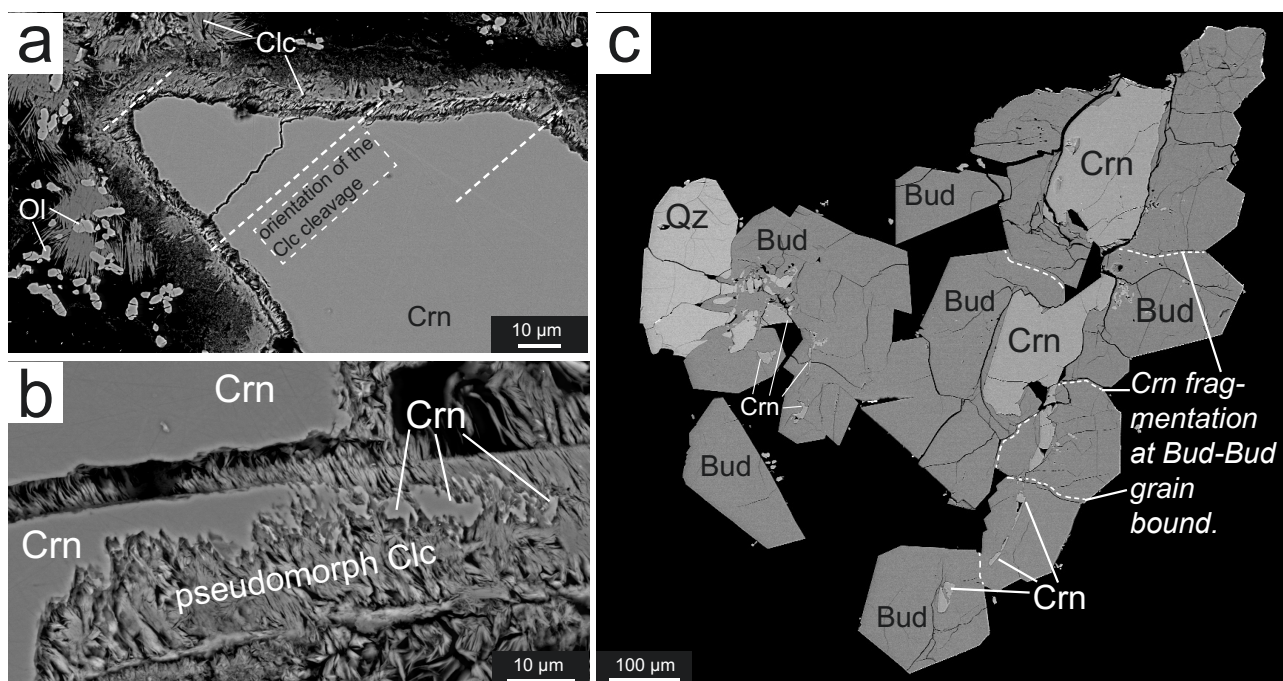


Fig. A4.5 BSE images of run products of experimental setup 3: Corundum (Crn) grain with dissolved silica and water plus MgO from run 30 in a) and b), and NH_3OH from run 29 in c). a) Cross section of a Crn grain with clinoclone (Clc) corona and Clc and forsterite-olivine (Ol) precipitates in the capsule. b) Pseudomorph Clc after Crn. c) Image of budding-tonite (Bud) coronas on highly fragmented and dissolved Crn grain. The fragmentation of Crn occurs preferably along Bud-Bud grain boundaries.

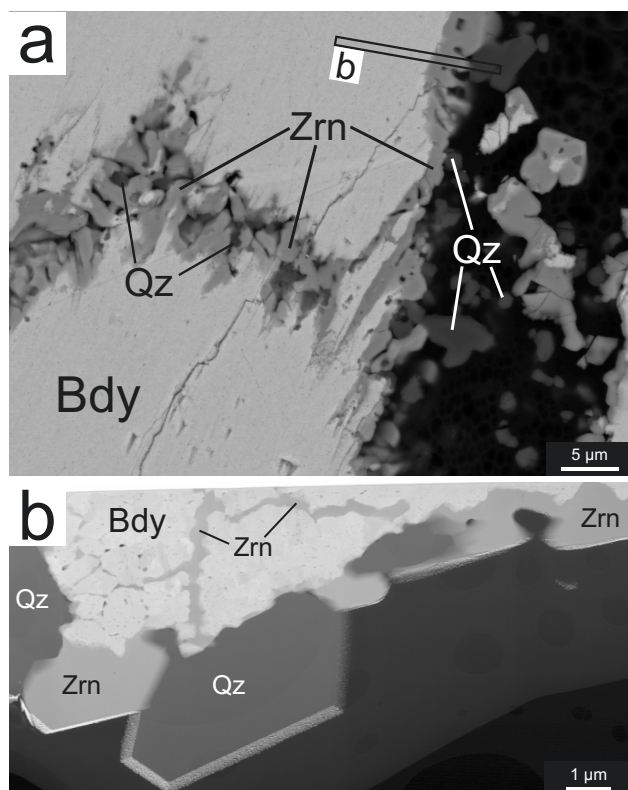


Fig. A4.6 Experimental product of setup 4 (run 31): Baddeleyite (Bdy) grain with silica saturated water. a) BSE image of Bdy grain with zircon (Zrn) corona and quartz (Qz) grains. Zrn also grows along cracks and cleavage of Bdy. b) TEM foil of Bdy-Zrn-Qz interface (indicated in a), Zrn and Bdy show closed phase boundary.

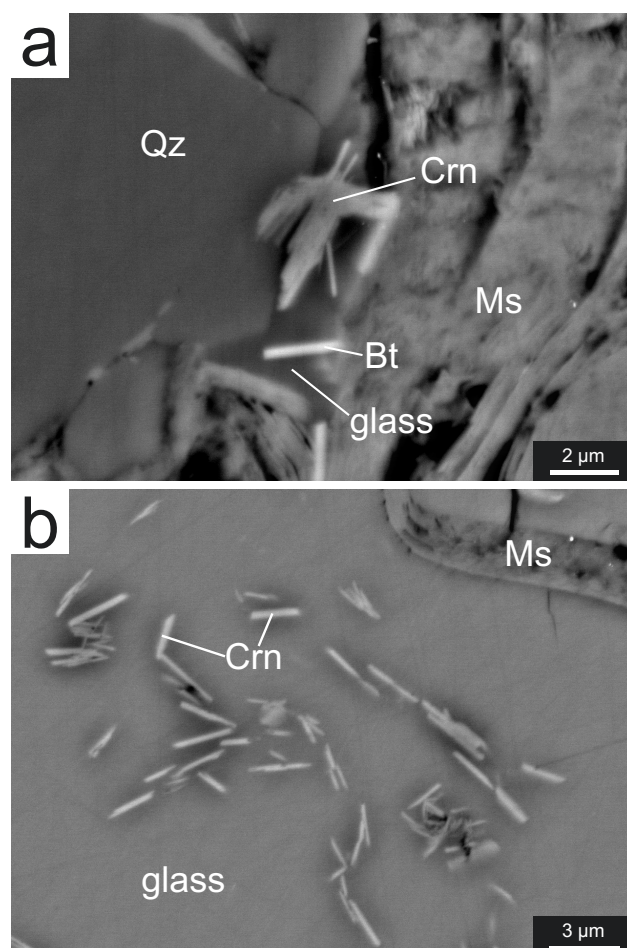


Fig. A4.7 a) and b) BSE images of corundum plates (Crn) grown in silicate melt (glass) of run 32 (Tab. 4.2). a) Crn in silica rich glass adjacent to a large Qz grain and incompletely decomposed muscovite (Ms), also a thin biotite (Bt) plate is found in the glass interstice. b) Crn plates in glass with near orthoclase composition.

Table A4.1. Si-rich, 200 nm wide layer (alt.Crn) on the (0001)-face of a synthetic corundum single crystal (unalt. Crn), experiment in quartz saturated aqueous solution (incl. HCl), at 500°C; 5kbar (run 11 see Table 2.1).

| | unalt. Crn 1 | unalt. Crn 2 | unalt. Crn 3 | alt. Crn 1 | alt. Crn 2 | alt. Crn 3 | alt. Crn 4 | alt. Crn 5 | alt. Crn 6 | alt. Crn 7 | alt. Crn 8 | D.L. |
|--------------------------------|--------------|--------------|--------------|------------|------------|------------|------------|------------|------------|------------|------------|-------|
| SiO ₂ | 0.038 | 0.058 | 0.072 | 5.348 | 7.231 | 10.29 | 12.96 | 17.70 | 19.78 | 20.36 | 20.60 | 0.018 |
| Al ₂ O ₃ | 100.47 | 99.94 | 100.70 | 88.67 | 94.77 | 95.26 | 84.70 | 86.53 | 84.71 | 83.80 | 83.46 | 0.019 |
| Total | 100.57 | 100.03 | 100.83 | 94.02 | 102.01 | 105.59 | 97.69 | 104.29 | 104.54 | 104.31 | 104.13 | |

Table A4.2. Element profile AA-AB (1 analysis point per 1.32 μm) through Si rich reaction rims developed along a fluid inclusion trail in a corundum single grain (run 6) see Fig. 4.4a (WDS results EMP).

| wt% | 0 | 1.32 | 2.64 | 3.96 | 5.28 | 6.6 | 7.92 | 9.24 | 10.56 | 11.88 | 13.2 | 14.52 |
|--------------------------------|--------|--------|--------|--------|--------|--------|--------|--------|--------|-------|--------|--------|
| SiO ₂ | 0.084 | 0.086 | 0.069 | 0.075 | 0.064 | 0.061 | 0.125 | 0.362 | 0.572 | 0.489 | 0.306 | 0.299 |
| TiO ₂ | b.d. | b.d. | b.d. | b.d. | b.d. | b.d. | b.d. | b.d. | b.d. | b.d. | 0.021 | 0.002 |
| Al ₂ O ₃ | 100.01 | 100.08 | 100.11 | 99.90 | 100.03 | 100.15 | 99.86 | 99.69 | 99.56 | 99.48 | 99.85 | 99.86 |
| Fe ₂ O ₃ | 0.082 | 0.057 | 0.029 | 0.090 | 0.071 | 0.039 | b.d. | b.d. | 0.009 | b.d. | b.d. | b.d. |
| Total | 100.18 | 100.22 | 100.21 | 100.07 | 100.17 | 100.25 | 99.99 | 100.05 | 100.14 | 99.97 | 100.18 | 100.16 |
| Si ppm | 393 | 402 | 323 | 351 | 299 | 285 | 584 | 1692 | 2674 | 2286 | 1430 | 1398 |
| Fe ppm | 575 | 396 | 202 | 630 | 497 | 272 | b.d. | b.d. | 62 | b.d. | b.d. | b.d. |
| wt% | 15.84 | 17.16 | 18.48 | 19.8 | 21.12 | 22.44 | 23.76 | 25.08 | 26.4 | 27.72 | 29.04 | D.L. |
| SiO ₂ | 0.651 | 0.490 | 0.146 | 0.073 | 0.073 | 0.067 | 0.063 | 0.071 | 0.079 | 0.059 | 0.075 | 0.020 |
| TiO ₂ | 0.040 | b.d. | b.d. | b.d. | b.d. | b.d. | b.d. | 0.020 | b.d. | b.d. | b.d. | 0.015 |
| Al ₂ O ₃ | 99.47 | 99.53 | 99.67 | 100.05 | 100.08 | 100.19 | 100.23 | 100.20 | 100.11 | 99.91 | 100.07 | 0.023 |
| Fe ₂ O ₃ | b.d. | 0.008 | b.d. | 0.009 | 0.083 | 0.072 | 0.059 | 0.089 | 0.042 | 0.026 | 0.058 | 0.005 |
| Total | 100.17 | 100.03 | 99.82 | 100.15 | 100.25 | 100.33 | 100.36 | 100.38 | 100.23 | 99.99 | 100.20 | - |
| Si ppm | 3043 | 2291 | 683 | 341 | 341 | 313 | 295 | 332 | 369 | 276 | 351 | - |
| Fe ppm | b.d. | 54 | b.d. | 62 | 583 | 505 | 412 | 622 | 295 | 179 | 404 | - |

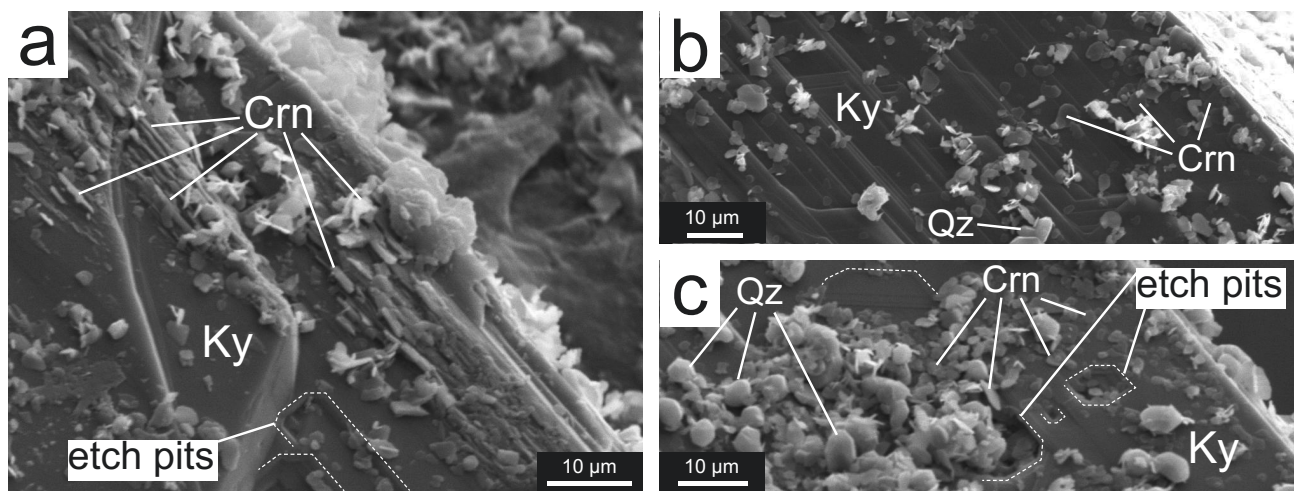


Fig. A5.1 SE images SEM of products of run 43 (decompression experiment). a) Ky seed with oriented Crn-plates grown on the surface and etch pit features, which indicate Ky dissolution. b) Ky grain surface with terrace structure and randomly distributed Qz and Crn precipitates. c) Ky etch pits next to Qz-Crn precipitates.

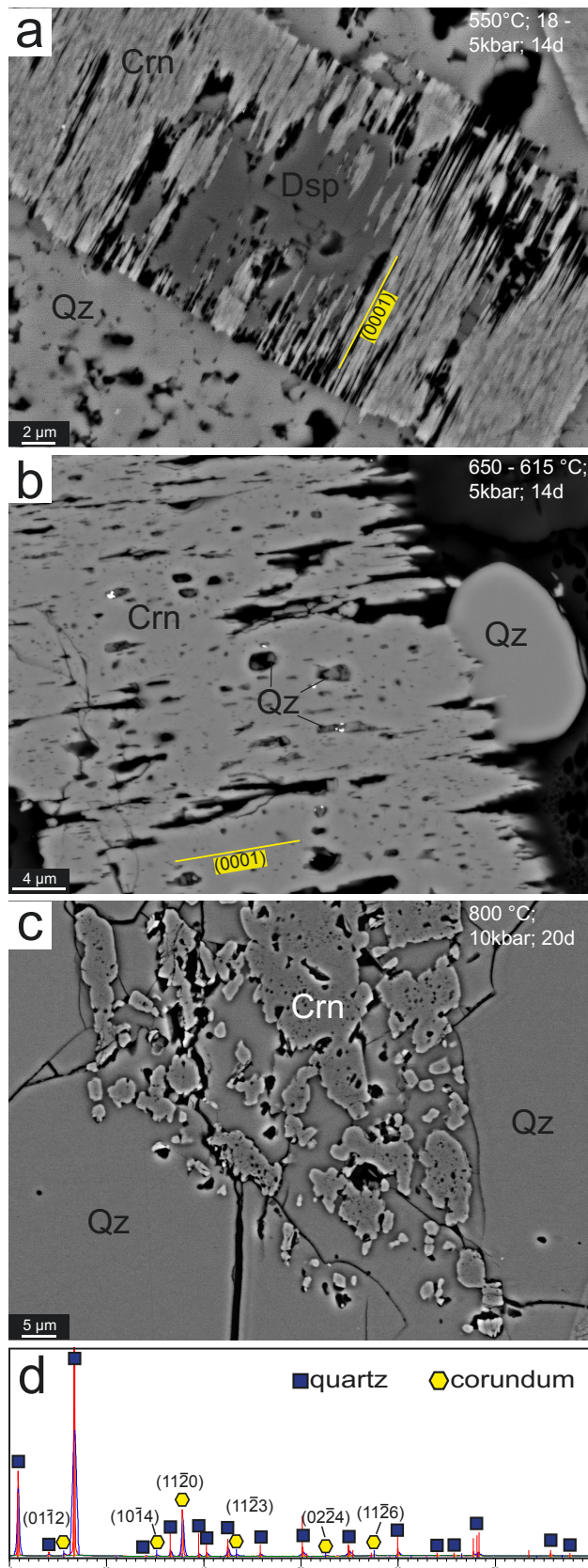


Fig. A5.2 a) Less than 200 nm wide, parallel Crn plates formed pseudomorph after diasporite (Dsp) in Qz matrix at 550°C (BSE; run 40). b) Crn after Dsp at 650-615°C, Crn plates are up to 3 μm thick and contain elongated quartz inclusions inside the plates and between inter-grown individuals (BSE; run 38). c) Crn after Dsp at 800°C is rounded and contains rounded Qz inclusions (BSE; run 34). d) XRD pattern of the experiment 38 in b, showing a disproportionately high (11 $\bar{2}$ 0) peak compared with the rest of the Crn spectra (raw XRD data of runs 35, 36, 37, 38, 39 in Tab. A5.3).

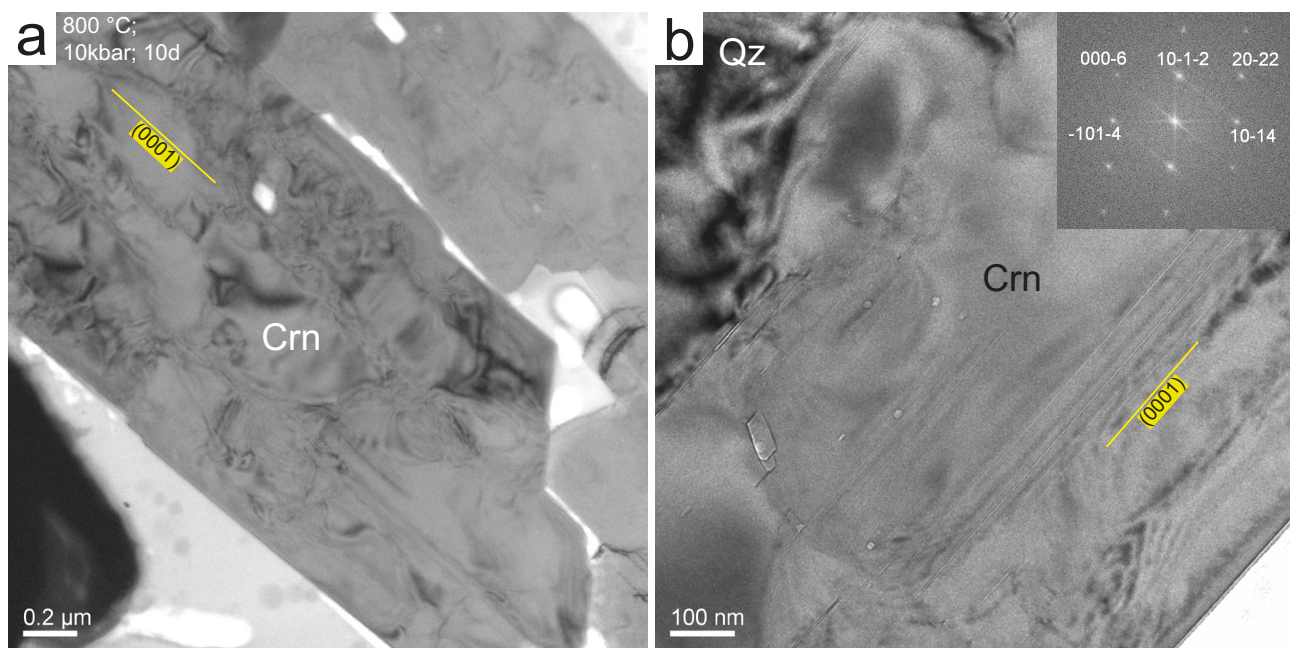


Fig. A5.3 TEM bright field images of Crn plates fromed in run 2, a) Crn grain with SNLs and numerous lattice defects. b) Crn grain with SNLs and fluid inclusion, the electron diffraction pattern of Crn shows the typical streak patetrn in [0001].

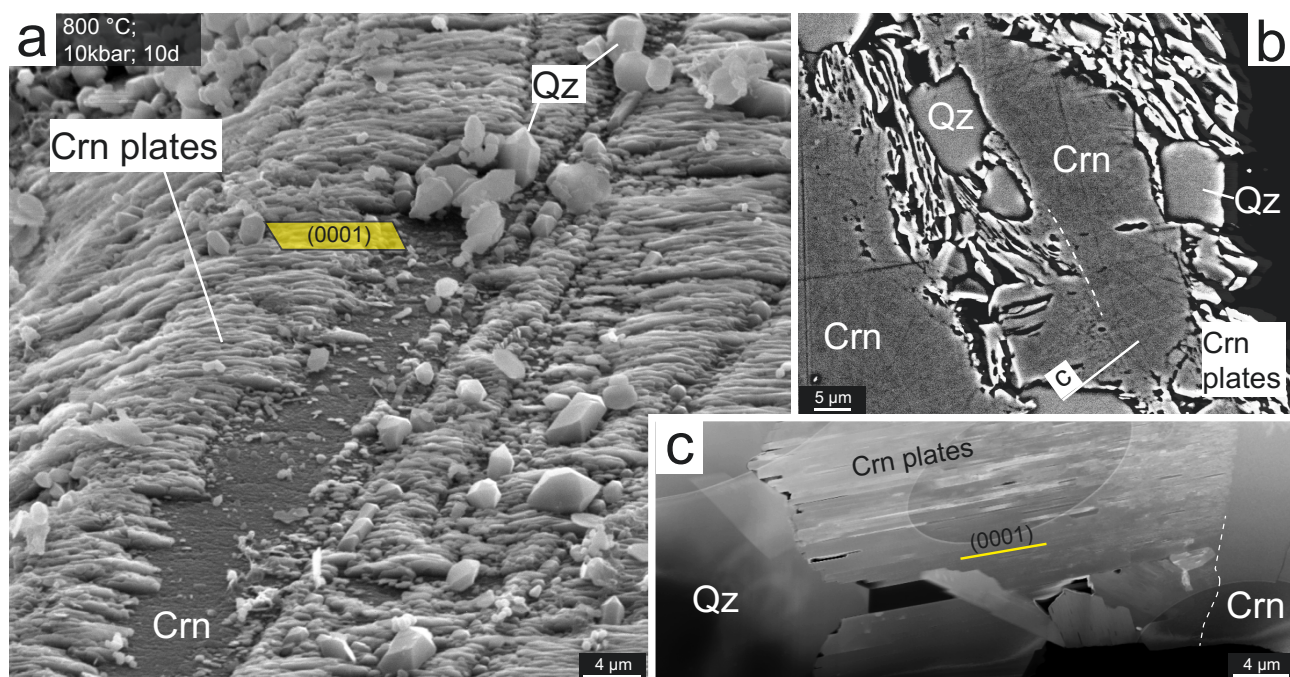


Fig. A5.4 a) Se image of Crn plates epitactically grown on Crn single crystal in run 39. b) Crn plate-reaction rim on single crystals, including Qz grains, the contact between plate rim and single crystal is indicated with a white dashed line (BSE; run 33). c) TEM foil (HAADF image) overview of a foil cut through Crn single crystal (on the right), plate rim (with identically oriented but not inter-grown Crn plates)(middle), and neighboring Qz grain (on the left)(foil position is indicated in b).

Table A5.1. Experimental quartz of runs 40, 34, 33 with elevated **Al-concentrations** (WDS results EMP)

| wt% | Run 34 (650-615°C) | | Run 33 (650°C) | | Run 40 (800°C) | | DL [ox. wt%] |
|------------------------------------|--------------------|--------------|----------------|--------------|----------------|--------------|-----------------|
| | 1 | 2 | 1 | 2 | 1 | 2 | |
| SiO ₂ | 96.86 | 96.64 | 95.29 | 97.15 | 95.20 | 98.37 | 0.009 |
| TiO ₂ | b.d. | b.d. | b.d. | 0.022 | b.d. | 0.013 | 0.009 |
| Al₂O₃ | 0.062 | 0.058 | 0.732 | 0.203 | 0.205 | 0.131 | 0.005 |
| Cr ₂ O ₃ | b.d. | b.d. | b.d. | b.d. | 0.011 | 0.064 | 0.006 |
| FeO | 0.018 | 0.017 | 0.015 | b.d. | b.d. | b.d. | 0.010 |
| Total | 96.95 | 96.72 | 96.04 | 97.37 | 95.45 | 98.61 | - |

Table A5.2. Experimental metastable corundum from run 2, 33, 34, and 38 with elevated SiO₂-concentrations (WDS results EMP)

| wt% | Run 34 | | | | | Run 33 | | | D.L. [ox.wt%] |
|--------------------------------|--------------|---------------|--------------|--------------|--------------|--------------|--------------|--------------|------------------|
| | 1 | 2 | 3 | 4 | 5 | 1 | 2 | 3 | |
| SiO₂ | 2.760 | 10.830 | 3.480 | 0.178 | 0.241 | 5.720 | 4.650 | 4.590 | 0.006 |
| TiO ₂ | 0.043 | 0.071 | 0.028 | 0.060 | 0.070 | b.d. | 0.050 | 0.027 | 0.010 |
| Al ₂ O ₃ | 94.92 | 89.36 | 93.67 | 99.02 | 98.69 | 92.14 | 94.16 | 95.03 | 0.007 |
| V ₂ O ₃ | b.d. | b.d. | 0.071 | 0.023 | 0.013 | 0.031 | 0.038 | 0.053 | 0.011 |
| Cr ₂ O ₃ | b.d. | 0.010 | b.d. | b.d. | b.d. | 0.014 | b.d. | 0.018 | 0.006 |
| FeO | 0.594 | 0.641 | 0.547 | 0.619 | 0.425 | 0.255 | 0.196 | 0.204 | 0.010 |
| Total | 98.33 | 100.91 | 97.80 | 99.93 | 99.44 | 98.16 | 99.11 | 99.94 | - |
| wt% | Run 38 | | | | | | Run 2 | | |
| | 1 | 2 | 3 | 4 | 5 | 6 | 1 | 2 | 3 |
| SiO₂ | 0.655 | 0.246 | 0.106 | 0.083 | 0.467 | 0.412 | 1.169 | 1.632 | 0.217 |
| TiO ₂ | 0.107 | 0.057 | 0.044 | 0.056 | 0.031 | 0.051 | 0.039 | 0.024 | 0.023 |
| Al ₂ O ₃ | 98.81 | 98.95 | 99.21 | 99.49 | 98.76 | 99.18 | 87.53 | 87.52 | 90.61 |
| V ₂ O ₃ | 0.037 | b.d. | b.d. | b.d. | 0.015 | b.d. | 0.125 | 0.077 | 0.024 |
| Cr ₂ O ₃ | 0.029 | b.d. | b.d. | b.d. | b.d. | b.d. | 9.240 | 5.130 | 2.600 |
| FeO | 0.368 | 0.378 | 0.318 | 0.274 | 0.229 | 0.306 | b.d. | 0.025 | 0.011 |
| Total | 100.01 | 99.63 | 99.68 | 99.90 | 99.54 | 99.97 | 98.12 | 94.41 | 93.50 |

Table A5.3. XRD raw data of runs 35, 36, 37, 38, 39 (Tab. 2.1); Qz (red), Crn (green, bold), Prl (blue), Rt (violet), unidentified peaks in italic (likely a Na-clay, e.g. sodalite, or bicchulite)

| Run 35 | | | Run 36 | | | Run 37 | | | Run 38 | | | Run 39 | | |
|--------------|---------------|-------------|--------------|---------------|-------------|--------------|---------------|-------------|--------------|---------------|-------------|--------------|---------------|-------------|
| Pos. [°2Th.] | Counts [ct/s] | d-value [Å] | Pos. [°2Th.] | Counts [ct/s] | d-value [Å] | Pos. [°2Th.] | Counts [ct/s] | d-value [Å] | Pos. [°2Th.] | Counts [ct/s] | d-value [Å] | Pos. [°2Th.] | Counts [ct/s] | d-value [Å] |
| 9.6423 | 99.69 | 9.17285 | 9.6117 | 218.68 | 9.20195 | 9.3734 | 49.75 | 9.43539 | 9.7118 | 35.58 | 9.10739 | 9.4877 | 67.51 | 9.32194 |
| 17.8464 | 54.18 | 4.97025 | 19.3116 | 40.9 | 4.59632 | 18.8693 | 809.11 | 4.70306 | 18.8306 | 65.57 | 4.71265 | 20.8538 | 1552.92 | 4.25977 |
| 18.87 | 61.84 | 4.70288 | 20.8623 | 504.86 | 4.25805 | 20.8814 | 1590.64 | 4.2542 | 20.8857 | 8869.52 | 4.25334 | 23.9813 | 28.92 | 3.71086 |
| 20.8844 | 2994.76 | 4.25359 | 25.7111 | 25.98 | 3.46498 | 24.0438 | 171.75 | 3.70135 | 24.0528 | 208.34 | 3.69998 | 25.5871 | 98.22 | 3.48149 |
| 24.0444 | 124.01 | 3.70125 | 26.6525 | 1906.25 | 3.3447 | 25.6362 | 132.87 | 3.47493 | 25.6286 | 249.93 | 3.47595 | 26.6407 | 3330.63 | 3.34615 |
| 26.6767 | 5802.63 | 3.34171 | 29.1571 | 90.22 | 3.06283 | 26.6727 | 4253.27 | 3.34221 | 26.6741 | 16222.81 | 3.34203 | 27.4548 | 1065.09 | 3.24875 |
| 36.5887 | 480.61 | 2.456 | 35.1906 | 44.63 | 2.55031 | 35.2043 | 148.97 | 2.54935 | 34.0376 | 72.38 | 2.63401 | 35.1598 | 86.87 | 2.55247 |
| 38.1172 | 20.72 | 2.36096 | 36.5697 | 54.75 | 2.45724 | 36.5783 | 205.95 | 2.45668 | 35.1873 | 176.54 | 2.55054 | 36.108 | 265.32 | 2.48759 |
| 39.5219 | 279.01 | 2.28023 | 37.8129 | 74.46 | 2.37926 | 37.8117 | 99.95 | 2.37933 | 36.5956 | 693.97 | 2.45556 | 37.8121 | 49.39 | 2.37931 |
| 40.3404 | 171.57 | 2.23583 | 39.5009 | 38.77 | 2.28139 | 38.2218 | 259.08 | 2.35474 | 37.8157 | 5414.96 | 2.37909 | 39.4918 | 114.91 | 2.2819 |
| 42.5061 | 331.5 | 2.1268 | 40.28 | 44.15 | 2.23904 | 39.5237 | 142.57 | 2.28013 | 39.5237 | 313.52 | 2.28013 | 40.3073 | 59.48 | 2.23759 |
| 45.8449 | 160.83 | 1.97937 | 42.4834 | 53.47 | 2.12788 | 40.3443 | 59.99 | 2.23563 | 40.3538 | 384.77 | 2.23512 | 41.2764 | 101.98 | 2.18727 |
| 50.1529 | 561.67 | 1.81899 | 43.3975 | 35.34 | 2.08516 | 42.4855 | 216.96 | 2.12778 | 42.5098 | 1123.87 | 2.12662 | 42.4664 | 214.48 | 2.12869 |
| 55.0106 | 79.73 | 1.66931 | 45.8585 | 23.42 | 1.97882 | 43.4105 | 118.93 | 2.08456 | 43.4021 | 250.55 | 2.08494 | 43.3951 | 88.64 | 2.08527 |
| 60.0186 | 243.58 | 1.54144 | 50.1723 | 64.66 | 1.81833 | 45.8349 | 64.47 | 1.97979 | 45.8594 | 276.58 | 1.97878 | 44.0504 | 31.55 | 2.05575 |
| 64.1231 | 40.04 | 1.45232 | 55.1305 | 13.68 | 1.66596 | 50.1865 | 213.43 | 1.81785 | 50.1929 | 456.43 | 1.81763 | 45.7976 | 51.09 | 1.98131 |
| 68.2838 | 183.71 | 1.37362 | 57.5617 | 22.4 | 1.60125 | 52.6668 | 31.7 | 1.73793 | 52.6145 | 95.28 | 1.73954 | 50.1622 | 130.76 | 1.81868 |
| 73.594 | 18.72 | 1.28708 | 59.938 | 27.73 | 1.54332 | 54.9423 | 56.04 | 1.67122 | 53.7347 | 28.57 | 1.70589 | 52.5932 | 33.5 | 1.74019 |
| 75.7058 | 50.47 | 1.25634 | 68.2719 | 56.83 | 1.37269 | 57.5943 | 82.06 | 1.60042 | 54.9584 | 530.95 | 1.67077 | 54.36 | 114.81 | 1.68774 |
| 77.6777 | 34.84 | 1.22829 | | | | 60.0084 | 86.35 | 1.54168 | 57.5176 | 116 | 1.60237 | 54.8557 | 179.65 | 1.67365 |
| 79.8817 | 36.21 | 1.20084 | | | | 64.1073 | 30.71 | 1.45264 | 60.0366 | 427.32 | 1.54102 | 56.6787 | 76.88 | 1.62408 |
| | | | | | | 67.8038 | 149.81 | 1.38217 | 64.1182 | 36.81 | 1.45242 | 57.5545 | 62.45 | 1.60143 |
| | | | | | | 68.2577 | 111.85 | 1.37408 | 65.8684 | 20.94 | 1.41801 | 59.9657 | 89.95 | 1.54267 |
| | | | | | | 73.5171 | 26.38 | 1.28824 | 66.5428 | 21.11 | 1.40527 | 64.0682 | 28.88 | 1.45344 |
| | | | | | | 75.7207 | 21.98 | 1.25509 | 67.7912 | 257.12 | 1.3824 | 67.7061 | 162.03 | 1.38393 |
| | | | | | | 79.8917 | 35.7 | 1.20072 | 68.2938 | 361.69 | 1.37344 | 68.2559 | 89.33 | 1.37411 |
| | | | | | | | | | 75.7326 | 138.31 | 1.25596 | 69.1054 | 24.95 | 1.35928 |
| | | | | | | | | | 77.7189 | 35.13 | 1.22774 | 69.8739 | 25.62 | 1.34509 |
| | | | | | | | | | 79.8965 | 464.49 | 1.20066 | | | |

Appendix chapter 7

Table A7.1. Whole rock data (XRF) of the muscovite-rich domain and kyanite-quartz layer (Fig. 7.1; Greiner shear-zone, Italian Alps)

| wt% | Ms-layer | Ky-layer | D.L |
|--------------------------------|----------|----------|-------|
| SiO ₂ | 48.71 | 49.59 | 38.00 |
| Al ₂ O ₃ | 27.72 | 28.31 | 0,20 |
| Fe ₂ O ₃ | 5.53 | 9.76 | 0,50 |
| MgO | 3.41 | 4.11 | 0,04 |
| CaO | 0.59 | 1.28 | 0,05 |
| Na ₂ O | 1.47 | 1.34 | 0,40 |
| K ₂ O | 7.97 | 2.83 | 0,10 |
| TiO ₂ | 1.19 | 1.1 | 0,10 |
| P ₂ O ₅ | 0.13 | 0.11 | 0,10 |
| SO ₃ | b.d. | b.d. | 0,05 |
| L.O.I | 3.33 | 1.53 | |
| Total | 100.334 | 100.66 | |
| ppm | | | |
| As | 4 | 3.9 | 4 |
| Ba | 1167.2 | 360.3 | 20 |
| Ce | b.d. | b.d. | 20 |
| Co | 10.7 | 7.2 | 3 |
| Cr | 561 | 962.9 | 10 |
| Cu | 10 | b.d. | 7 |
| F | b.d. | b.d. | 500 |
| Ga | 31 | 26 | 3 |
| La | b.d. | 15.6 | 10 |
| Mn | 131 | 2476 | 30 |
| Nb | 10.3 | 18.3 | 5 |
| Nd | b.d. | 12.8 | 10 |
| Ni | 40.4 | 48.9 | 3 |
| Pb | 6 | 15 | 5 |
| Pr | b.d. | b.d. | 10 |
| Rb | 165 | 96 | 10 |
| Sm | 4 | b.d. | 3 |
| Sn | b.d. | b.d. | 20 |
| Sr | 250 | 99 | 10 |
| Th | 10 | 13 | 5 |
| V | 198 | 187 | 10 |
| Y | 8.1 | 103.3 | 5 |
| Zn | 25 | 30 | 10 |
| Zr | 213 | 221 | 10 |

Table A7.2. Kyanite chemistry in different Ky-Qz veins (V1 and V2), major elements are WDS results (EMP), trace elements are LA-ICP-MS data, for V2 zonation colors are indicated (see Fig. 7.2).

| | V1-kyanite | | | | | | | V2-kyanite | | | | | | | | | | DL (EMP) |
|--------------------------------|------------|-----------|-----------|-----------|-----------|-----------|-----------|------------|--------|--------|--------|--------|-------|--------|-----------|-----------|-----------|----------|
| color | 1 | 2 | 3 | 4 | 5 | 6 | 7 | 1 | 2 | 3 | 4 | 5 | 6 | 7 | 8 | 9 | 10 | |
| | colorless | colorless | colorless | colorless | colorless | colorless | colorless | blue | blue | blue | blue | blue | blue | blue | colorless | colorless | colorless | |
| wt% (EMP) | | | | | | | | | | | | | | | | | | |
| SiO ₂ | 37.04 | 37.08 | 37.17 | 37.16 | 37.27 | 36.92 | 37.21 | 37.15 | 37.18 | 37.17 | 36.99 | 37.19 | 37.08 | 37.21 | 37.17 | 37.25 | 37.11 | 0.013 |
| TiO ₂ | b.d. | b.d. | b.d. | b.d. | b.d. | b.d. | b.d. | b.d. | b.d. | b.d. | 0.037 | 0.039 | 0.032 | b.d. | b.d. | b.d. | b.d. | 0.010 |
| Al ₂ O ₃ | 62.77 | 62.71 | 62.75 | 62.91 | 62.89 | 62.69 | 62.81 | 62.50 | 62.59 | 62.51 | 62.59 | 62.60 | 62.55 | 62.78 | 62.70 | 63.01 | 62.55 | 0.011 |
| V ₂ O ₃ | b.d. | b.d. | b.d. | b.d. | b.d. | b.d. | b.d. | b.d. | b.d. | b.d. | b.d. | b.d. | b.d. | 0.011 | b.d. | b.d. | b.d. | 0.007 |
| Cr ₂ O ₃ | b.d. | b.d. | b.d. | b.d. | b.d. | b.d. | b.d. | b.d. | 0.029 | b.d. | b.d. | b.d. | b.d. | b.d. | b.d. | b.d. | b.d. | 0.004 |
| Fe ₂ O ₃ | 0.064 | 0.044 | 0.038 | 0.036 | 0.056 | 0.067 | 0.052 | 0.324 | 0.302 | 0.263 | 0.260 | 0.261 | 0.234 | 0.217 | 0.191 | 0.194 | 0.249 | 0.008 |
| Total | 99.87 | 99.83 | 99.96 | 100.11 | 100.21 | 99.67 | 100.07 | 99.97 | 100.10 | 99.94 | 99.88 | 100.09 | 99.90 | 100.22 | 100.07 | 100.45 | 99.91 | - |
| ppm (LA-ICP-MS) | | | | | | | | | | | | | | | | | | |
| Mg | 110.58 | 70.25 | 43.6 | 20.77 | 98.12 | 178.08 | 44.14 | 52.62 | 41.28 | 35.84 | 27.59 | 36.86 | 31 | 24.92 | 46.92 | 45.21 | 56.2 | |
| Ti | 39.32 | 27.04 | 8.98 | 2.99 | 67.49 | 126 | 31.71 | 253.31 | 208.99 | 202.68 | 210.32 | 235.26 | 203.8 | 109.97 | 26.75 | 11.17 | 15.11 | |
| V | 4.89 | 4.74 | 6.51 | 4.54 | 4.75 | 4.71 | 5.09 | 41.8 | 36.94 | 34.17 | 36.16 | 36.12 | 37.6 | 34.43 | 36.72 | 32.35 | 29.8 | |
| Cr | b.d. | 3.345 | 0.542 | 1.304 | 0.964 | 2.225 | 3.533 | 4.35 | b.d. | 3.57 | 3.87 | 2.96 | 4.75 | 2.84 | 1.35 | 3.219 | 1.88 | |
| Mn | b.d. | 4.807 | 2.951 | 1.461 | 6.246 | 17.203 | 2.602 | b.d. | b.d. | 1.24 | 0.33 | 0.23 | 1.29 | b.d. | b.d. | 0.472 | 1.34 | |
| Fe | 499 | 446 | 356 | 269 | 414 | 542 | 370 | 1994 | 1901 | 1848 | 1855 | 1927 | 1852 | 1875 | 1445 | 1610 | 1834 | |
| Zn | 494.34 | 285.56 | 137.69 | 24.34 | 318.27 | 757.9 | 170.16 | 1.03 | 3.1 | b.d. | 0.14 | 2.93 | 3.4 | 0.2 | 0.329 | 0.925 | 30.36 | |
| Nb | 2.45 | 1.7 | 0.14 | 0.02 | 3.75 | 11.52 | 7.09 | 0.015 | b.d. | 0.007 | 0.013 | 0.008 | 0.002 | 0.013 | b.d. | 0.1 | 0.003 | |
| Pb | 0.645 | 0.604 | 0.531 | 0.419 | 0.75 | 0.521 | 0.432 | 0.051 | 0.032 | 0.019 | 0.045 | b.d. | 0.004 | 0.044 | 0.041 | 0.053 | 0.03 | |
| Th | 0.017 | 0.003 | 0.02 | 0.002 | 0.022 | 0.013 | 0.032 | b.d. | 0.007 | b.d. | b.d. | 0.001 | 0.001 | b.d. | b.d. | 0.003 | b.d. | |
| U | 0.007 | b.d. | 0.012 | 0.006 | 0.008 | 0.002 | 0.015 | b.d. | b.d. | b.d. | 0.001 | b.d. | b.d. | b.d. | 0.002 | b.d. | b.d. | |
| Y | 0.04 | b.d. | 0.04 | b.d. | 0.11 | 0.03 | b.d. | 0.02 | b.d. | 0.03 | b.d. | 0.01 | 0.03 | b.d. | 0.02 | 0.02 | 0.02 | |
| Hf | b.d. | b.d. | b.d. | 0.02 | b.d. | 0.01 | b.d. | b.d. | b.d. | 0.01 | b.d. | b.d. | b.d. | b.d. | b.d. | b.d. | b.d. | |
| Ta | 0.041 | 0.023 | 0.002 | 0.009 | 0.104 | 0.275 | 0.228 | b.d. | 0.002 | 0.007 | 0.006 | 0.009 | 0.005 | b.d. | 0.002 | 0.018 | 0.003 | |

Table A7.3. Interstitial glass composition in selvage of Ky-Qz layer (Fig. 7.3, Greiner shear-zone) (EDS results EMP)

| | | | | | | | |
|--------------------------------|-------|-------|-------|-------|-------|-------|-------|
| SiO ₂ | 65.44 | 72.59 | 68.63 | 76.84 | 75.24 | 79.11 | 87.73 |
| Al ₂ O ₃ | 18.86 | 20.92 | 13.43 | 7.92 | 8.11 | 3.85 | 2.44 |
| MgO | 0.00 | 0.00 | 0.27 | 0.00 | 0.10 | 0.00 | 0.00 |
| FeO | 0.00 | 0.00 | 0.36 | 0.00 | 0.09 | 0.00 | 0.00 |
| Na ₂ O | 0.69 | 0.00 | 0.36 | 0.00 | 0.19 | 0.00 | 0.00 |
| K ₂ O | 5.16 | 0.00 | 3.25 | 0.00 | 1.36 | 0.19 | 0.57 |
| Total | 90.14 | 93.50 | 86.31 | 84.76 | 85.09 | 83.16 | 90.74 |

Table A7.4. Kyanite element profile A-B; see Fig. 7.4a' (WDS results EMP)

| wt% | μm distance to A | | | | | | | | | | | | |
|--------------------------------|------------------|-------|-------|--------|-------|--------|-------|--------|--------|--------|--------|--------|--------|
| | 0 | 15 | 30 | 45 | 60 | 75 | 90 | 105 | 120 | 135 | 150 | 165 | 180 |
| SiO ₂ | 36.69 | 36.69 | 36.80 | 36.83 | 36.86 | 36.90 | 36.86 | 36.79 | 36.88 | 36.86 | 36.43 | 36.56 | 36.66 |
| TiO ₂ | 0.006 | 0.003 | 0.005 | 0.018 | 0.014 | 0.003 | 0.023 | 0.034 | 0.024 | 0.023 | 0.059 | 0.048 | 0.085 |
| Al ₂ O ₃ | 62.02 | 61.72 | 61.78 | 61.67 | 61.80 | 62.05 | 61.84 | 62.16 | 62.05 | 62.22 | 61.84 | 61.94 | 62.27 |
| Cr ₂ O ₃ | 0.136 | 0.376 | 0.320 | 0.420 | 0.414 | 0.311 | 0.356 | 0.297 | 0.313 | 0.334 | 0.355 | 0.281 | 0.123 |
| Fe ₂ O ₃ | 0.271 | 0.309 | 0.237 | 0.375 | 0.370 | 0.324 | 0.401 | 0.341 | 0.399 | 0.386 | 0.780 | 0.566 | 0.479 |
| V ₂ O ₃ | 0.031 | 0.035 | 0.038 | 0.034 | 0.041 | 0.037 | 0.047 | 0.035 | 0.046 | 0.038 | 0.037 | 0.035 | 0.038 |
| Total | 99.15 | 99.13 | 99.18 | 99.35 | 99.50 | 99.62 | 99.53 | 99.66 | 99.71 | 99.86 | 99.50 | 99.43 | 99.65 |
| wt% | μm distance to A | | | | | | | | | | | | |
| | 195 | 210 | 225 | 240 | 255 | 270 | 285 | 300 | 315 | 330 | 345 | 360 | 375 |
| SiO ₂ | 36.63 | 36.77 | 36.77 | 36.92 | 37.00 | 37.12 | 36.89 | 36.86 | 36.23 | 37.13 | 37.18 | 35.07 | 36.62 |
| TiO ₂ | 0.089 | 0.047 | 0.041 | 0.040 | 0.030 | 0.107 | 0.107 | 0.078 | 0.024 | 0.026 | 0.000 | 0.016 | 0.054 |
| Al ₂ O ₃ | 62.18 | 62.21 | 62.17 | 62.26 | 62.47 | 62.34 | 62.26 | 62.32 | 63.21 | 62.39 | 62.57 | 61.19 | 61.99 |
| Cr ₂ O ₃ | 0.104 | 0.124 | 0.229 | 0.263 | 0.086 | 0.076 | 0.050 | 0.053 | 0.043 | 0.141 | 0.116 | 0.247 | 0.238 |
| Fe ₂ O ₃ | 0.540 | 0.482 | 0.473 | 0.421 | 0.365 | 0.344 | 0.590 | 0.658 | 0.581 | 0.362 | 0.225 | 0.468 | 0.786 |
| V ₂ O ₃ | 0.030 | 0.044 | 0.041 | 0.047 | 0.034 | 0.031 | 0.028 | 0.032 | 0.034 | 0.051 | 0.024 | 0.041 | 0.026 |
| Total | 99.57 | 99.68 | 99.72 | 99.95 | 99.98 | 100.02 | 99.93 | 100.00 | 100.12 | 100.10 | 100.12 | 97.03 | 99.71 |
| wt% | μm distance to A | | | | | | | | | | | | |
| | 390 | 405 | 420 | 435 | 450 | 465 | 480 | 495 | 510 | 525 | 540 | 555 | D.L. |
| SiO ₂ | 36.61 | 36.94 | 37.05 | 37.31 | 35.96 | 36.97 | 36.85 | 36.84 | 37.05 | 37.19 | 37.14 | 37.16 | 0.0019 |
| TiO ₂ | 0.050 | 0.088 | 0.116 | 0.088 | 0.065 | 0.059 | 0.055 | 0.030 | 0.017 | 0.022 | 0.015 | 0.021 | 0.0023 |
| Al ₂ O ₃ | 61.94 | 62.21 | 62.23 | 62.04 | 61.22 | 62.24 | 62.22 | 62.06 | 62.08 | 62.27 | 62.31 | 62.18 | 0.0034 |
| Cr ₂ O ₃ | 0.227 | 0.186 | 0.212 | 0.232 | 0.217 | 0.191 | 0.188 | 0.350 | 0.468 | 0.386 | 0.256 | 0.423 | 0.0016 |
| Fe ₂ O ₃ | 0.863 | 0.502 | 0.308 | 0.439 | 0.516 | 0.468 | 0.537 | 0.554 | 0.473 | 0.391 | 0.334 | 0.411 | 0.0026 |
| V ₂ O ₃ | 0.039 | 0.043 | 0.044 | 0.038 | 0.036 | 0.030 | 0.029 | 0.038 | 0.042 | 0.049 | 0.026 | 0.049 | 0.0025 |
| Total | 99.73 | 99.97 | 99.96 | 100.15 | 98.01 | 99.96 | 99.88 | 99.87 | 100.13 | 100.31 | 100.08 | 100.24 | - |

Table A7.5. Run 5 kyanite chemistry (WDS results EMP), glass chemistry (EDS results EMP)

| wt% | Kyanite run 36 | | D.L. | wt% | REE rich glass | REE free glass |
|--------------------------------|----------------|--------|-------|--------------------------------|----------------|----------------|
| SiO ₂ | 37.15 | 37.14 | 0.006 | SiO ₂ | 46.51 | 65.31 |
| TiO ₂ | 0.010 | 0.012 | 0.010 | Al ₂ O ₃ | 13.68 | 17.87 |
| Al ₂ O ₃ | 62.11 | 62.05 | 0.007 | La ₂ O ₃ | 6.38 | 0.00 |
| V ₂ O ₃ | 0.013 | b.d. | 0.011 | Ce ₂ O ₃ | 11.47 | 0.00 |
| Cr ₂ O ₃ | b.d. | b.d. | 0.006 | MgO | 0.70 | 0.00 |
| Nb ₂ O ₅ | 0.018 | b.d. | 0.013 | CaO | 0.00 | 4.63 |
| FeO | 1.053 | 0.984 | 0.010 | FeO | 10.73 | 0.00 |
| Total | 100.35 | 100.19 | - | Na ₂ O | 3.53 | 4.58 |
| | | | | K ₂ O | 0.00 | 1.45 |
| | | | | Cl | 0.61 | 0.62 |
| | | | | Total | 93.60 | 94.47 |

Table A7.6. Kyanite and corundum chemistry from Ky-Bt rock (Naxos) (WDS results EMP)

| wt% | Kyanite | Corundum | | D.L. [wt%] |
|--------------------------------|---------|-----------|-----------|------------|
| | | dark blue | colorless | |
| SiO ₂ | 37.04 | 0.02 | 0.28 | 0.007 |
| TiO ₂ | 0.000 | 0.493 | b.d. | 0.007 |
| Al ₂ O ₃ | 62.98 | 98.39 | 97.94 | 0.010 |
| Cr ₂ O ₃ | 0.012 | 0.047 | b.d. | 0.006 |
| MgO | 0.006 | - | 0.006 | 0.003 |
| FeO | 0.396 | 0.972 | 0.790 | 0.012 |
| Total | 100.43 | 99.93 | 99.02 | - |